Université du Québec
Institut National de la Recherche Scientifique
Centre Énergie Matériaux Télécommunications

On-surface formation of graphene-like materials through Ullmann coupling

Par

Galeotti Gianluca

Mémoire ou thèse présentée pour l'obtention du grade de
Philosophiae doctor (Ph.D.)
en sciences de l'énergie et des matériaux

Jury d'évaluation

Président du jury et examinateur interne	Emanuele Orgiu INRS-EMT
Examinateur externe	Fabio Cicoira Département de Génie Chimique Polytechnique Montréal
Examinateur externe	James D. Wuest Département de Chimie Université de Montréal
Directeur de recherche	Federico Rosei INRS-EMT

DEDICATION

To my family, to Federica and to those who are in my heart

«All truths are easy to understand once they are discovered;

the point is to discover them»

(Galileo Galilei)

ACKNOWLEDGEMENTS

First of all, I would like to thank Federico, he proposed me this PhD, and he gave me scientific freedom. This was not due, and I appreciate it. I would also like to give a sincere thanks to Giorgio. He is the reason why I moved to Canada, and his impact on my career has been huge. Hopefully, I repaid their trust with this work. I would also like to thank Josh and Maryam, my day-to-day supervisors. Josh taught me to be a scientist, and to follow my curiosity. Maryam taught me to let my voice be heard in the scientific world and guided me through my first publication. Heartfelt thanks go to Mark, Sarah and Fabyola, who have ensured that this thesis was correctly written, both in English and in French

Being a researcher is a full-time job, and study surface science means to spend ludicrous amount of time in the lab. Therefore I would like to thanks all the people that worked with me and helped me during the periods of work at INRS (Fabrizio, Daniele, Luca, Mark, Riccardo, Stefano, Sarah, Jennifer, Daling, Penghui, Dominik) at CNR, Université de Lorraine, Tor Vergata and anyone who shared time and gave me an hand inside a lab. I would also like to thank all the other students from INRS. It has been an experience, I met amazing people from everywhere in the world and I will bring with me all those experiences.

A big *thank you* goes to all my friends. They are a reason to hold on and to live life with a positive attitude, so thanks to all my childhood friends, my friend from Montreal, and to all the friends who shared my university experience.

I would like to thank my family. My parents, ready to support me during good and bad times, and encouraging me to face the challenges of life. My brother and all the other relatives. A special thanks goes to Federica, with whom I am sharing my life, who knows anything of me and still loves me. Without you I do not know if I would have found the strength and motivation needed, you are simply too important for me.

In the end, I want to thank and remember all the people with whom I shared moments of my life but now are gone. I will bring them in my heart forever.

STATEMENT OF ORIGINALITY

The work presented herein has been performed in its integrity by the author during his PhD years. The experimental part of the thesis (Chapters 3 to 6) is based upon published works, in which the Author was either first author or part of the collaboration. The role of the Author in each work is reported at the beginning of the chapter, but it can be summarized as the following: all experimental procedures, from sample preparation and deposition to data analysis were developed or performed by the Author, sometimes in collaboration with other researchers (mostly Fabrizio De Marchi for STM experiments and Marco Di Giovannantonio for XPS and synchrotron beamline experiments). Theoretical calculations, namely DFT simulation and kinetic system modeling, have been performed by various collaborators, and the role of the author was to provide the initial structures or experimental data, apply the kinetic model to those data, and control the agreement of the calculations with the experimental results. The used molecular precursors were either bought from commercial sources or synthesized by collaborators from McGill University and Université Laval.

RÉSUMÉ

La réalisation de nano-dispositifs de quelques couches d'épaisseur est l'un des grands défis de la nanotechnologie. Cependant, le besoin de miniaturisation constante a introduit une nouvelle criticité qui pourrait casser l'équation électronique = silicium. Une solution possible pourrait être d'utiliser le graphène en tant qu'élément actif, car il s'agit d'un matériau naturel épais d'une couche possédant des propriétés optoélectroniques incroyables. Toutefois, l'inconvénient du graphène est sa bande interdite nulle, ce qui limite ses applications possibles. Cela a mené à l’étude de matériaux analogues au graphène, c’est-à-dire des polymères conjugués 1D et 2D aux propriétés accordables, développés par des approches ascendantes. L'objectif est d'utiliser les interactions molécule-molécule et molécule-substrat pour auto-assembler directement la structure souhaitée, ainsi que les manipuler pour obtenir un polymère étendu doté de la bonne architecture et de possibilités d’adaptation. Les réactions en surface sont une voie alternative à la réaction en solution, qui est l’approche habituellement utilisée pour obtenir la structure polymérique souhaitée. La présence de la surface permet de contrôler la dimensionnalité et de réaliser des réseaux 1D et 2D, tout en participant à la réaction en tant que source d’adatomes ou en jouant le rôle de catalyseur, abaissant les barrières d’énergie. Des nouvelles et intéressantes voies de réaction sont offertes par la surface, où des réactifs insolubles pourraient également être impliqués, mais une connaissance et un contrôle précis de tous les paramètres de réaction – en particulier des interactions critiques substrat-molécules – sont nécessaires pour exprimer pleinement le potentiel de cette approche. Dans cette thèse, nous explorerons les réactions en surface utilisées pour obtenir des polymères conjugués, en nous concentrant sur la réaction de couplage de Ullmann, tout en donnant des informations générales sur d'autres approches, telles que la polymérisation du diacétylène. Le couplage Ullmann en surface est la réaction la plus utilisée – et la plus efficace – pour la préparation ascendante de polymères conjugués 1D et 2D sur des substrats métalliques, avec des propriétés adaptées au choix du précurseur moléculaire. Celui-ci est établi comme le moyen principal de réaliser des matériaux analogues au graphène, c’est-à-dire des feuilles de graphène avec un taux de trame élevé ou avec une présence ordonnée d’hétéroatomes ou de lacunes. En combinant des techniques morphologiques (microscopie à effet tunnel) et compositionnelles (spectroscopie par photoémission), étayées par des modélisation théoriques (théorie de la densité fonctionnelle), nous avons exploré les paramètres de réaction afin de mieux comprendre le mécanisme réactionnel et la cinétique: l'effet de la couverture, de l'halogène, de la surface et des hétéroatomes soufrés ont été étudiés. Les résultats ont été mis en perspective pour permettre de mieux comprendre la formation de matériaux de l’ordre de la longue distance analogues au graphène .

Mots-clés: Science des surfaces, Polymérisation à la surface, Couplage Ullmann, Matériaux analogues au graphène, STM, XPS, Fast-XPS

ABSTRACT

The realization of few-layer thick nano-devices is one of the great challenges of nanotechnology. The need for constant miniaturization has however introduced new challenges that may break the electronics = silicon equation. A possible solution could be to use graphene as an active element, since it is a natural one-layer thick material with incredible opto-electronic properties. The downside of graphene is however its zero bandgap, which limits its possible applications. This led to the study of graphene-like materials, *i.e.* 1D and 2D conjugated polymers with tunable properties, grown through bottom-up approaches. The goal is to use molecule-molecule and molecule-substrate interactions to directly self-assemble the desired structure, and to further manipulate them into extended polymers with the correct architecture and tailoring possibilities.

On-surface reactions are an alternative route to the common solution-based approach to obtain the required polymeric structure. The presence of the surface enables control of the dimensionality, constrains the growth and allows realization of 1D and 2D networks, while at the same time participating in the reaction as a source of adatoms or working as a catalyst, lowering energy barriers. New and interesting reaction pathways are enabled by the surface, in which insoluble reagents can also be involved, but a precise knowledge and control of all the reaction parameters – in particular of the critical surface-molecule interactions – is necessary to fully convey the potential of this approach. In this thesis we will explore the on-surface reactions used to obtain conjugated polymers. The main focus will be on the Ullmann coupling reaction, but general information will be given on other approaches, such as diacetylene polymerization.

On-surface Ullmann coupling is the most used – and successful – reaction for the bottom-up preparation of 1D and 2D conjugated polymers on metallic substrates, with properties tailored by the choice of molecular precursor. It is established as the main way to realize graphene-like materials, *i.e.* graphene sheets with a high aspect ratio (*e.g.* nanoribbons) or with the ordered presence of heteroatoms or vacancies (*e.g.* porous graphene). By using a combination of morphological (scanning tunneling microscopy) and compositional (photoemission spectroscopy) techniques, supported by theoretical modeling (density functional theory), we explored the reaction parameters, to improve the understanding of the reaction mechanism and kinetics: the effect of the coverage, of the choice of halogen, of the surface and of including sulphur heteroatoms. The results were put into perspective to gain insight into the formation of long-range ordered graphene-like materials.

Keywords: Surface science, On-surface polymerization, Ullmann coupling, graphene-like materials, STM, XPS, fast-XPS.

TABLE OF CONTENTS

LIST OF ACRONYMS

a-Si – amorphous silicon
AES – Auger electron spectroscopy
AEY – Auger electron yield
Ar-X – aryl halides
ARPES – angle-resolved photoelectron spectroscopy
BCB – 1,4-bromoclorobenzene
BE – binding energy
CNTs – carbon nanotubes
CCM – Constant Current Mode
CHM – Constant Height Mode
CMOS – complementary metal-oxide semiconductor
CVD – thermal chemical vapor deposition
DBDA – di-benzonitrile-diacetylene
dCB – 1,4-dichlorobenzene
dBB – 1,4-dibromobenzene
dIB – 1,4-diiodobenzene
DFT – density functional theory
DOS – density of states
FET – field-effect transistors
finFETs – fin field-effect transistor
GNRs – graphene nanoribbons
HOCO – highest occupied crystal orbital
HOPG – highly oriented pyrolytic graphite samples
HREELS – high resolution electron energy loss spectroscopy
IBB – 1,4-iodobromobenzene
IntS – intermediate state
LEED – low-energy electron diffraction
LUCO – lowest unoccupied crystal orbital
MOF – metal-organic framework
MST – minimal spanning tree

NEXAFS – near edge X-ray absorption fine structure
OM – organometallic
OLED – organic light-emitting diodes
OFET – organic field-effect transistors
PEY – partial electron yield
PPP – poly-para-phenylene
SAMs – self-assembled monolayers
SET - single-electron transfer
SiO_2 – Silicon dioxide
SR – synchrotron radiation
STM – scanning tunneling microscopy
STS – scanning tunneling spectroscopy
TBB – 1,3,5-tris(4-bromophenyl)benzene
TEY – total electron yield
TIB – 1,3,5-tris(4-iodophenyl)benzene
TBTANG – tribromo-triangulene
TBTTB – tribromo-terthienobenzene
TFTs – thin-film transistors
TMDs – transition metal dichalcogenides
UHV – ultra-high vacuum
XPS – X-ray photoelectron spectroscopy

1 INTRODUCTION

Over the last several years, there has been a tremendous effort to develop new and innovative solutions that could revolutionize device design and fabrication.[1] This is due to the fact that silicon-based technology, though it has driven the semiconductor industry until now, could soon become unable to offer the ever-increasing need for constant miniaturization at the same time as improved device performance.[2-4] Therefore, a natural solution is to undertake a fundamental change, moving from the seemingly "doomed" silicon technology to something different, but the transition involves considerable challenges. For example, the isolation of graphene[5] and its development in the last decade has given rise to rejuvenated interest in carbon-based electronics. This interest is easily explained by the remarkable properties of this material[6-7] such as astonishingly-high thermal and electrical conductivity. Such properties can be exploited in various applications, from transistors,[8] to gas[9] (or even isotope[10]) separation, to nano-devices.[11] This is surprising for a material that based on thermodynamic considerations by Landau and others should not even exist.[12-13] Despite its unique properties, graphene's zero electronic bandgap limits its application in electronics. Recent studies have addressed this problem and tried to suggest some solutions,[14] however an easy and repeatable process to achieve this is still missing.

The flexibility of organic synthesis offers a broad playground to create organic analogues of graphene with high charge mobility and tunable bandgaps. Among organic materials, polymers can be commonly obtained through bottom-up building methods which result in small ordered structures. Therefore, instead of making graphene and then trying to modify it, a different and maybe more promising approach would be the bottom-up realization of different two-dimensional (2D) polymer analogues to graphene, with a different geometry in which heteroatoms could be incorporated. The idea is to identify processes that can couple small organic molecules into 2D polymers, where the building blocks can be chosen based on the desired properties. This *a priori* step could be performed using *ab initio* calculations.[15] It should be noted that in solution, polymers tend to fold and roll up, and to avoid this a possible solution is to constrain the growth on a surface, obtaining 1D or 2D polymers. The substrate can also be used as a catalyst, lowering energetic barriers and further guiding the reaction.[16] The result would be conjugated polymers with electronic band structures similar to that of graphene but with different properties (*e.g.* charge-carrier transport velocity and Fermi velocity) and an adjustable bandgap.

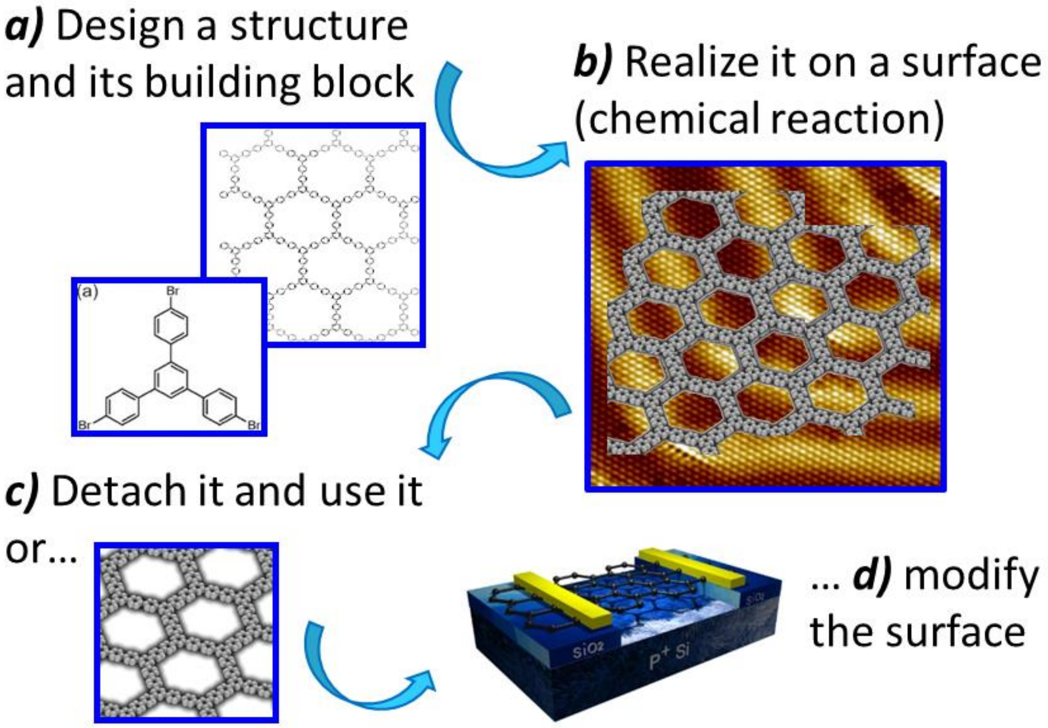

Figure 1-1 **Scheme of the necessary steps to realize devices using on-surface polymerization; a) the selected building block is chosen; b) it is dosed onto a surface where it reacts to form 2D polymers; at this point it can either be detached from the surface (c), or the underlying surface can be modified to obtain a working device (d).**

The whole process needed to realize practical devices starting from simple molecules is shown in Figure 1-1, which can be described as the take-away message of this thesis. From the pioneering works of Okawa and Aono,[17] most of the effort have been put into finding the right monomers and controlling the polymerization reaction,[18] which can result in the formation of 1D[19] and 2D[20] polymers. Accordingly many different reactions have been studied, such as polycondensation, Glaser Hay and Sonogashira coupling.[21-23] Once made, the properties of these materials will depend on the density of defects,[24] and therefore the chemical purity and the structural order are essential parameters to take into account for these systems. Although it is relatively easy to obtain long-range ordered molecular self-assembled monolayers (SAMs) on surfaces, such a level of order has not been achieved for covalently-bonded structures. The reversible nature of the intermolecular forces in a SAM yields enough surface mobility to the molecules to reach a minimum energy geometry, and results in large ordered domains. A possible approach to form long-range ordered covalent structures is to use a multi-step reaction, in which the molecules would arrange in such a way that the functional groups of the neighboring molecules can easily and efficiently interact. This step can then guide the formation of irreversible covalent bonds into the final ordered structure or network.[15, 25]

One of the most common reactions that expresses these features is Ullmann coupling, a two-step reaction which exploits the catalytic activity of a supporting transition metal substrate,[26] to de-halogenate aryl halide precursors, and subsequently couple the radicals into polymers.[27] Both steps are temperature dependent,[16] with the activation energy depending on the molecule[28] and the surface.[29] In most cases, the obtained structure after deposition on noble metal surfaces is an organometallic (OM) compound, the intermediate of the reaction that is stable up to the polymerization temperature.[30-31] Since the first report of an on-surface Ullmann reaction,[32] various groups tried to gain insight into the reaction mechanism and kinetics,[26-27, 33] however, we can safely state that, even after a decade of study, there are still open questions about these systems, regarding both the fundamental understanding and the practical realization of the process.[34]

The work presented in this thesis is focused on studying these questions, both from a fundamental point of view, studying the role of the halogen and the reaction mechanism of simple molecules (**Chapters 3-4**), and a practical perspective, guiding the reader through the difficulties of forming a two-dimensional organic structure (**Chapter 5**). **Chapter 6** will explore instead a different way to realize polymeric structures on a surface, namely diacetylene polymerization. The first two chapters will focus on the knowledge necessary to grasp the experimental results, with **Chapter 1** describing to the reader the “why” of the research and **Chapter 2** focusing on the “how”. The concluding **Chapter 7** will give an overview of the results obtained, how they fit within the existing literature, and how they could be further expanded and improved. **Chapter 8** will provide a summary of the thesis background and results for the French readers, while **Chapter 9** will include a list of references used in the text.

1.1 **Moore's Law**

Since the invention of the transistor in 1947, electronics has driven technological innovation, in what can be described as a historical revolution as important as the industrial revolution of the 18th century. Electronics is now fundamental to almost every device we use and most aspects of our life, to the point where it is quite hard to think about working, connecting with other people, or even spending one day without being affected by it.

The most impressive feat of this revolution is the remarkable speed with which it proceeded, to the point that nowadays a common chip made of billions of transistors has a size of a few millimeters. This rate of reduction in the transistor's size and cost was predicted by Gordon Moore in an article he wrote for Electronics Magazine.[35] Moore predicted that for each new generation of memory chip and microprocessor unit on the market, the device size would reduce by 33%, the chip size would increase by 50%, and the number of components on a chip would quadruple every three years.[2] This prediction has been valid for more than 50 years, and the technology industry still expects to follow an exponential increase in complexity of integrated circuits. However, as Greg Yerig, director of future silicon technology for ARM Research, said in 2017: "past progress in Moore's law has been achieved by implementing the easy ones. Now we are faced with more difficult choices".[36]

At the moment, the further scaling of transistors faces various problems from fundamental issues, such as the Abbe diffraction limit for photolithography or the Amdahl limit for parallel processing, to more specific ones related to device architecture and materials properties, such as the carrier mobility, gate oxide thickness, current leakage or cross-talk, and many more.[37-39]

One of the main problems that will need to be addressed is the oxide gate thickness.[2] Silicon dioxide (SiO_2) is an almost perfect insulator with a resistivity higher than 10^{16} Ω×cm. The insulating SiO_2 films grown on silicon are smooth and coherent, with no holes in a thickness range down to few atomic layers,[40] and only a few electrically active defects at the interface.[41] Such thin films are required to maintain the current response of the transistor to lower voltages at the gate electrode. But reducing the transistor size will require a reduction in the oxide thickness, and, as Figure 1-2 shows, such reduction will mean that parasitic resistance could become comparable to, or even exceed, the channel resistance.

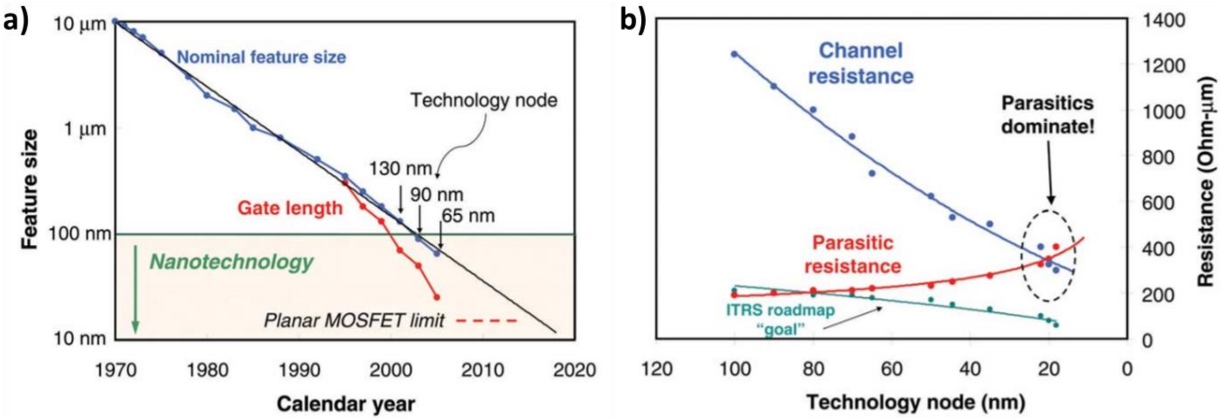

Figure 1-2 **a) evolution of the gate length for planar MOSFET up to the year 2020, and b) graph of the corresponding channel resistance vs the gate size. A limit for the gate size is obtained when the parasitic resistance dominates over the channel resistance. Adapted from Ref.[42]**

With Si complementary metal-oxide semiconductor (CMOS) scaling limits in sight, the obvious questions are "What nanotechnology is on the horizon to replace planar Si CMOS transistors and in what time frame can this happen?".[36] Though these are difficult and perhaps foolhardy questions to try and answer, it is important to attempt to do so since this affects a $330 billion worldwide industry and the careers of many engineers.[43] It is clear however that, to follow Moore's exponential growth, new ideas or even a change of paradigm are necessary.

1.2 Organic electronics

Solving the Si scaling problem is going to be challenging, and while some attempts have already been made to extend silicon life (such as multi chip technologies, or even changing the chip architecture by introducing the fin field-effect transistor (finFETs)),[44-45] one of the solutions could be breaking the electronics = silicon equation. A possible new player in this arena could be found in organic materials. Organic molecules have in fact been used as active components in electronic devices for years,[46] and their use continues to grow, guided both by the promise of cost reduction and by the possibility of introducing new features.[47] A practical example of this can be found in organic light-emitting diodes (OLED) for displays, which can be printed on lightweight and even flexible/foldable plastic substrates.[48]

The first report of organic conductive materials traces back to the work of Heeger, MacDiarmid and Shirakawa in the '70s, when they found that polyacetylene could become highly electrically conducting after undergoing a structural modification.[49-50] They observed an increase in the electrical conductivity of the materials by orders of magnitude after exposing it to vapors of I_2. The I_2, which is an electron acceptor compound, was abstracting electrons from the polymer, hence doping it. The same effect was shown also for Cl_2, Br_2 and AsF_5, which are all p-type dopants. The conductivity is believed to be a result of the creation of charge-transfer complexes between the polymer and the halogens and is preserved even after exposing the material to air for several days. Heeger, MacDiarmid and Shirakawa's work started a prolific field of research, which led to the development of organic field-effect transistors (OFET)[51] and was later recognized by awarding them the 2000 Nobel prize in Chemistry.

The polyacetylene used in their studies is part of a class of polymers called conjugated polymers. This conjugation refers to the alternation between single and double (or triple) bonds, so that all carbon atoms in the backbone have sp^2 (or sp) hybridization.[52] This hybridization allows for delocalization through the whole system, so that the electrons are free to move and become charge carriers, making the polymer conductive.[52] The electrons in these delocalized orbitals have higher mobility when the material is "doped", *i.e.* oxidized. The oxidation removes electrons from the one-dimensional electronic band, which becomes partially empty, enabling the electrons within the band to become mobile. In principle, the same effect can be obtained by reduction, which adds electrons to an unoccupied band. Examples of n-type dopants are lithium, sodium and potassium.

However, most organic conductors are doped oxidatively (*i.e.* p-type materials), and n-type doped materials are more sensitive to air and moisture. The doping of such organic conductors can be seen as an analogue to the doping of semiconducting silicon. The band structures of conductive polymers can easily be calculated using a tight binding approach. Conjugated polymers can exhibit metallic or semiconducting behavior and their electrical properties can be tuned by modifying the structure of molecules. This is of crucial importance because the tunability enables these materials to be used as active components in multiple devices for different applications.[53-55]

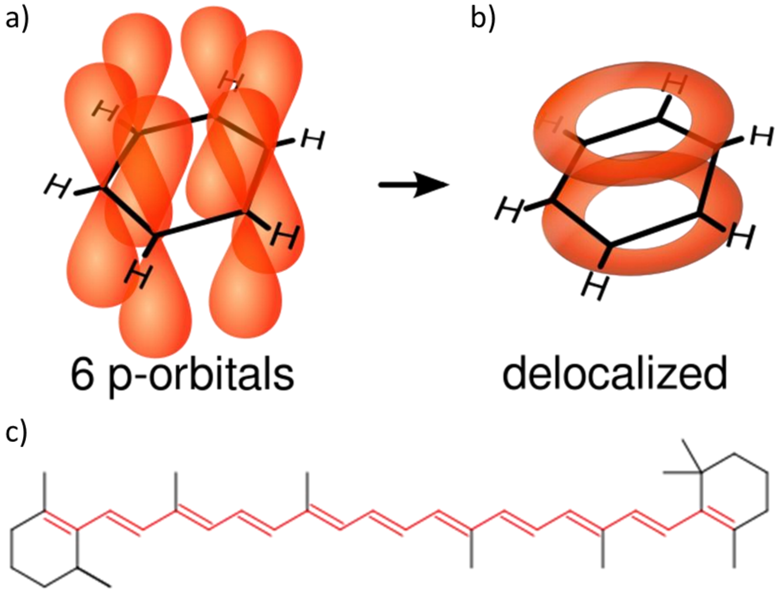

Figure 1-3 **a) benzene molecule with the C 2p$_z$ orbitals drawn in red; b) drawing of the delocalization of the charge density above and below the benzene ring plane; c) schematic of a longer molecule (beta-carotene) with the conjugated carbon backbone highlighted in red. a,b) Adapted from Ref.[56] CC BY-SA 3.0**

1.3 Graphene

A significant leap towards the usage of organic electronics beyond niche applications was spurred by the isolation of graphene in 2004 by Geim and Novoselov, for which they were granted the Nobel prize shortly afterwards.[57] Graphene is an allotrope of carbon whose structure is a single planar sheet of sp^2 bonded carbon atoms, that are densely packed in a honeycomb crystal lattice.[58]

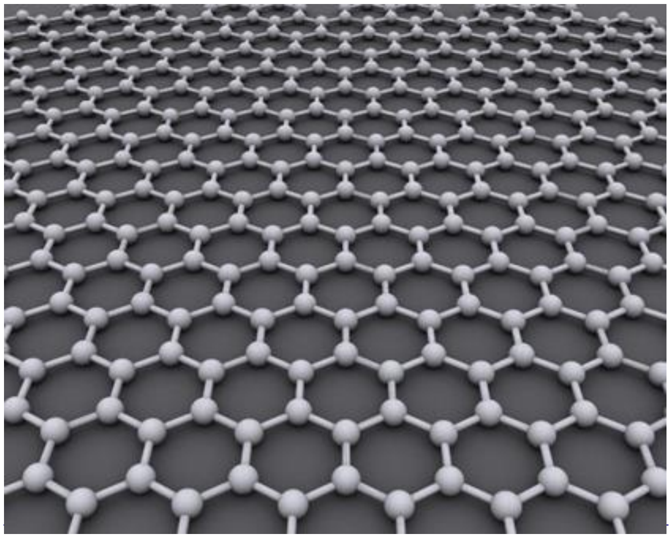

Figure 1-4 **Graphical representation of a graphene single layer. Reproduced from Ref.[59] CC BY-SA 3.0**

The interest in graphene lies in its unique properties.[6-7] It is a zero-gap semimetal, with a linear E *vs* k relation for low energies near the six corners of the two-dimensional hexagonal Brillouin zone, where cone-like structures, called Dirac cones, are formed.[6] Charge transport measurements show that graphene charge carriers are massless Dirac fermions,[60] which is reflected in astonishingly high thermal and electrical conductivity. The properties would make graphene a perfect component for integrated circuits, but its usage has been limited by two main factors: *i.* single sheets of graphene are remarkably hard to produce, particularly on top of substrates appropriate for device fabrication and *ii.* the zero bandgap. The first problem was solved by transferring graphene layers from the growth substrate to destination substrates, while the latter issue is yet to be solved, and the work in this thesis is an attempt at a solution.

1.3.1 Graphene fabrication

Graphene was first isolated and identified in 2004, but existed in nature as a single layer in graphite, and was already studied in the '70s. In 1975, B. Lang synthesized a few-layer graphite sample via chemical decomposition methods on a single crystal platinum surface.[61] Epitaxial growth on transition metals was fairly common during the '70s,[62] but it was only with the advancement of surface science, in particular with the more widespread use of techniques such as low-energy electron diffraction (LEED), Auger electron spectroscopy (AES), high resolution electron energy loss spectroscopy (HREELS) and scanning tunneling microscopy (STM) that real progress was made, and single-to-few layer graphene flakes were obtained on SiO_2 by mechanically exfoliating highly oriented pyrolytic graphite samples (HOPG).[63] After the work of Geim and Novoselov[6, 58] the interest in graphene skyrocketed, and nowadays there are multiple ways to reliably synthesize graphene: mechanical cleaving (exfoliation),[57] chemical exfoliation,[64] chemical synthesis,[65] thermal chemical vapor deposition (CVD),[66] unzipping nanotubes[67] and microwave synthesis.[68] A graphical representation of those techniques is reported in Figure 1-5.

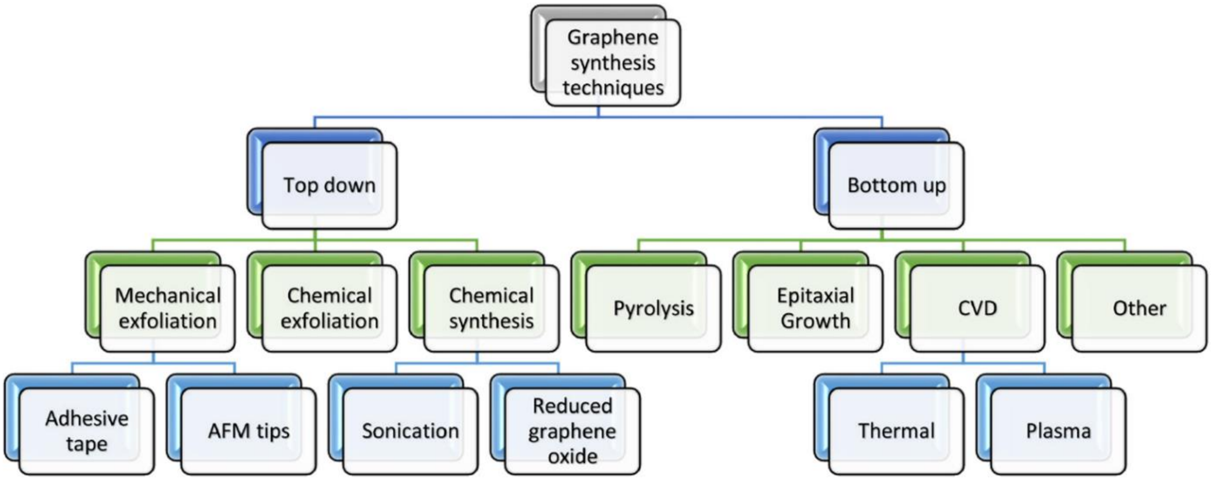

Figure 1-5 **Process flow chart of various graphene synthesis techniques. Reproduced from ref.[69-70], CC BY-SA 4.0**

1.3.2 Graphene, nanomaterials and transistors

While high-performance microprocessors based on MOSFETs are what we commonly refer to when we speak about current technology, numerous applications do not require the use of high cost MOSFETs, such as optical detectors, chemical sensors and even pixel-driving circuits for displays.[43] The backplane electronics of flat panel displays are in fact the most prominent use of transistors aside from in microprocessors, and use low-cost amorphous silicon (a-Si) thin-film transistors (TFTs). Such TFTs have a lower requirement for performance and size but need to be lower-cost, and could therefore be the right market niche for graphene transistors.[43, 71] An important aspect of graphene transistors, or more generally of nanomaterial transistors, is that the device architecture is pretty similar for high-performance and thin film transistors (Figure 1-6a).[43]

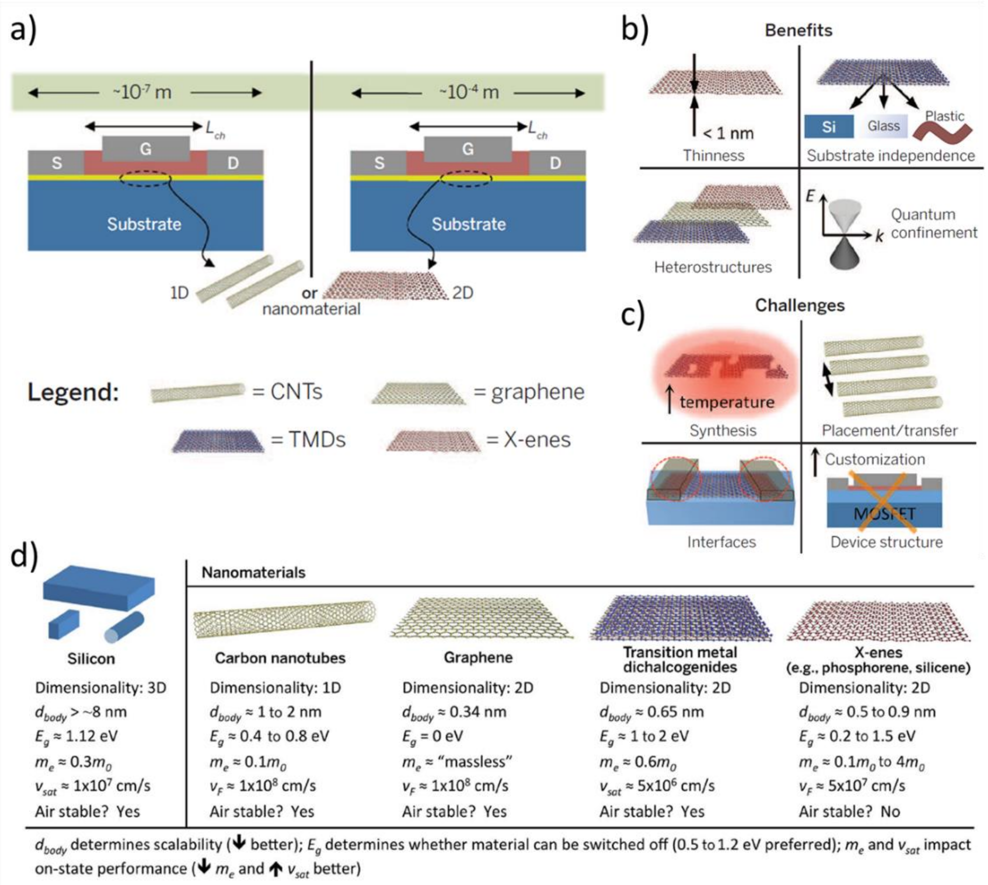

	Nanomaterials			
Silicon	Carbon nanotubes	Graphene	Transition metal dichalcogenides	X-enes (e.g., phosphorene, silicene)
Dimensionality: 3D	Dimensionality: 1D	Dimensionality: 2D	Dimensionality: 2D	Dimensionality: 2D
$d_{body} > \sim 8$ nm	$d_{body} \approx 1$ to 2 nm	$d_{body} \approx 0.34$ nm	$d_{body} \approx 0.65$ nm	$d_{body} \approx 0.5$ to 0.9 nm
$E_g \approx 1.12$ eV	$E_g \approx 0.4$ to 0.8 eV	$E_g = 0$ eV	$E_g \approx 1$ to 2 eV	$E_g \approx 0.2$ to 1.5 eV
$m_e \approx 0.3m_0$	$m_e \approx 0.1m_0$	$m_e \approx$ "massless"	$m_e \approx 0.6m_0$	$m_e \approx 0.1m_0$ to $4m_0$
$v_{sat} \approx 1\text{x}10^7$ cm/s	$v_F \approx 1\text{x}10^8$ cm/s	$v_F \approx 1\text{x}10^8$ cm/s	$v_{sat} \approx 5\text{x}10^6$ cm/s	$v_F \approx 5\text{x}10^7$ cm/s
Air stable? Yes	Air stable? Yes	Air stable? Yes	Air stable? Yes	Air stable? No

d_{body} determines scalability (↓ better); E_g determines whether material can be switched off (0.5 to 1.2 eV preferred); m_e and v_{sat} impact on-state performance (↓ m_e and ↑ v_{sat} better)

Figure 1-6 **a) Cross-sectional schematics showing the general structure of high-performance and thin film transistors using nanomaterials for the channels; there are small differences in the structure but vast differences in size; b-c) overview of benefits and challenges of including nanomaterials into transistors; d) comparison of key intrinsic attributes between silicon and the four most prominent families of nanomaterials. Adapted from Ref.[43] with permission from The American Association for the Advancement of Science.**

Apart from graphene, other nanomaterials could be used, such as carbon nanotubes (CNTs), transition metal dichalcogenides (TMDs) and the class of X-ene 2D materials, *i.e.* silicene and phosphorene (Figure 1-6). Using nanomaterials as channels would provide a number of benefits, the first being thinness. The atomic thinness of nanomaterials, especially in their monolayer form, offers ideal electrostatic control over the channel, one of the main problems with further downscaling in the size of Si transistors. 2D materials could also be stacked, to modify their properties, and could be synthetized on one particular substrate and then transferred onto the device. As of now, however, there are huge challenges to overcome before nanomaterials offer a real alternative to silicon, such as producing high-quality materials, controlling their placement onto a device, and the need to improve the interfaces (contact and dielectric) and device architectures, to fully utilize their advantages (Figure 1-6b,c).[43] Finally, in Figure 1-6d I show an overview of the key intrinsic attributes of the four families of nanomaterials and compare them with silicon. While graphene clearly shows the best properties, as highlighted before, the main drawback is the zero bandgap, which hinders its application as a semiconductor.

1.3.3 Graphene modification

For most applications in electronics, a bandgap and the ability to tune its value is required, meaning that finding a way to reliably and easily modify the bandgap of graphene will have a tremendous technological impact. The carbon atoms in the single atomic sheet are sp^2 hybridized and each atom has an unsaturated dangling bond, making it possible to perform various surface modifications. There are different ways to tackle the problem, and the most common are: *i.* substrate-induced bandgap opening, *ii.* substitutional doping, *iii.* BCN hybrids and *iv.* quantum confinement (Figure 1-7). Substrate-induced bandgap opening was the first method explored, and interestingly was reported for the first time a few years before the work of Geim and Novoselov. In 2002 a graphene/h-BN/Ni (111) system was studied by scanning tunneling spectroscopy (STS), showing a 0.5 eV bandgap, thus confirming a gap opening.[72] The method has been widely used since and has been demonstrated also for adsorbed molecules[73] and even hydrogen.[74] Chemical substitution doping is conceptually similar to conventional semiconductor doping, and consists of substituting carbon atoms with either boron or nitrogen to obtain *n*- or *p*-type semiconductors, respectively. However, it is still in the early stages of development, and obtaining uniform doping over large areas of graphene remains a challenge.[69] Hybrids consist of BCN solid solutions in a hexagonal lattice, but mostly multilayers have been reported, and it is therefore more convenient to work with distinct layers of graphene and h-BN systems. A major drawback of the previous methods is that the carrier mobility was reduced by the graphene modification, thus affecting the device performance. One way to avoid such a problem while introducing a gap is to confine the electrons in graphene by making graphene nanoribbons (GNRs).[75] As I will present in Section 1.5.2, on-surface polymerization has been shown to be a reliable way to produce GNRs, and some experimental results on this aspect will be discussed in Chapter 3. Studies on Graphene modification are ongoing, and an increasing number of scientists and associated laboratories are starting to venture into such modification. A new class of graphene-like materials was also proposed, 2D π-conjugated polymers, whose properties are defined by the precursors, and easier to tune, being defined by the used monomer.

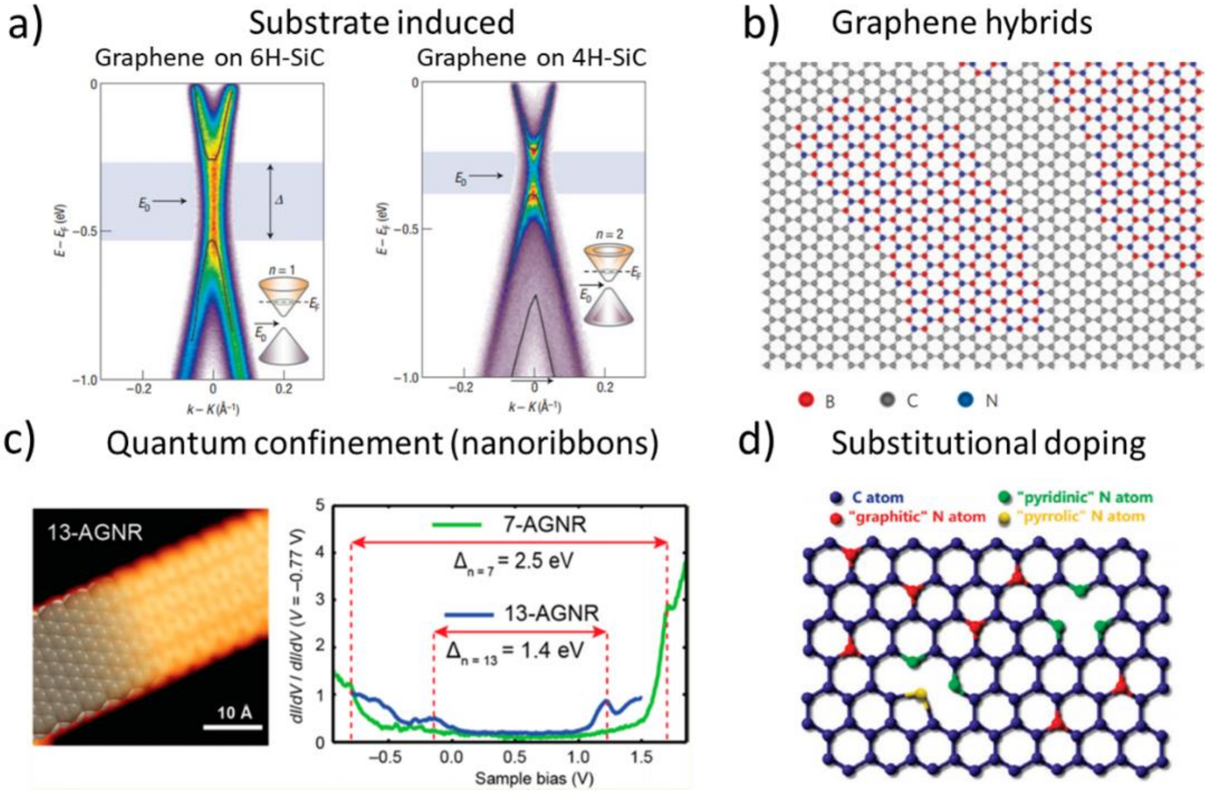

Figure 1-7 **Schematic of various methods of bandgap opening in graphene. Reproduced with permission from: Ref.[76] (a), Ref.[77] (b), Ref.[78] (c) and Ref.[79] (d).**

1.3.4 2D polymers: Organic analogues of graphene

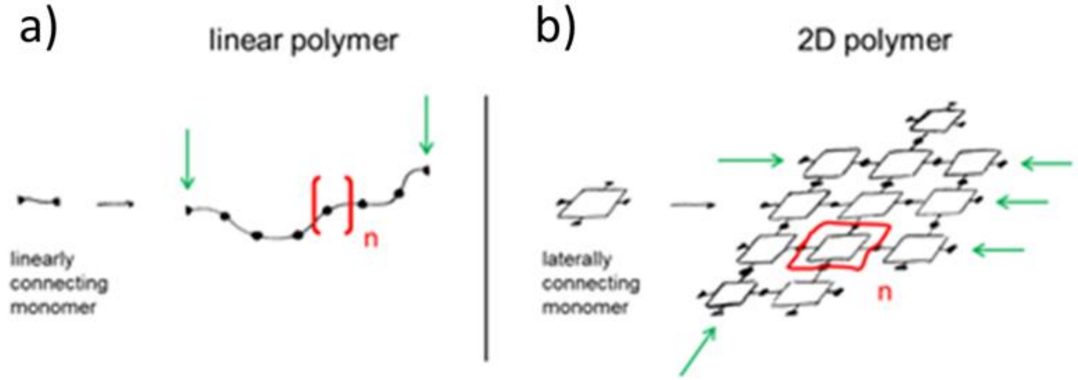

Figure 1-8 **Graphical representation of the formation of linear (a) and 2D (b) polymers starting from their building blocks. Adapted from Ref.[80] CC BY-SA 3.0**

According to Hermann Staudinger's definition from the 1920s, a polymer is a covalent long-chain molecule composed of a sequence of linearly-connected repeating units and end groups.[81] A sheet-like macromolecule of connected repeating units, such as graphene. can be defined as a 2D polymer.Graphene is therefore the simplest example of a 2D polymer, with only carbon atoms as the repeat unit, but it is possible to imagine a whole class of polymers with different properties and characteristics, depending on the initial building block used. The final result can include heteroatoms and have different geometries, as shown in Figure 1-9.

Thus, it would be possible to change both the physical (such as optical and electrical) and chemical (such as reactive) properties of the obtained layer, including the aforementioned bandgap. Such modifications will open paths to whole new classes of applications, such as chemical sensors or active optoelectronic components, which explains the increasing interest in this field.[15, 82] The macromolecular nature of these materials provides a great number of degrees of freedom, through the choice of monomer geometry and composition as well as the co-deposition of different monomers.

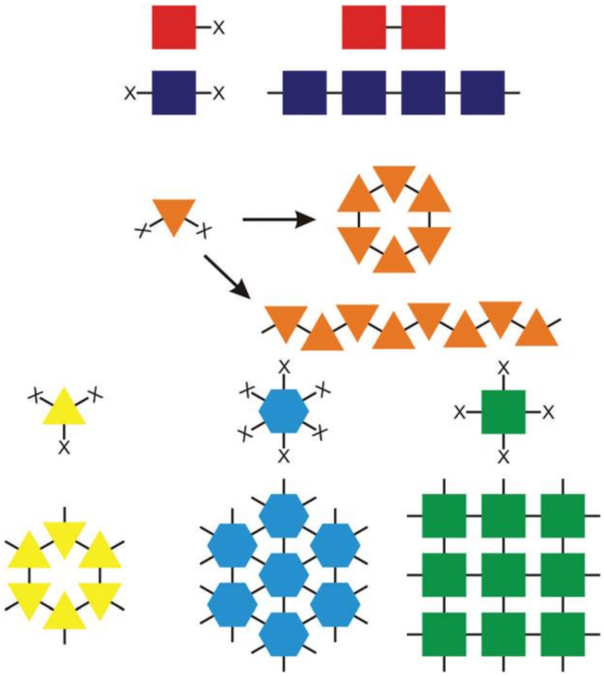

Figure 1-9 **Scheme of the relation between the precursor halogen functionalization and the dimensionality and topology of the resulting polymeric network. Reproduced from Ref.[34] With permission of The Royal Society of Chemistry.**

1.4 Surface *vs* Solution polymerization

In the introduction, I stated that to realize our 2D structures it is necessary to dose the precursors on top of a surface, let them assemble, and react directly on the substrate. But why is it necessary? In other words, could this whole process be done using a more traditional solution-based chemistry approach? The short answer of course is that yes, the surface is necessary, since the realization of dimension-limited polymeric structures in solution will pose almost insurmountable difficulties.However, the causes of these difficulties are subtle and worth discussing, to let the willing reader understand the perspectives of this on-surface approach and its advantages and its drawbacks compared with the more common solution-polymerization approach. In the previous sections I introduced 2D materials, including graphene and organic polymers, but before 2004 they were considered impossible to create, and merely useful as models for theoreticians to better understand solid state physics. Graphene has been studied theoretically for almost 60 years and was believed to be a highly unstable material, but now you can buy a 50 mL solution of graphene flakes for less than $50, so the question arises: how is this even possible?

The idea of unstable 2D systems arose in the 30s with the work of Peierls,[83] who, based on the harmonic approximation, showed that there can be no one- or two-dimensional long-range order. (To be more accurate, he gave a quantitative argument only for the 1D case but showed the obvious connection to two dimensions). An independent proof was found a few years later (in 1937) by Landau, using his general theory of second-order phase transitions.[84] Those arguments were later extended by Mermin, in 1968,[85] who studied the case of N classical particles interacting through a pair potential in two dimensions. Using the Bogoliubov inequality (that satisfies the free energy of a Hamiltonian system), he found that conventional crystalline order in two dimensions is forbidden for Lennard-Jones type potentials.[85] The reason is that there is a divergence in the displacement autocorrelation function, and so positional long-range order does not exist.[85] However, he found weaker bounds than those found by Peierls with the harmonic approximation, and stated that short-range order could still exist. Essentially, the divergence can be seen as a divergent contribution of thermal fluctuations, which means that at any finite temperature the atom displacement is comparable to interatomic distance, and so there is no ordering (basically, the crystal melts). This was also supported by experimental observations, which stated that the melting temperature of thin films is directly proportional to the thickness of the films, and that thin layers will have low melting points.[86-87] However, in 2004 Geim and Novoselov isolated and studied a single layer of graphene,[57] and the problem, thought to be closed since the 60s, once again became open. Based on their observation, detailed analysis of the 2D crystal problem beyond the harmonic approximation started, which ultimately led to the conclusion that the interaction between long-wavelength bending and stretching phonons could in principle stabilize atomically-thin membranes via a deformation in the third dimension: theory may not allow a perfect 2D crystal in space, but does not forbid nearly perfect 2D crystals, in which some quenching or gentle crumpling make them stable by expanding into the third dimension.[88] The expansion in the third dimension was proved, once again, by the Geim and Novoselov group in 2007, when they found that freely suspended graphene crystals exhibit random elastic deformations in all three dimensions.[89] When the crystals are on a surface, however, bonding with the underlying substrate reduces the thermal instability. Thus, the surface is an attractive template for the reaction, and on-surface growth is a favorable approach compared with a solution one, where 2D materials could instead fold on themselves to minimize their energy.

Besides thermodynamic reasons, on-surface polymerization has other advantages compared with the solution counterpart. Being solvent-free, it allows for the polymerization of insoluble precursors, which would otherwise be impossible. Other benefits come from the templating function of the surface: in addition to making 2D materials energetically stable, the surface can control the patterning of the material. Particular crystal orientations, or even highly-stepped vicinal surfaces, can be exploited to produce polymers with a preferred orientation. Working in ultra-high vacuum (UHV) conditions also increase the degree of control over the reaction parameters, making it easier to control reactions or to perform hierarchical growth.

1.4.1 Adsorption on solid surfaces

Before discussing on-surface polymerization specifically, I have to introduce some general concepts, such as adsorption, coverage and self-assembly. Adsorption is the process by which molecules are deposited on a surface. During this process the molecules can interact with the substrate, *via* a chemical bond, involving redistribution of the electronic density between the substrate and the adsorbate, or *via* a physical interaction, most often Van der Waals. The first case is referred to as chemisorption, and the latter as physisorption. Regardless of the nature of the interaction, one of the most important parameters in adsorption is the *coverage*, the fraction of surface covered by molecules, denoted by θ and defined as:

$$\theta = \frac{N}{M} \tag{1-1}$$

where M is the total number of available positions and N is the number of occupied positions. It is known that, in the case of adsorption from a gaseous phase, N depends mainly on the system temperature and the gas pressure. One of the simpler models describing this behavior is the Langmuir Isotherm, in which T is taken to be constant, and θ gives the coverage as a function of pressure, as described in the following equation:

$$\theta = \frac{Pk(T)}{1+Pk(T)} \tag{1-2}$$

in which P represents the pressure and k(T) the equilibrium constant of the adsorption reaction, which is dependent on the temperature. This law is valid if the following hypotheses hold: *i.* all adsorption sites are equivalent, *ii.* each site can adsorb only one molecule at a time and *iii.*

molecules adsorbed in different sites do not interact with each other, so that the enthalpy of adsorption is independent of the θ value. In the limit of P → ∞, θ tends to 1, meaning that every site will contain one molecule and the surface will be saturated. Another important parameter of adsorption is the sticking coefficient, **S_c**, which describes the ratio of the number of adsorbate molecules (or atoms) that adsorb (or "stick") to a surface to the total number of molecules that impinge upon that surface during the same period. The value is between 1 (each impinging molecule sticks) and 0 (none stick). The coefficient is a function of surface temperature and coverage, and additionally depends on the degrees of freedom of the adsorbate and its kinetic energy.[90]

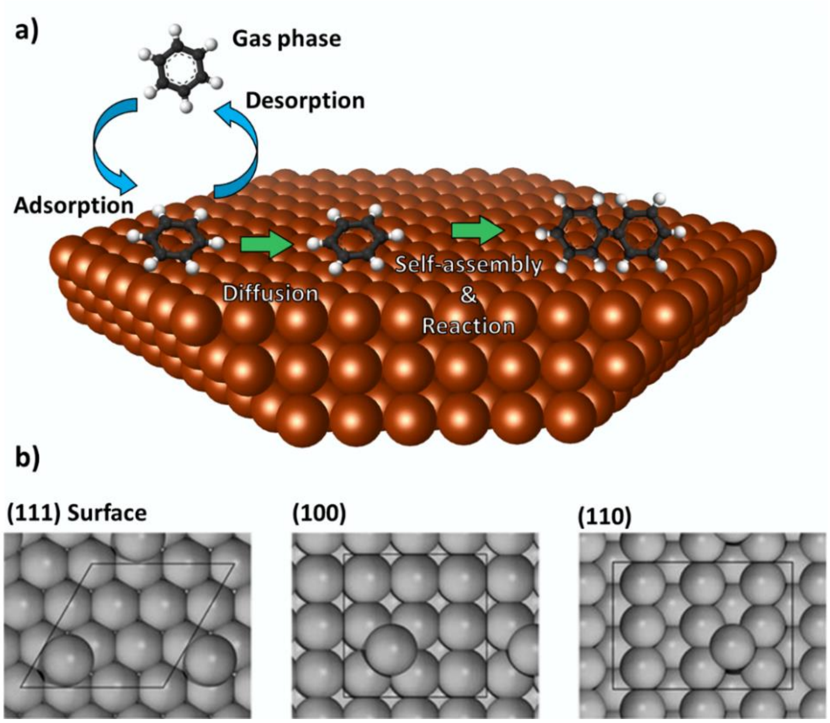

Figure 1-10 **a) Schematic of possible molecular behavior on a surface; b) Geometries of the (001), (110) and (111) crystal planes of a face-centered cubic lattice, like the one studied in this work.**

Once adsorbed, the molecules can either diffuse on the surface and react or desorb (Figure 1-10), depending on the different energy barriers. Those barriers are case specific, depending on the precursor structure and concentration and the substrate composition, temperature and orientation, with both thermodynamic and kinetic factors playing a role, making it hard to *a priori* predict the molecular behavior.[91] When dosed on a surface, molecules can also self-assemble, meaning that they form an organized structure or pattern driven by interactions between the components without any external input.

1.5 On-surface polymerization

Molecular self-assembly at surfaces allows the realization of 2D ordered nanostructures with complex architectures, held together by weak and reversible forces, such as Van der Waals interactions or metal complexation.[92-94] However, there are some drawbacks: the structures are inherently fragile, due to the weak interactions, which precludes mechanical stability and limits charge transport. To overcome these limitations, robust covalent bonding between the molecules is needed, and requires the precursors to undergo on-surface chemical reactions. To control and reduce the possibility of unwanted side-reactions, UHV conditions are often involved. The main advantage of UHV is that it allows the use of highly reactive surfaces, which would immediately react with the chemical species in atmosphere. The use of UHV prevents oxidation and opens the possibility of using a number of characterization techniques to follow the reaction, such as LEED, STM and X-ray photoelectron spectroscopy (XPS).

Different paths have been followed to synthetize 2D polymers, *via* both reversible and irreversible reactions. While reversible reactions are more suited to form a regular network of molecules (due to intrinsic self-healing properties), the desired polymers should include stable covalent bonds in order to withstand the mechanical and thermal stresses involved in incorporating them into a useful device.[15] On the other hand, irreversible reactions form a more stable bond, but have the drawback that the structure is not able to adjust after the bonds are formed. It has been proposed that a potential solution is to use a two-step reaction, in which only the second step is irreversible and involves a covalent bond.[15, 25] In this way, it would be possible to deposit the molecules and arrange them to form the desired ordered structure, which polymerize only in a subsequent step, so that a well-ordered covalently-bonded polymer can be obtained. A reaction that exhibits these features is on-surface Ullmann coupling.

1.5.1 Ullmann reaction

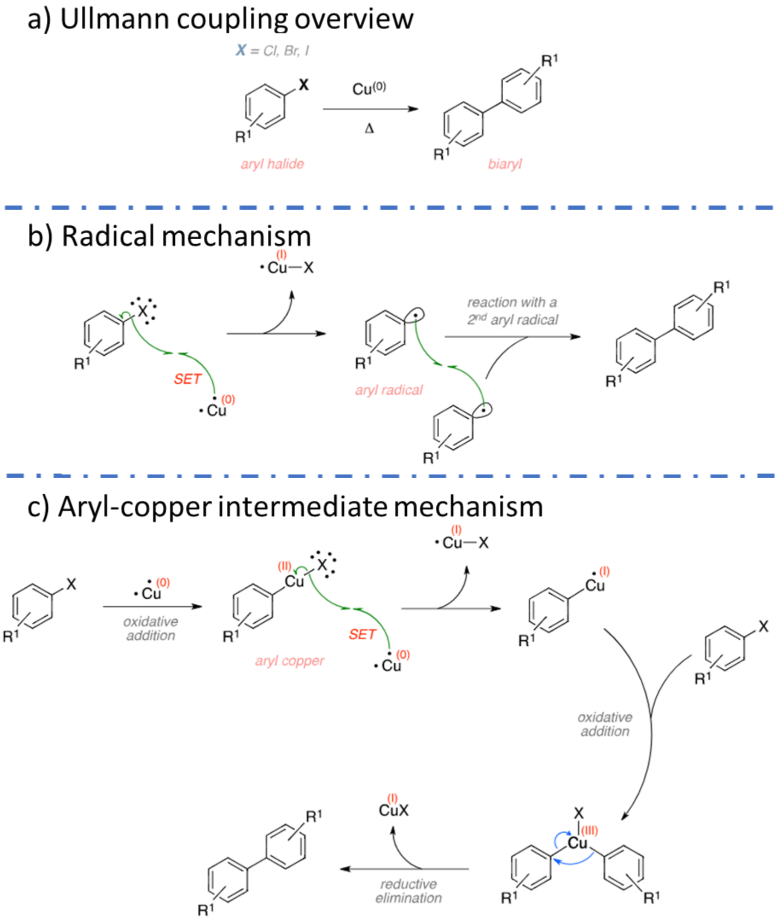
a) Ullmann coupling overview

b) Radical mechanism

c) Aryl-copper intermediate mechanism

Figure 1-11. **Scheme of Ullmann coupling, showing the overall reaction (a) and the two main possible mechanisms, involving either a radical species (b) or an aryl-copper intermediate (c); SET stands for single-electron transfer. Adapted from Ref.[95]**

First discovered in 1901 by the German scientist Fritz Ullmann,[96-97] it has been used since then as the most common way to produce biphenyls starting from aryl halides in solution (Figure 1-11a). The reaction is assisted by copper, which needs to be present in the solution in the form of copper powder. The Ullmann coupling is a complex reaction, where different reaction mechanism can be followed depending on the starting precursors, as described by Sambiagio et al.[98] In a simplified description, there are two main mechanisms: the first where an aryl radical is produced as an intermediate, and the second where the intermediate is an aryl-copper species. In the radical mechanism (Figure 1-11b), a single-electron transfer takes place between metallic copper and the aryl halide, to produce the aryl radical and a Cu-X species as a side-product. The aryl radicals then couple to produce the final biphenyl. In the second mechanism, the reaction is started by oxidative addition to a copper atom to form the aryl-copper intermediate. Oxidative addition of a second aryl halide molecule and subsequent reductive elimination produces the final biphenyl. In both cases, dimers of the same aryl halide precursors (homocoupling) or of different precursors (cross-coupling) can be produced. The first instance of on-surface Ullmann reaction was reported by Xi and Bent in 1992. In a series of papers, they described the reaction of iodobenzene precursors on a Cu(111) surface.[26, 32, 99] The reaction mechanism was also described, in which a copper atom is inserted into the Cu-I bond to form an organometallic intermediate. The intermediates then react to produce the final biphenyl. Interestingly, they found that two mechanism could be followed, analogous to the ones reported in Figure 1-11 for the solution chemistry case. The reaction pathway depends on the copper atom state, which can be a lattice atom or a surface adatom (Figure 1-12). Xi and Bent were also the first to report a coverage dependence of the on-surface Ullmann coupling, reporting different adsorption behaviors dependent on the surface coverage.[26]

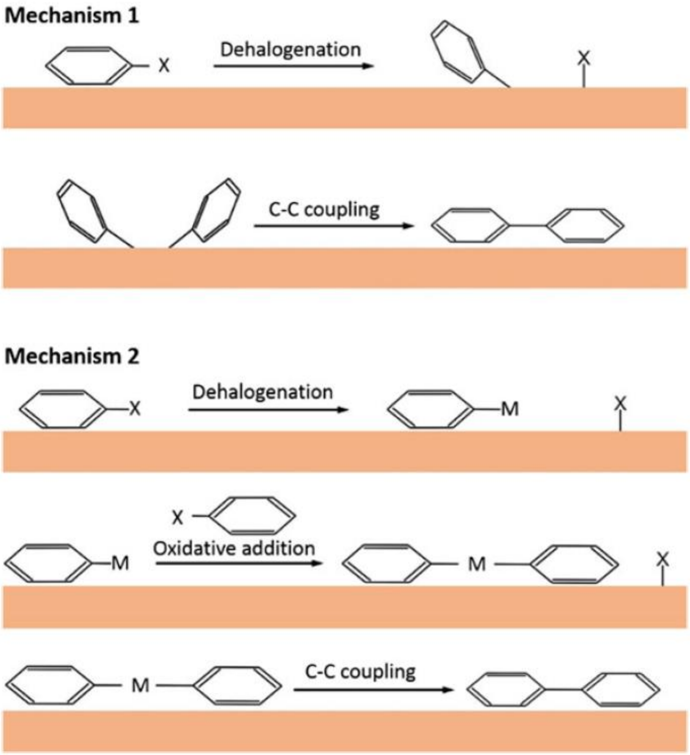

Figure 1-12 **Scheme of on-surface Ullmann coupling: two mechanisms can be observed, depending on whether the involved metallic atoms are from the surface lattice (Mechanism 1) or are adatoms (Mechanism 2). Reproduced from Ref.[100] with permission from Springer Nature.**

1.5.2 On-surface Ullmann reaction: properties and products

Since 2010, Ullmann coupling has been established as the most common way to produce conjugated polymers on metallic surfaces. The reasons for its popularity are multiple, but the leading ones are the selectivity over the coupling sites and the possibility to perform hierarchical growth offered by the halogen substituents.[18, 20] Combined, these two factors allow for precise control of the nanostructures grown, as confirmed by the variety of structures that have been realized, from linear to two-dimensional polymers and even macrocycles. As stated previously, Ullmann coupling is a two-step reaction, in which the first produces aryl radicals that subsequently react, coupling to form a polymer. The radical species are formed by breaking the C-X bonds. By selecting the building block, it is easy to choose the coupling position and therefore *a priori* decide the final structure obtained.

a. Precise control of radical sites

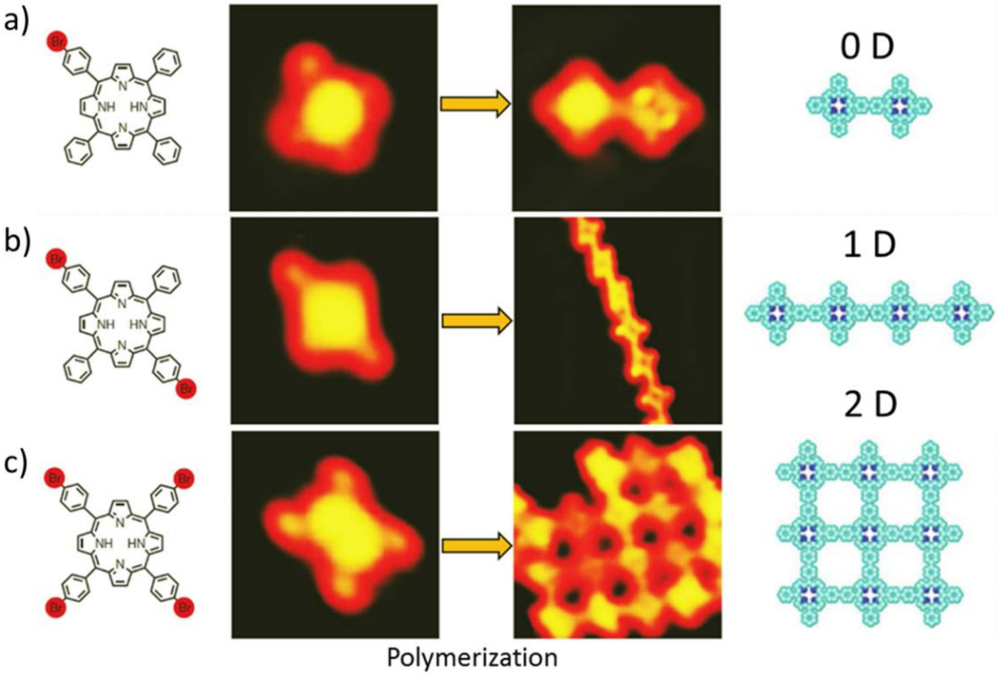

Figure 1-13 **Various porphyrin precursors with 1 (a), 2 (b) or 4 (c) halogens, together with their STM images of a single molecule and the resulting polymeric structure (schematized in the right column); dimers are formed with precursor a, linear chains with b and 2D networks with c. Adapted from Ref.[20] with permission from Springer Nature.**

The number of reaction sites (*i.e.* C-X bonds) will control the dimensionality of the nanostructures, as beautifully demonstrated by Grill et al.,[18, 20] and reproduced here in Figure 1-13. In their work they used porphyrin precursors substituted with 1, 2, or 4 halogen atoms to produce dimers, linear chains, and 2D polymers, respectively.

b. Hierarchical growth

Both steps of the Ullmann reaction can be thermally activated, but the energy required for each step is different and varies depending on the molecule, the surface, and the halogen used. A C-X bond will break at different temperatures depending on the halogen involved. This temperature difference can be exploited to promote hierarchical growth, as first demonstrated by Lafferentz et al.[18] in 2012 (Figure 1-14), and subsequently used by multiple researchers with success.[101-102] This interesting approach can increase the overall control over the reaction, allowing the initial production of linear chains and then only afterwards converting them into a 2D conjugated structure. It also provides the possibility of studying how the properties change with the dimension of the polymer.[101]

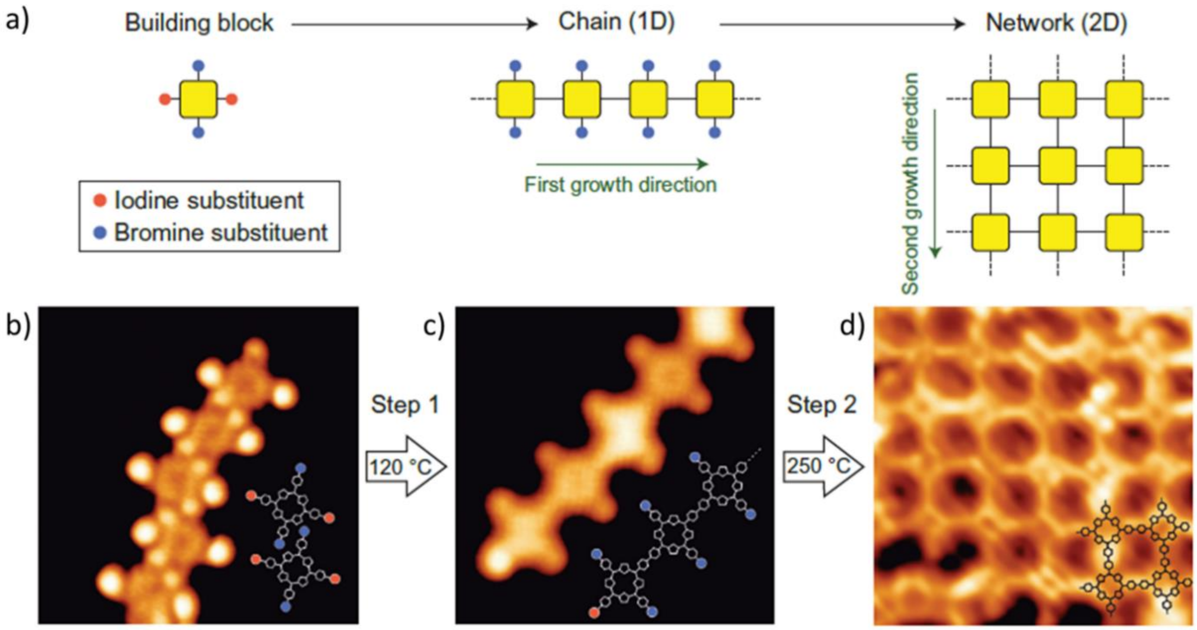

Figure 1-14 **Scheme of hierarchical Ullmann polymerization (a) from an intact molecule to linear chains to 2D networks, together with the respective STM image for each structure in (b), (c), and (d), respectively. Adapted from Ref.[18] with permission from Springer Nature.**

c. Different possible nanostructures

The properties summarized above can be exploited to realize the desired nanostructures, ranging from simple linear polymers to complex macrocycles or 2D networks, as showed in Figure 1-15.[100-101] In some cases, the Ullmann reaction can be coupled with de-hydrogenation reactions to produce a different variety of graphene nanoribbons.[103-104]

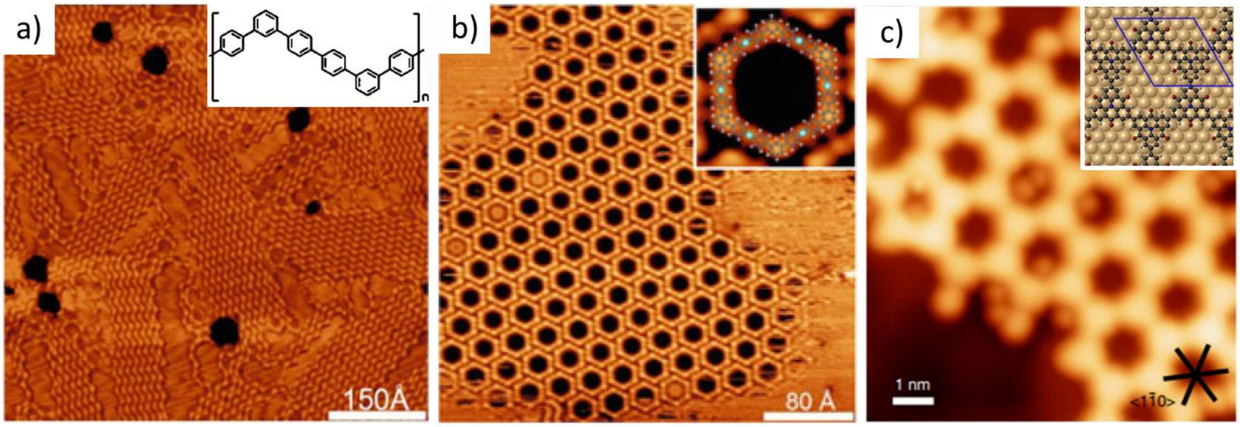

Figure 1-15 **STM images of various 1D and 2D structures obtainable with Ullmann coupling, the precursor used and repeating units are reported for each as an inset; a) linear chains, stacked to form 2D domains; b) macrocycles, again stacked to obtain a 2D assembly; c) a 2D conjugated structure with a honeycomb symmetry. a,b) adapted from Ref.[100], with permission from Springer Nature c) adapted from Ref.[101] CC BY 4.0**

Linear polymeric chains

The easiest kind of polymers that can be obtained *via* Ullmann coupling on a surface are linear chains, obtained using two halogens per molecule, in a meta or para position. The archetypal precursor for this class of nanostructure is 1,4-dihalobenzene, which was used in the first works to demonstrate the proof-of-concept of on-surface Ullmann coupling. The first studies worth mentioning in this regard were all based on 1,4-dihalobenzenes,[19, 30-31, 105-107] and led to a few interesting observations: *i.* upon absorption on a surface at room temperature, either intact molecules or an OM complex can be formed, *ii.* whether one or the other is formed is a complex matter, dependent on the halogen type, the surface, and the building-block backbone and *iii.* to obtain a polymeric structure it is necessary to add energy to the system, either by applying heat, by exposing the system to UV-light or by electron-induced reaction with the STM tip.

Later work focused on the reaction parameters, and discovered that the structures formed also depend on the molecular backbone in addition to the halogen type and the surface.[19, 30, 108] All steps of the transformation, from intact molecules to polymers, were studied by Di Giovannantonio et al. with both STM and fast-XPS in 2012,[30] showing that even techniques which average over the surface can be used to follow the reaction. In this work they demonstrated the possibility of following the polymerization step of the on-surface Ullmann coupling, by tracking the evolution of the C 1s molecular peak with temperature and comparing the spectroscopic shift with STM measurements of relative changes in the molecular adlayer. Density functional theory (DFT) calculations were also used to check the validity of the hypotheses made from the STM observations. A number of studies have utilized DFT modeling, to calculate the molecular geometry, to reproduce experimental *dI/dV* curves by calculating the density of states (DOS), or simply to check if the desired final polymer would be stable and have interesting properties. The widespread application of DFT confirms the importance of this approach, which is complementary to the experimental techniques.[16, 109-110] An example of the process and the formed nanostructures can be found in Figure 1-16.

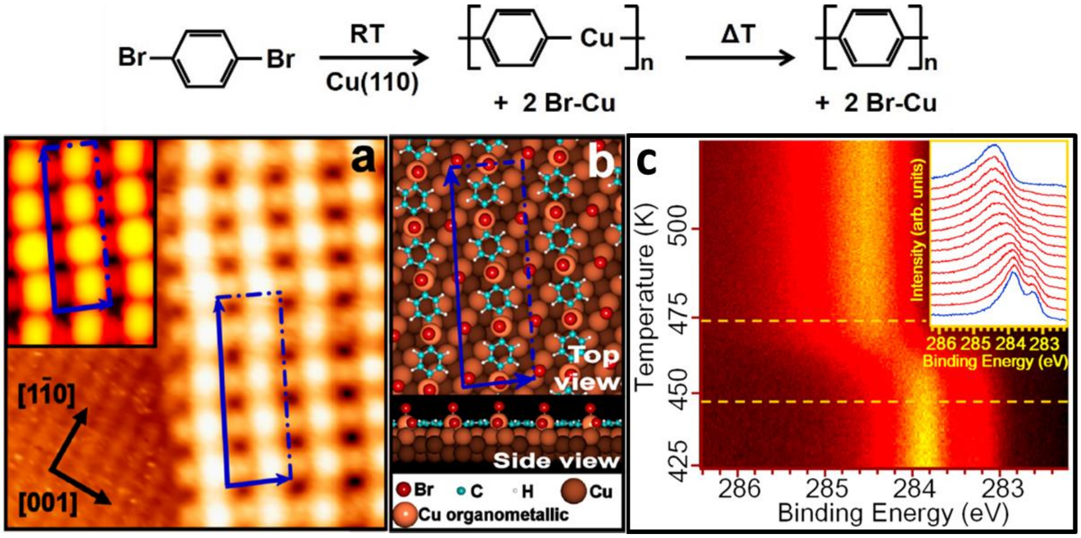

Figure 1-16 **Top: scheme of the formation of PPP chains starting from 1,4-dibromobenzene. Bottom: a) STM image of the obtained OM chains together with b) the respective DFT optimized structure; c) fast-XPS map of the evolution of the C 1s peak during the polymerization reaction, with single line scans between 450 and 475 K as an inset. Adapted from Ref.[30] with permission from the American Chemical Society.**

Macrocycles

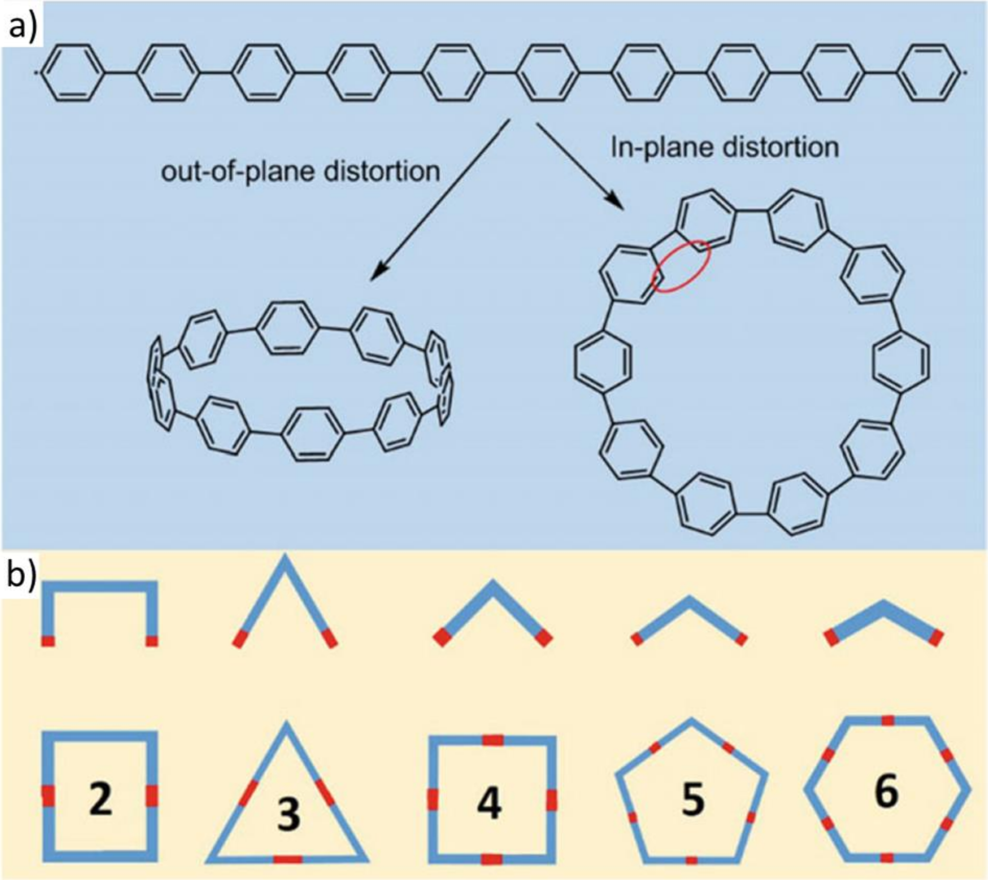

Figure 1-17 **a) different ways to obtain the cyclization reaction of linear chains; the vicinity of the C-H groups is highlighted in red. b) Possible geometries of the building block to obtain various closed pore macrocycles upon polymerization. Reproduced from Ref.[100]**

Precursors with two terminal halogens can yield a linear polymer as explained above, but can also undergo a cyclization reaction, via ring-closure. Similar to the case in solution chemistry, precursors with the right structure can form macrocycles via coupling of the reactive ends. An advantage of the surface approach compared with the solution case, is that, being a solvent-free process, insoluble reactants can also be used. However, there are also a few drawbacks, such as the fact that high molecular weight molecules cannot be used, since they would degrade before being sublimated onto the surface (there are ways to cope with this problem however, such as directly dosing liquids in UHV).[111] Another drawback of on-surface cyclization is shown in Figure 1-17a. In solution the reactants have more degrees of freedom, and thus cyclization can be achieved by bending the C–C σ bond in a direction perpendicular to the plane of the phenylene units, whereas on a surface, out-of-plane deformation is likely forbidden or limited. The allowed in-plane C-C bending can also lead to disadvantageous strain or, depending on the building block, to steric hindrance (red circle in Figure 1-17a). To avoid these problems, small angles between the phenylene units are required. Depending on the building block, various macrocycles can be formed (Figure 1-17b). However, most of the meta-precursors used can results in both macrocycles and linear chains, depending on the orientation of each added oligomer. For example, in the case of 4,4″-dibromo-meta-terphenyl studied by Fan et al.,[100] where the angle between the two C-Br bonds is 120°, both zig-zag chains and closed cycles are formed. In the same work it was shown that the formation of one structure or the other was dependent on the underlying surface, its temperature during deposition, and the deposition rate. The substrate strongly influences the structure, with three-fold symmetric macrocycles having an higher formation probability on a three-fold symmetric surface, like Cu(111), rather than on a two-fold symmetric one, like Cu(110).[112] In addition, low deposition rates favor cyclization over formation of zig-zag chains.[100, 113]

2D polymers

The *holy grail* of on-surface polymerization is the formation of long-range ordered 2D conjugated structures, with selected (tunable) properties.[34, 114] Various attempts have been made to realize such structures, the first of which was reported by Grill et al. in 2007, where small patches of 2D conjugated polymers were obtained.[20] Various researchers tried to improve on this result, varying both the precursors used and the underlying surface, but up to now no polymer structures exhibiting sufficient extent and degree of order to be studied using averaging techniques have been reported, making this the biggest open challenge in the field. Despite falling short, a number of results are worth mentioning that have helped to explain the role of the surface (Figure 1-18),[108] show the DOS of 1D and 2D networks,[101, 115] understand how the growth procedure affects the order,[102] or determine the effect of introducing heteroatoms into the molecular backbone.[116]

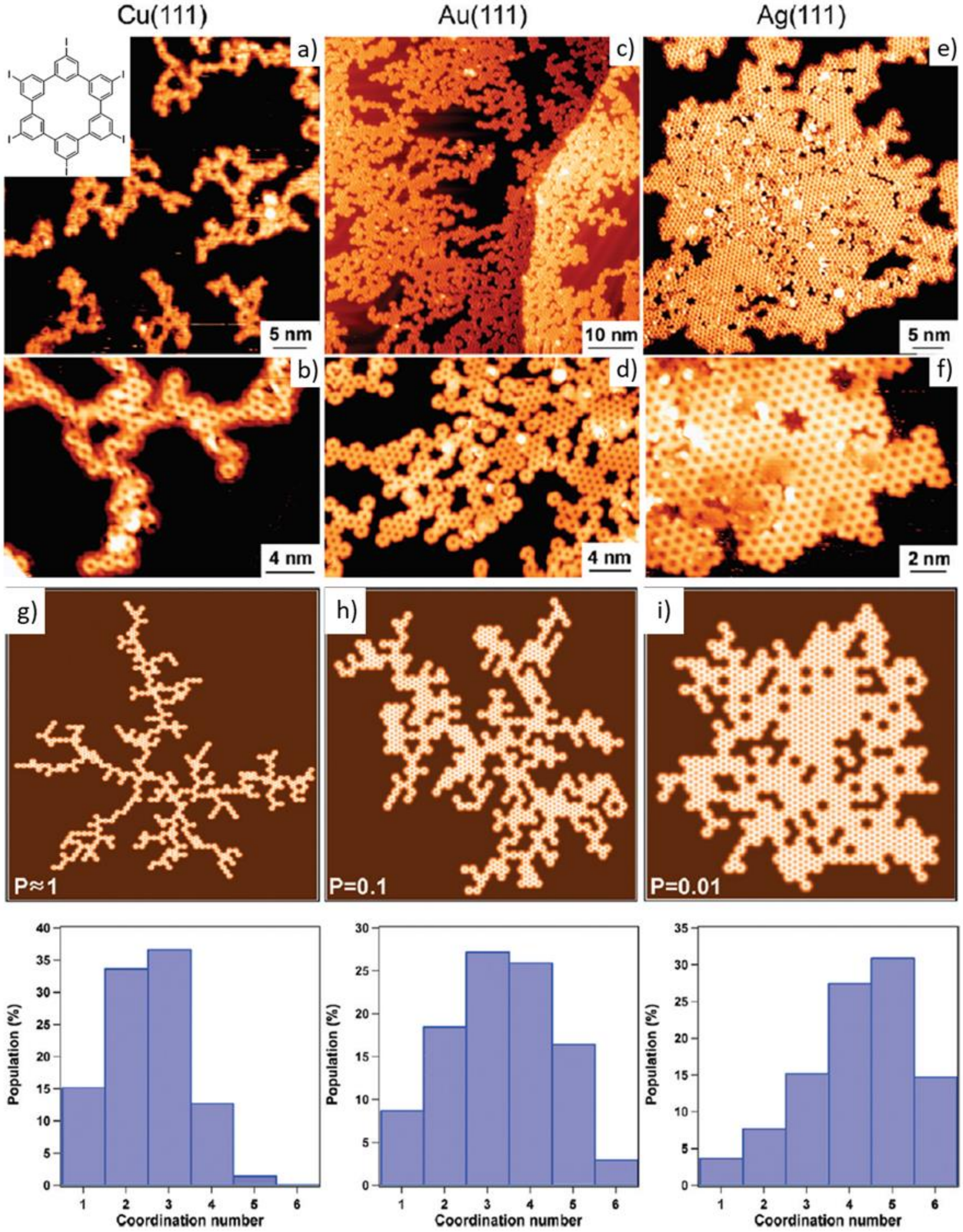

Figure 1-18 a-f) STM images of polyphenylene networks on Cu(111) (a,b), Au(111) (c,d), and Ag(111) (e,f); g-i) Mont Carlo simulations of molecular network growth: coupling probabilities of P = 1, 0.1, and 0.01, for g, h and i respectively, were used for the growth of clusters, which consist of 400 molecules. Below each simulation, the corresponding coordination-number distribution of the molecules in the cluster is given. Adapted from Ref.[108] with permission from the American Chemical Society.

Graphene nanoribbons

The most advanced and successful application of on-surface Ullmann polymerization so far is the realization of GNRs. This is due to the fact that not only have multiple nanoribbons of various size have been realized, but their extension is sufficient to study them using both STS and angle-resolved photoelectron spectroscopy (ARPES).[115] This allowed researchers to obtain information on their properties and even the effect of including heteroatoms in the structures.[116-117] Both armchair and zigzag GNRs have been realized and studied, and different procedures were developed to realize one or the other starting from the building block selection.[103, 118] Depending on their orientation, these structures possess interesting properties: quantum confinement opens a bandgap in armchair nanoribbons, while zigzag edges are instead expected to host spin-polarized electronic edge states, from which interesting magnetic properties would arise.[118] In most cases, Ullmann reaction needs to be coupled with a dehydrogenation step to obtain fully-conjugated GNRs, as shown in Figure 1-19. The hierarchical approach described above was used also for the realization of nanoribbons,[119] and procedures have been developed to monitor the synthesis by using solely mass spectroscopy.[120]

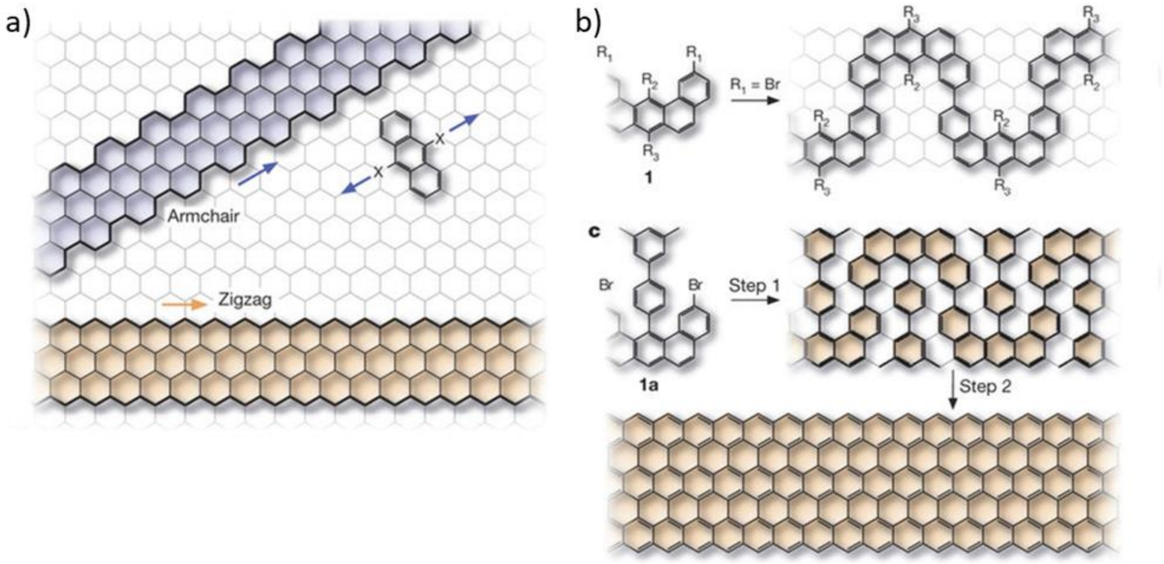

Figure 1-19 **a) armchair and zigzag graphene nanoribbon structures, together with an exemplary precursor for armchair GNRs; b) U-shaped dibenzo[a,j]anthracene monomer (1) with halogen functions $R_1 = Br$; c) monomer (1) with an additional dimethyl-biphenyl group in R_2 position, to obtain a zigzag GNR upon polymerization and de-hydrogenation. Reproduced from Ref.[118]**

d. *Surface and energies*

The outcome of dosing halogenated precursors on a metallic surface can be *a priori*, but it is a complex function of various parameters, including the choice of building block, the halogen used, the underlying surface (both its composition and orientation), and the substrate temperature.[34] While a complete report of all the existing examples in the literature is outside the scope of this thesis, I will give two examples, to allow the reader to understand the complexity of the problem and how important it is to control the parameters and chose the right system.

A good explanation of the surface effect in the dehalogenation process can be found in the 2013 work by Bjork et al.[16] In this theoretical paper, they simulated the adsorption of a halobenzene monomer containing either Br or I on three different (111) surfaces of Au, Ag and Cu. They showed that the energy barrier for the de-halogenation strongly depends on both the halogen and the surface, with a lower barrier for iodine, and decreasing from Au to Ag to Cu (Figure 1-20).

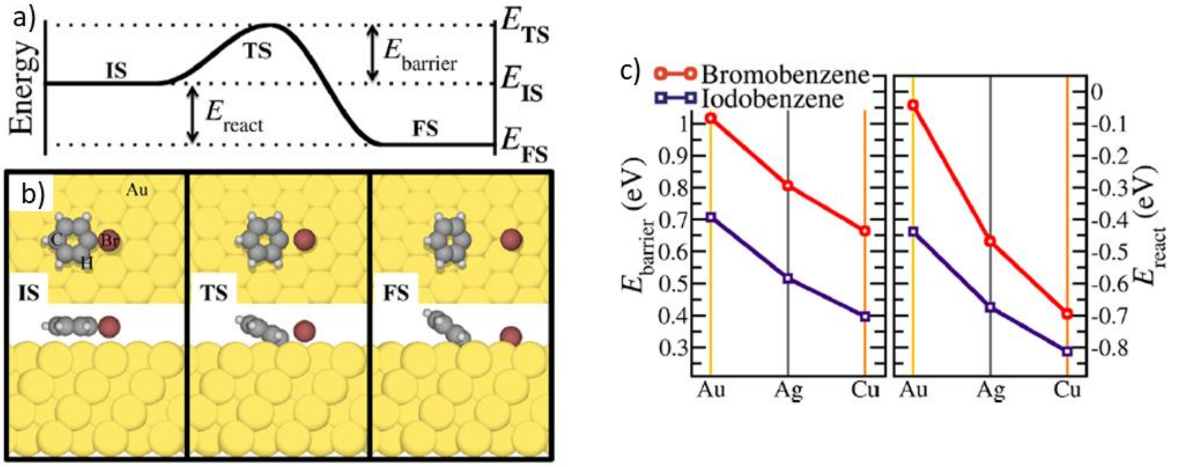

Figure 1-20 **a) scheme of the energy barrier and reaction energy for a dehalogenation reaction; b) dissociation of bromobenzene on Au(111), depicting top and side views of the initial state (IS), transition state (TS), and final state (FS) of the reaction; c) Energy barrier (left) and reaction energy (right) for the dissociation of bromobenzene and iodobenzene on the (111) facets of Au, Ag, and Cu. Adapted from Ref.[16] with permission from the American Chemical Society.**

In the same work, they also studied the diffusion of the benzene monomer on the three surfaces, and found that molecular hopping was favored on Au while flipping motion was favored on Ag and Cu. Finally, they addressed the polymerization step, finding an overall lower energy barrier for Cu (Figure 1-21).

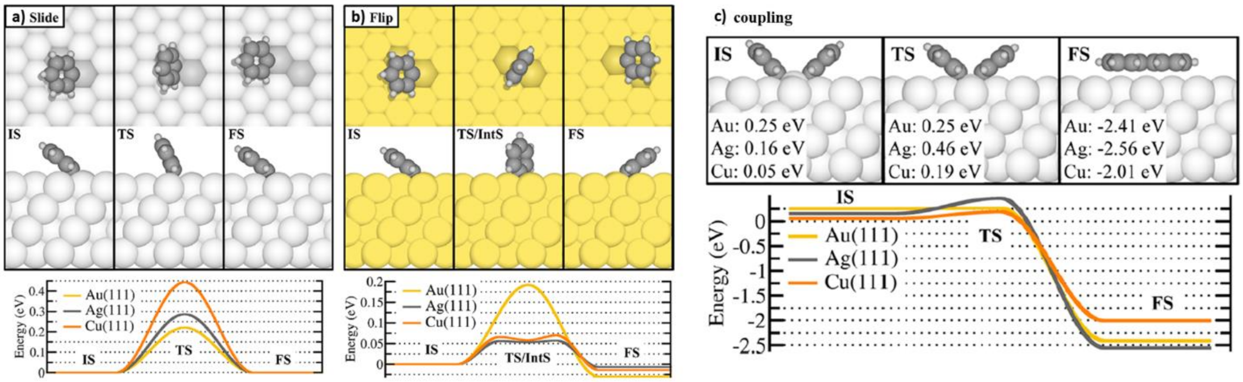

Figure 1-21 **Energy diagrams for (a) sliding diffusion and (b) flipping diffusion of phenyl on Au(111), Ag(111), and Au(111), where the top and side views of the paths are depicted in the top panel for (a) Ag(111) and (b) Au(111). The flipping diffusion (b) is a two-step process on Cu(111) and Ag(111); c) energy diagram for the coupling reaction of two phenyls into biphenyl on the close-packed facets of Au, Ag, and Cu. Adapted from Ref.[16] with permission from the American Chemical Society.**

From an experimental point of view, the best example is arguably found in the 2017 work by Dong et al.,[121] who studied the reaction of a 1,3,5-4-bromophenyl-benzene on four different surfaces, adding a platinum layer (grown on silver) to the commonly studied copper, gold and silver substrates. As can be seen in Figure 1-22, the resulting structures following RT adsorption are strongly dependent on the substrate, with OM networks observed on Cu and Pt and intact molecules on Au and Ag. Annealing these systems yields polymers on all the surfaces, however on Ag the overlayer passes through an OM phase, whereas on Au a polymer is formed directly upon dehalogenation. The polymerization temperature is also strongly dependent on the surface, and while some C-C coupling can occur at RT on Pt, a temperature of almost 500 K is required on Ag.

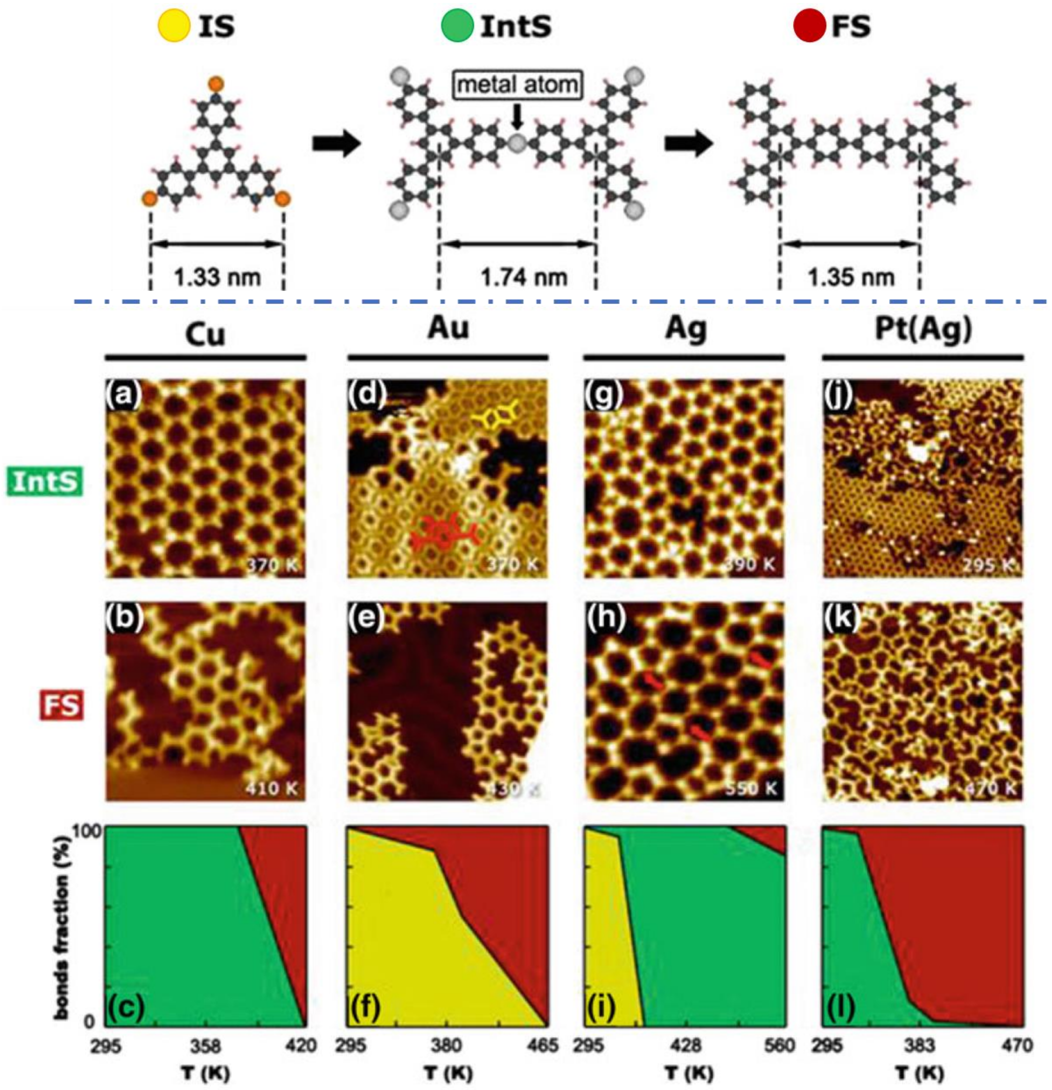

Figure 1-22 **Top row: reaction scheme from intact precursor (IS) to OM intermediate state (IntS) to polymer (FS) together with key distances optimized by DFT. Middle rows: STM images of the various systems after dosing (a,d,g,j) and after polymerization (b,e,h,k); bottom row: plots of the bonds fraction vs T(K), with color code identifying intact molecules (yellow), OM (green) or polymers (red). Adapted from Ref.[121]**

The most interesting aspect of this work is the fact that no OM bonds are observed on Au. Dong et al.[121] assigned the lack of OM networks on Au surfaces to the fact that they are short-lived and thermodynamically unstable. As reported in Figure 1-23, they assign the Au OM phase a higher energy than that required to form the final polymeric phase, concluding therefore that it is only a brief transient of the reaction instead of a stable intermediate as found on other surfaces.

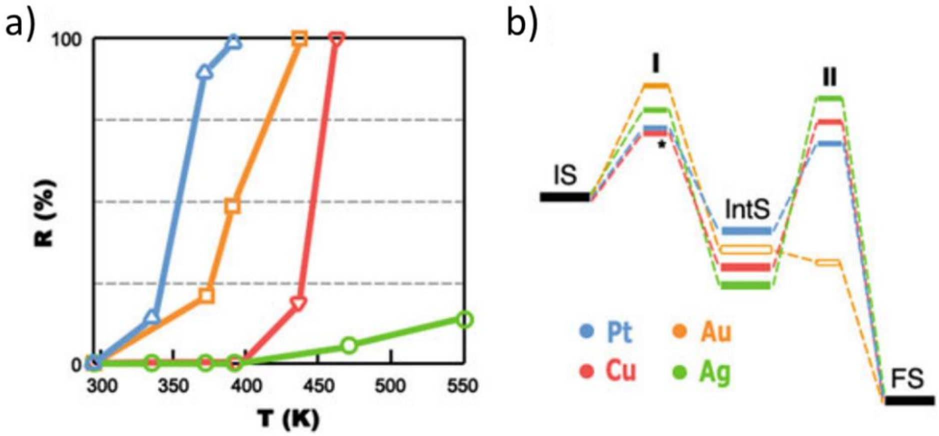

Figure 1-23 a) percentage of polymerized molecules vs T(K); chart of the energies for the initial (IS), intermediate (IntS) and final (FS) states, together with the respective reaction activation energies for all the substrates. Adapted from Ref.[121]

e. *Previous studies & State of the art*

The first connection between Ullmann coupling and surface chemistry can be traced back to the works of Xi and Bent in 1992,[26, 32] who used thermal desorption spectroscopy to study the coupling of iodobenzene on copper. The first direct observation was by Hla et al.[27] in 2000, which followed all the steps of the Ullmann coupling using STM as the probing technique, from intact molecules, to OM units, to dimers. A few years later the first 1D and 2D polymers were obtained,[20] and since 2009 on-surface Ullmann coupling has been an active field of research, as can be seen from the selected list of important papers reported in Table 1.1.

Table 1.1 History of on-surface Ullmann coupling ; selected works with reported the stimulus to start the reaction, the final structure obtained, the surface used for the growth and the year of publication.

Reaction	Stimulus	Surface	Final structure	Year	Reference
Ullmann coupling	STM-tip	Cu(111)	Dimers	2000	Hla et al. Phys. Rev. Lett.[27]
	Heat	Cu(111)	1D polymers	2004	McCarty et Weiss. J. Am. Chem. Soc.[105]
	Heat	Au(111)	1D, 2D polymers	2007	Grill et al. Nat. Nano.[20]
	Heat	Cu(110)	1D polymers	2009	Lipton-Duffin et al. Small [19]

Heat	Cu(110)	2D polymers	2009	Gutzler et al. Chem. Commun.[122]
Heat	Ag(110)	2D polymers	2009	Bieri et al. Chem. Commun.[123]
Heat	Au(111)	1D polymers	2009	Bombis et al. Angew. Chem. Int. Ed.[124]
Heat	Cu(110)	1D polymers	2010	Lipton-Duffin et al. Proc. Natl. Acad. Sci. U.S.A.[125]
Heat	Au(111)	2D COF, hosting C60	2010	Blunt et al. Chem. Commun.[126]
Heat	Cu(111), Cu(111), Ag(111)	2D polymers	2010	Bieri et al. J. Am. Chem. Soc.[108]
Heat	Au(111), Au(100)	Hierarchical 1D and 2D polymers	2012	Lafferentz et al. Nat. Chem.[18]
Heat	Au(111)	1D polymers	2013	Lin et al. J. Am. Chem. Soc.[127]
Heat	Ag(111)	2D polythiophene(b)	2013	Cardenas et al. Chem. Sci.[24]
Heat	Au(111)	1D polymers	2014	Adisoejoso et al. Chem. Eur. J.[128]
Heat	Au(111)	Hierarchical 2D polymers	2014	Eichhorn et al. ACS Nano[102]
UV light	Au(111)	1D OM chains	2015	Basagni et al. Chem. Commun.[129]
Heat	h-BN/Ni(111)	2D polymers	2016	Zhao et al. Chem. Commun.[130]
Heat	Au(111)	Hierarchical 1D and 2D polymers	2017	Steiner at al. Nat. Commun.[101]

Ullmann coupling + dehydrogenation	Heat	Au(111), Ag(111)	GNR	2010	Cai et al. Nature[103]
	Heat, STM-tip	Au(111)	Intra-GNR heterojunctions	2012	Blankenburg et al. ACS Nano[131]
	Heat	Cu(111)	Chiral-edges GNR	2014	Han et al. ACS Nano[132]
	Heat	Au(111)	GNR	2015	Basagni et al. J. Am. Chem. Soc.[133]
	Heat	Au(111)	Sulfur-doped GNR	2016	Nguyen at al. J. Phys Chem. C[117]
	Heat	Au(111)	GNR + Porous graphene	2018	Moreno et al. Science.[134]
	Heat	Au(111)	Zigzag-edge GNR	2019	Beyer et al. J. Am. Chem. Soc.[135]
Dehydration + Ullmann coupling	Heat	Au(111)	2D porous polymers	2012	Faury et al. J. Phys. Chem. C[136]

During the 20-year life of on-surface Ullmann polymerization, a variety of 1D and 2D polymers and GNRs have been reported, together with several theoretical papers, which have used DFT, Monte Carlo or other simulations to understand or predict experimental data. While an extensive database of investigated precursors and surfaces has been created, there are still open questions and definitely room for improvement. Nowadays the quest is no longer the demonstration of the proof-of-concept, but the true realization of long-range ordered 2D polymers with the desired properties. Several papers have already shown how electrical properties such as the bandgap should scale with polymer extent and order, particularly the beautiful presentation by Gutzler and Perepichka in 2009,[137-138] who calculated the HOMO/LUMO bandgap dependence for various 1D and 2D polymers by extending polymerization from 1 unit up to an infinitely extended polymer (Figure 1-24).

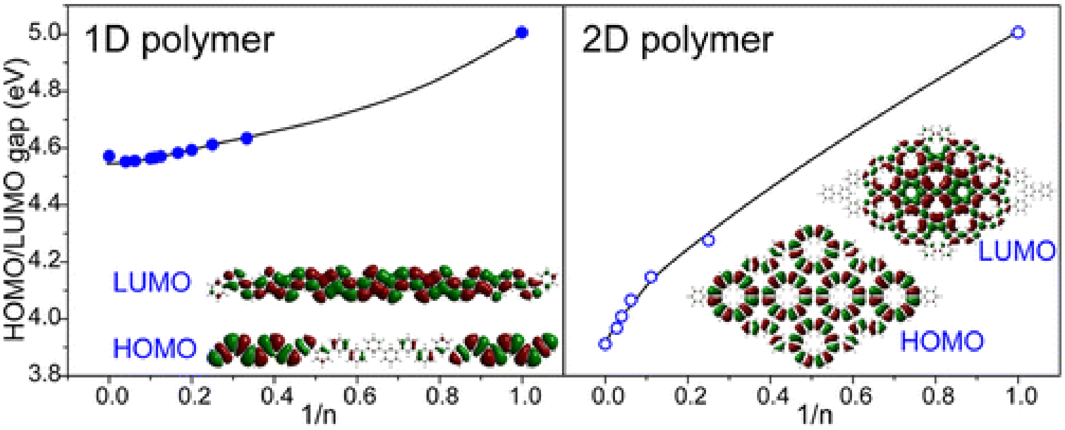

Figure 1-24 **Dependence of the simulated HOMO/LUMO bandgap of a 1D and 2D polymer vs the size of the polymer: the bandgap reduces as more monomers are added to the polymer, until reaching a set value when an infinitely extended polymer is considered (0.0 point on the X axis). Reproduced from Ref.[139]**

While bandgaps of various 2D polymers have already been reported from a theoretical point of view, we are still lacking the experimental confirmation. Only in a few 1D cases was it possible to obtain sufficiently large and ordered domains to be studied with averaging techniques such as ARPES, and most of the available 2D examples in literature present STS analysis, on selected parts of the sample with the desired structure. An example of this can be found by Steiner et al. in 2017,[101] and is reported in Figure 1-25. In their work they studied the polymerization of triphenylamine precursors, obtaining various structures on the surface, from isolated molecules and linear polymeric chains, to stacked chains and small 2D polymeric patches. They were able to perform STS measurements on these structures, obtaining results of the variation of the material band structure with polymer size, and polymer dimension from 0D to 2D.

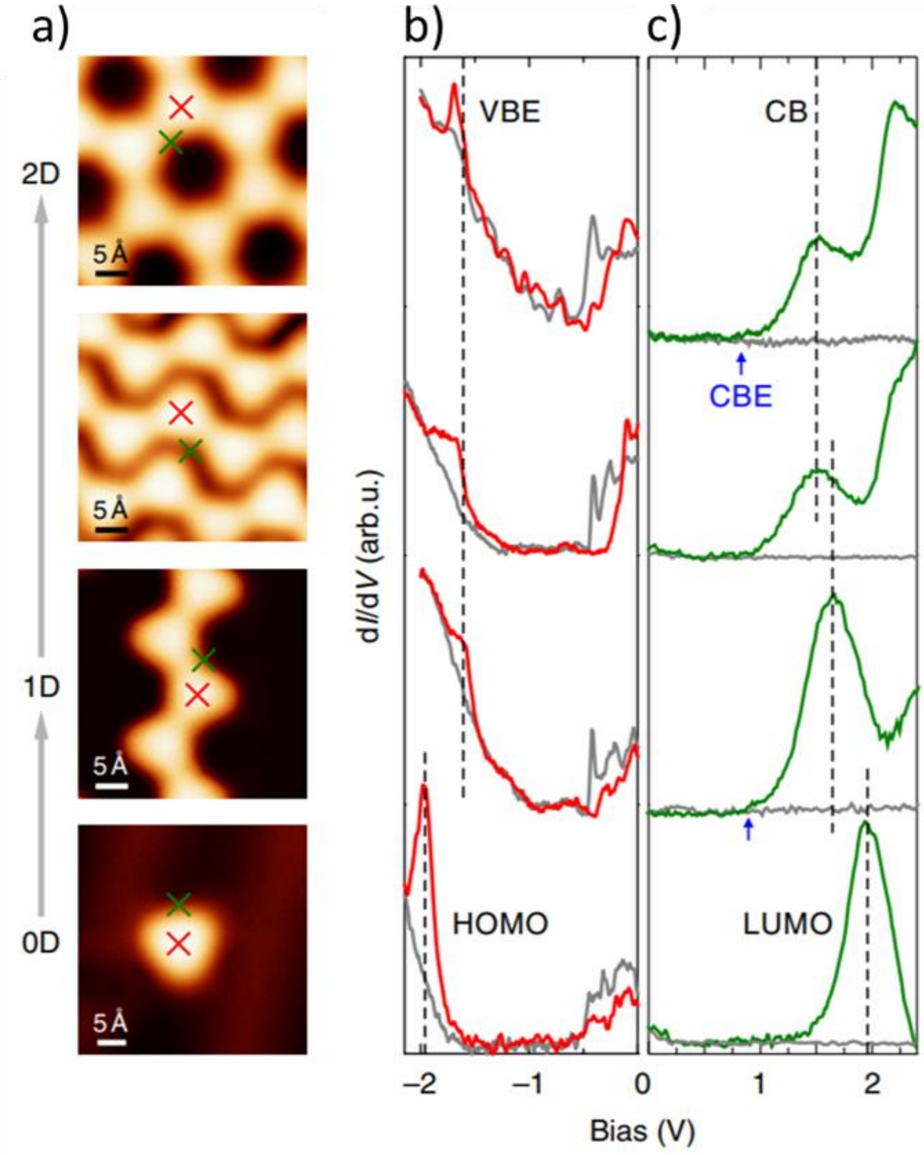

Figure 1-25 *dI/dV* spectra of different polymeric structures made from the same triphenylamine precursor; a) STM images indicating the location of the STS spectra; b,c) STS of the valence band (b) and the conduction band (c) of the 2D network (top), self-assembled 1D chains (second row) and isolated 1D chains (third row), and the corresponding HOMO and LUMO of the monomer (bottom); grey spectra refers to the bare Au(111) surface as a reference, while blue arrows indicate the onset of the conduction band. Reproduced from Ref.[101] CC BY 4.0

1.5.3 Other on-surface reactions

Ullmann coupling is the most common approach to produce a conjugated polymer on a surface but is not the only one. From 2000 onward, multiple chemical pathways have been exploited to obtain the desired nanostructures, each with peculiar advantages and drawbacks. Examples include Glaser coupling, decarboxylation, cyclo-dehydrogenation, boronic acid condensation, Wanzlick coupling, polymerization of diacetylene derivatives, Schiff-base coupling, and the trimerization of ethynylenes.

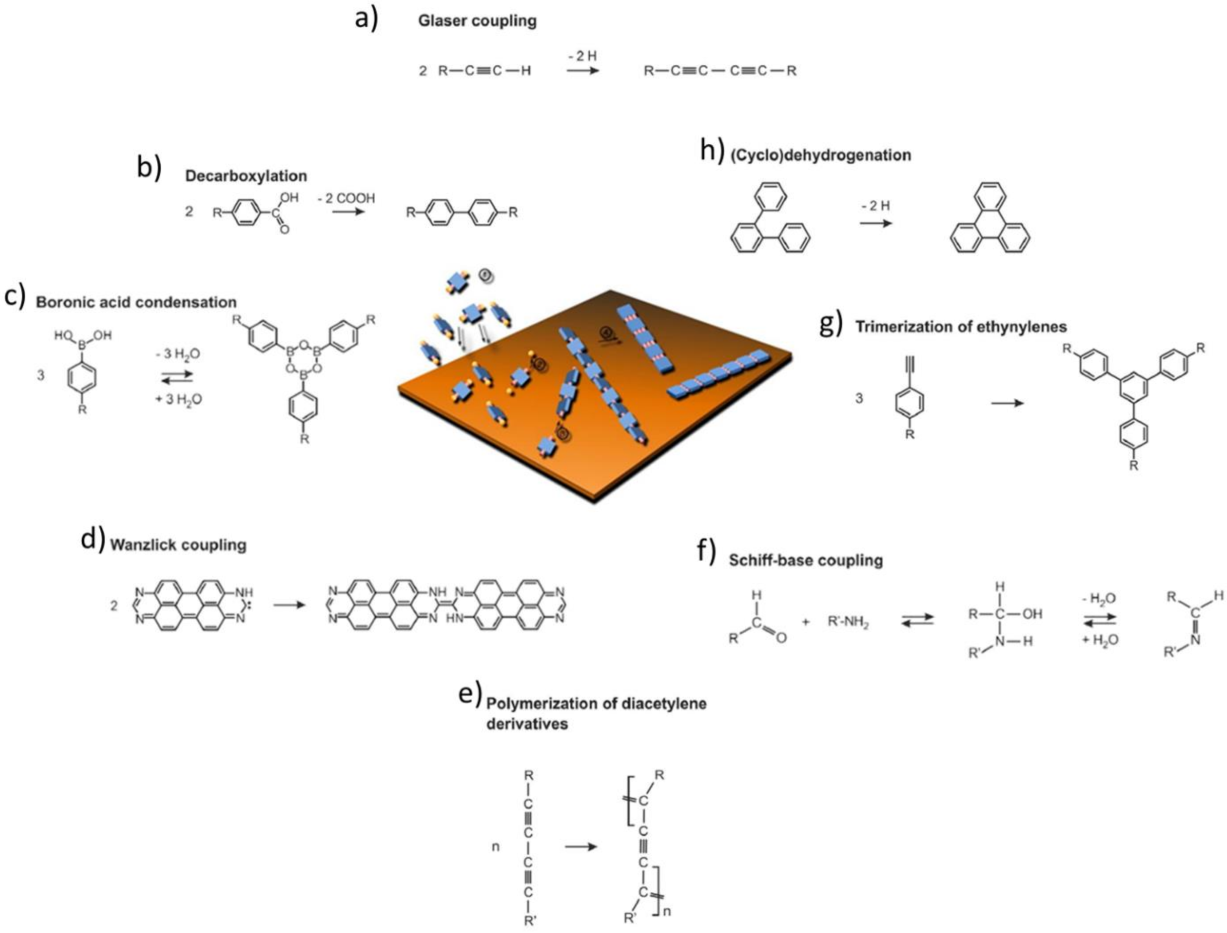

Figure 1-26 Scheme of various reactions used to produce on-surface polymers. Adapted from Ref.[25]

While most of this thesis is focused on the Ullmann reaction, a small part of my time (and of the work reported here) was spent to pursue different ways to polymerize on a surface. It is also necessary to report alternative polymerization pathways to give the reader a complete picture of this research field. Figure 1-26 includes some of the reactions used to obtain on-surface polymers. While they all result in covalently-bonded structures, only in some case are the structures π-conjugated. Deciding which reaction to use is a question of balancing the needed structure with the reaction parameters and activation energies required. For example, boronic acid condensation is most suited for solution-solid interface systems, where the reversibility of the reaction will assure the presence of a long-range ordered layer with self-healing properties. Other reactions, such as the diacetylene polymerization, can be easily activated using an STM tip or UV light in addition to the aforementioned thermal heating, making it more versatile. An attempt to realize on-surface polymerization of diacetylene derivatives with UV light is the focus of Chapter 6 of this thesis.

2 THEORY AND EXPERIMENTAL METHODS

The study of nanostructures on a substrate requires specific techniques that are surface-sensitive with the required resolution. In this chapter I will introduce the basic theoretical concepts necessary to understand the results presented in the following chapters. The main techniques used to perform the experiments will be briefly described, giving the reader the possibility to understand the results without the need to be an expert. I will explain the working principles of STM, used to study the morphology of the formed structure, and introduce synchrotron radiation and the XPS spectroscopy used.

2.1 Scanning tunneling microscope

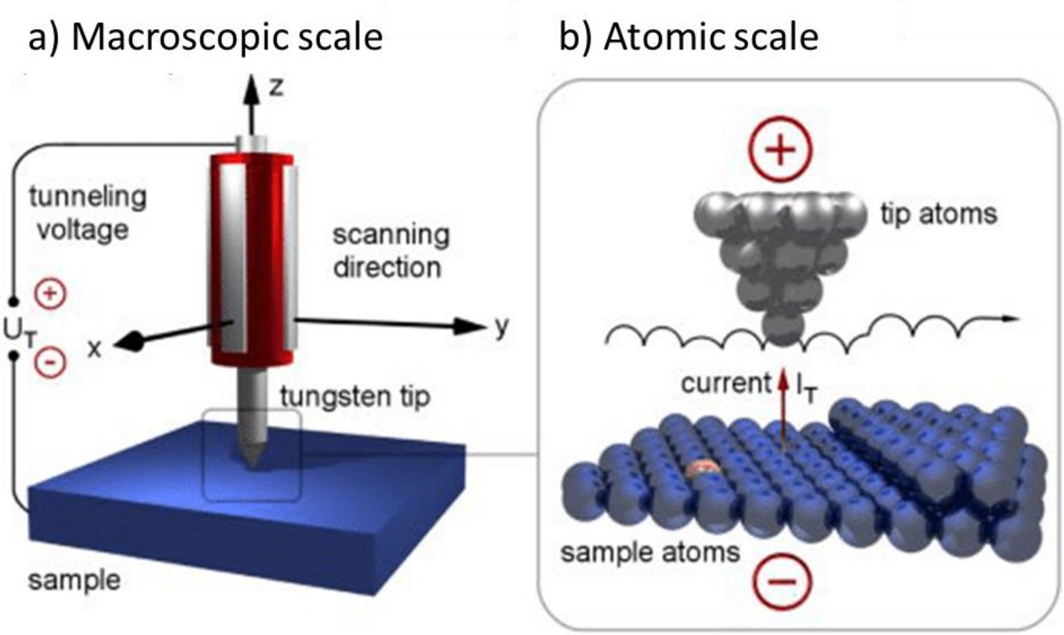

Figure 2-1 **a) scheme of an STM at a macroscopic scale, with the tip mounted on a XYZ piezoelectric motor that controls its position, and put close to (but not in contact with) a sample; a tunneling voltage is then applied between the tip and the sample; b) zoom-in on the tip-sample region of a: the tunneling current I_T is represented by the red arrow, while the black curve represents the tip movement on the Z axis to keep I_T constant while scanning the sample. Adapted from Ref.[140]**

STM is a surface analysis techniques which gives real-space images of a conducting or semiconducting surface down to the single-atom length scale, with a lateral resolution of approximately 1 Å and 0.1 Å of depth resolution.[141] Invented by Binnig and Rohrer at the IBM laboratories in 1981, it is based on a probe (a sharp conductive tip) mounted on a *xyz* piezoelectric transducer able to control the tip position in space. When the tip is brought close to but not in contact (1-10 Å) with a conductive surface and a voltage is applied between the two, electrons move between the tip and the sample, thanks to the quantum tunneling effect, and the current is measured, yielding information on the local DOS of the sample in the proximity of the tip. A basic graphical description of the STM and its working principle is shown in Figure 2-1. For this invention, Binning and Rohrer were awarded the 1986 Nobel prize in physics. Since its invention various STM instruments have been made, allowing not only the imaging of atoms but also their manipulation, as well as being able to operate in different conditions (UHV, air, liquid) and in an extended temperature range (from close to zero to above 1000 K).

2.1.1 Basic principle

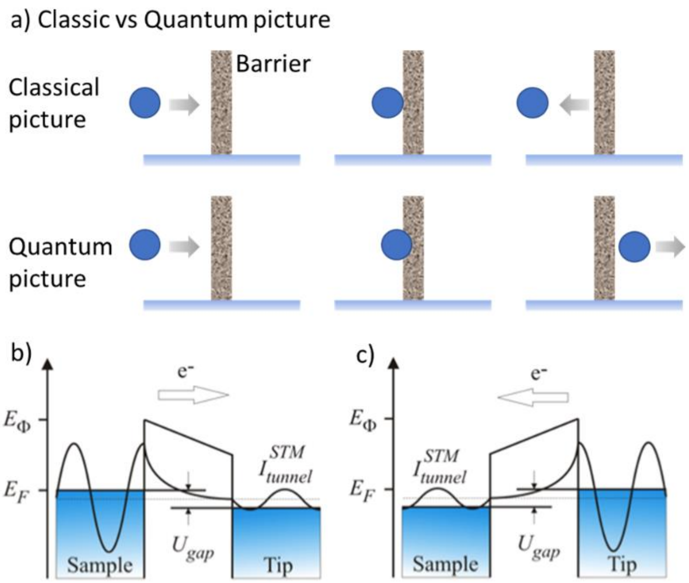

Figure 2-2 **a) classical vs quantum version of going through a barrier: in the classical picture, if the particle has an energy lower than the barrier height it cannot pass through, while in a quantum picture passing through is possible; b) energy levels of the tip and the sample when a positive (b) or negative (c) bias voltage is applied between them; the direction of the tunneling current is indicated by an arrow in both cases. b,c) adapted from Ref.[142]**

The working principle of the STM is based upon the "tunneling effect". Tunneling is a quantum effect that states that a particle has a finite probability to tunnel through an energy barrier even if the potential barrier is higher than the energy of the particle. This is of course impossible in the classic case, in which the barrier space is forbidden, and the particle can pass only if its energy is higher than the potential barrier (Figure 2-2a). According to quantum physics, applying an external voltage V between the sample and the tip will shift the respective Fermi levels (E_{FS} and E_{FT}), creating an energy gap (U_{gap}) between the two. Electrons are now free to move from occupied states at higher energy to unoccupied states on the other side, resulting in a tunneling current I_{tunnel}. The direction of the current will depend on the polarity of the applied voltage, and electrons will pass from the sample to the tip (Figure 2-2b) or vice versa (Figure 2-2c). A one-dimensional model of an electron and a potential barrier can be expressed by the equation:

$$\frac{p_z^2}{2m} + V(z) = E \tag{2-1}$$

Where p_z is the momentum in the z direction, m is the mass of the electron, E is its energy, and V(z) is the potential barrier. From a strictly classical point of view the electron is able to pass the barrier only if its energy E > 0.

In a quantum mechanics approach, we can instead describe the electron with the Schrödinger equation:

$$-\frac{\hbar^2}{2m}\frac{\partial^2}{\partial_z^2}\Psi(z) + V(z)\Psi(z) = E\Psi(z) \tag{2-2}$$

And we will have a solution for E > 0:

$$\Psi(z) = \Psi(0)e^{\pm ikz} \quad \text{with} \quad k = \frac{\sqrt{2m(E-V)}}{\hbar} \tag{2-3}$$

But also, for E < 0:

$$\Psi(z) = \Psi(0)e^{-kz} \quad \text{with} \quad k = \frac{\sqrt{2m(V-E)}}{\hbar} \tag{2-4}$$

We can also introduce the probability density of finding an electron at a given point z, that is:

$$P = |\Psi(z)|^2 = |\Psi(0)|^2 e^{-2kz} \tag{2-5}$$

Equation (2-5) gives the finite probability of having electrons across the potential barrier. Starting from the tunneling effect, Fowler and Nordheim found a relation that describes the tunneling of electron through a barrier. This relation states that the intensity of electron emission toward another electrode at distance *s* from the first is:

$$I = Ve^{-As\sqrt{\Phi}} \quad (2\text{-}6) \quad \text{with} \quad \Phi = \frac{\varphi_1+\varphi_2}{2} \quad (2\text{-}7)$$

Where $\boldsymbol{\Phi}$ is the average of the two electrodes work functions, *s* is the sample-to-tip distance, and *V* is the voltage between the electrodes.

2.1.2 Bardeen metal-insulator-metal model

To describe the relationship between the current I, the voltage V and the surface properties, we can refer to the model of Bardeen, proposed in 1961 to explain the observation of tunneling in a system of superconducting electrodes separated by oxide barriers.

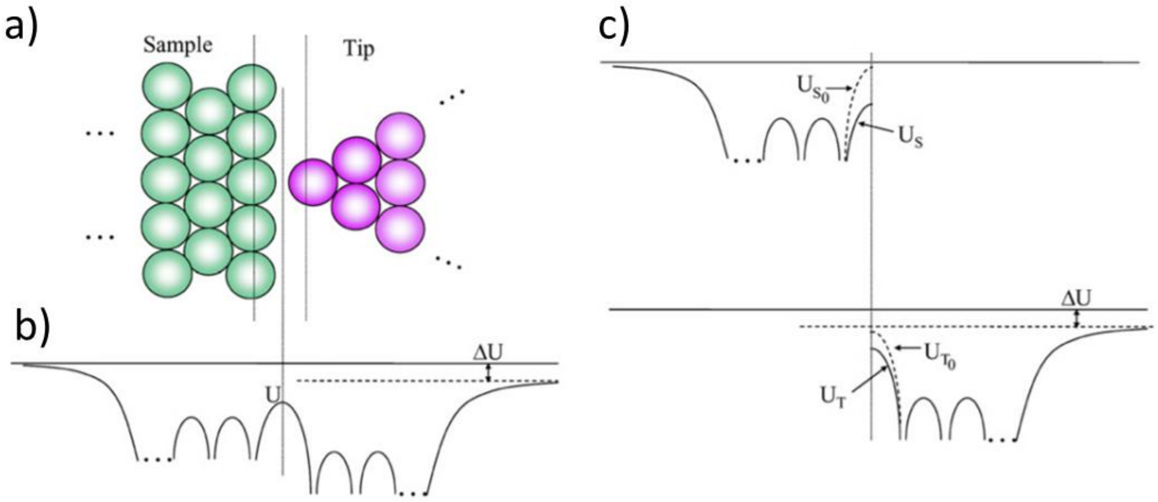

Figure 2-3 **Representation of the tip-sample system and their potential in accordance with Bardeen theory; b) Energy diagram. The system is split into the sample (c) and the tip (d) parts; U_{S0} and U_{T0} represent the surface potentials for the independent sample and tip, respectively; ΔU represents the induced electrostatic interface dipole that aligns the metal work functions. Reproduced from Ref.[143] with permission from Elsevier.**

A modified approach of the Bardeen model is obtained by introducing a surface of separation between the tip and the sample, identifying two regions, described by the potential surfaces U_S and U_T. It is possible to show that the exact position of the selected surface is not important.

For t < 0, the potential will be zero on the tip and the sample is in a steady state:

$$(T + U_S)\phi_\mu = E_\mu \phi_\mu \qquad (2\text{-}8)$$

Where T is the kinetic energy. At time t > 0, the potential on the tip is switched on and the sample begins to evolve according to the time-dependent Schrödinger equation.

$$-i\hbar \frac{\partial \Psi}{\partial \mathrm{t}} = (T + U_S + U_T)\Psi \qquad (2\text{-}9)$$

On the other hand, the wave functions of the tip are defined as:

$$(T + U_T)\chi_\nu = E_\nu \chi_\nu \qquad (2\text{-}10)$$

It is convenient to develop the time-dependent wave function Ψ as a function of χ_ν, making it possible to write:

$$\Psi = \sum_\nu \mathrm{a}_\nu(\mathrm{t})\, \chi_\nu e^{\frac{-iE_\nu t}{\hbar}} \qquad (2\text{-}11)$$

For a state $\varphi_{\mu,}$ at t = 0, we can write:

$$\mathrm{a}_\nu(\mathrm{t}) = \langle \chi_\nu | \phi_\mu \rangle e^{\frac{-i(E_\mu - E_\nu)t}{\hbar}} + c_\nu(t) \qquad (2\text{-}12)$$

With $c_\nu(0) = 0$, then:

$$\Psi = \phi_\mu e^{-\frac{-E_\mu t}{\hbar}} + \sum_\nu c_\nu\, \chi_\nu e^{\frac{-iE_\nu t}{\hbar}} \qquad (2\text{-}13)$$

The exact equation for $c_\nu(t)$ can be derived by replacing the (2-13) into (2-9), obtaining:

$$i\dot{c}_\nu = \langle \chi_\nu | U_T \phi_\mu \rangle e^{-\frac{-E_\mu t}{\hbar}} + \sum_\lambda c_\nu \langle \chi_\nu | U_S \chi_\lambda \rangle e^{\frac{-iE_\lambda t}{\hbar}} \qquad (2\text{-}14)$$

According to the first order perturbation theory, the probability of transition of an electron from χ_ν to ϕ_μ is given by Fermi's golden rule:

$$w_{\mu\nu}^{(1)} = \frac{2\pi}{\hbar} \left| M_{\mu\nu} \right|^2 \delta(E_\nu - E_\mu) \qquad (2\text{-}15)$$

With the matrix element equal to: $M_{\mu\nu} = \int_{\Omega_\mathrm{T}} \chi_\nu^* U_T \psi_\mu d\tau$. (2-16) Since U_T has a value only in the body of the tip, the matrix element is evaluated only within its volume, Ω_T.

The matrix element (2-16), according to the equation (2-10), can be rewritten as:

$$M_{\mu\nu} = \int_{\Omega_\mathrm{T}} \chi_\nu^*(E_\nu - T)\psi_\mu d\tau \qquad \text{(2-17)}$$

The δ in equation (2-15) requires that $E_\nu = E_\mu$. Furthermore, considering that U_S is 0 in Ω_T, it is possible to obtain the matrix element converted into a surface integral in terms of modified wave functions.

$$M_{\mu\nu} = \int_{\Omega_\mathrm{T}} \left(\chi_\nu^* E_\mu \psi_\mu - \psi_\mu T \chi_\nu^*\right) d\tau = \int_{\Omega_\mathrm{T}} \left(\chi_\nu^* T \psi_\mu - \psi_\mu T \chi_\nu^*\right) d\tau = -\frac{\hbar}{2m} \int_{\Omega_\mathrm{T}} \left(\chi_\nu^* \nabla \psi_\mu - \psi_\mu \nabla \chi_\nu^*\right) d\tau$$

(2-18)

So, the intensity of the tunneling current can be seen as transition probability from energy states E_F to eV, and it can therefore be expressed as:

$$I_{sample\rightarrow tip} = -2e\frac{2\pi}{\hbar}\int_{-\infty}^{\infty} |M|^2 \rho_s(E_F - eV + \epsilon)\rho_t(E_F + \epsilon)[f(E_F - eV + \epsilon) - f(E_F + \epsilon)]\, d\epsilon$$

(2-19)

where the factor 2 comes from the spin, *-e* is the electron charge and $\frac{2\pi}{\hbar}$ comes from time-dependent perturbation theory, $f(\varepsilon)$ is the Fermi distribution with energy ε and $\rho(E)$ is the density of states with energy ε.

2.1.3 STM operation modes

The movement of the tip and the measurement of the interaction between the tip and the sample is entrusted to a piezo-electric system, which approaches the surface on the z axis and is capable of tiny movements along the surface of the sample.

The STM can work in different modes: by maintaining a constant tunneling current (CCM, constant current mode), or, vice-versa, by keeping constant the height of the tip from the plane of the sample (CHM, constant height mode). In CCM mode, an electronic feedback system maintains a constant current as the tip is scanned in the *x-y* plane (the plane of the sample), and the variation of height is measured relative to the *z* axis. This information represents a surface of constant charge density whose contrast is due to the variations in height. Vice-versa, in the CHM mode, the feedback loop maintains a constant height relative to the plane, recording the variation of the tunneling current in relation to the position in the *x-y* plane.

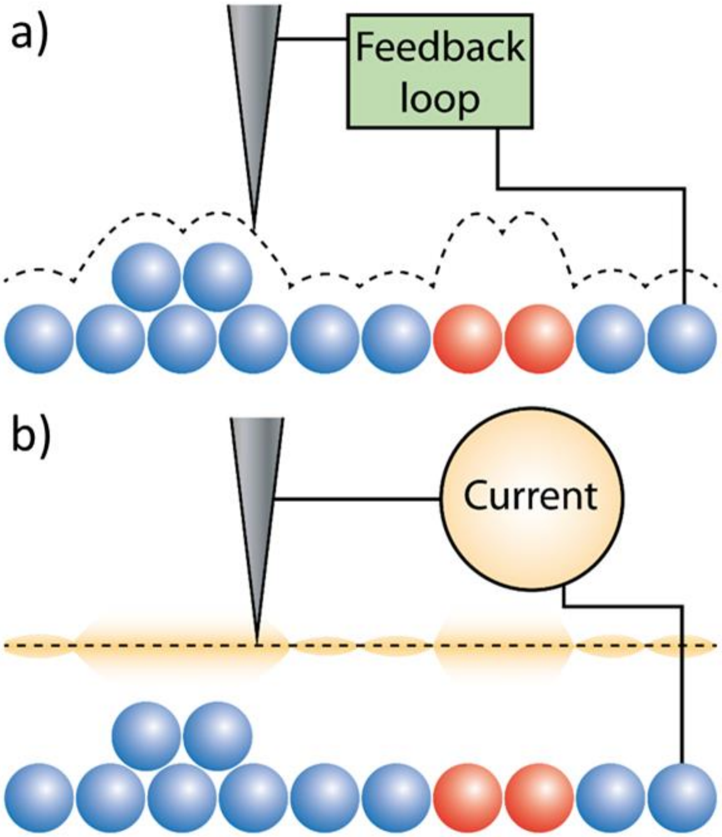

Figure 2-4 **Scheme of two possible STM operation modes: constant current (a) and constant height (b). Reproduced from Ref.[144] under CC BY-SA 4.0.**

Besides morphological information, with STM instruments it is also possible to perform scanning tunneling spectroscopy (STS) by obtaining the spectrum of the I/V, linked to the conductance (dI/dv)/(I/V). Of course, STS requires longer scanning times and a very stable tip-surface system.

2.2 X-ray photoelectron spectroscopy

XPS is a non-destructive photoelectron spectroscopy used in material science to study surfaces. It allows for the recognition of all the chemical elements that make up a material surface and to determine their chemical state. An XPS spectrum is obtained by irradiating a material with X-rays (photons with an energy of a few keV) and subsequently measuring the kinetic energy of outgoing electrons from the topmost layers (the mean free path of electrons in solids is about 1-10 nm).[145] The electron emission is due to the photoelectric effect, observed by H. R. Hertz in 1887 and shortly after by A. Righi and explained by A. Einstein in 1905. The law that regulates this process is the following:[145]

$$E_K = h\upsilon - E_B - \phi \qquad (2\text{-}20)$$

Where E_K is the kinetic energy of the detected electron, E_B is the binding energy (BE) that such an electron had in the material, $h\upsilon$ is the energy of incident photon and $\boldsymbol{\Phi}$ is the work function. The work function is given by the difference in energy between the Fermi level of the material and the vacuum level of the analyzer, so it will depend on the instrument. It is therefore possible to obtain qualitative information by knowing the E_B of the atoms, but also quantitative information, since the intensity of detected electrons for a particular element is related to its concentration (in the area from which the photoemitted electron comes), through the following proportion:[145]

$$I_E \propto [E]\sigma_E \lambda_E T \cos\vartheta \qquad (2\text{-}21)$$

Where $[E]$ is the concentration of the analyzed element, I_E the intensity of detected electrons corresponding to a specific orbital of the element E, σ_E is the photoionization cross section for that orbital, λ_E is the mean free path of these electrons, T is a parameter dependent on the analyzer and ϑ is the electron emission angle.

The binding energies can also provide information about the chemical state of the atom and therefore on the chemical bonds within a molecule at the surface. Indeed, the energy of the measured photoemission peak will depend on the chemical state of the element, and different energetic shifts can be observed. As introduced before, the necessary instruments for this technique are an X-ray source and an analyzer for the emitted electrons. These instruments should be placed in a UHV environment to allow for electron detection.

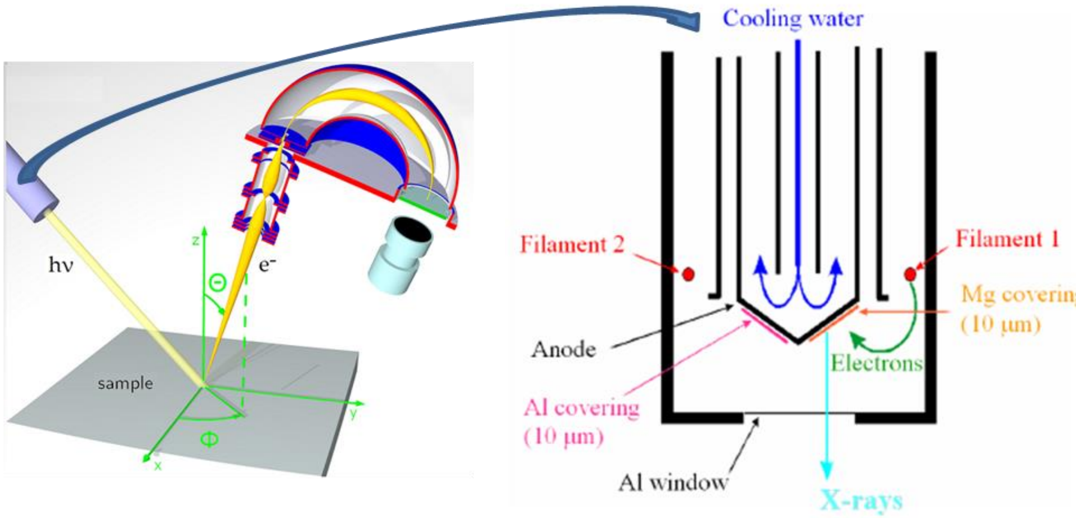

Figure 2-5 **Scheme of the XPS apparatus (left) with details of a dual filament X-ray source (right). Adapted from Ref.[146]**

An X-ray source (represented in Figure 2-5) is usually a "lamp", in which these rays are obtained by electronic bombardment of particular metallic anodes. A spectrum of X-rays emitted in this way is represented in Figure 2-6. It is formed by a continuous curve and by some peaks, typical of the decelerating material used (usually Mg or Al). The continuous curve, also called "white radiation", is due to the bremsstrahlung effect. Bremsstrahlung (which is German for breaking radiation) refers to the electromagnetic radiation produced by deceleration of charged particles due to other charged particles. Usually we refer to electrons decelerated by nucleus, and the intensity of the X-rays produced depends on the target atomic number and filament current. The characteristic peaks, first observed by C. G. Barkla, are produced when electrons from outer shells fill vacancies in inner shells, left by collisions with incoming (high-energy) electrons. These lines depend on the target material and are narrow and intense with respect to the white radiation, as showed in Figure 2-6. The K_α and K_β Siegbahn notations refer to the electronic transitions, with the first being a transition from a 2p orbital to 1s and the latter from a 3p to a 1s. The produced photons cross a thin metal window, usually made of aluminum, used to block any secondary electrons created in the process. As one can see from Figure 2-5, the anode is water cooled, as the process develops large quantities of heat.

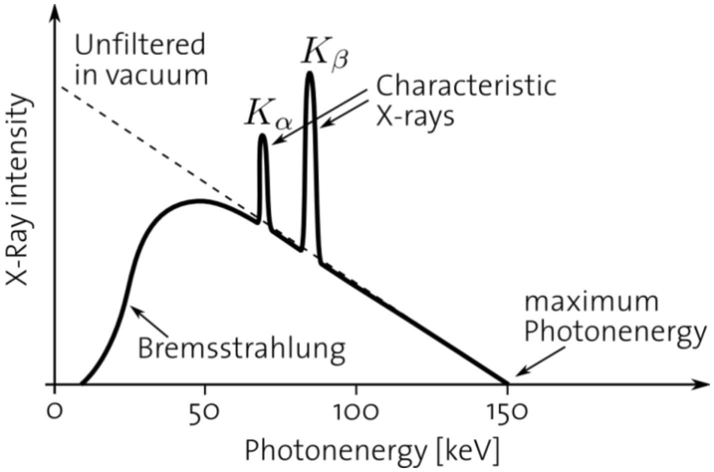

Figure 2-6 **Typical behavior of the relation between emitted X-ray intensity versus their energy: continuous curve with some evident peaks, dependent on the emitting metal. Adapted from Ref.[147]**

2.3 Synchrotron light-source facility

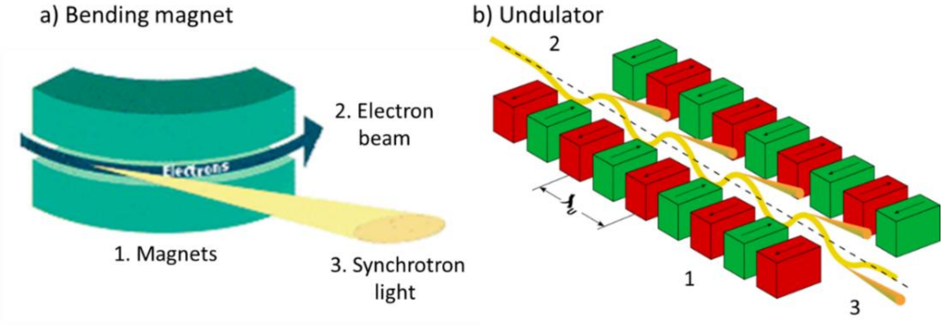

Figure 2-7 **Schemes of two possible ways to produce X-ray radiation by deflecting electrons in a synchrotron using a bending magnet (a) or an undulator (b). Reproduced from Ref.[148] under CC BY-SA 3.0**

A synchrotron is a kind of particle accelerator, in which a beam of accelerated particles travels in a cyclic path and where the magnetic and electric fields, necessary to bend or accelerate the beam, are synchronized with the particle beam, hence the name. Charged particles, like electrons, emit an electromagnetic radiation, called synchrotron radiation (SR, also referred to as magneto-bremsstrahlung radiation) when accelerated in a direction perpendicular to their velocity. A synchrotron light-source facility is therefore a circular accelerator which produces synchrotron radiation in a controlled way and uses it for scientific experiments. The electrons are circulated around the storage ring by a series of magnets separated by straight sections. SR can be produced using various devises, such as bending magnets or insertion devices (Figure 2-7). Bending magnets are used to curve the beam, while insertion devices (multipole wigglers and undulators) are used on the straight sections. In a modern synchrotron facility, such as the SOLEIL facility in Paris (a schematic of which is depicted in Figure 2-8), electrons are usually generated and accelerated in a linear accelerator. Those electrons are collected in a booster, where they are further accelerated up to operational velocity and then injected into the storage ring. Inside this ring the electrons pass through bending magnets and insertion devices, where the SR is produced. The ST in turn goes into the experimental beamlines, where series of mirrors and monochromators shape, focus and collimate the beam as required, so that a high photon flux over a small area is produced and used to study samples. The electron injection from the booster is usually performed in the so called "Top-mode", which means that the current of electrons is kept constant, so that there will be a constant flux of SR into the beamlines.

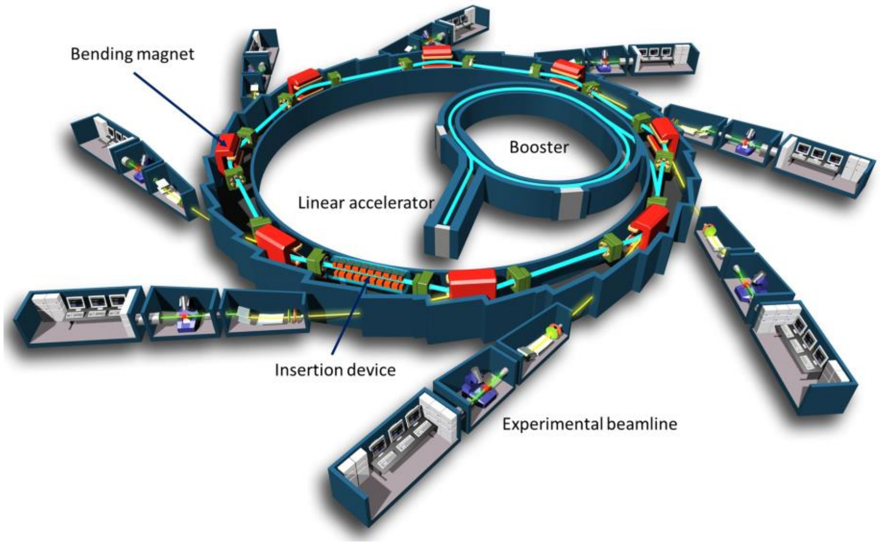

Figure 2-8 **Graphical representation of a 4th generation synchrotron facility such as the SOLEIL one in Paris. Electrons are produces in a linear accelerator and stored in a booster. From the booster they are introduced in the main ring, where bending magnets or insertion devices deflect them to produce X-rays which are focused into an experimental beamline, to be used for analysis. Reproduced from Ref.[149] with permission from EPSIM 3D, J.F. Santarelli.**

In the context of this thesis the use of synchrotron facilities was necessary to perform some of the analysis shown in the following chapters, in particular fast-XPS, ARPES and near-edge X-ray absorption fine structure (NEXAFS) spectroscopies.

2.3.1 Fast-XPS

Fast-XPS (also known as rapid-XPS or Temperature programmed XPS), is a technique that involves continuously acquiring an elemental core-level spectrum, to follow its evolution with time or temperature.[150] First developed to study the thermal desorption of CO from Rh(110),[150] it was adapted by Di Giovannantonio et al. to follow the Ullmann coupling of dBB on Cu(110).[30] The temporal resolution that can be obtained is strongly affected by the signal-to-noise ratio, hence the necessity of SR, where the high brilliance enables a large ratio. The brilliance is defined as $(\frac{emitted\ photons}{s \cdot mrad^2 \cdot mm^2 \cdot 0.1\%BW})$, measures how the flux is distributed in space and angular range (flux/emittance), and is commonly used to compare various radiation sources.[151] Additional improvement of the signal-to-noise ratio can be obtained by increasing the number of detected electrons. Such increase can be obtained using a 2D detector, based on multichannel plates, able to capture photoelectrons separating them for energy and angle of emission. Coupling 2D detectors with high brilliance means that a single spectrum of a few eV in width can be obtained in seconds, making it possible to follow dynamic processes (*e.g.* a chemical reaction) occurring in this timescale, in comparison to the hours necessary to obtain a spectrum using laboratory sources and few-channeltron detectors. The same 2D detectors also enable angular-resolved photoelectron spectroscopy to be performed, as described below. A typical fast-XPS result is commonly presented as 2D intensity maps of BE vs time, and an example can be observed in Figure 1-16.

2.3.2 Angle-resolved photoemission spectroscopy (ARPES)

Angle-resolved photoemission spectroscopy is a spectroscopic method that allows for the measurement of the momentum-dependent electronic band structure of a solid. ARPES experiments collect photoemitted electrons along particular directions as a function of the kinetic energy. Such spectra are called energy distribution curves, and show various peaks, corresponding to direct optical transitions. By acquiring different curves at different emission angles and photon energy, the electronic band structure of a system can be reconstructed.

To understand how the experiment can provide us insight into the quantum description of the solid state, I have to explain the complexity of the photoemission process. This process can be described as a single quantum-mechanical step[152-153] where the photoelectron is removed from the sample after photon absorption, and subsequently detected in vacuum. However, this approach, which requires the Fermi golden rule to write the transition probability between the initial and final states, is often too complex and requires numerous approximations to be solved. It is therefore convenient to describe the photoemission process using a three-step model. This model, introduced by Berglund and Spicer in 1961, divides the process into three separated steps: an optical excitation of the electron (from initial to final state) inside the solid, the transport of the photoelectron to the surface and the transmission across the surface to the vacuum.[154]

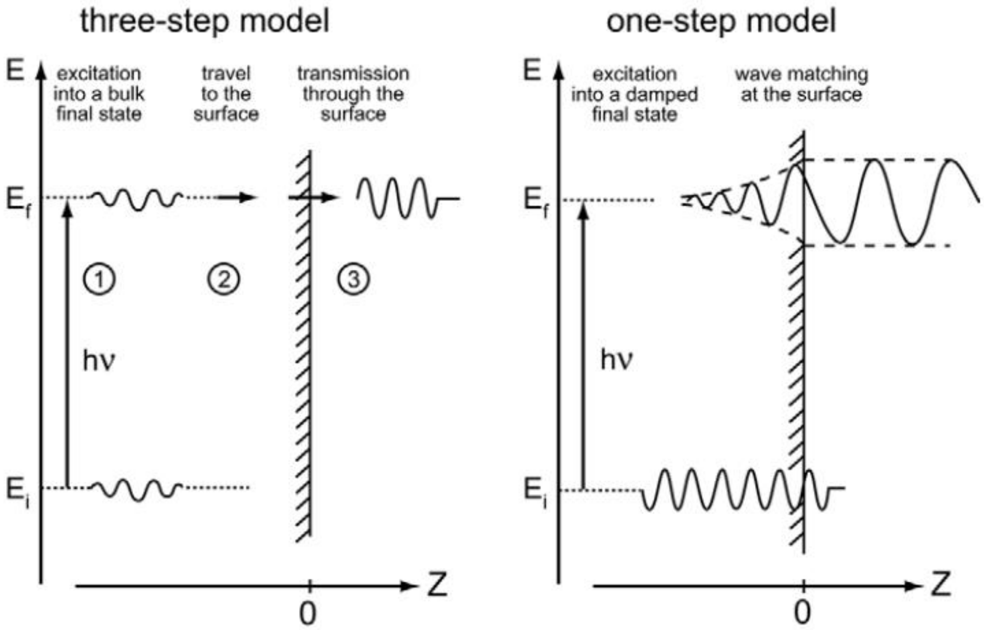

Figure 2-9 **Schematic representation of the three- and one-step models of the photoemission process. Reproduced from Ref.[155-156]**

Optical excitation of the electron in the bulk: During the photoemission process, an electron absorbs a photon of energy $h\nu$ and transitions from an initial Bloch state $|\psi_i\rangle$ to a final empty state $|\psi_f\rangle$. During this transition, in the UV range, the momentum transfer can be neglected, which leads to the conservation laws in the form:

$$h\nu = E_f - E_i \qquad \text{and} \qquad \boldsymbol{k}_f = \boldsymbol{k}_i \qquad (2\text{-}22)$$

where $\boldsymbol{k}_f, \boldsymbol{k}_i$ are the wave vectors of the initial and final states. This means that the photoemission process conserves the crystal momentum $\boldsymbol{k}$.

Travel of the excited electron to the surface: During this stage, the electron propagates towards the surface so that it can then be emitted in the vacuum. However, it can undergo inelastic collisions and so that the information on the energy and the wave vector of the initial state is lost, thus contributing to the inelastic background of the spectrum. The current of the electrons conserving the original kinetic energy and momentum will depend on the inelastic mean free path λ, which represent the average distance between successive inelastic events. This distance is strongly dependent on the energy used, but for the electron energies involved in ARPES experiments (10-200 eV) it is limited to a maximum of 10 Å, making ARPES a technique sensitive only to the surface.

Escape of the photoelectron into vacuum: During this step the electrons leave the sample with certain emission angles (θ, φ) and are collected by the analyzer. In the direction parallel to the surface, during the transmission of the photoelectron in the vacuum, the component of the wave vector $\boldsymbol{k}_{//}$ is conserved, so that its momentum outside the crystal can be written as:

$$\boldsymbol{k}_{i//} = \boldsymbol{k}_{f//} = \boldsymbol{q}_{//} \qquad \text{(2-23)}$$

$\boldsymbol{k}$ is defined as a vector of the reciprocal network inside the crystal, $\boldsymbol{q}$ as the wave vector of the electron outside the crystal. Considering only the first Brillouin zone, we can obtain from equation (2-23) the value of the parallel component of the wave vector:

$$\boldsymbol{q}_{//} = \sqrt{\frac{\boldsymbol{2m}}{\hbar^2}\boldsymbol{E_K}} \cdot \boldsymbol{sin\vartheta} \qquad \text{(2-24)}$$

On the other hand, perpendicularly to the surface, the electrons feel a potential step, *i.e.* the work function $\phi = E_V - E_F$, and the wave vector component is not conserved ($\boldsymbol{k}_{f\perp} \neq \boldsymbol{q}_{\perp}$). In this case we have to first consider the electrons in the final state as free electrons – which is the case for transitions well above the vacuum level – and to describe a potential V_0, a mean potential felt by the electrons inside the crystal. We can therefore obtain:

$$\boldsymbol{k}_{f\perp} = \sqrt{\boldsymbol{q}_{\perp}^{2} - \frac{\boldsymbol{2m}}{\hbar^2}\boldsymbol{V_0}} = \sqrt{\frac{\boldsymbol{2m}}{\hbar^2}\boldsymbol{E_K} \cdot \boldsymbol{cos^2\vartheta} - \frac{\boldsymbol{2m}}{\hbar^2}\boldsymbol{V_0}} \qquad \text{(2-25)}$$

2.3.3 Near-edge X-ray absorption fine structure (NEXAFS) spectroscopy

NEXAFS spectroscopy is a technique that studies the photoabsorption cross-section of a sample exposed to X-rays and provides chemical and structural information on the sample under analysis. It works by scanning the X-ray photon energy and measuring the X-ray intensity absorbed by excitation of core electrons to unoccupied states.[157] The X-ray absorption cross-section usually decreases with increasing photon energy, however, sudden increases are observed at discrete photon energies, located at the photoionization threshold and called an absorption edge. These edges are element-specific, and various regions in energy before and after them can be studied. NEXAFS refers to the study of the fine absorption structures that are present close to these edges, up to 30 eV above.[157] It requires a tunable monochromatic light source, with high intensity and energy resolution, hence the necessity of synchrotron facilities.

It can be described as a two-step process (Figure 2-10).[157] In the first, a core hole is produced by exciting a core electron to an unoccupied state by absorption of a photon. The second step consists of the recombination process of the core hole. The recombination can follow different processes, both radiative, where a photon is emitted (*i.e.* fluorescence), and non-radiative, where electrons are produced (*i.e.* Auger-like transitions), as shown in Figure 2-10a. In the work for this thesis, X-ray absorption was measured by the detection of Auger-like electrons. Those are generated by two different processes, the first, called participator decay, in which they participate in the core-hole decay process and the second, called spectator decay, in which the excited electron remains in the unoccupied level, and two valence electrons are removed (Figure 2-10a). The number of Auger electrons produced from the sample is directly proportional to the X-ray absorption cross section. During the first step, core electrons can be excited to various unoccupied states: π^*, Rydberg, σ^* and continuous states. Rydberg transitions are atomic-like features in core excited molecules, such as carbon 1s $\rightarrow$ 3s, carbon 1s $\rightarrow$ 3p transitions. Such peaks are usually sharp, but weak in intensity and appear below the ionization potential. Usually, core $\rightarrow \pi^*$, Rydberg and σ^* transitions can be differentiated by their energy position and the shape of the corresponding feature. The width of the resonance is determined by the resolution of the monochromator, the lifetime of the core excited state, and by molecular vibrations. As a rule of thumb, core $\rightarrow \pi^*$ transitions are sharper than core $\rightarrow \sigma^*$ transitions. The broadening of the core $\rightarrow \sigma^*$ transitions is due to an increased decay probability to the continuum state.

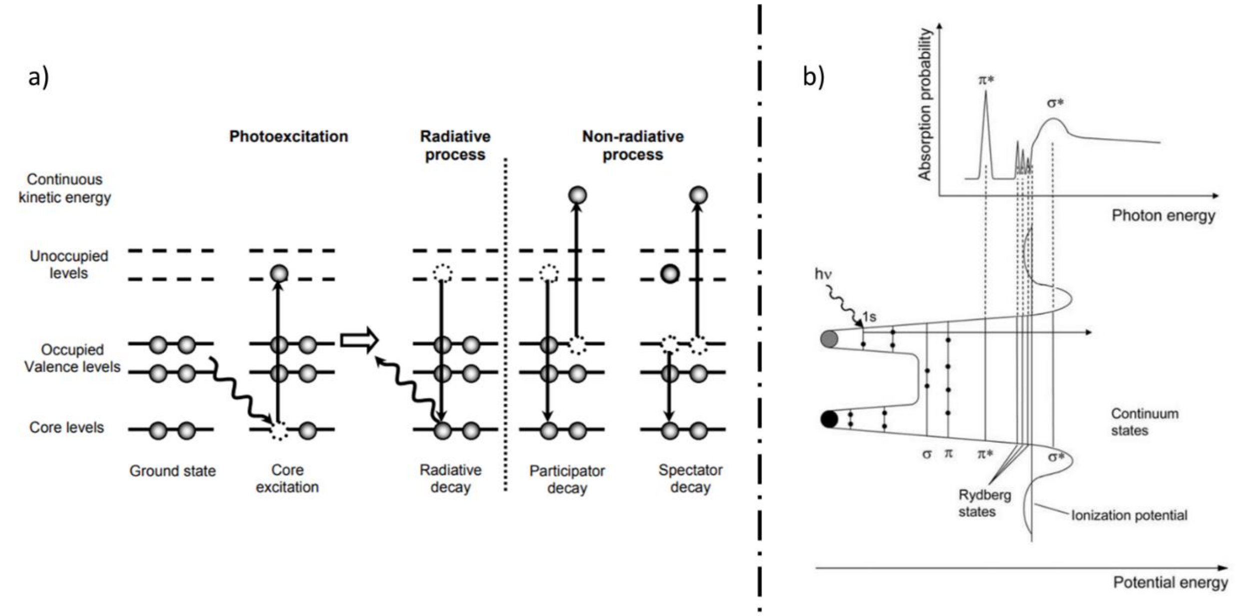

Figure 2-10. a) Schematic diagram of photoexcitation and recombination processes, where a core hole can be filled either through a radiative or non-radiative process by electrons from an higher shell; b) schematic potential and corresponding NEXAFS K-shell spectrum of a diatomic molecular group example, reproduced from Ref.[157]

The common method to detect the absorption is to measures the emitted electrons that are created by the absorbed X-ray, which is called electron yield measurement. In this method either all electron produced are measured (total electron yield, TEY) or only a fraction of them, by placing a retarding voltage in front of the detector (partial electron yield, PEY) or by setting the energy analyzer at a specific Auger transition energy (Auger electron yield, AEY). AEY will assure a higher signal-to-noise ratio, while TEY will provide higher signal rates. The data presented in this thesis have been acquired using PEY.

X-ray absorption cross-section and relation to molecular geometry: The X-ray absorption cross section or rate, σ_x is defined as the number of electrons excited per unit of time divided by the number of the incident photons per unit of time and area.[157] The transition probability from the initial to the final state will therefore be calculated using Fermi's golden rule, where the matrix depends on the interaction between the linear momentum operator of the electron, $\boldsymbol{p}$, and a unit vector of electric field of polarized incident light, $\boldsymbol{e}$:

$$\sigma_x \propto \langle \psi_f | \boldsymbol{e} \cdot \boldsymbol{p} | \psi_i \rangle \tag{2-26}$$

This matrix is directly related to the molecular orbitals involved in the excitation and can therefore provide information on the molecular geometry. The electron transitions must obey the dipole selection rules, thus, only transitions with the change of angular momentum quantum number $\Delta l = \pm l$ are allowed and will contribute to the measured spectra. NEXAFS spectra can therefore be used to determine the molecular orientations of the adsorbates on the surfaces, usually by analyzing the K-shell resonance, which in a molecular-orbital picture correspond to transition from the 1s orbital (K-shell) initial state to $\sigma^*$and π^*empty final states. Those states have a well-defined symmetry, which, coupled with the linearly polarized nature of SR, cause a strong angular dependence of the NEXAFS spectra. The direction of the orbital depends on the chemical nature of the C bonds, *i.e.* single, double, triple or aromatic ring. As illustrated in Figure 2-11a, if we represent single orbitals by a vector and two orthogonal orbitals by a plane, for aromatic rings the σ^* system is characterized by a plane, with the π^* being represented by a vector perpendicular to this plane.

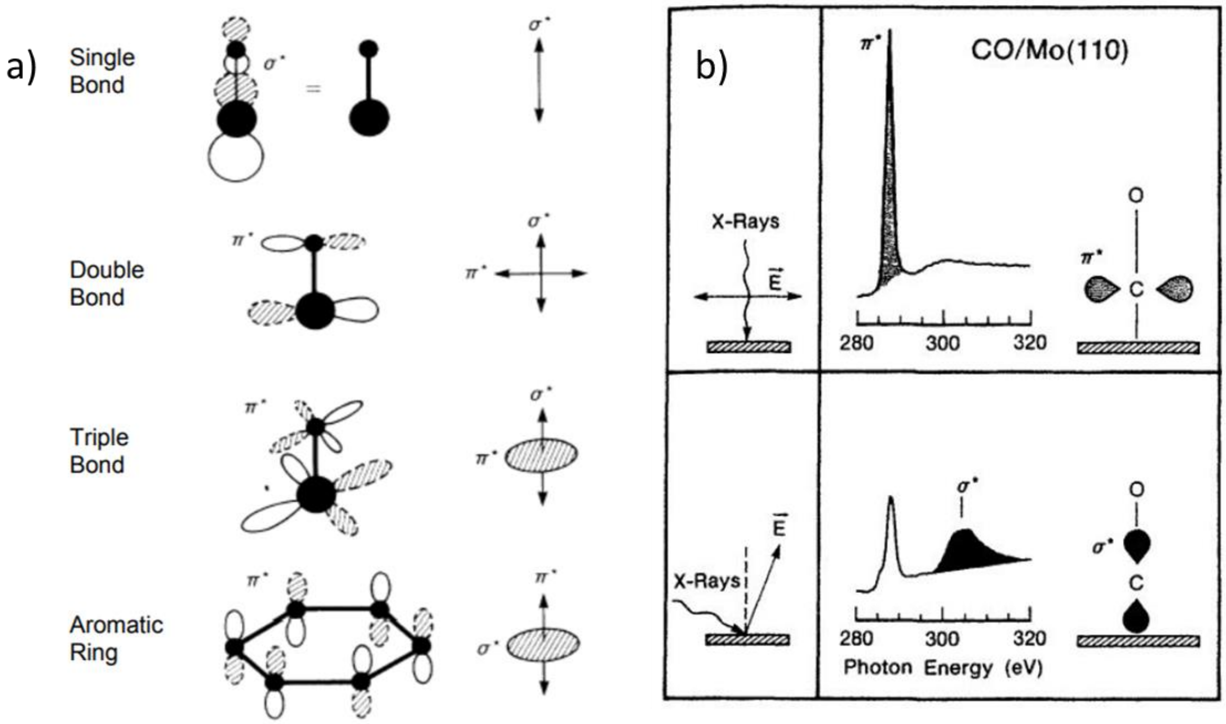

Figure 2-11 **a) Illustration of $\sigma^*$and π^*molecular orbital depending on the C bond type; b) Polarization dependence of resonances, illustrated for vertically oriented CO on Mo(110); the bottom spectrum was recorded at a 20° grazing X-ray incidence angle such that E made a 20° angle with the surface normal. Reproduced from Ref.[158]**

2.4 Precursors investigated

On-surface reactions are dependent on a number of parameters – of which the molecular-substrate interaction is the most important – that need to be taken into account for every surface polymerization experiment. Depending on the specific reaction pathway involved, different parameters need to be considered. The scope of this thesis is to study and understand those parameters, and use this knowledge to realize the desired polymeric nanostructure. Different molecules have been studied to obtain insight into different parameters and how they guide the process. Most of this thesis (Chapters 3 to 5) involves the Ullmann reaction, while Chapter 6 is instead focused on diacetylene polymerization. As explained previously, the Ullmann reaction is a two-step reaction, the first being dehalogenation and the latter polymerization. It is therefore necessary to study molecules containing different halogens, to understand the role it has on the reaction, and how changing it affects the final product. To do so, five dihalobenzene precursors have been studied: 1,4-diiodobenzene (dIB), 1,4-iodobromo-benzene (IBB), 1,4-dibromobenzene (dBB), 1,4-bromoclorobenzene (BCB) and 1,4-diclorobenzene (dCB), shown in Figure 2-12. In each molecule the halogens are in the para position, so that the final product would be identical, namely poly-para-phenylene (PPP) chains. The results for these molecules are reported in Chapters 3 and 4.

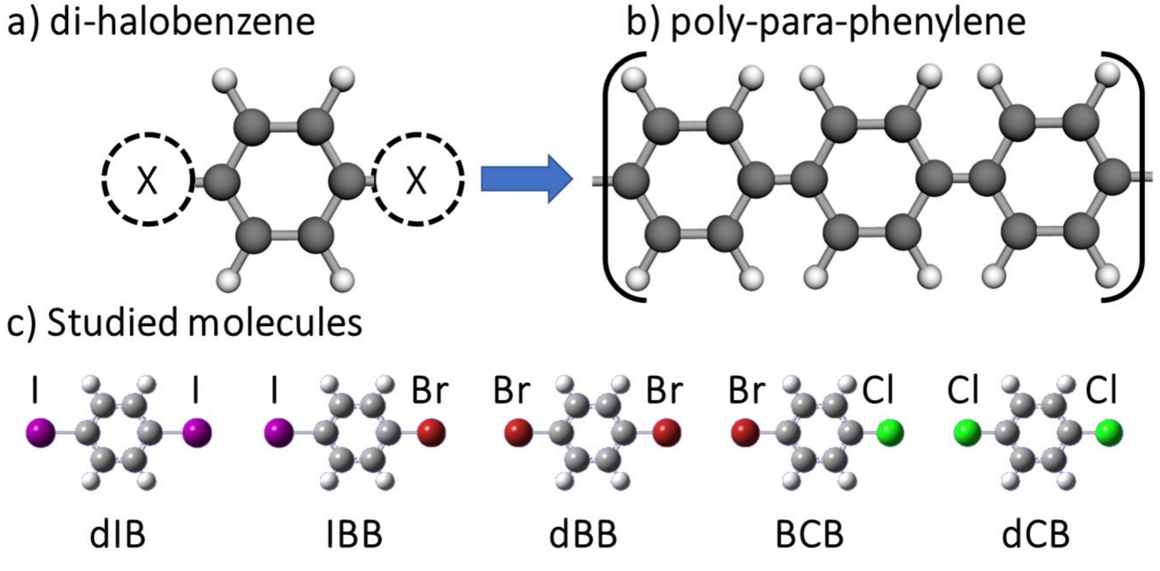

Figure 2-12 : **di-halobenzene molecules (a) used to produce poly-para-phenylene polymers (b); various precursors including different halogens (c) were used to produce the same final structure.**

The necessity to study the Ullmann reaction is however motivated by the realization of graphene-like materials, or 2D polymers with optimal optoelectronic properties. We therefore studied threefold symmetric precursors, which would form hexagonal 2D lattices upon polymerization. The precursor used in Chapter 5 of this thesis, TBTTB, is presented in Figure 2-13, together with another precursor currently under study, TBTANG. Both have a triangular shape and use Br as the halogen. Heteroatoms are present in the molecular backbone, S for TBTTB and N and O for TBTANG. N and S atoms are used as electron-donor species, while O is used to keep TBTANG planar, restricting out-of-plane rotation of the phenyls. TBTTB is also a prochiral molecule, and both *R* and *S* trans isomers are expected to be found after deposition.

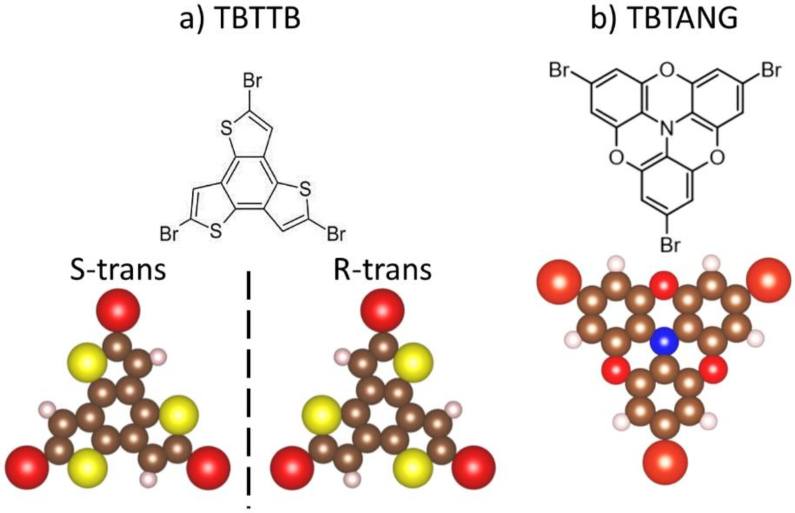

Figure 2-13 **Molecular scheme and graphical representation of two triangular molecules used to realize 2D structures; a) TBTTB; b) TBTANG; TBTTB is prochiral, meaning that it can absorb on the surface in two different enantiomers S and R.**

Besides halogen-containing molecules which undergo Ullmann reaction, we also explored a different polymerization reaction. Acetylene coupling was interesting because is easily initiated by UV exposure instead of annealing. We therefore studied the self-assembly and polymerization of di-benzonitrile-diacetylene (DBDA, Figure 2-14) on Ag(111). This molecule was appealing because, apart from the acetylene polymerization reaction, it could be modified with para Br atoms, to exploit a hierarchical polymerization in which Ullmann coupling was induced following the acetylene polymerization. The study of this molecule is reported in Chapter 6.

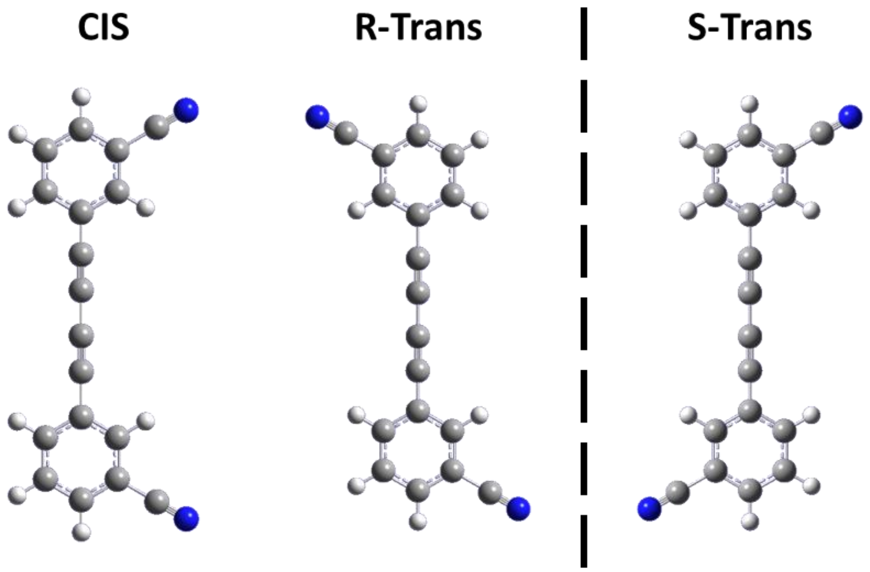

Figure 2-14 **molecular scheme for di-benzonitrile-diacetylene (DBDA); the molecule is prochiral, meaning that three different isomers, S and R and cis, can be present at the same time on the surface.**

3 THE COMPLEXITY OF A SIMPLE SYSTEM: THE CASE OF DBB ON Cu(110)

Based on the works:

a) "*Quasi one-dimensional band dispersion and surface metallization in long-range ordered polymeric wires*" published in Nature Communication, 2016, *7*, 10235. Contributions from: G.Vasseur, Y. Fagot-Revurat, M. Sicot, B. Kierren, L. Moreau, D. Malterre, L. Cardenas, **G. Galeotti**, J. Lipton-Duffin, F. Rosei, M. Di Giovannantonio, G. Contini, P. Lefevre, F. Bertran, V. Meunier, L. Liang and D. F. Perepichka[115] - where the author participated in the synchrotron measurements and data analysis.

b) "*A Mechanistic Picture and Kinetic Analysis of Surface-Confined Ullmann Polymerization*" published in Journal of the American Chemical Society, **2016,** *138* (51), 16696-16702. Contributions from: M. Di Giovannantonio, M. Tomellini, J. Lipton-Duffin, **G. Galeotti**, M. Ebrahimi, A. Verdini, N. Kharche, V. Meunier, G. Vasseur, Y. Fagot-Revurat, D. F. Perepichka, F. Rosei and G. Contini[159] - where the author participated in all the experiments and data analysis and in the discussion of the kinetic modeling.

c) "*An Unexpected Organometallic Intermediate in Surface-confined Ullmann Coupling*" published in Nanoscale, **2019**, *11*, 7682-7689. Contributions from: **G. Galeotti**, M. Di Giovannantonio, A. Cupo, S. Xing, J. Lipton-Duffin, M. Ebrahimi, G. Vasseur, Y. Fagot-Revurat, V. Meunier, D. F. Perepichka, F. Rosei and G. Contini[160] - where the author participated in all the experiments and data analysis and wrote the manuscript together with Marco Di Giovannantonio.

3.1 Introduction

The realization of low-dimension graphene-like materials with selected opto-electronics properties which could be used to realized real-life devices requires the comprehension of the physical and chemical parameters involved in the material growth. Starting with a "model", a simple system which could be used as a case study, to control and understand each parameter independently, or to demonstrate proof of concepts, is often necessary before working with more complex systems.

In this chapter, a comprehensive study of 1,4-dibromobenzene on Cu(110) will be presented. Such molecule was chosen due to its inherent simplicity (a benzene with two halogens of the same type in para position) and because it was known to yield both organometallic and polymeric structure when dosed on the Cu(110) surface.[30] As it will become evident while reading this chapter, this simple system showed itself to be anything but simple, demonstrating the complexity of the Ullmann reaction and how each parameter may have a significant impact on the whole reaction.

The first part will revolve around the study of the kinetic of reaction, studied for the high coverage case. It will be shown, using both experimental data and theoretical analysis, that the polymerization reaction follows a nucleation and growth mechanism, dominated by diffusion and with the presence of a transient state. For the high coverage case, the electronic properties were also studied, showing the presence of a quasi-one-dimensional metallic behavior.

The second part of the chapter will instead study the effect of the coverage, showing that two different organometallic structures can be obtained after dosing dBB at RT, both bringing to different polymeric structures upon polymerization. In this context, the coverage effect can be considered as an analogue of the effect that concentration has in solution chemistry. It will be also shown that the coverage can affect the reaction kinetic and mechanic: an additional intermediate phase is observed for the polymerization reaction of an uncomplete monolayer.

3.1.1 Materials and methods note

Scanning tunneling microscopy experiments were carried out using an Omicron VT-STM at RT and an Omicron LT-STM at a temperature of 5 K. STM images were recorded at constant tunneling current (0.2 nA) and constant bias voltage (applied to the sample) unless specified. The dI/dV spectra were recorded in the open feedback loop mode (V_{stab} = 2 V) using the lock-in technique (peak to peak modulated voltage V_{pp} = 30 mV, f = 1100 Hz). ARPES and fast-XPS experiments were performed at the SOLEIL (Cassiopèe beamline) and Elettra (Aloisa beamline) synchrotrons respectively. ARPES maps were normalized by subtracting a background corresponding to the clean surface. The data presented in Figure 3-5 were measured at 30 K using a Scienta SES 200 high-resolution hemispherical analyzer, with linear p-polarized 35 eV photons.

3.2 Results and discussion

3.2.1 Reaction Kinetics for dBB/Cu(110) at 1 ML

The polymerization of dBB was already studied by Di Giovannantonio et al.[30-31] in their seminal paper in which they showed that, once dosed on a Cu(110) surface, the precursors dehalogenates and form organometallic chains, stacked to form domains (Figure 1-16). Annealing these structures yields PPP polymers on the surface. In the same work they also showed that it was possible to use fast-XPS as a probe to follow the polymerization reaction (Figure 3-1). To do so, they analyzed each line of the fast-XPS map, which is a 1 sec scan of the C 1s spectra. By performing a spectral deconvolution of the initial and final line, it was possible to identify three components for the OM and two for the polymeric phase. Each line of the fast-XPS map was then analyzed to extract the fraction of reacted monomers (sum of curves 4 and 5) and the temperature onset of polymerization, as showed in Figure 3-1. STM images of the initial and final phases of the reaction are reported in Figure 3-2, with the atomic structure in the inset (Cu atoms in red and yellow, Br in green and phenyls in white). As can be seen from the images, the OM and polymeric chains are oriented along different path, suggesting that a diffusive process is indeed necessary to obtain the polymerization.

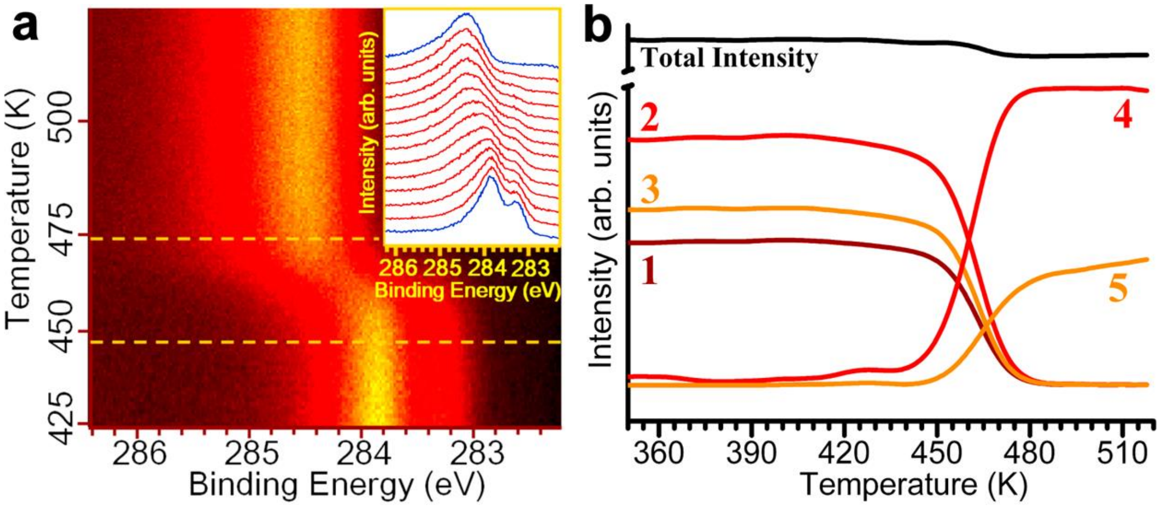

Figure 3-1. **a) fast-XPS measurement of C 1s core level during annealing, showing the evolution of the spectrum lineshape through the transition from organometallic to polymeric phases; the inset shows individual spectra from an area in between the yellow dotted lines; b) intensities of the RT and 500 K fitting functions for C 1s core levels, reported as a function of the annealing temperature. Reproduced from Ref.[30] with permission from American Chemical Society.**

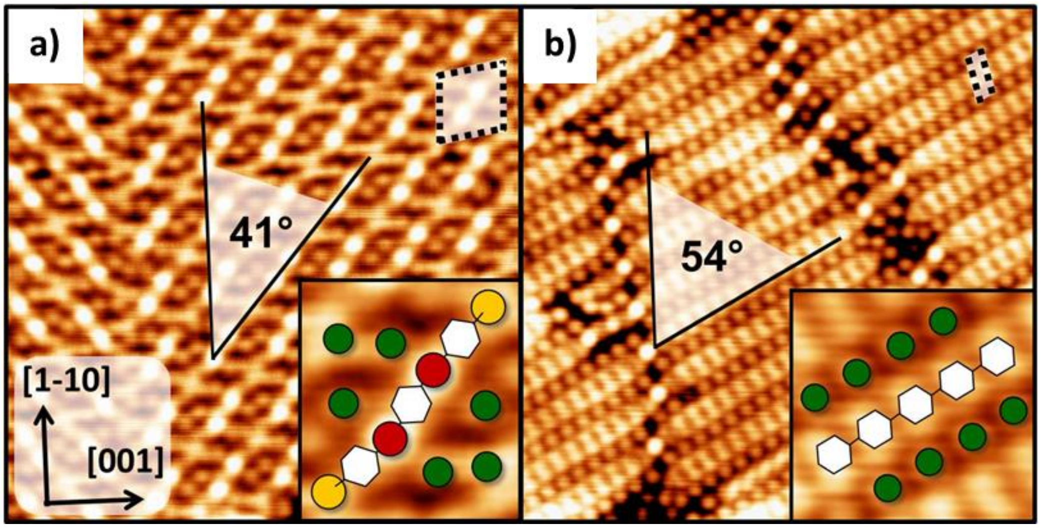

Figure 3-2. **STM images (11.5×11.5 nm^2, I_t = 0.5 nA, V_b = 20 mV) of (a) dBB OM chains, and (b) after annealing to 500 K, obtaining 1D polymers. The epitaxy matrices are (1, -4 | 6, 0) and (1, -1 | 4, 1), respectively (black dashed lines). Insets report drawings of the structures. White hexagons and green circles represent phenylene units and Br atoms, respectively. Yellow and red circles represent copper atoms linked respectively to one or two phenylene units.**

To study the polymerization reaction and to obtain insight into its mechanism, we repeated the same experiment, by taking fast-XPS spectra of the polymerization reaction using different heating rates. The result of such experiments, together with the fraction of OM, extracted by performing a spectral analysis of each line of the maps, are reported in Figure 3-3. A change in the onset of the reaction is observed with different heating rates, reflecting the non-equilibrium nature of the observed transition, with the composition of the surface controlled not only by temperature but also by reaction time (*i.e.* by kinetics). The transition is accompanied by a change in the orientation of the OM and polymeric phases, implying a diffusion of the precursors which will be taken into account in the modeling reported below. Most recently, a number of studies have addressed the kinetics of this coupling process using Monte Carlo simulations to model molecular surface diffusion.[16, 102, 108] These simulations start with a seed molecule fixed at a given position on a surface, and other molecules that randomly walk until reaching a site adjacent to the seed (reactive site), where they can either couple to the seed (irreversible process) or back-diffuse. The coupling probability (P) is therefore defined as:

$$P = \frac{\nu_c}{\nu_c + \nu_d} \qquad (3\text{-}1)$$

where ν_c and ν_d are the probabilities per unit time of the two complementary processes of coupling and back-diffusion, respectively. Monte Carlo simulations show that for $P \sim 1$ (*i.e.*, coupling is the more favorable mechanism) fractal-like polymer structures are obtained, while for $P \ll 1$ (*i.e.*, back-diffusion is more favorable) domains ordered over a long range are formed on the surface. These simulations qualitatively match the morphologies observed by STM of polymers obtained by use of different molecule/surface combinations, and thereby provide an indication that this type of model is able to capture salient features of Ullmann polymerization in two-dimensions.[102, 108, 161] However, the Monte Carlo approach described above only provides a qualitative picture, affording no quantitative insight into the energetics of the coupling reaction, nor the time dependent yield of polymerization from the organometallic phase. Using the shape of the curves in Figure 3-3 it is instead possible to comment on the kinetic order of the reaction. A completely ordered *topotactic*[162-163] transformation of the organometallic to polymer should ideally follow zero-order reaction kinetics: $\frac{dn_1}{dt} = -k$, where n_1 is the surface density of phenylene units in the organometallic phase, and k is the temperature dependent rate constant.

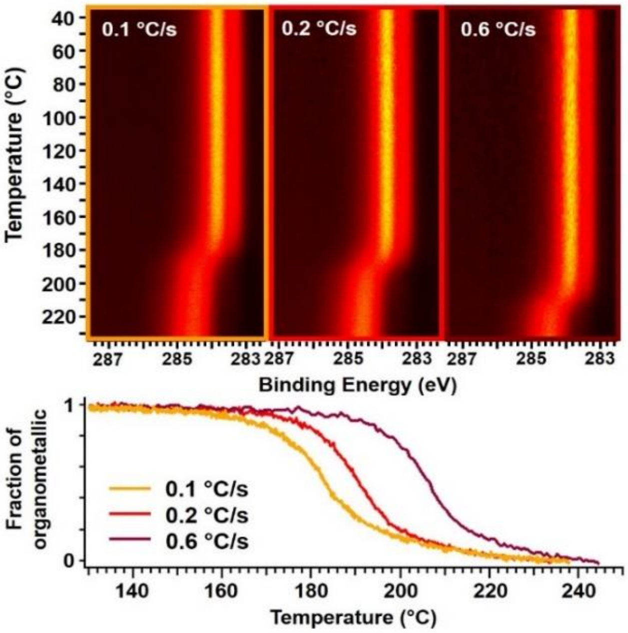

Figure 3-3. ***Top:*** **fast-XPS maps for the C 1s core level signals of dBB on Cu(110) annealed using three different heating rates: 0.1 ºC/s, 0.2 ºC/s and 0.6 ºC/s;** ***bottom:*** **kinetic curves extracted from the fast-XPS maps; these curves represent the normalized surface density of reactant molecules present on the surface in the organometallic phase as a function of the temperature.**

In this scenario the growing polymer chain has always a next neighbor monomer available for coupling and surface density has no bearing on the rate equation. A characteristic feature of zero-order kinetics is that polymerization reaches completion with a non-zero constant rate. This is clearly not the case for the curves shown in Figure 3-3. Instead, the progressively decreasing reaction rate observed near completion of the reaction is a hallmark of a diffusion-controlled process. To account for this behavior, the surface density of the phenylene units must be taken into account in the kinetic model.

Therefore, we develop an approach based on a system of mean field rate equations which describes the key processes during polymer formation: *i.* coupling between monomers to produce dimers, and *ii.* growth of polymeric aggregates through monomer addition. The surface density of monomers and its evolution in temperature are quantified *via* the fast-XPS measurements, using the method from Figure 3-1. In the model we explicitly account for the formation of a transient state that mediates dimer and polymer formation (Figure 3-4a). The presence of this state arises from the definition of the probability (P) introduced in the Monte Carlo approach which implies coupling and back-jump diffusion as two competing processes. The addition of a monomer to an existing chain (two units or longer) is considered energetically inequivalent to dimerization, because of the different species involved in the process. The surface density of halogens (byproduct of the dehalogenation reaction after RT adsorption of dBB on Cu(110)) is not directly considered in the kinetic model, although their effect enters implicitly in the rate constants. This is reasonable, because the halogen diffusion rate is much higher than that of the monomers. Based on the above discussion, the mean field rate equations of the kinetic model can be written as follows:

$$\begin{cases} \frac{dn_1^*}{dt} = k_1\ n_1 - n_1^*(k_{-1} + k_2\ n_1 + k_c\ N) \\ \frac{dN}{dt} = k_2\ n_1 n_1^* \\ \frac{dn_1}{dt} = -k_1\ n_1 + n_1^*(k_{-1} - k_2\ n_1) \end{cases} \tag{3-2}$$

where n_1 and n_1^* are the surface densities of free monomers and monomers in the transient state, respectively. N is the surface density of stable aggregates on the surface, *i.e.* chains made up of a number of monomers greater than or equal to 2: $N = \sum_{i\geq 2} n_i$ where n_i is the surface density of polymer chains with i monomers. k_1 and k_{-1} are first order rate constants for the formation of the transient and its back-transformation, respectively, while k_2 and k_c are second order rate constants for dimerization and the addition of a monomer to a longer chain, respectively.

We consider the transient state as short-lived, and its surface density to be low. This allows the use of the steady state approximation, *i.e.* we may set $\frac{dn_1^*}{dt} \cong 0$ and assert that n_1^* is small compared to the other species ($n_1^* \ll n_1$). The first equation in (3-2) becomes $n_1^* \cong n_1 \left[\frac{k_1}{k_{-1}+k_2\ n_1+k_c\ N}\right]$ and since $n_1^* \ll n_1$, we know $\frac{k_1}{k_{-1}+k_2\ n_1+k_c\ N} \ll 1$. The system of equations (3-2) reduces to:

$$\begin{cases} \frac{dN}{dt} = \frac{k_1\ k_2\ n_1^2}{k_{-1}+k_2\ n_1+k_c\ N} \\ \frac{dn_1}{dt} = -k_1\ n_1 + \frac{k_1\ n_1(k_{-1}-k_2\ n_1)}{k_{-1}+k_2\ n_1+k_c\ N} \end{cases} \tag{3-3}$$

The condition: $\frac{k_1}{k_{-1}+k_2\ n_1+k_c\ N} \ll 1$, can be fulfilled in three distinct cases, corresponding to different energy barriers for the polymerization process, as sketched in Figure 3-4b. For case (i) (k_{-1} greater than $k_2\ n_1$, $k_c\ N$ and k_1), transients are more likely to back-diffuse and remain as monomers rather than couple to neighbors ($P \ll 1$). For both cases (ii) ($k_2\ n_1$ greater than k_{-1}, $k_c\ N$ and k_1) and (iii) ($k_2\ n_1$ greater than k_{-1} and k_1) coupling is instead more probable ($P \sim 1$). However, case (ii) favors dimerization only, whereas case (iii) favors any type of coupling. The system of coupled first-order differential equations is finally reduced to a single second order non-linear differential equation for the normalized density of monomers $n_1/n_1(0)$, where $n_1(0)$ is the density of monomers in the organometallic state at the start of the experiment. The equation is solved numerically and the activation energies for nucleation and growth (E_n and E_g, respectively) can be extracted by fitting the solution of the equation to the experimental kinetic curves extracted from the fast-XPS experiments.

Figure 3-4 shows that the best fit is obtained for case (i) (k_{-1} is the dominant term), where coupling is less likely than back-diffusion. For this case equations (3-3) simplify to:

$$\begin{cases} \frac{d\eta}{dT} = \frac{1}{\phi}\frac{k_1\ \tilde{k}_2}{k_{-1}} x_1^2 \\ \frac{dx_1}{dT} = -\frac{1}{\phi}\left[2\frac{k_1\tilde{k}_2}{k_{-1}} x_1^2 + \frac{k_1\tilde{k}_c}{k_{-1}}\eta x_1\right] \end{cases} \tag{3-4}$$

where, $\phi = \frac{dT}{dt}$ is the heating rate, $\tilde{k}_2 = n_1(0)k_2$, $\tilde{k}_c = n_1(0)k_c$, $\eta = \frac{N}{n_1(0)}$ and $x_1 = \frac{n_1}{n_1(0)}$. Interestingly, the system of equations (3-4) is equivalent to the one usually employed for modeling nucleation and growth of thin films.[164-165] Setting $k_n = \frac{k_1\tilde{k}_2}{k_{-1}}$ and $k_g = \frac{k_1\tilde{k}_c}{k_{-1}}$ in equations (3-4) allows us to define effective rate coefficients for nucleation (dimerization) and growth, with activation energies given respectively by $E_n = E_1 + E_2 - E_{-1}$ and $E_g = E_1 + E_c - E_{-1}$.[164-165]

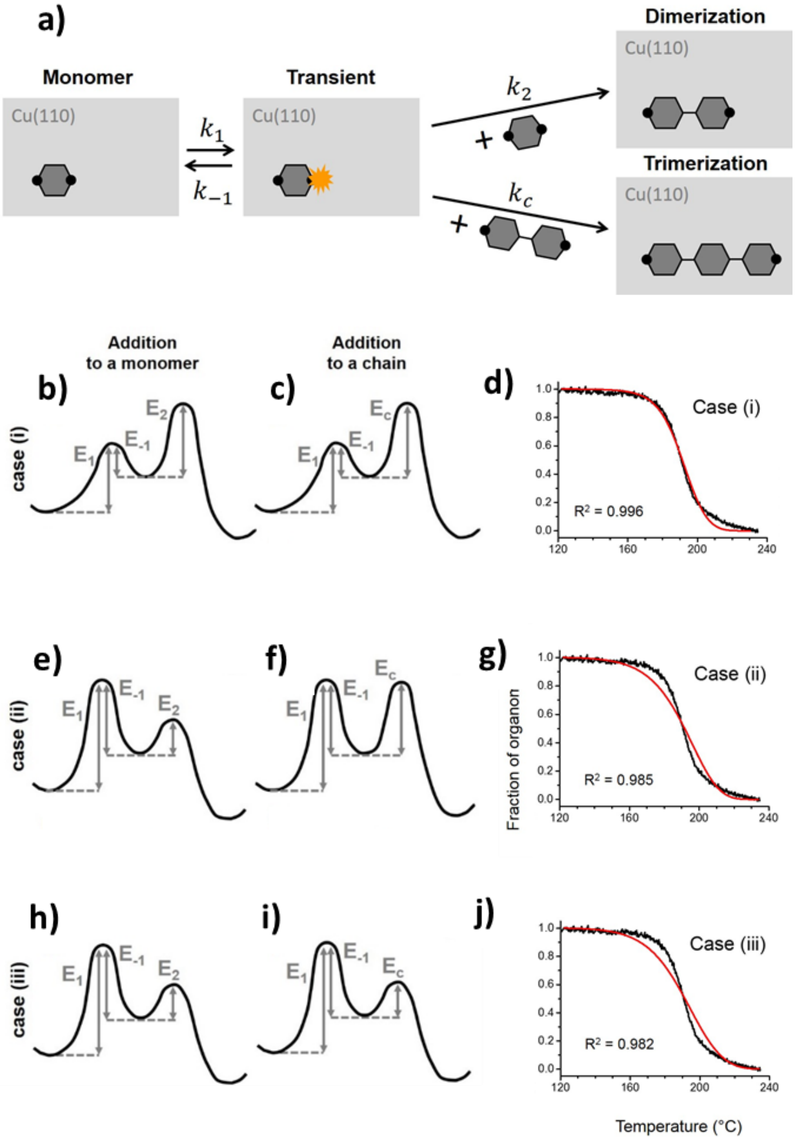

Figure 3-4. a) Proposed kinetic model described by kinetic equation (3-2); bottom: energy barriers for the possible interactions of the species present on the surface in the three cases. E_1 and E_{-1} are for the formation and disappearance of the transient, E_2 for the dimerization and E_c for the addition of a monomer to a longer chain; the fit to the experimental data for each case is reported (d, g, j).

By fitting the curves using case (i) we find values for the activation barriers for the nucleation and growth to be 1.310±0.005 eV and 1.090±0.005 eV, respectively. Even for this case (i), where the model best fits the experimental kinetics, there is a slight deviation of the two curves as the reaction completes (Figure 3-4d). This may arise from the increasing spatial extent of the polymers, which hinder the free diffusion of monomers and thereby add a coverage-dependence to the rate constant that is not taken into account in the present model. Our results for the energy barriers and pre-exponential factors are comparable to those experimentally determined by temperature programmed reaction experiments for biphenyl formed from halobenzenes on Cu(111): in that work the activation energies and pre-exponential factors range from 0.9 to 1.5 eV and from 6×10^{11} to $7 \times 10^{15} s^{-1}$ respectively.[108]

3.2.2 Band structure and bandgap for dBB/Cu(110) at 1 ML

The polymers showed in Figure 3-2b cover all the surface, and grows along two different directions [1-1±2], with each domain covering about 50% of the surface. In addition, they also show a small distribution of the average length, allowing the use of averaging techniques to study their properties. ARPES measurements were therefore performed to study the band structure of the PPP polymers on Cu(110). Such results are shown in Figure 3-5. Prior to this work, ARPES measurements had only been used to reveal quantum well states in molecules[166] or to reconstruct the discrete electronic orbitals of self-assembled individual molecules at surfaces,[167-168] and no direct evidence of a band-structure associated with on-surface C-C covalent bonding and a long range delocalization of charge carriers has been reported to date, apart from the graphene case. ARPES intensity maps were measured along the [1-12] axis (parallel to the chains direction) on both the clean surface and the PPP/Cu(110) polymer interface. The incident photons were p-polarized, with an energy of hν = 35 eV. Only the domains oriented parallel to [1-12] are probed in this geometry (roughly half the monolayer). Comparison between clean and polymer surfaces permits the identification a strongly dispersive band, that crosses the 3*d* states of the substrate, labeled in Figure 3-5a using yellow arrows. High-resolution measurements taken in the 2nd Brillouin zone (Figure 3-5b) close to the top of the occupied molecular band show that the molecular spectral weight disperses up to a BE of -1.4 eV at $k_{//}$ = 1.42 Å^{-1}, while a small portion of a higher energy band dips below the the Fermi level.

A direct bandgap of 1.15 eV is found between the minimum of this band and the top of the high-energy band described above. A comparison between the measured and calculated electronic DOS is shown in Figure 3-5c. The DOS of pristine Cu(110) (filled blue line) is flat between 0 and -2 eV and originates from copper s-p bands. The additional spectral weight arising from the PPP overlayer appears clearly as peaks corresponding to the top and bottom of the valence and conduction molecular bands, respectively. The separation between these peaks corresponds to a bandgap of 1.15 eV. The calculated gap is approximately 0.90 eV, which is slightly smaller than the experimental value, but this is a common drawback of DFT calculations, which neglect correlation effects.

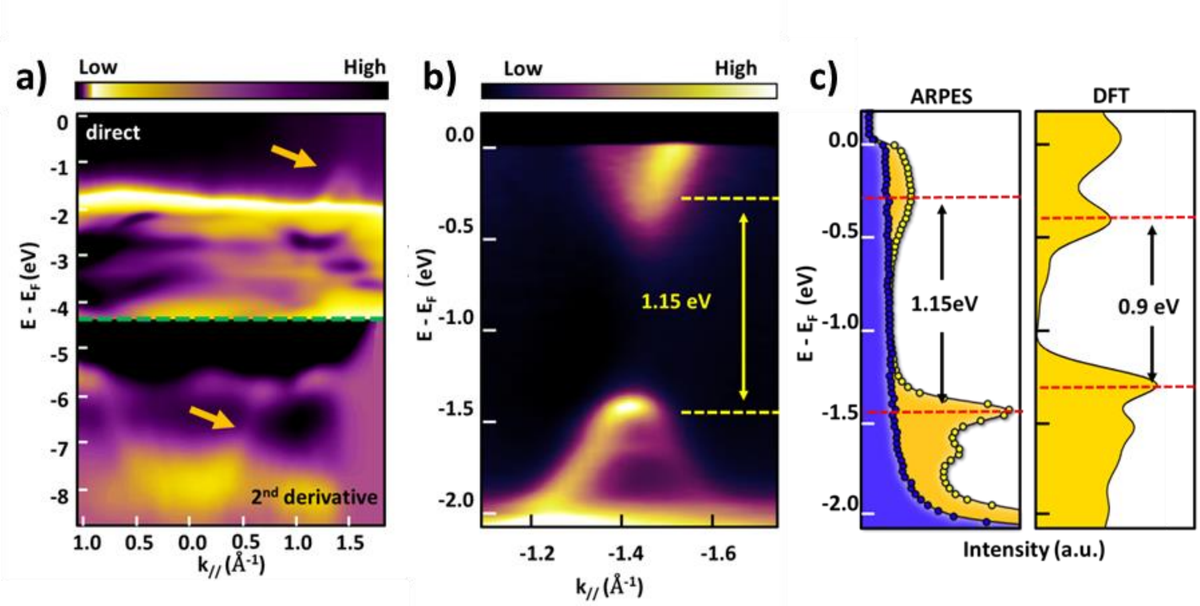

Figure 3-5 **a) ARPES intensity map measured along the [1-12] direction, parallel to the polymers chains; the bottom part is displayed in second derivative. Arrows indicate bands due to the presence of polymers; b) high-resolution ARPES intensity map recorded close to the Fermi level showing the HOMO–LUMO bandgap; k-integrated photoemission DOS on the Cu(110) substrate (left panel, blue), on PPP/Cu(110) (left panel, yellow) and corresponding DFT DOS of PPP/Cu(110) (right panel, yellow).**

3.2.3 Effect of the coverage – a new intermediate of the Ullmann coupling

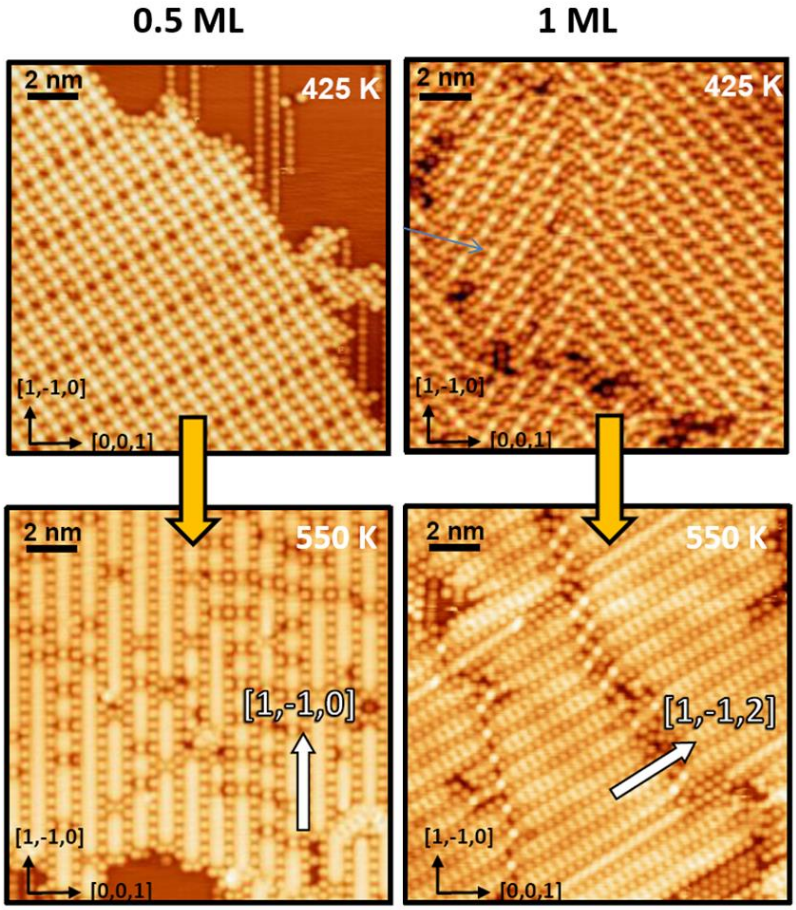

Figure 3-6 **STM images of dBB on Cu(110) at 0.5 ML (left) and 1 ML (right) before and after polymerization; the coverage affects both OM and polymer structures, varying their length and orientation on the surface.**

As shown in Figure 3-2, dosing 1 ML of dBB on Cu(110) yield a Chevron OM phase, with epitaxial matrixes (1, -4 | 6, 0) and (1, -1 | 4, 1), which converts after polymerization into polymers along the [1-1±2] directions. However, the same system was studied by Di Giovannantonio at submonolayer coverage, observing that at RT we form long OM chains along the [1-1±1] directions, with epitaxial matrixes equal to (2, -2 | 4, 9) and (2, 2 | -4, 9). Those OM chains yield polymers along the [1-1 0] direction (Figure 1-16). A recap of the two cases is reported here in Figure 3-6 to help the reader. Such stunning difference demonstrates that the coverage is an important reaction parameter, that needs to be considered. To better understand its effect, we further investigated the reaction at low coverages by means of fast-XPS.

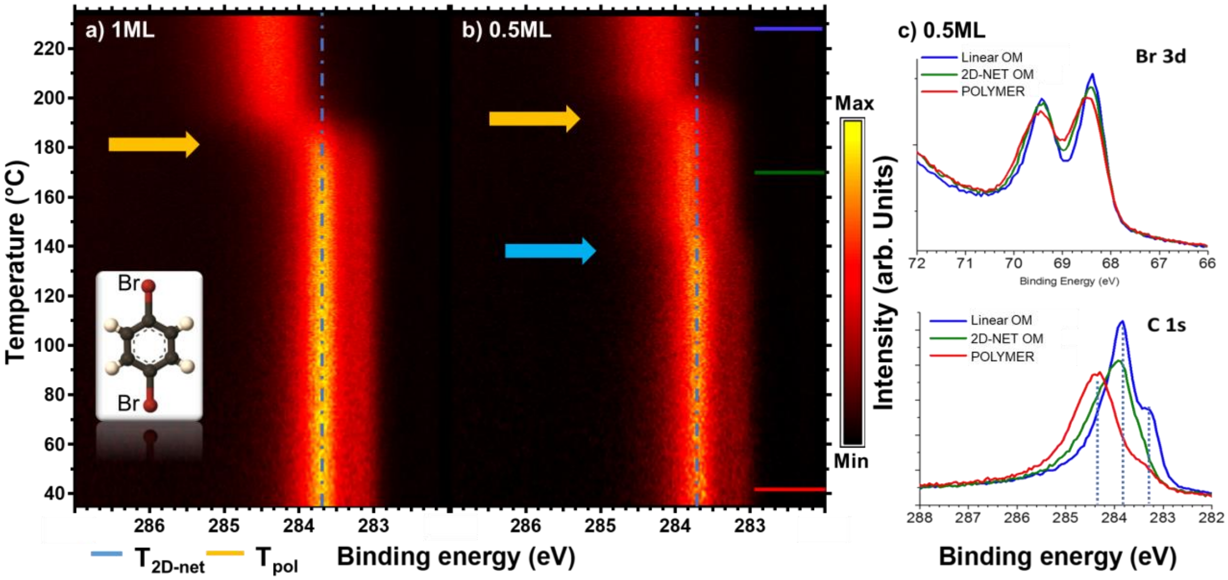

Figure 3-7. **C 1s fast-XPS maps for dBB on Cu(110) at 1ML (a) and 0.5ML (b); orange and azure arrows refer to the polymers formation and to the transition from linear OM to the 2D OM phase, respectively; blue, green and red horizontal lines indicate the temperature at which the spectra in panel c) have been acquired; c) C 1s and Br 3d XPS spectra for dBB on Cu(110) at 0.5ML obtained at three different T.**

The C 1s fast-XPS spectra performed during the polymerization reaction of saturated (1 ML) dBB coverage on Cu(110) show one transition from OM to polymer at about 180 °C (Figure 3-7a).[30-31, 169] Differently, on the C 1s fast-XPS spectra of unsaturated (0.5 ML) dBB coverage (Figure 3-7b) two reactions are identified, at about 140 °C and 190 °C. The changes in the C 1s XPS spectra (peak shape and BE positions, Figure 3-7c) demonstrate that an additional unexpected intermediate phase, stable between these temperatures and different from the linear OM at RT or the polymer phase, is formed. Fast-XPS maps at different dBB coverages illustrates that both transition temperatures (orange and azure arrows in Figure 3-7b) depends on the coverage. The additional phase is observed up to 0.6ML and is not present at 0.88ML (Figure 3-8). As showed before, when more than 0.8 ML of dBB are dosed at RT on Cu(110), the linear OM chains become shorter and follow a chevron pattern, which is likely connected with the disappearance of this additional phase.[115] In line with our fast-XPS analysis, STM measurements of 0.5 ML dBB reaction on Cu(110) at different temperatures confirm the presence of this additional intermediate phase (Figure 3-9b), different from the linear OM and polymer phases (Figure 3-9a,c).

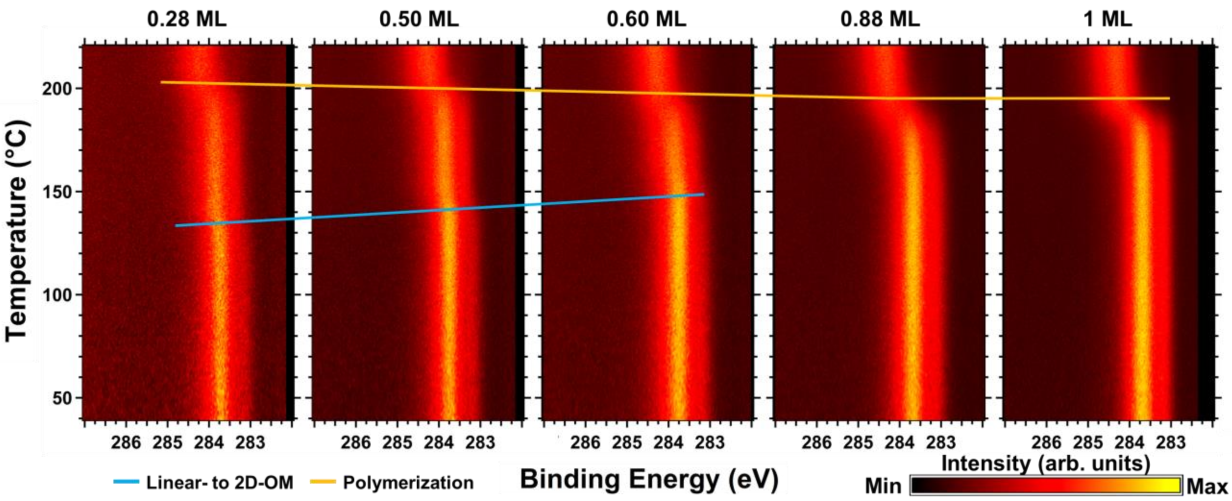

Figure 3-8 **C 1s fast-XPS maps of dBB on Cu(110) at different molecular coverages, from 0.28 to 1 ML.**

The network of the additional intermediate phase is formed by a 2D array of four bright spots, identified as the unit cell (red box in Figure 3-9b), with parameters of: $a = 1.08\,nm, b = 1.02\,nm, \vartheta = 90°$. The unit cell repeats to form 2D domains (cyan box in Figure 3-9b), extending between 3- to 6-unit cells on a side.

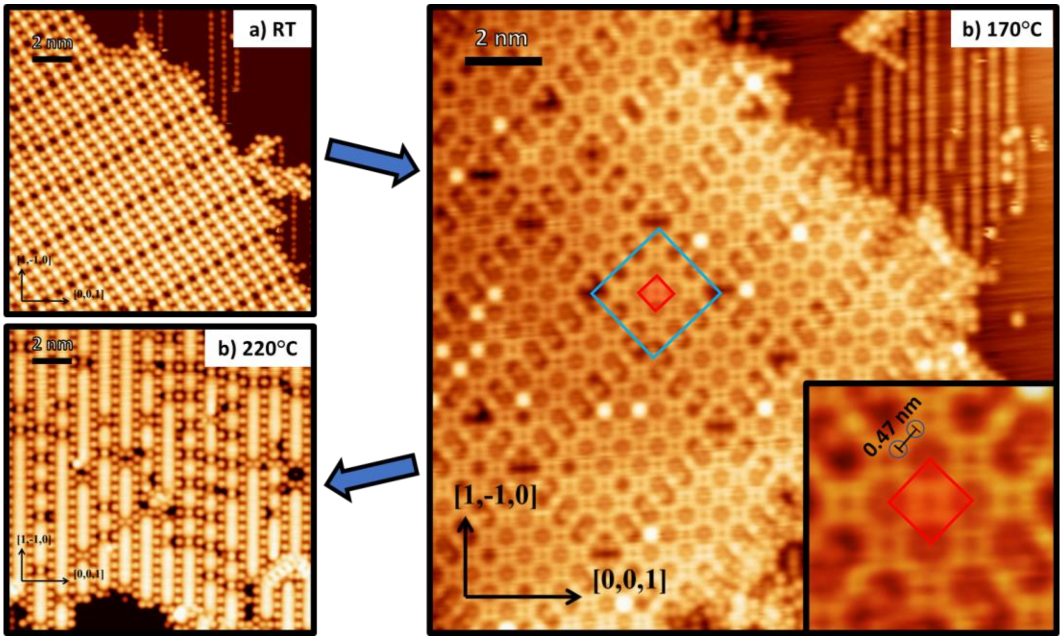

Figure 3-9 **30x30 nm^2 STM images of the phases observed during the polymerization reaction of a 0.5ML coverage of dBB on Cu(110); a) linear OM phase at RT, b) 2D OM phase at 170 °C, c) polymer phase at 220 °C; b) red and cyan boxes indicate the unit cell and one domain of the 2D OM phase, respectively; the inset shows a 4x4 nm^2 zoom (with reported the distance between the two protrusions along the [1-1 1] direction).**

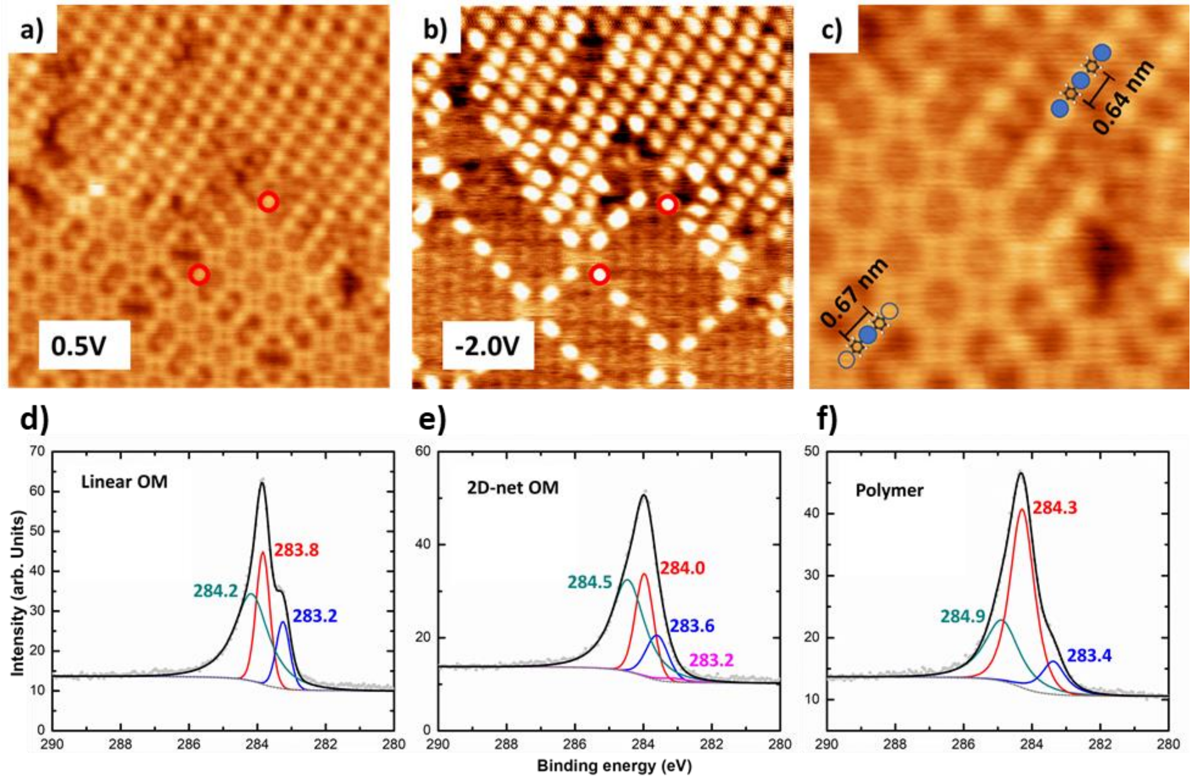

Figure 3-10 **a) STM image of the 2D OM phase (bottom) together with the linear OM phase (top); b) conductance map of the same area, recorded at -2.0 eV (± 50 mV range); c) zoom of a), the bright protrusions can be identified as Ph-Cu-Ph segment; d-f) spectral deconvolution of the XPS spectra of the three phases: 1D OM (d), 2D OM (e) and polymeric (f).**

To develop a model for this additional phase it is necessary to obtain insights from the STM images, in particular from the boundaries between its repeating domains (cyan box in Figure 3-9b), which are connected by lines with a different STM contrast. These lines are short OM chains, made of Ph-Cu-Ph units, being the building block of the 1D OM phase.[19, 30] The nature of those chains was inferred by comparison of distances and DOS with the 1D OM phase. Conductance maps and STM line profiles obtained from a surface were the 1D and 2D OM phases coexist show that the DOS at -2.0V and the Ph-Cu-Ph distances are the same for the two phases (Figure 3-10b,c). Useful information can also be obtained by the lower BE contribution of the C 1s XPS data, as obtained by spectral deconvolution (Figure 3-10d-f). The peak at 283.2 eV obtained for the 1D OM phase is attributed to Ph-Cu-Ph bond.[30, 169] In the case of polymer, the lower BE peak, at 283.4 eV, is attributed to Ph-Cu bond that are present at the end of the chains, related to the presence of short polymers (see Figure 3-10f). For 2D OM the spectrum can be fitted by a component at 283.6 eV, attributed to Ph-Cu, and at 283.2 eV, with very small intensity, attributed to Ph-Cu-Ph that are present at the grain boundaries of the domains. The small difference between the two BE found for the Ph-Cu bonds can be probably related to the different nature of the copper atoms: adatoms for the 2D OM, and bulk copper for polymers.

We can therefore build our model, which consists of a 2D OM network with an array of four Cu atoms at the nodes (Figure 3-11a, blue circles) and phenyls as the linkers, oriented along the [1-1±1] directions. The bright features observed at the vertexes of the unit cell can be attributed to Br atoms (Figure 3-11a, red cycles).[30, 169] The proposed structure was optimized by DFT, and the obtained structure is presented in Figure 3-11b. The simulated STM image is in good agreement with the observed experimental one as shown in Figure 3-11c. Given the non-trivial assignment of the 2D OM phase, DFT calculations were performed considering different models (Figure 3-12) to determine the atomic structure. Between the other possible structures (discussed later), the structure reported in Figure 3-11 has been selected due to a good overall agreement between simulated and experimental STM images.

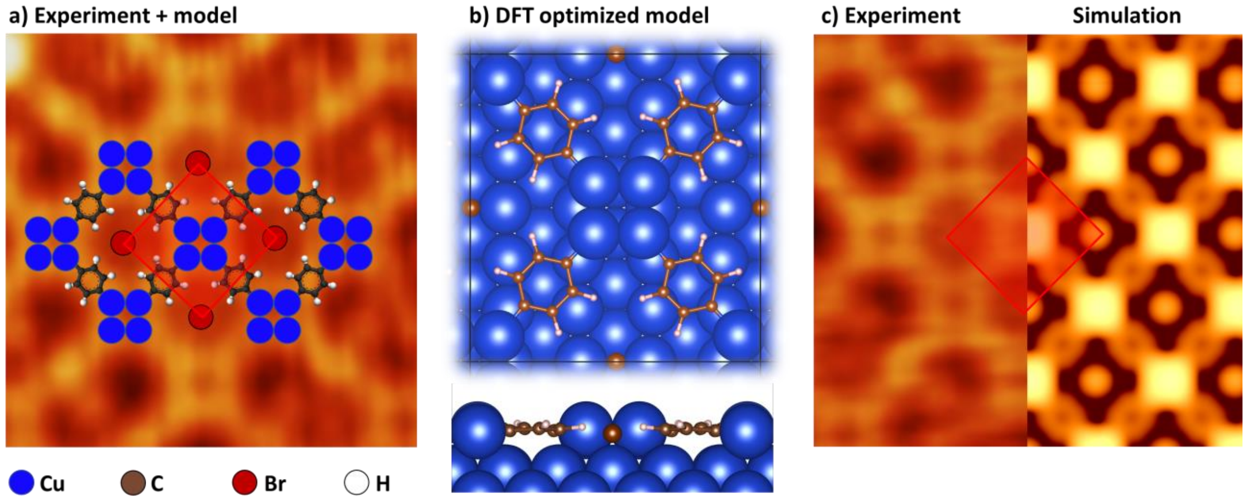

Figure 3-11 STM image (4x4 nm^2) superimposed with the proposed structure of the 2D OM phase; b) top and side view of DFT optimization of the 2D OM structure; c) Side-by-side view of experimental (4x3 nm^2) and DFT simulated STM images at -2.0 V bias; the red boxes in panels a) and c) indicate the unit cell of the 2D OM network.

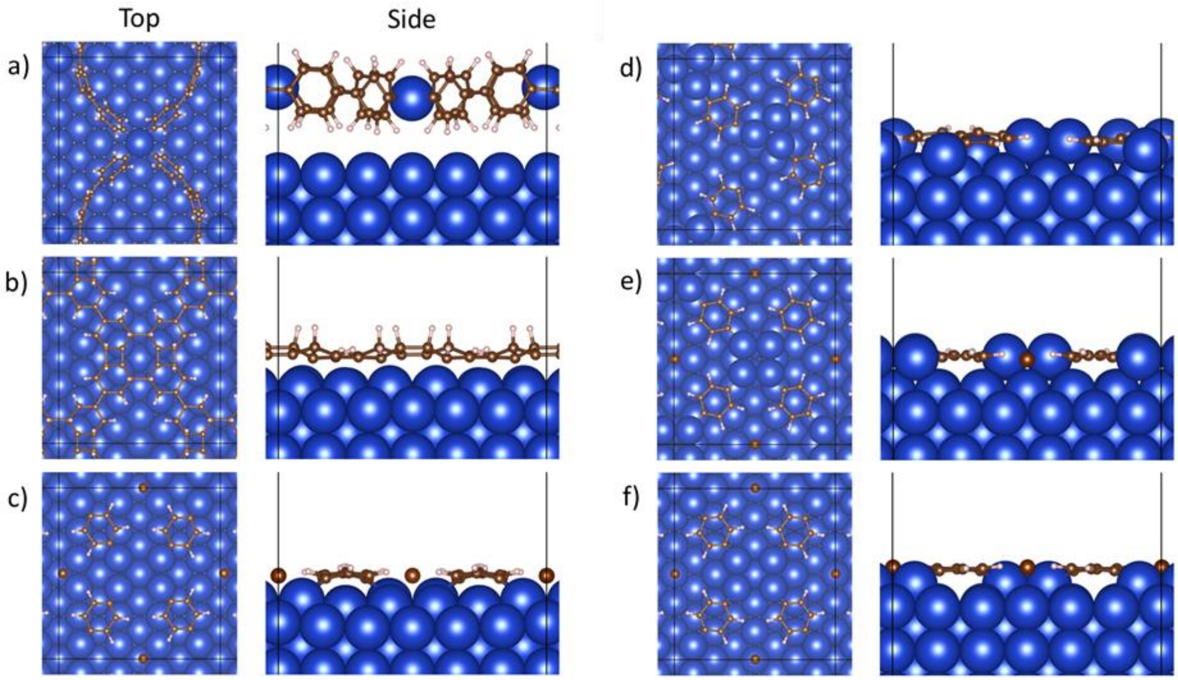

Figure 3-12 **Top and side views of the considered atomic models for the 2D OM phase: (a) diphenyls distorted out-of-plane; (b) diphenyls kept in-plane and H atoms forced out-of-plane; (c) phenyl bounded to surface Cu atoms; (d) phenyl bounded to on-top Cu adatoms; (e) phenyl bounded to short bridge Cu adatoms; (f) phenyl bounded to hollow Cu adatoms.**

The experimental distance between the two protrusions along the [1-1±1] directions, equal to 0.47 ± 0.05 nm, as showed in Figure 3-9b, is compatible with either a Cu-Ph-Cu unit or a biphenyl. Therefore, two classes of structures were considered, with building blocks consisting of either biphenyls or single phenyls, and the results are reported in Figure 3-12. For the biphenyls, we examined two structures. In the first (case a) the four biphenyls form a junction at a Cu adatom and the phenyls are twisted out-of-plane from the surface to prevent overlap of the H atoms. The resulting ring-like structure corresponds to a local minimum of the complex energy landscape but disagrees with the phenyls being almost parallel to the surface, as observed in the STM images. In the second structure (case b) an attempt was made to keep the dimers in-plane. To preserve the H atoms attached to the phenyls near the intersection of the dimers, the H atoms have been forced vertically with respect to the plane of the structure. From a solution chemistry stand-point the sp^3 hybridization is unusual; however, chemistry in 2D can be drastically different due to interaction with the substrate and symmetry breaking imposed by the surface. Despite their relative stability, the biphenyl-based structures are not compatible with the experimental STM results from the boundaries between 2D-OM domains. This issue can be resolved by considering the second class of structures based on single phenyls, for which four cases have been considered. In the first, Cu atoms are pulled out of the surface to anchor the phenyls (case c). For the other three Cu adatoms in the on-top (case d), short bridge (case e), and hollow (case f) surface positions are bounded to phenyls. The adatoms are not stable in the on-top position and the resulting structure (case d) presents a symmetry which does not match with the experiments.

To further discern between the three remaining models, Br atoms have been added between the phenyl junctions (Figure 3-13). For cases c and e, the Br atoms are found to be located in the relatively stable hollow and long bridge positions, respectively. For case f, the Br atoms are located in the top position, and stabilized by the surrounding phenyls (an isolated Br atom is however not stable in the top position). The STM images simulated for each case at four different biases (Figure 3-13) show that a better agreement with the experimental results is obtained for the structure with the Cu adatoms in the short bridge position (case e).

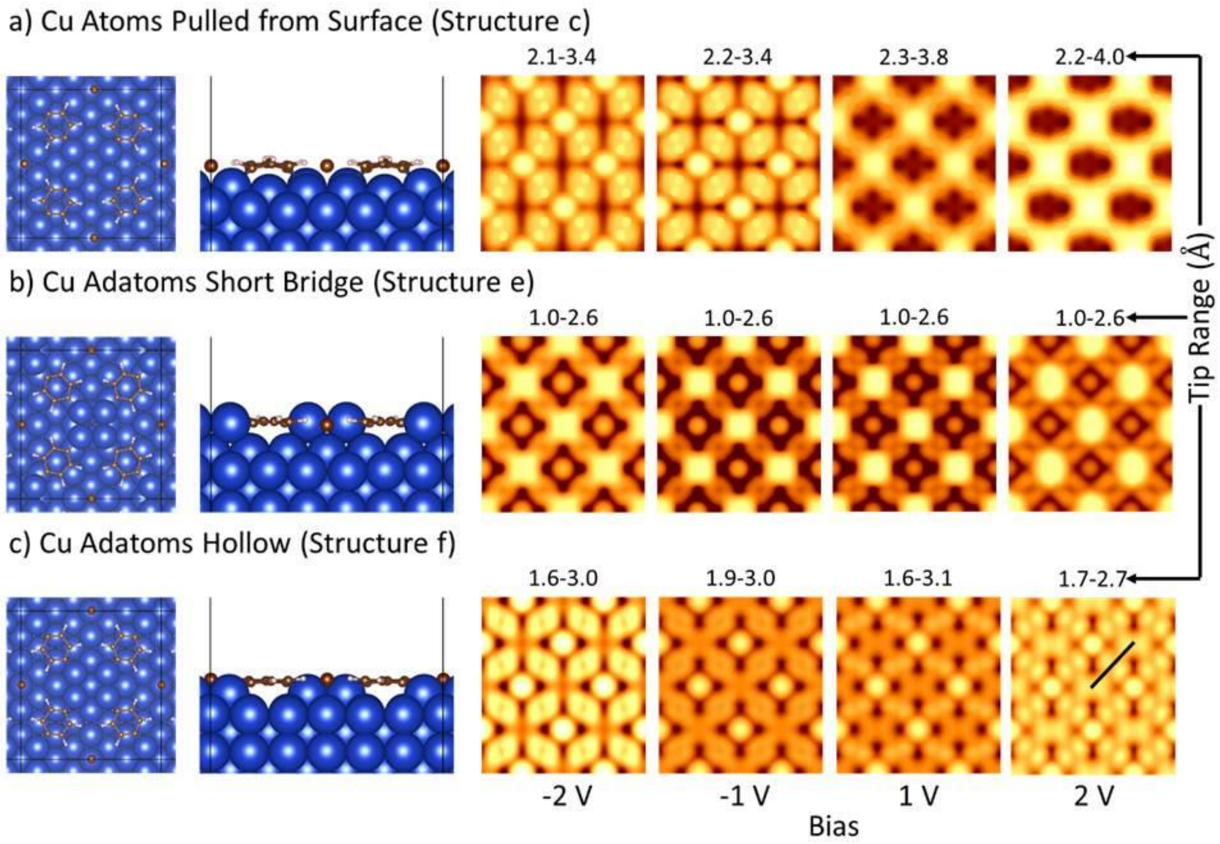

Figure 3-13. **Simulated STM images (2.8x2.8 nm^2) at different bias voltages (tip radius = 0.9-0.95 Å) for three models reported in Figure 3-12; the center of each image corresponds to the four Cu atoms cluster; the simulated STM images for model e are in reasonable agreement with the experimental STM images, and is therefore chosen as the model to fit the experiments.**

3.2.4 Reaction Kinetics for dBB/Cu(110) at 0.5 ML

At the beginning of the chapter we presented a kinetic model to explain the polymerization reaction of dBB/Cu(110) at 1 ML coverage, which showed a nucleation and growth mechanism. We therefore applied the same model to both transitions present in our C 1s fast-XPS of the 0.5 ML case, obtaining a good fit for both (R-squared value > 0.98), as reported in Figure 3-14, showing that also in this case we can assume a similar nucleation and growth mechanism. The activation energies for the 1D to 2D transition are 1.175±0.010 eV and 0.980±0.010 eV for nucleation and growth, respectively, while the activation energies for the 2D to polymers transition are 1.320±0.010 eV and 1.100±0.010 eV, in agreement with those reported for the high coverage polymerization (section 3.2.1, Figure 3-4d). The high temperature deviation of the model from the experimental curve when studying the polymerization process can be ascribed to the fact that at such temperatures we are depleting the number of free phenyls to be added to the chains, and instead starting to move (and couple) small polymeric chains, thus slowing the reaction with respect to the theoretical model.

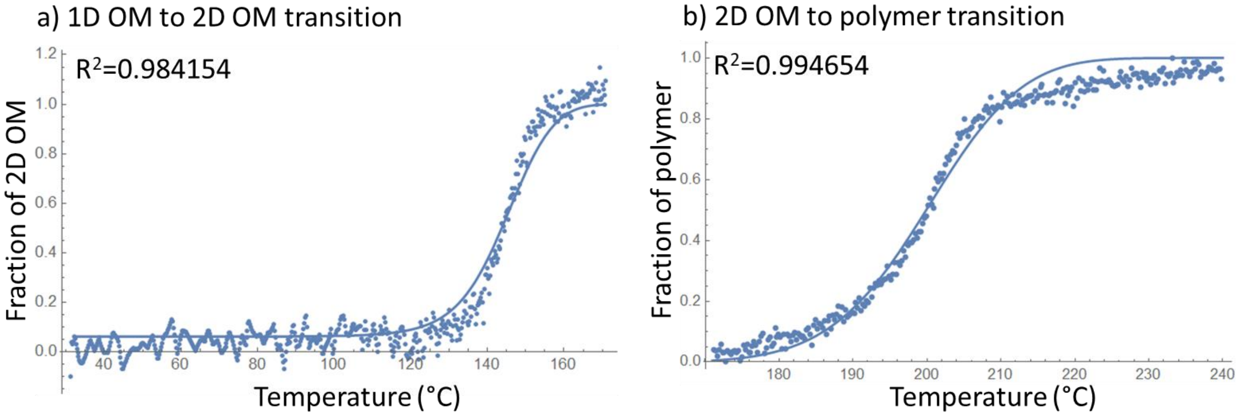

Figure 3-14 **Fit of the experimental kinetic curves reported in Figure 3-7b using a nucleation and growth model for the formation of the 2D OM phase (a) and the polymeric phase (b).**

Despite the large number of published studies on surface-confined Ullmann polymerization, the 1D to 2D transition presented in this chapter shows that the complexity of its mechanistic pathways is not yet fully understood, even for simplest reactive monomers. In particular, the observation of two distinct and stable OM phases (linear and 2D OM) is unusual given that no such result has yet been reported for this system[30-31, 115, 159, 170] nor for systems using similar precursors.[19, 105-107, 170] To date, only linear (1D) OM phases have been reported for bidentate monomers. Moreover, the stabilization of the OM intermediate by metal clusters (four Cu adatoms) instead of single atom bridges, has not been observed in on-surface Ullmann coupling, although the role of Cu clusters in homogenous catalysis is well established.[171]

3.3 Conclusions and perspectives

In this chapter we reported the study of dBB on Cu(110) following the reaction from adsorption to polymerization, proposing a kinetic model to explain the reaction process and studying the effect of the substrate coverage on the reaction. High coverage yields long-range domains of short OM chains, which produce long polymeric chains along the [1-1±2] directions, while low coverage yields long OM chains which produce polymers along the [1 1 0] direction. In both cases the polymerization reaction follows a nucleation and growth mechanism. For the low coverage however, an additional step is observed before polymerization, where a 1D to 2D phase transition takes place. Such 1D to 2D reorganization is the first case of on-surface transition between two isomeric OM phases, driven solely by temperature. Being able to control the self-assembly ordering and tessellation is a crucial aspect of supramolecular chemistry, which requires a deep understanding of molecular interactions in order to drive the system towards the wanted structure. It has been shown that the molecular ordering of intact halogenated molecules can be controlled by the temperature,[172-173] and that the tessellation of metal-organic self-assemblies can be controlled by changing the type of the metal.[174-177]

The behavior described herein could be of general interest: additional stable intermediates could also exist in the case of other reactions and systems, maybe in a short range of temperatures or for a precise set of parameters, and not experimentally observed so far. While enriching the fundamental understanding of the mechanism of the most important on-surface coupling reaction, our finding of multiple intermediates, with different molecular density and dimensionality, could also have implications for the structural quality of the final polymers. In fact, the presence of intermediate phases is an essential feature for design of hierarchical on-surface polymerization, which could be a key tool for increasing the order and control dimensionality of the final polymer.[18, 102, 101]

4 A SYSTEMATIC STUDY:
HOW TO INFER THE ROLE OF THE HALOGENS

Based on the work "*The role of halogens in on-surface Ullmann polymerization*" published in Faraday Discussions, **2017**, *204*, 453-469. Contribution from: G. Galeotti, M. Di Giovannantonio, J. Lipton-Duffin, M. Ebrahimi, S. Tebi, A. Verdini, L. Floreano, Y. Fagot-Revurat, D. F. Perepichka, G. Contini, and F. Rosei.[170] - where the author participated in all the experiments and data analysis, and wrote the manuscript.

4.1 Introduction

As explained in the introduction chapter of this thesis, Ullmann coupling reaction have established itself as the primary way to obtain conjugated polymers on metallic surfaces, and countless studies have been published in the last decades.[25, 34, 178-179] The majority of these studies, however, focused on understanding the structure and order of the polymers on different substrates[108] or the density of defects of such structures,[24] while the effects of the halogen by-product have not been explored in detail. A few theoretical[16] and experimental[180-181] studies have reported the dissociation of halobenzenes on metallic surfaces, addressing the differences in the adsorption energies, but also in this case the effects of halogens on the reaction outcome were not explored.

At the start of my PhD project this was still an open question, with only few works even addressing the problem. In one case for example, the derivatives of 1,3,5-tris(4-bromophenyl)benzene functionalized with bromine (TBB),[122, 182] iodine (TIB)[28] and both the halogens (TBIB)[183] have been studied on various surfaces, yet a coherent comparison to reveal the role played by the halogens was not reported. Arguably the only work concerning the question was Di Giovannantonio et al. ACS Nano from 2013, which described the contribution of halogens in the formation of 1D polymers *via* Ullmann coupling,[30-31] showing that they are part of the OM unit cell after the deposition of dBB on Cu(110). This study also illustrates that the structures obtained from dBB[30] and dIB[19] on Cu(110) are different, which suggests the importance of studying the influence of halogens on the processes that transform the intermediate phase into a polymeric structure. In line with this finding, it was interesting to address how the type of halogen can influence the design of the OM and polymer structures.

We therefore performed a systematic study of five different 1,4-dihalobenzene molecules (Figure 2-12), on Cu(110). This study was performed using a combination of spectroscopy, microscopy and theoretical calculation, in order to illustrate the role of metal halide by-product in determining the rate of C-C coupling step and the structure of the formed π-conjugated polymers based on Ullmann coupling.

4.2 Materials and Methods notes

The precursors dBB (98% purity), dIB (99%), 1,4-dichlorobenzene (dCB, ≥99%), 1-bromo-4-chlorobenzene (BCB, 99%) and 1-bromo-4-iodobenzene (BIB, 98%), shown in Figure 2-12 and Figure 4-4, were purchased from Sigma-Aldrich and were deposited through a leak valve onto Cu(110) (MaTecK GmbH), with the substrate held at RT. All experiments were performed starting from a saturated monolayer coverage, except when specified. Fast-XPS curve have been acquired at the ALOISA beamline of the Elettra synchrotron, while heating the system with a 0.2 °C/s rate.

4.3 Results and discussion

4.3.1 Fast-XPS and reaction overview

As explained in Chapter 1, on-surface Ullmann coupling is a two-step reaction, with the formation of an OM intermediate and metal halide byproduct in the first step, followed by the formation of a C-C bond in the second, *rate-limiting* step.[30, 107, 184] As such, the nature of the halide is not generally considered to affect the overall rate of reaction. However, we show in this chapter that the C-C coupling step is in fact halogen-dependent (Figure 4-1). The role of the halogen is clearly manifested in the OM chain termination at RT, in which the partial dehalogenation of the chlorine-containing molecules results in the short chlorine-terminated OM chains, which change to Cu-terminated chains after dechlorination is completed at 150 °C. By contrast the bromine- and iodine-containing molecules produce Cu-terminated chains at RT (Figure 4-1).

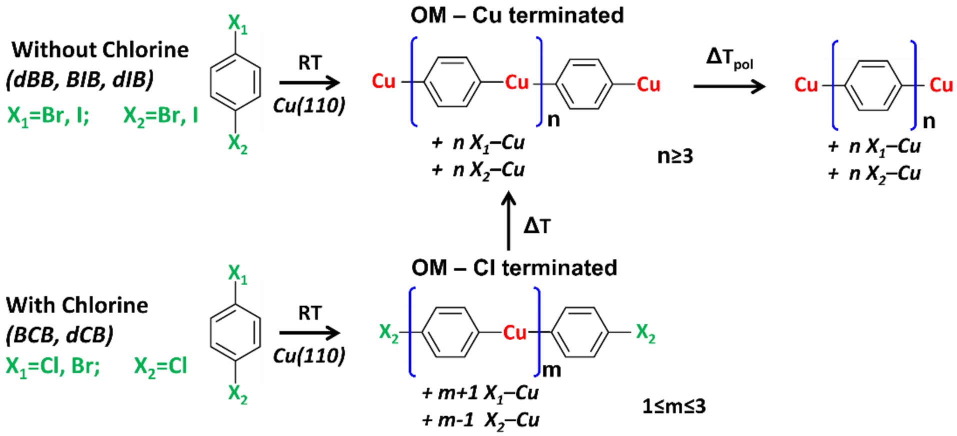

Figure 4-1. **Reaction schemes of dihalobenzenes polymerization. dBB, BIB and dIB on Cu(110) follow a two-step reaction forming an OM intermediate at RT, and polymers at higher temperatures. Chlorine-containing precursors (BCB and dCB) first form short chains OM due to incomplete dehalogenation of Cl at RT. Increasing the temperature results in a complete dehalogenation, forming OM with longer chain. The polymerization step of the reaction is the same for all the five precursors. m and n represent the OM chain size.**

The chemical state of the different carbon species involved in the dehalogenation and polymerization processes can be identified by the measurement of the C 1s photoemission spectra, as reported in Figure 4-2. At RT, the C 1s spectra are dominated by a main peak corresponding to the four closely equivalent *sp*^{2} carbon atoms (C-C) at the BE of 284.0 eV. The dehalogenated carbon atoms bound to Cu surface adatoms (C-Cu), give their contribution at a lower BE (283.3 eV). In the case of chlorinated molecules, the whole C 1s spectrum is shifted (0.3-0.4 eV) towards higher BE, in which an additional minority component is detected at 285.5 eV, attributed to the intact C-Cl component. Similar to the bromine-containing molecules, the C 1s spectrum of the BCB precursor contains a shoulder at the lower BE, characteristic of Br dehalogenation. In case of the doubly chlorinated molecule (dCB), the similar C-Cu component at the lower BE is clearly detected, thus suggesting a partial Cl dehalogenation. This weak component is more resolved at higher temperature (150 °C) when the Cl dehalogenation is completed.

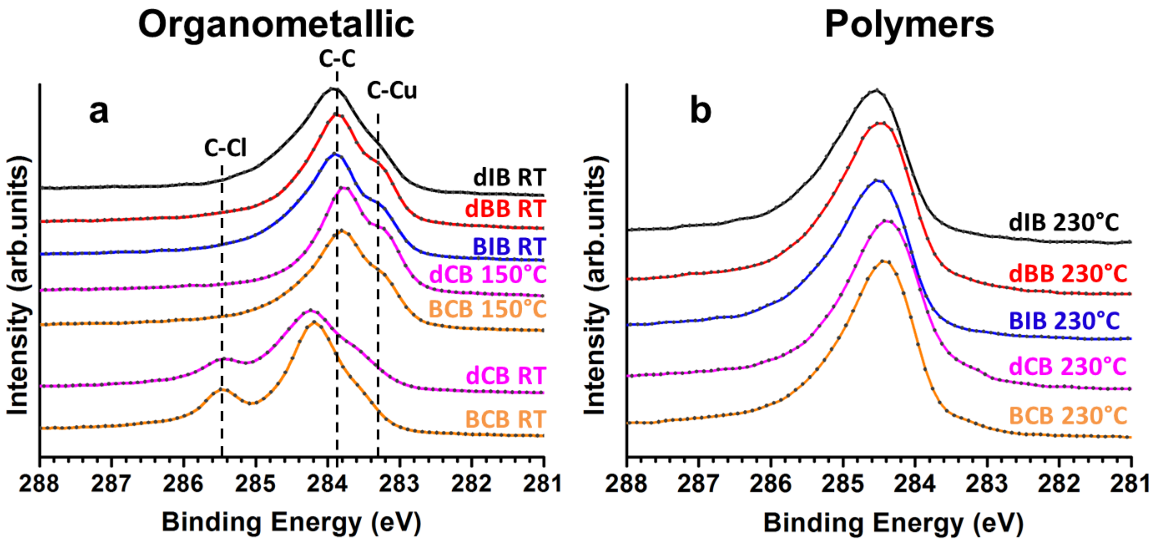

Figure 4-2. **C 1s spectra for a saturated coverage of each precursor on Cu(110) for the organometallic (a) and polymer (b) phases.**

This observation is consistent with the Cl 2p and Br 3d spectra of BCB reported in Figure 4-3. The doublet Br 3d peak at 68.4 eV BE is in agreement with the dehalogenated C-Br at RT and 150 °C, whereas the (mostly) undissociated C-Cl is confirmed by only one doublet at ~200.0 eV (Cl $2p_{3/2}$) at RT. The dCB, on the other hand, has undergone nearly 50% of C-Cl dehalogenation at RT as indicated by the additional doublet at the much lower BE of 198.0 eV, associated with Cl atoms directly bound to the Cu surface.

The evolution from the OM to polymeric phase for the five studied precursors was examined by acquiring fast-XPS spectra of the C 1s core level as a function of temperature. The fast-XPS maps presented in Figure 4-4 show the differences for every precursor, indicating a halogen-dependent effect on the activation energy (starting temperature) and the kinetics (interval) of the corresponding reaction. All the fast-XPS maps exhibit a shift in the C 1s spectra towards higher BE above 140 °C. This is a signature of polymerization, and is correlated with the progressive vanishing of the C-Cu component (at 283.3 eV) and growth of the C-C component at higher BE,[30, 159] shown in Figure 4-4. The correlation of polymerization and the halogen type is seen in the starting temperature (T_{start}) of the conversion of OM to polymer, at 125±2 °C for the dIB and BIB, at 175±2 °C for dBB and BCB, and at 185±2 °C for dCB, showing that T_{start} increases from the iodine- to the bromine- to the chlorine-containing molecules (green lines, Figure 4-4).

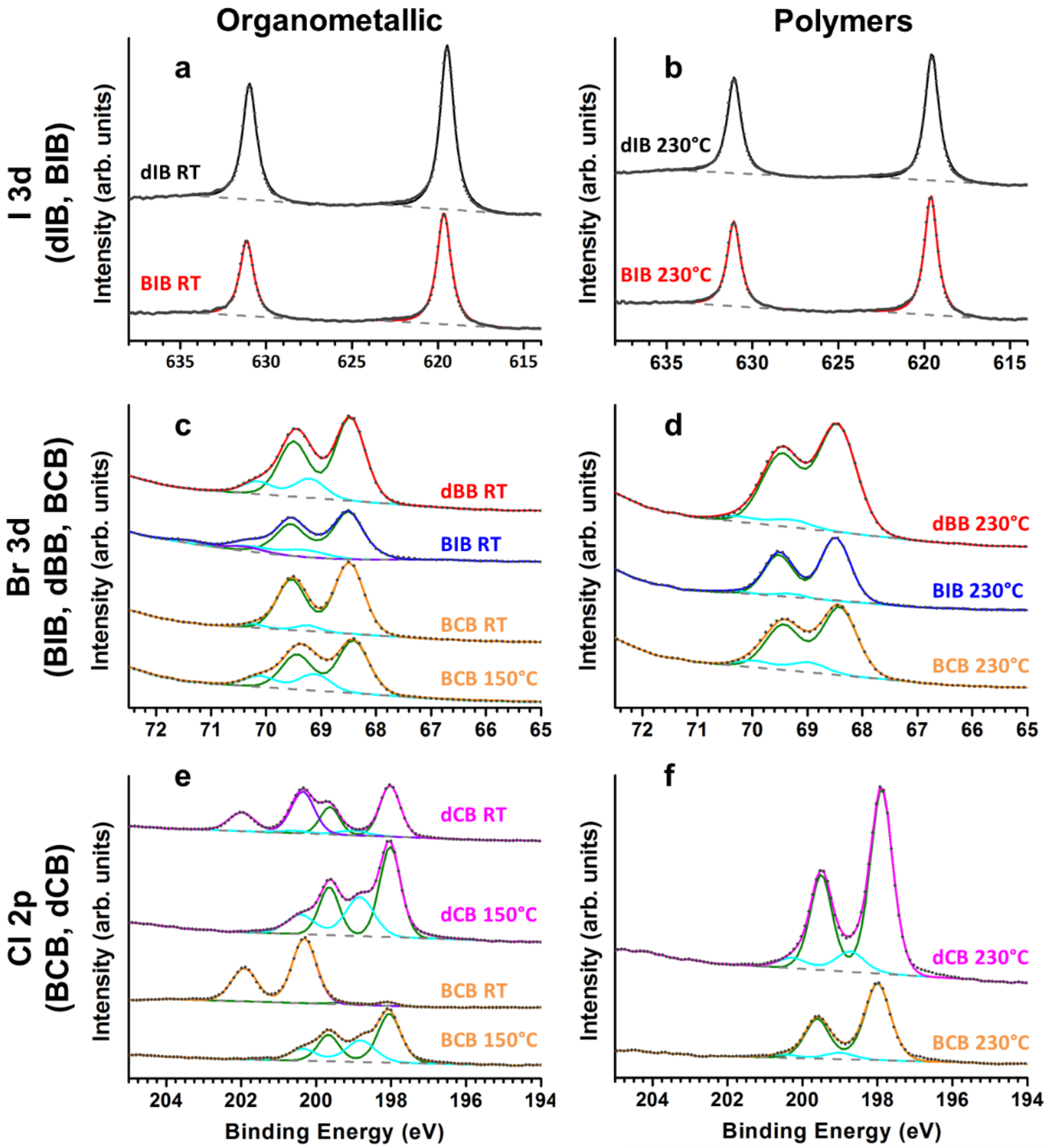

Figure 4-3. **XPS spectra (I 3d, Br 3d, Cl 2p) of organometallic (left panels, a, c, e) and polymer (right panels, b, d, f) for the saturated coverage of five precursors on Cu(110) at different temperature; the component in green is attributed to the dissociated halogens, also observed for the polymers' spectra; the component in light blue, observed for the long OM chains is reduced after polymerization, and likely originates from different adsorption sites of the halogens when long chains are present.**

While for every molecule the reaction is completed within an approximately 40 °C range, the reaction for dIB proceeds across an 80 °C range (Table 4-1). The final position of the main C 1s peak is found at 284.5 eV with the small variations of ±0.1 eV between the various precursors, which remains within the experimental resolution. The maps for chlorine-containing molecules present an earlier transition at about 120 °C, witnessed by the C 1s shift towards lower BE, as highlighted by the white arrows in Figure 4-4, which we can ascribe to the complete C-Cl dissociation. The full C-Br and C-I bonds dehalogenation takes place below RT and, therefore, does not appear in the fast-XPS maps of non-chlorinated precursors. It is however known that the dehalogenation of iodobenzene on Cu(110) takes place at approximately -100 °C.[26] Although the dissociation temperature of Br for bromobenzene or dBB on Cu(110) is not available in the literature, the aryl halides (Ar-X) have shown the reactivity trend of Ar–I > Ar–Br > Ar–Cl. The dissociation of Br is therefore expected to happen at a higher temperature than iodine.[99, 185] This trend agrees with DFT calculated dissociation energies of iodobenzene and bromobenzene,[16] and with the experimental values of dissociation enthalpy of a Ph-halogen bond: 67±2 kcal/mol for Ph-I, 84±1 kcal/mol for Ph-Br and 97±1 kcal/mol for Ph-Cl.[186] The fast-XPS maps not only identify the critical temperature of the on-surface chemical reactions, but also highlight that the C-C coupling step of the reaction is halogen-dependent. For the iodine- and bromine-containing molecules, the scheme is similar to the previous reports,[30-31, 107, 159] where a fully dehalogenated phase of OM chains forms at RT, and remains stable up to the polymerization temperature.

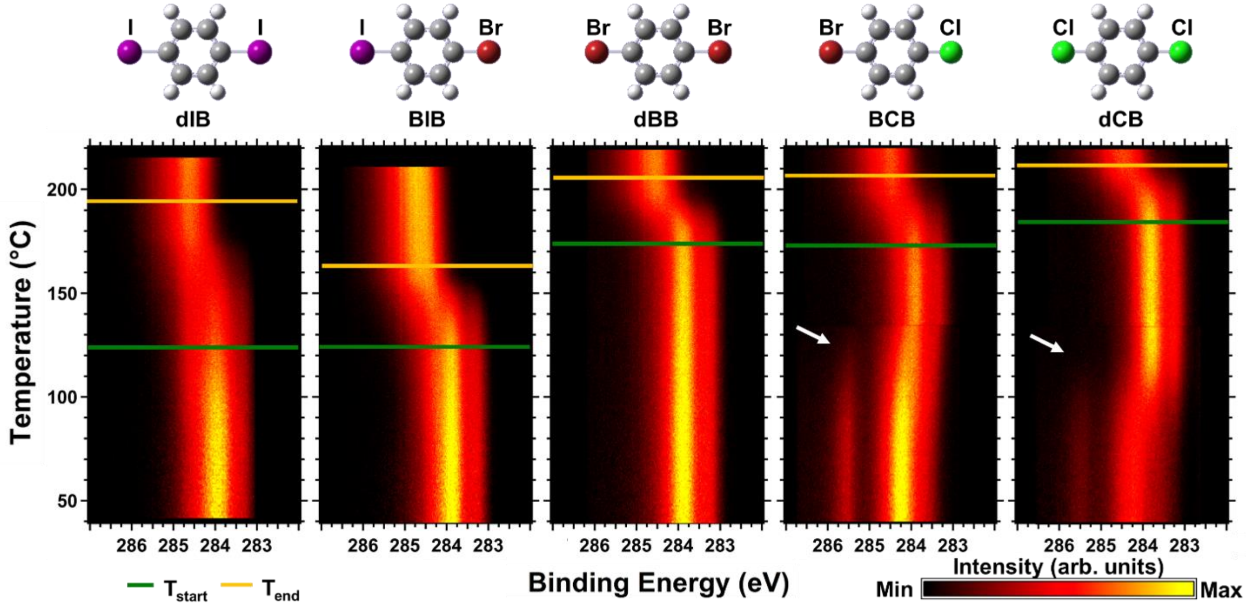

Figure 4-4. **Fast-XPS measurements of C 1s during annealing of a saturated monolayer of each precursor on Cu(110) dosed at RT; the temperatures at which 10% and 90% of the polymerization reaction is completed are marked with T_{start} (green) and T_{end} (orange) lines, respectively; white arrows indicate the change in the C 1s spectra due to C-Cl dissociation.**

For chlorine-containing molecules, the RT phase, which is stable up to 120 °C, is rather associated with the incomplete dehalogenation of dCB and BCB precursors. As a result, most of the phenyl groups would be Cl-terminated and forms short OM chains on the surface (2 to 4 phenyls long). The XPS spectra for Cl 2p presented in Figure 4-3e shows that approximately 50% of the Cl-C bonds are dissociated for dCB, but only a small fraction for BCB. C-Cl bond dissociation is completed at temperatures above 120 °C (Figure 4-4), and longer chains are formed (>20 phenylenes long). For dBB, BIB and dIB, the C-Br and C-I bonds are dissociated upon adsorption at RT on Cu(110), as can be seen from the Br 3d (Figure 4-3c) and I 3d (Figure 4-3a) spectra, in which their $3d_{5/2}$ components at 68.3 eV and 619.5 eV, respectively, are attributed to Cu-Br[30-31] and Cu-I bonds.[19] A single chemical state was observed for I 3d at every temperature during the reaction. For Br 3d and Cl 2p, the dominant states are found at 68.3 eV ($3d_{5/2}$) and 198.0 eV ($2p_{5/2}$), respectively, and additional components at higher BE were observed at 69.1 eV (Br $3d_{5/2}$) and 198.8 eV (Cl $2p_{5/2}$) (Figure 4-3c,e). In the case of dBB and BIB, these components were present at RT, while for the chlorine-containing molecules, they became apparent only after annealing to 150 °C, when dehalogenation is complete (Figure 4-3e). The other chemical states (0.7 eV higher BE shift) in Br 3d and Cl 2p spectra can be tentatively attributed to different adsorption sites of the halogen within the OM structure. BIB spectra at RT exhibit a weak peak at 70.7 eV (Br $3d_{5/2}$), attributable to a minor fraction of Br-C bonds still being intact at RT.

Table 4-1. **T_{start} and T_{end} of the polymerization reaction, obtained from fast-XPS map in Figure 4-4, at the temperatures at which 10% and 90% of the reaction is completed, and temperature range of polymerization (ΔT, measured as T_{end}-T_{start}).**

Molecule	T_{start}(°C)	T_{end}(°C)	ΔT(°C)
dIB	126	208	82
BIB	123	166	43
dBB	175	209	34
BCB	174	210	36
dCB	185	220	35

A comparison of fast-XPS maps and XPS spectra between dIB and dBB is presented in Figure 4-5. dBB is taken as the representative of the other bromine- and chlorine-containing molecules (BIB, BCB and dCB) because their fast-XPS maps show similar behavior for the polymerization process, both in the temperature range of the polymerization reaction (Table 4-1, temperature range) and in the OM chains, all along the same directions (Figure 4-6).

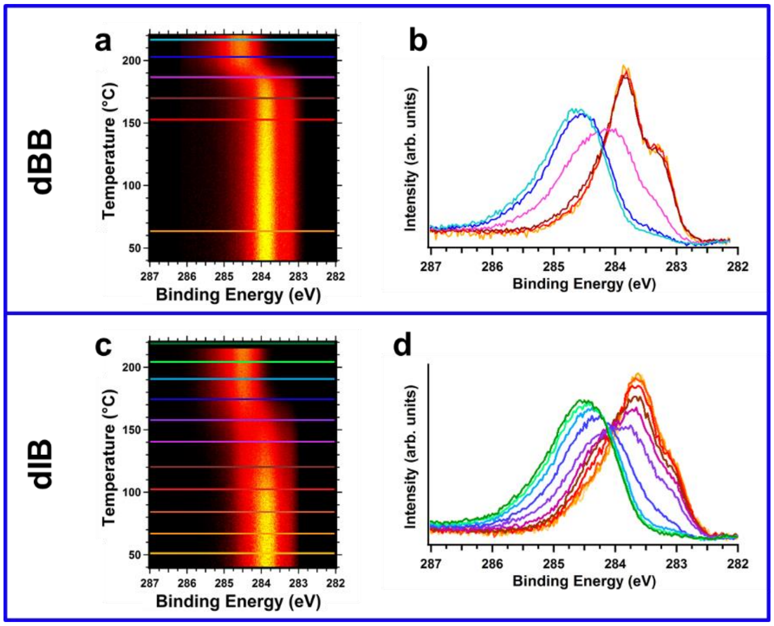

Figure 4-5. **Fast-XPS measurements of C 1s core level during annealing of a saturated coverage of dBB (a) and dIB (c) on Cu(110). C 1s spectra from map at 20 °C interval are reported in the panels b and d.**

Figure 4-5a,c reports the fast-XPS maps, where the C 1s line profiles at various temperatures through the ramp are shown every 20 °C in panels b,d (identical profiles have been omitted). While for dIB the shift is continuous and gradual toward higher BE values, it is sharp and sudden for dBB. STM images (Figure 4-6) also show a clear difference between dBB and dIB structures on the surface, likely due to the fact that for dIB the OM chains are oriented along the same directions of the polymer, whereas for all other molecules this is not the case. Therefore, for dIB the coupling can happen for two monomers in an OM chain without affecting the other adjacent ones, *i.e.* the reaction can take place gradually, while for the other precursors a rotation is required for the phenyl-phenyl coupling, affecting the neighboring chains, which, we speculate, may require overcoming an additional barrier for the monomers to couple.

4.3.2 Structural characterization by STM

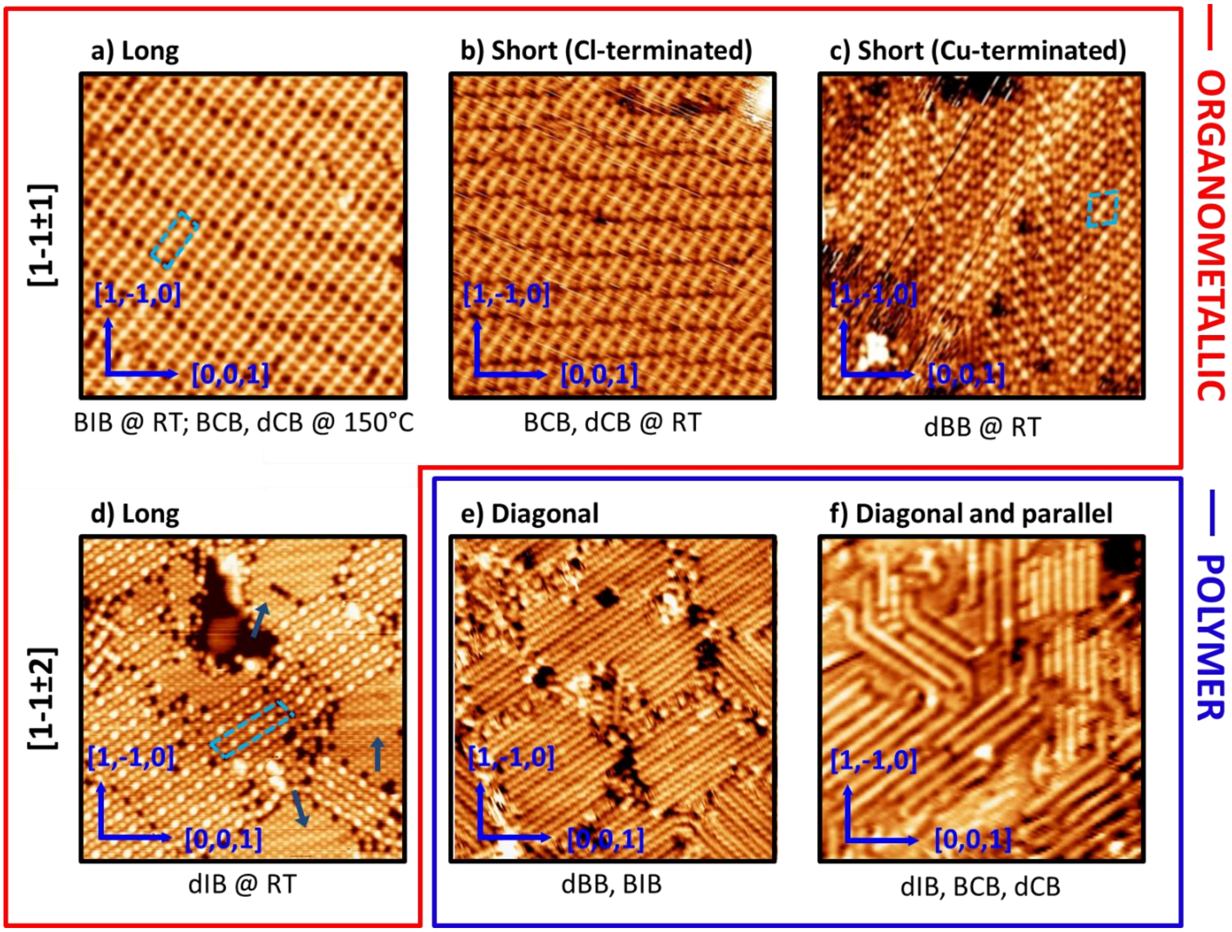

Figure 4-6. **STM images (20×20 nm^2) obtained for the five precursors on Cu(110). The OM phases (a-d) are shown in the red box; the blue arrows in d indicate the c(2×2) iodine superstructure; light blue dashed lines represent the molecular unit cells. BCB and dCB show two different OM phases at RT (b) and after annealing at 150 °C (a). The polymer phases (e-f), formed when annealing above 200 °C are presented in the blue box.**

Deposition of each precursor on Cu(110) at RT results in distinctive self-assembled OM structures, oriented along different lattice directions, which produce poly(para-phenylene) (PPP) polymers upon annealing. The OM (red frame) and polymer (blue frame) structures obtained for the five precursors at different temperatures are shown in Figure 4-6. The assignment of these phases is based on the distances between the protrusions in the STM data for OM and polymer (6.3 Å and 4.4 Å, respectively),[30] together with the C 1s analysis described above.

Organometallic chains: All the OM phases (Figure 4-6a-d) appeared in two domains related by mirror symmetry with respect to the [1-10] direction, and are made of chains of phenylene groups linked through copper atoms, and stacked into a 2D structure. The OM chains are oriented along either the [1-1±1] directions (Figure 4-6a-c, dCB, BCB, dBB, BIB) or the [1-1±2] directions (Figure 4-6d, dIB), and are interdigitated by rows of protrusions, identified as halogens.[30, 115] The directions of the molecular domains are shown in Figure 4-7. DIB OM chains are composed of ordered domains of long chains (limited only by the size of the terraces, defects and other domains), with a periodic strain-relieving kink every seven phenyls (Figure 4-7), and a surface reconstruction corresponding to the epitaxy matrices (1, -4 | 11, 10) and (1, 4 | -11, 10). For iodine-containing molecules, a portion of the surface is covered by the c(2×2) iodine superstructure (Figure 4-6d). Higher resolution STM images of every phase for each precursor are presented in Figure 4-8, superimposed with the proposed molecular structure. For the structures that produce [1-1±1]-oriented OMs, we observe two different types of chains: *long* (for BIB) and *short* (for dBB, BCB and dCB) at RT. The short chain structures are made of a smaller number of phenyls, between two to four for BCB and dCB (Figure 4-6b) and exclusively three for dBB chevron phase (Figure 4-6c).[115]

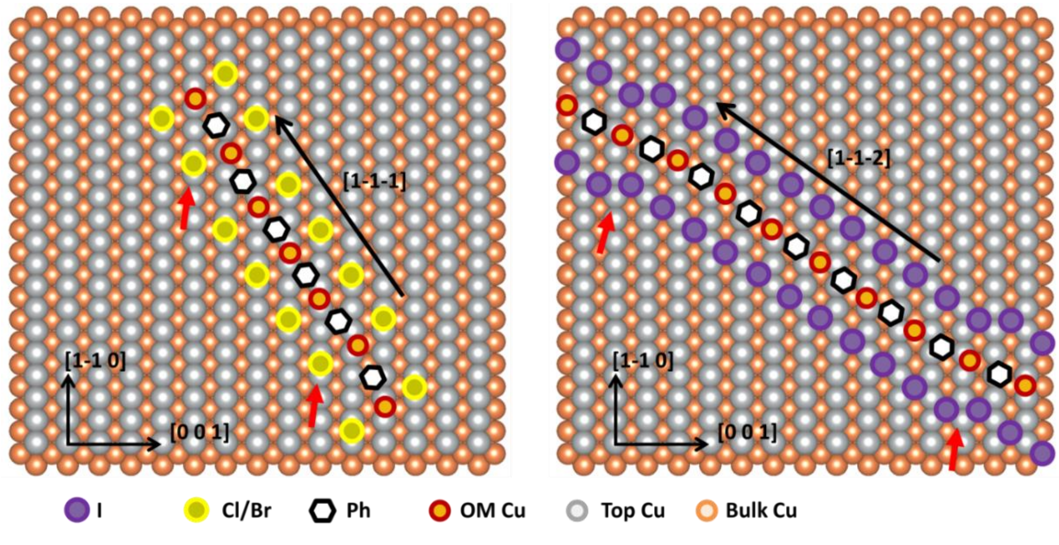

Figure 4-7. Scheme of the long OM structures along [1-1-1] direction (BCB, dCB, BIB) and [1-1-2] direction (dIB) on Cu(110) surface; dIB follows a different behavior compared to the other precursors; iodine atoms adsorb at the hollow positions, while Br and Cl prefer short-bridge positions, thus forcing the OM chains to self-assemble along different directions.

For dBB, the short chains are always Cu-terminated (Figure 4-8c), while for BCB and dCB, they are Cl-terminated (Figure 4-8d, e), as inferred from the XPS spectra in Figure 4-3. The presence of Cl to the chain-end forces molecular aggregate to bend upwards the terminal phenyls, resulting in an apparent projected length in the STM profiles obtained along the [1-1-1] direction of the Cu-Ph-Cl group equal to 4.9 Å, which is shorter than the 6.4 Å known length of a Cu-Ph-Cu, as shown in Figure 4-9. The reduced dichroism in the NEXAFS measurements supports the hypothesis of partial lifting of some benzene rings (see paragraph 4.3.3).

The RT structure for dBB is characterized by longer-range order and described by epitaxy matrices (1, -4 | 6, 0) and (1, -1 | 4, 1).[159] An epitaxy matrix cannot be written for BCB and dCB at RT, due to a lack of long-range order. The dBB chevron phase is stable up to the polymerization temperature (175 °C), while the chain length of BCB and dCB increases when the dehalogenation process is completed at 150 °C, and long OM chains made of a higher number of phenyls (>20) are observed on the surface (Figure 4-9d). As for BIB at RT, these chains comprise two domains along the [1-1±1] directions, have a periodic strain-relieving kink every four phenyls (Figure 4-7) and are described by the epitaxy matrices (2, -2 | 4, 9) and (2, 2 | -4, 9). The difference between the OM chain direction for dIB and that of the other molecules (BIB, dBB, BCB and dCB) can be inferred from the halogens' preferred adsorption site on a Cu(110): iodine atoms occupy hollow sites,[19] while Br and Cl atoms are located at short-bridge sites (Figure 4-7).[30-31, 187]

STM line profiles of the halogen atoms between the OM chains show that for dIB, iodine atoms adsorb along the [1-1±2] directions, with a 4.4 Å periodicity and are located in hollow positions; while for the other molecules, Br and Cl atoms follow the [1-1±1] directions, with a 6.3 Å periodicity and are located at short-bridge positions. For BIB, Br atoms occupy the positions between the OM chains, and iodine segregate into c(2×2) domains. We can therefore suppose that in the BIB case, bromine atoms decorate the OM chains, while iodine atoms are segregated into the c(2×2) domains. At the boundaries between c(2×2) domains and OM chains, both Br and I atoms are located along the chains, with two atoms in hollow position and one atom at short-bridge position.

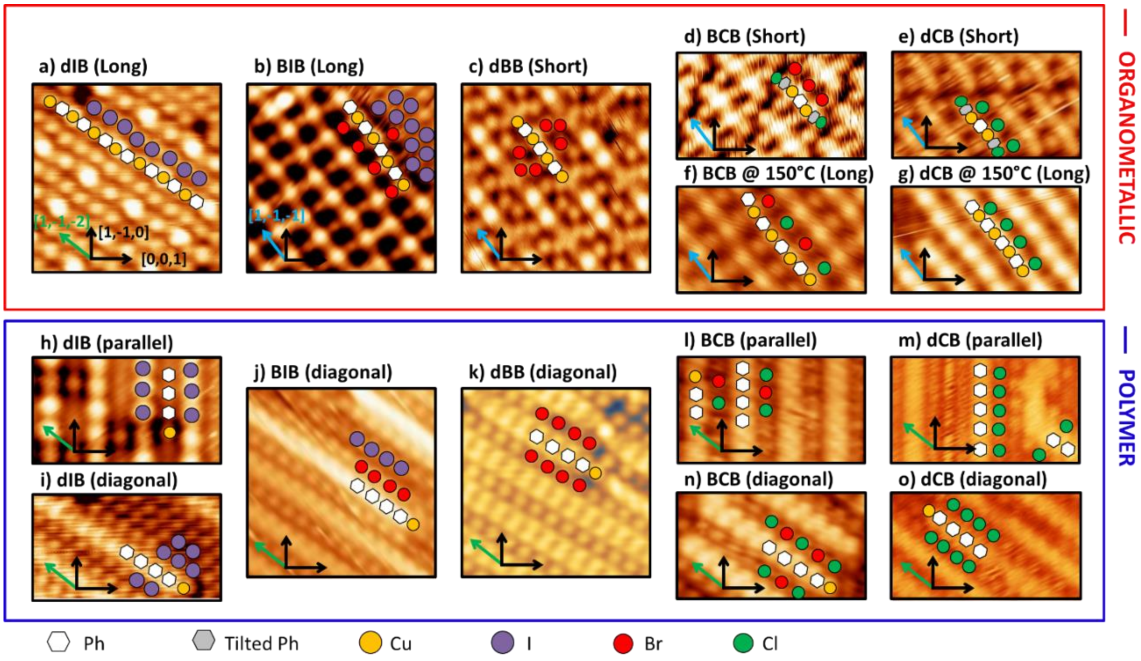

Figure 4-8. **STM images (square 5×5 nm^2, rectangular 2.5×5.0 nm^2) of the OM (RT except f, g) and polymeric phases (230 °C) observed for each precursor, superimposed with molecular structures and copper lattice directions. OM chains for dIB (a) are orientated along the [1-1-2] direction, same as the direction of the polymeric chains, while all the other OM chains are along the [1-1-1] direction.**

Polymer chains: The polymer phase (Figure 4-8h-o), is made of linear chains of π-conjugated phenyls decorated by halogen atoms. dBB and BIB exclusively produce polymers along the direction [1-1±2] (the 'diagonal' direction of the Cu(110) surface unit cell), while BCB, dCB and dIB show polymers along both the diagonal [1-1±2] and parallel (to the Cu(110) close-packed row, [1-10]) directions. The phenyl-phenyl distance is 4.4 Å for all the polymers, a distance which is commensurate with the diagonal direction and incommensurate for the parallel direction.[115] Commensurability with the surface permits diagonal polymers to grow with little to no strain penalty, and results in the formation of large islands of polymers with a mean length greater than 20 phenyl units. However, the electronic properties are strictly related to the polymer length,[115, 137] and whether a particular halogen or an intermediate phase favors longer chains is therefore important for selecting the right building block.

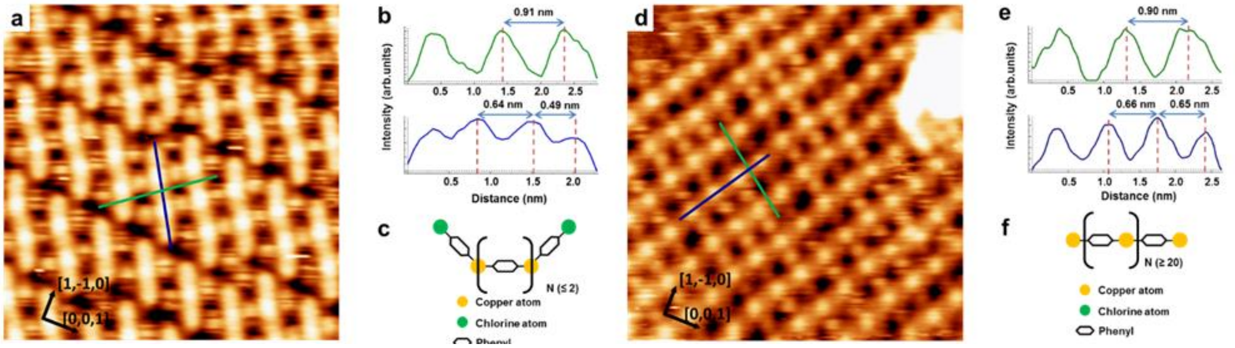

Figure 4-9. **STM images of OM chains formed by BCB on Cu(110), short chains are formed at RT, while long chains are formed after annealing at 150 °C. a) 8×8 nm^2 STM image of short OM chains along the [1-1-1] direction (V = -0.81 V, I = 1.46 nA); b) profiles intensities along the paths in (a); c) side view of the hypothesized structure, with the terminal phenyls raised from the surface; d) 8×8 nm^2 STM image of long OM chains along the [1-11] direction (V = -0.87 V, I = 0.70 nA); e) profiles intensities along the paths in (d); f) side view model of the long OM structure where the phenyls are Cu-terminated and flat.**

4.3.3 NEXAFS and molecular orientation

C K-edge NEXAFS spectra obtained at RT as a function of the photon's polarization for all precursors (Figure 4-10) present two π* transitions, π_1* and π_2* at ~284.5 and ~288.5 eV, respectively, in agreement with the cases of dBB on Cu(110)[30] and halobenzenes on Cu(111).[188] These spectra show that the phenyl rings are mostly flat on the surface, supporting the orientational hypotheses derived from the STM images. The C K-edge NEXAFS spectra at RT for chlorine-containing molecules show higher tilt of the phenyl ring, according to the change in the intensity of the π* states as a function of the polarization vector of incoming photons with respect to the surface normal, particularly for π_2* resonance (black line in Figure 4-10), where a peak is visible for θ = 0°.[158] This feature is not present for the non-chlorinated molecules at RT (Figure 4-10a), and is consistent with a fraction of the molecules being tilted away from the surface. We additionally note the presence of a shoulder on the high-energy side of the π_1* resonance at θ = 90° (Figure 4-10b), a feature not observed for the other precursors.

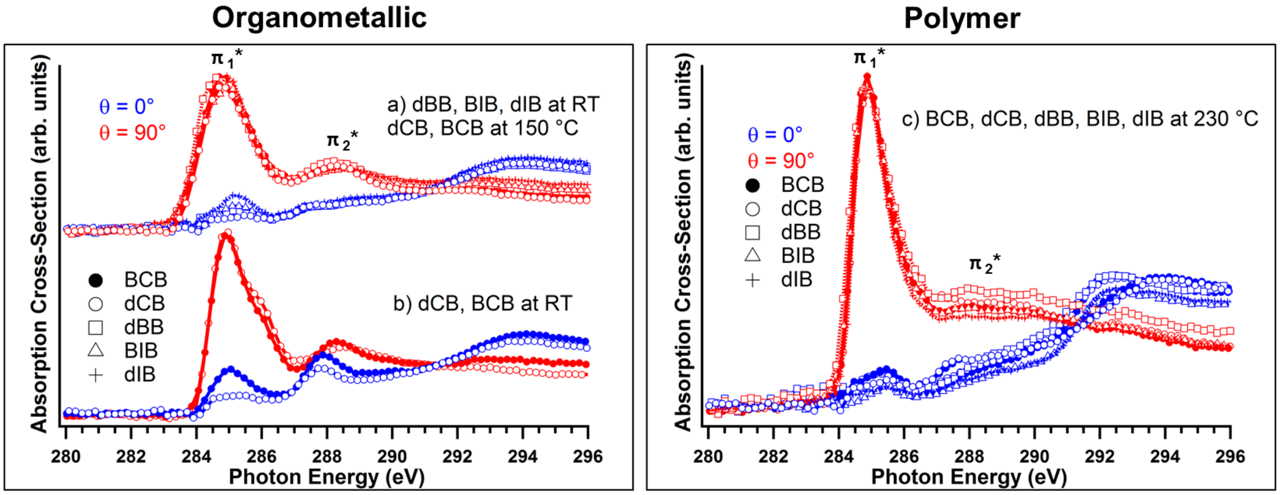

Figure 4-10. **Polarization-dependent C K-edge NEXAFS spectra for the five studied precursors; a) dBB, BIB and dIB at RT and BCB and dCB at 150 °C; b) dCB and BCB at RT; c) all precursors at 230 °C. For each sample we report θ = 90° (red, TM geometry, close to p-polarization) and θ = 0° (blue, TE geometry, s-polarization) with the incident radiation falling in the plane containing the sample normal and the [1-10] lattice direction.**

After annealing to 150 °C, the intensity of the π_2* resonance at θ = 0° for dCB and BCB is strongly suppressed, and the spectra in all polarizations become qualitatively indistinguishable from the RT spectra observed for the other molecules. This is consistent with the STM data, where OM structures along the same directions are observed for all molecules but dIB, and the C 1s XPS data, where the spectra are identical for dCB and BCB at 150 °C and dIB, BIB and dBB at RT. Annealing all the precursors to 230 °C completely suppress the π_2* resonance intensity, indicating the planarity of the aromatic rings, expected for the PPP polymers (Figure 4-10).[30-31, 189]

4.3.4 Role of the halogen in the reaction

The halogen might affect the reaction mechanism and the barrier energies in a variety of ways. Here, we present two hypotheses based on the (i) effect of differing diffusion barriers for the halogens, and (ii) possible presence of the halogen atoms on-top of the copper atoms in the OM structure. The hypotheses are not mutually exclusive, and the observed behavior could contain contributions from both effects. To explore the first hypothesis, nudged elastic band (NEB) calculation for the diffusion of the halogens along different directions of the Cu(110) surface were performed ([001], [1-10] and [1-12]).

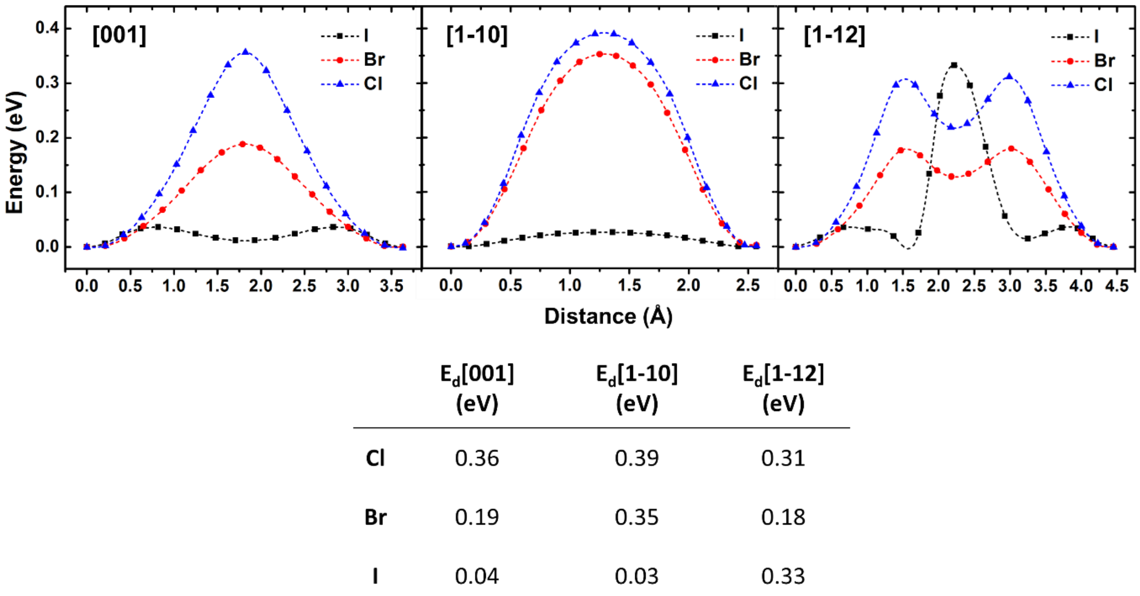

	E_d[001] (eV)	E_d[1-10] (eV)	E_d[1-12] (eV)
Cl	0.36	0.39	0.31
Br	0.19	0.35	0.18
I	0.04	0.03	0.33

Figure 4-11. (top panels) NEB plots of the minimum energy path for the diffusion of iodine, bromine and chlorine along one unit cell in the [1-1 0], [0 0 1] and [1-1 2] directions of Cu(110); for Br and Cl, the starting equilibrium position is short-bridge, while for I is hollow; (bottom panel) Diffusion energies (E_d) for I, Br and Cl along the studied directions.

These simulations consider the diffusion of the halogen alone and use as starting position a hollow position for I atom and a short-bridge position for Br and Cl atoms, known to be the respective preferred adsorption site for the halogens.[8, 187, 190-191] The overall trend of the diffusion energy as I<Br<Cl (Figure 4-11) is consistent with the starting temperature of the OM-to-polymer conversion reaction found in the fast-XPS maps (Figure 4-4), where the polymerization of dCB starts at the highest temperature and at the lower temperature for iodine-containing molecules. Unlike chlorine and bromine, the diffusion barrier for iodine along the [1-12] direction is higher than the other two directions. This could be explained by the diffusion of iodine along the [1-12] direction, which needs to pass from a stable hollow adsorption site to an on-top location on the Cu surface. Therefore, having the lower diffusion energy barriers along the other two directions, the iodine atoms can make a two-step movement, along [1-10] and [001], instead of diffusing directly through the [1-12]. We can further speculate that a lower diffusion barrier for the halogens also facilitates monomer diffusion, thereby reducing the transition temperature. Conversely, a higher diffusion barrier for the halogens requires an overall higher temperature for the polymerization to occur, as observed experimentally.

The second hypothesis is connected with the halogen being integrated into portions of the OM chains, as proposed by Di Giovannantonio *et al*.[30-31] In this work Br atoms were proposed to occupy two different positions of the unit cell of OM chains for dBB on Cu(110), four per unit cell on the short-bridge lattice site between adjacent OM chains, and four adsorbed on top of the Cu atoms forming the OM (i.e. between the phenyls). This hypothesis is based on simulated STM images, which show a better qualitative match with the experimental STM images when top Br atoms are included. To complete the polymerization reaction, the copper atoms in the OM structure need to be expelled from the chains to permit covalent binding between adjacent phenyls. If a halogen atom is present on top of these Cu atoms, the energies involved in the reaction must depend on the type of halogen and will result in different polymerization temperatures.

4.4 Conclusions and perspectives

The role of the halogen in Ullmann coupling polymerization of five 1,4-dihalobenzene precursors containing Cl, Br, and I on Cu(110) was studied by combined fast-XPS, NEXAFS and STM analysis. We show that the nature of the halogen atom, hence the strength of its bond to carbon atoms, affects the temperature of the dehalogenation step. The type of halogen also drives the geometry of the OM structures obtained at RT as well as the orientation of the polymers as *i.* the length of the OM chains depends on the carbon-halogen bond dissociation energy and *ii.* the OM structures for precursors containing Br and Cl (dBB, dCB, BCB, BIB) are aligned along the [1-1±1] directions, as opposed to alignment along the [1-1±2] directions for precursors containing only iodine (dIB). The OM structures follow different reaction kinetics, exhibiting a gradual transition for dIB, while the others undergo a sudden transition into PPP polymers. A key finding of this study is that the temperature range of the polymerization is affected by the type of halogen and is qualitatively correlated to the halogen’s diffusion energy. Our results show that the halogen is not merely a reaction byproduct, but rather an important parameter governing the on-surface Ullmann polymerization reaction. A further confirmation of these point comes from the fast-XPS of the five halo-benzenes on Cu(111) at 0.5 ML of coverage, presented in Figure 4-12. Here we can see that the additional OM phase (Chapter 3, Figure 3-7) is observed only when using the dBB precursor and is not present for the others. Fast-XPS maps for chlorine containing molecules present a second transition (green arrow in Figure 4-12), connected to the dehalogenation of the precursors, the first step of the Ullmann reaction, with the consequent formation of 1D OM chains (due to C-Cl bond being intact after deposition at RT on Cu(110) as observed also for the 1 ML case in Figure 4-4). While is not easy to infer the reasons for which the 2D OM observation is unique to the dBB precursor, we could speculate on it given the different behaviour and energetic of the three used halogens. Iodine forms c(2×2) islands on the surface, separated from the molecules, adsorbs preferentially in hollow positions on the Cu(110) surface, and yield a different 1D-OM phase. Br and Cl instead share the short-bridge adsorption sites and yield the same 1D-OM phase. However, the diffusion energies for Br and Cl are different along different direction of the Cu(110), with Br having the lower diffusion energy on all the studied paths ([001], [1-10], and [1-12]). We can therefore hypothesize that a necessary matching of both halogen and precursor diffusion energies, as well as the availability of surface adatoms, are necessary to form the observed 2D-OM phase. Further studies to explain this Br-only related effect are ongoing at the time of redaction of this thesis, but this result confirms once again the pivotal role of the halogen in Ullmann coupling.

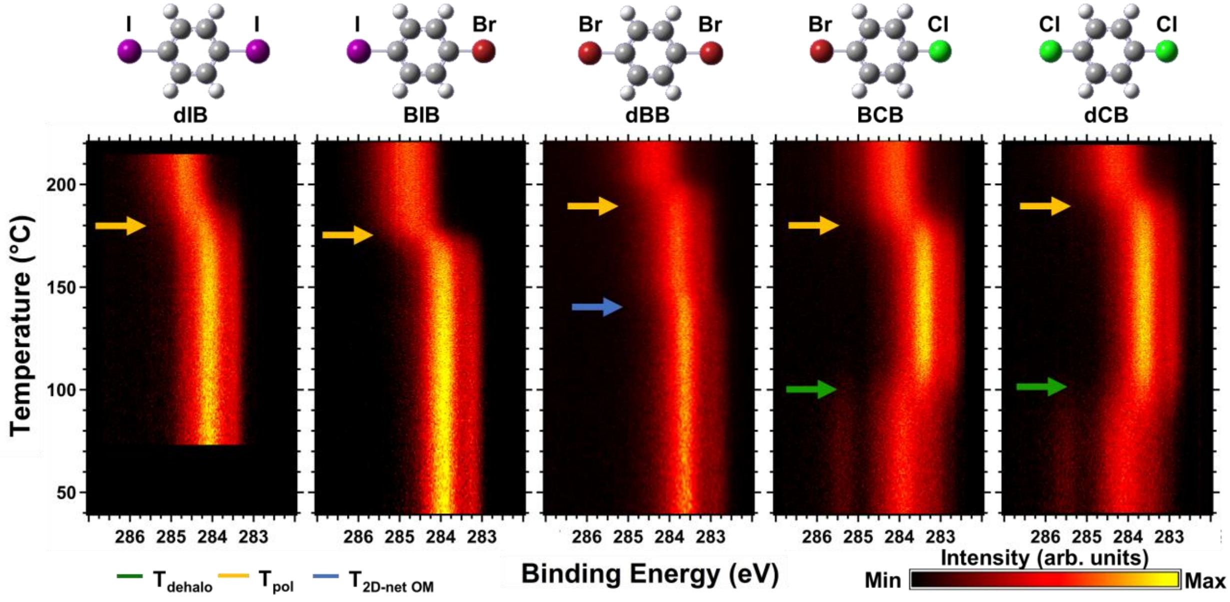

Figure 4-12 **Fast-XPS measurements of C 1s during annealing of a 0.5 ML coverage layer of each precursor on Cu(110) dosed at RT; polymerization, C-Cl dissociation and 1D-OM to 2D-OM reaction temperatures are indicated by the yellow, green and blue arrows respectively.**

5 FROM 1D TO 2D:
CAN WE MAKE GRAPHENE-LIKE MATERIALS?

Based on the work "*Surface-mediated Assembly, Polymerization and Degradation of Thiophene-based Monomers*" published in Chemical Science, **2019**, *10* (19), 5167-5175. Contribution from: Gianluca Galeotti, Fabrizio De Marchi, Maryam Ebrahimi, Lucas Vasquez Besteiro, Tyler Taerum, Mohammed El Garah, Josh Lipton-Duffin, Dmitrii Perepichka, and Federico Rosei - where the author participated in all the experiments and data analysis and wrote the manuscript together with Fabrizio De Marchi.

5.1 Introduction

2D nanomaterials have been studied extensively due to their unprecedented properties arising from reduced dimensionality.[192] However, such systems are exceedingly challenging to prepare because it is not possible to control the dimensionality during the growth of a polymer sheet using the conventional solution-based synthetic methods,[193-194] and, while various building blocks have been used in on-surface synthesis of π-conjugated 2D polymers, the resulting electron delocalization is actually rather limited, due to cross-conjugation, sterically-induced twist and other effects.[139] In this context, thiophene-containing monomers are highly promising building block for π-conjugated 2D polymers, due to their synthetic/structural diversity, highly efficient π-conjugation, and have already exhibited excellent semiconducting properties in conventional (1D) polymer electronic devices.[195-196] However, as discussed in Chapter 1 and in previous work from our group[24, 125, 197] on-surface polymerization of thiophene monomers *via* common Ullmann-coupling is challenging due to the need to control the competing desulfurization reactions.

In this chapter, we present a comprehensive comparative study of self-assembly and reactivity of a tridentate tribromoterthienobenzene (TBTTB) on Au(111), Ag(111) and Cu(111). The TBTTB molecule, shown in Figure 5-1a is a threefold symmetric molecule with a terthienobenzene (TTB) core and functionalized with Br atoms. TBTTB is pro-chiral and can therefore be adsorbed as R- and S- enantiomers on a surface. Identification of R- and S-enantiomers within molecular self-assembly and OM structures illustrates the chirality of each domain, whether an enantiomeric phase or a racemic mixture is favored. The design of the nanostructures formed upon adsorption at RT and the subsequent surface reactions, proceed by sequential annealing on each substrate are controlled by the molecule's functional groups, intermolecular forces and molecule-substrate interactions. Our data exhibits the formation of 2D self-assembled molecular networks on Au, and an OM structure on Ag (and Cu) at RT. We report the formation of an extended ordered 2D OM polymer containing thiophene building blocks on Au(111) at 200 ºC which is similar to the phase observed on Ag(111) at RT. Unlike Ag and Cu, the formation of an OM network on Au has been rarely reported,[198-201] considering that the halogenated molecules often directly undergo the reaction yielding covalent polymers upon dehalogenation.[18, 202] Complementary data acquired by STM, XPS and DFT calculations was used to understand and explain the obtained structures, and to demonstrate that the adsorbates would undertake different chemical pathways depending on the strength of the molecule-metal interaction. This study shows that surface reactivity plays a critical role in the formation and distinctive design of the nanostructures, formed upon adsorption, and the subsequent chemical processes induced by heat.

5.2 Results and discussion

5.2.1 TBTTB on Au(111)

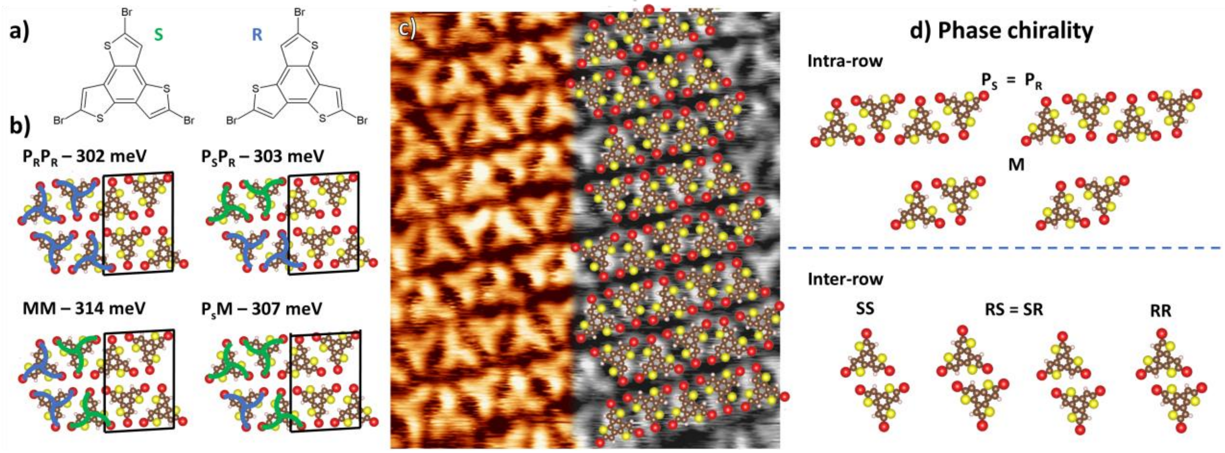

Figure 5-1. a) Molecular structures of *S* and *R* TBTTB enantiomers; b) possible configurations for the RT phase of TBTTB on Au(111) and their calculated cohesive energy per molecule; black boxes represent the unit cells. c) 7.5 × 7.5 nm^2 STM image of TBTTB on Au(111) superimposed with the RSRS DFT calculated structure (I_t = 0.63 nA; V_t = 1.25 V). d) different combinations of R and S enantiomers in the unit cell were calculated; two main classes of interactions can be identified: intra- and inter-rows; the figure highlights the equivalent interactions

After deposition on Au at RT, the molecules organize into a close-packed 2D row structure (Figure 5-1c). The unit cell, with dimensions of (1.73 ± 0.05) × (2.45 ± 0.05) nm^2 and an angle of 87 ± 3° between two vectors, contains four molecules in two rows of alternating R/S enantiomers. To confirm this assignment, we performed DFT gas phase calculations (PBE-GGA with D3 dispersion correction), calculating all the possible combinations of enantiopure (P_S or P_R) and racemic (M) rows (Figure 5-1b). The total cohesive energies indicate that the racemic networks are more stable ($\Delta E \approx 0.05$ eV per unit cell) than the homo-enantiomeric assemblies. As such, the simulations point toward the MM combination as the most stable assembly, as inferred from STM images.

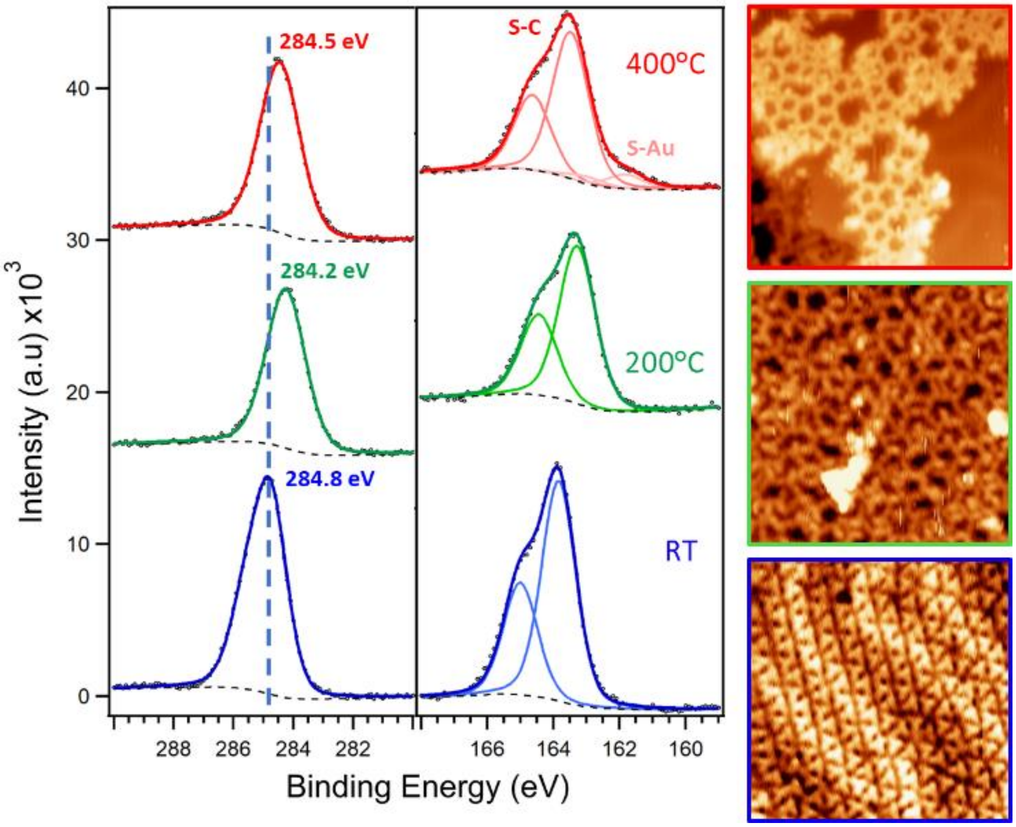

Figure 5-2. STM images and XPS C 1s, S 2p, Br 3p spectra (left, middle, right panel) of TBTTB deposited on Au(111) at RT (blue), and sequentially annealed to 200 °C (green) and 400 °C (red). XPS at RT shows a C 1s main peak at 284.8 eV, which undergoes a shift toward lower BE (284.2 eV) at 200 °C, before going back toward higher BE (284.4 eV) after annealing to 400 °C. The first shift is assigned to molecular dehalogenation (breaking C-Br bond) and formation of OM chains (C-Au-C), the latter to polymerization (C-C formation). STM image at RT (15×15 nm^2) shows an ordered phase of molecules. This order is lost upon annealing, both in the OM (200 °C, 15×15 nm^2) and polymeric (400 °C, 20×20 nm^2) phase.

The herringbone reconstruction of the Au(111) surface is maintained (Figure 5-2, STM blue panel), consistent with weak molecule-substrate interactions.[198, 203] XPS analysis shows a Br 3p doublet at BEs of 183.7 eV (Br 3p $_{3/2}$) and 190.2 eV (Br 3p $_{1/2}$) and a S 2p doublet at BEs of 163.9 eV (S 2p $_{3/2}$) and 165.1 eV (S 2p $_{1/2}$), which are plausible for Br-C and S-C bonds, confirming that the molecules are intact (Figure 5-2 and Figure 5-3).[197]

Annealing the chiral phase on Au(111) reduces the level of order of the molecular network. Starting from 100 °C, additional arrangements are observed to coexist with the intact RT phase (Figure 5-3a, b). XPS shows the emergence of a new Br 3p$_{3/2}$ peak at a BE of 181.4 eV (Br-Au), due to partial Br-C dissociation (Figure 5-3c). We infer that the new arrangements are produced by the presence of partially debrominated monomers and Br atoms that locally perturb the previous self-assembled structures. As the temperature increases, the Br-Au peak grows at the expense of the Br-C signal, while Br progressively desorbs leaving the surface bromine-free at 400 °C (Figure 5-3c). After annealing for 30 minutes at 200 °C, this gradual dehalogenation results in the formation of disordered networks (Figure 5-2), with the C and S peaks shifting toward a lower BE (S 2p$_{3/2}$ at 163.5 eV, C 1s at 284.2 eV). These changes in the core levels can be ascribed to the increased electron density on the emitter atoms after binding to electropositive Au atoms.[30, 182]

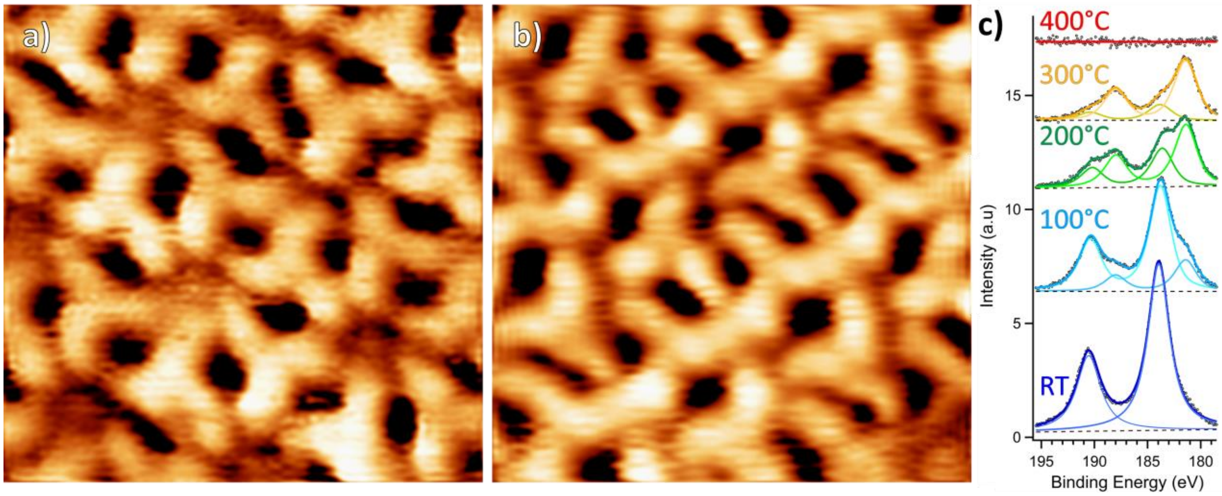

Figure 5-3. **a, b) 4.5×4.5 nm^2 STM images of TBTTB on Au(111) annealed @ 100 °C; the SAMNs formed at RT are partially warped upon annealing, and patches of hexagonal (a) or linear (b) domains are found on the surface (a: I_t = -0.29 nA ; V_t = -0.45 V; b: , I_t = -0.12 nA ; V_t = -0.31 V); c) Br 3p XPS spectra of 1 ML of TBTTB at various temperatures.**

OM networks were further investigated by direct deposition on a surface held at 200 °C. While XPS shows no chemical differences from a sample dosed at RT and annealed to 200 °C, the STM images reveal striking differences, with domains of well-ordered morphologies (Figure 5-4a). When dosed on a heated surface (200 °C), the dehalogenated molecules do not react with their immediate neighbors but possess sufficient thermal energy and time to diffuse to an optimal conformation, permitting the formation of a low-density hexagonal structure. This observation is consistent with previous work[113] for the Ullmann reaction of dibromo-*m*-terphenyl on Cu, where the formation of macrocycles was favoured by low deposition rates.

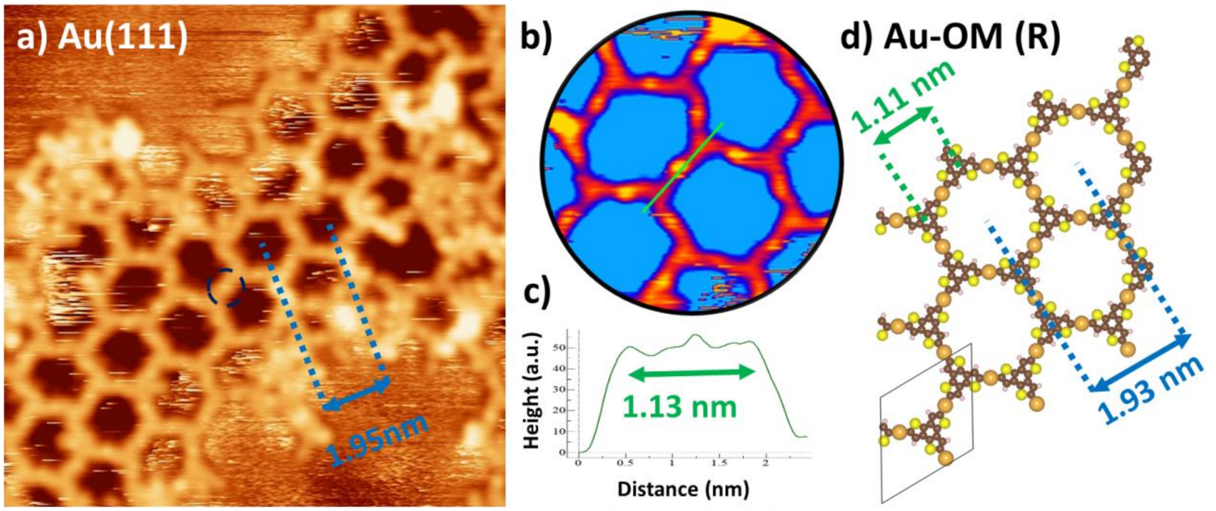

Figure 5-4. a) 15×15 nm^2 STM images of TBTTB deposited on a heated Au(111) surface kept at 200 °C, the average center-to-center distance is reported, I_t = 0.23 nA ; V_t = 0.97 V); b) DFT calculated structure of dehalogenated R- TBTTB molecules forming a 2D Au-OM structure; the evaluated center-to-center distance between two hexagons is 1.935±0.005 nm; the unit cell dimensions are: a = 19.30 Å, b = 19.37 Å, c = 30.00 Å, with a 60° angle between a and b.

DFT calculations were performed to simulate the observed OM hexagonal phase. The center-to-center distance measured in STM images (1.95±0.10 nm) is in agreement with a calculated OM structure (1.93 nm, Figure 5-4b), and is considerably larger than expected for a polymer structure (1.48 nm). The STM images also exhibit bright spots between every vertex (Figure 5-4b), attributed to a bridging Au atom. Post-annealing at various temperatures up to 400 °C (or direct deposition at 300 °C) does not further improve the order of the OM phase, but instead produces a disordered phase (Figure 5-2, STM red inset). The XPS spectra show a shift toward higher BE, *i.e.* 163.3 eV for S $2p_{3/2}$ and 284.4 eV for C 1s, consistent with the expected depletion of C-Au and formation of C-C bonds.[30] However, the simultaneous appearance of the Au-related

S $2p_{3/2}$ peak at 161.8 eV suggests that a fraction of the thiophene rings are open. By comparing the size of the two S 2p components, we estimate that a 10% of the thiophenes present broken C-S bonds. Moreover, there is also an overall decrease of both C 1s and S 2p peaks areas as the annealing temperature increases, suggesting that even more molecule may have broken and desorbed from the surface.

5.2.2 TBTTB on Ag(111)

Deposition of TBTTB on silver at RT immediately yields an OM network (Figure 5-5, STM blue inset) composed of both open and closed polygons, with 4 to 8 vertices and irregular shapes. The order of the molecular phase increases with annealing until it forms a hexagonal closed structure at temperatures higher than 200 °C (Figure 5-5, STM green inset).

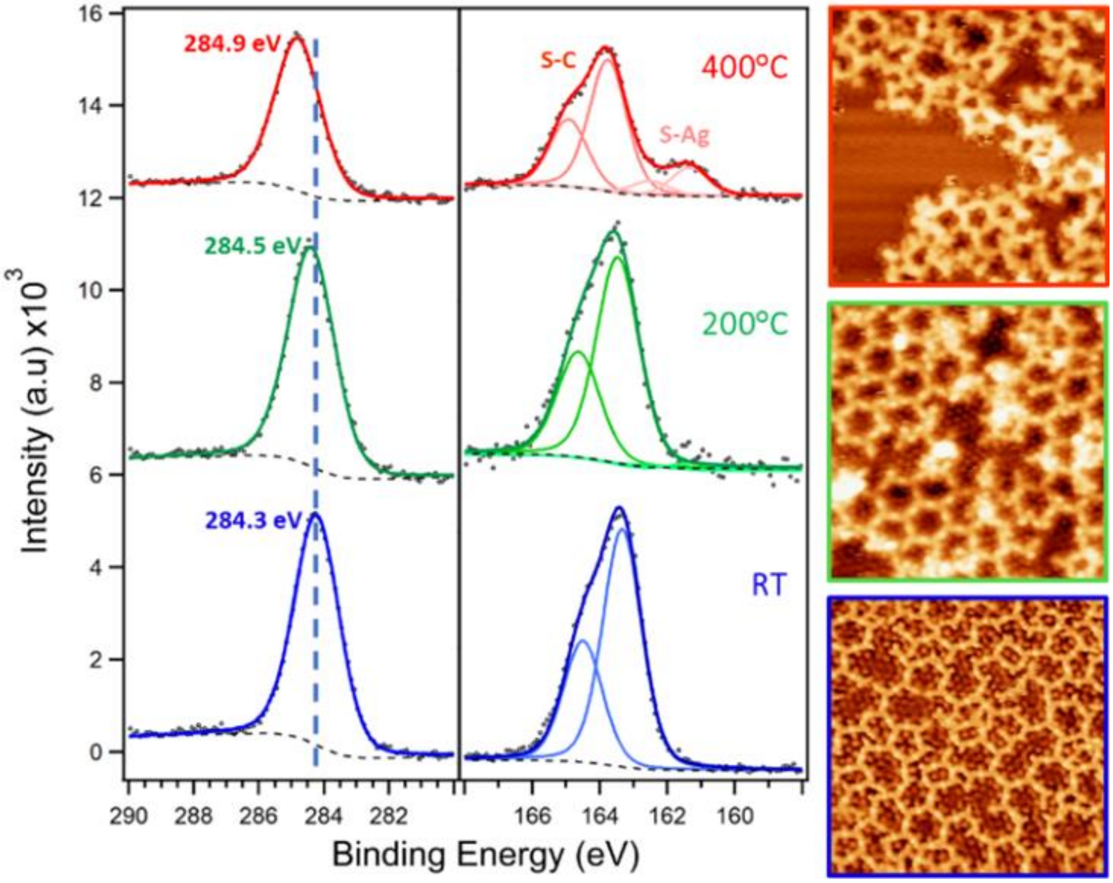

Figure 5-5. **STM images and XPS C 1s and S 2p spectra (left and middle panels) of TBTTB deposited on Ag(111) at RT (blue, $I_t = -0.48$ nA ; $V_t = -0.11$ V), and sequentially annealed to 200 °C (green, $I_t = -0.30$ nA ; $V_t = -1.40$ V) and 400 °C (red, $I_t = 0.30$ nA ; $V_t = -1.16$ V).**

This suggests that the dynamic nature of the C-Ag bond is an essential feature for the network's self-assembly and "self-repair",[102, 183] whereas this was not observed on gold, possibly because of the higher bond dissociation energy of the C-Au bond (1.39 eV for C-Ag vs 1.99 eV for C-Au).[204] This ordering does not occur in experiments starting at saturated coverage with subsequent annealing, presumably because molecular diffusion is hindered or even suppressed at higher densities. The Ag OM phase (Figure 5-5 green inset and Figure 5-6) is commensurate with the Ag(111) substrate with an overlayer matrix of $\left(4\sqrt{3}\times 4\sqrt{3}\right)R30°$ containing two TBTTB molecules in the unit cell (Figure 5-6c). The experimental pore-to-pore distance for a hexagonal network is measured to be 2.02±0.10 nm, in agreement with the calculated 2.05 nm distance of OM (Figure 5-6c). In contrast to the close-packed self-assembled molecular networks on Au(111), submolecular resolution reveals that the porous OM networks on silver are composed of a randomly distributed mixture of *R* and *S* enantiomers (Figure 5-7). This is consistent with the difference in chirality expression between close-packed and porous networks observed for the related TTB-tricarboxylic acid.[205]

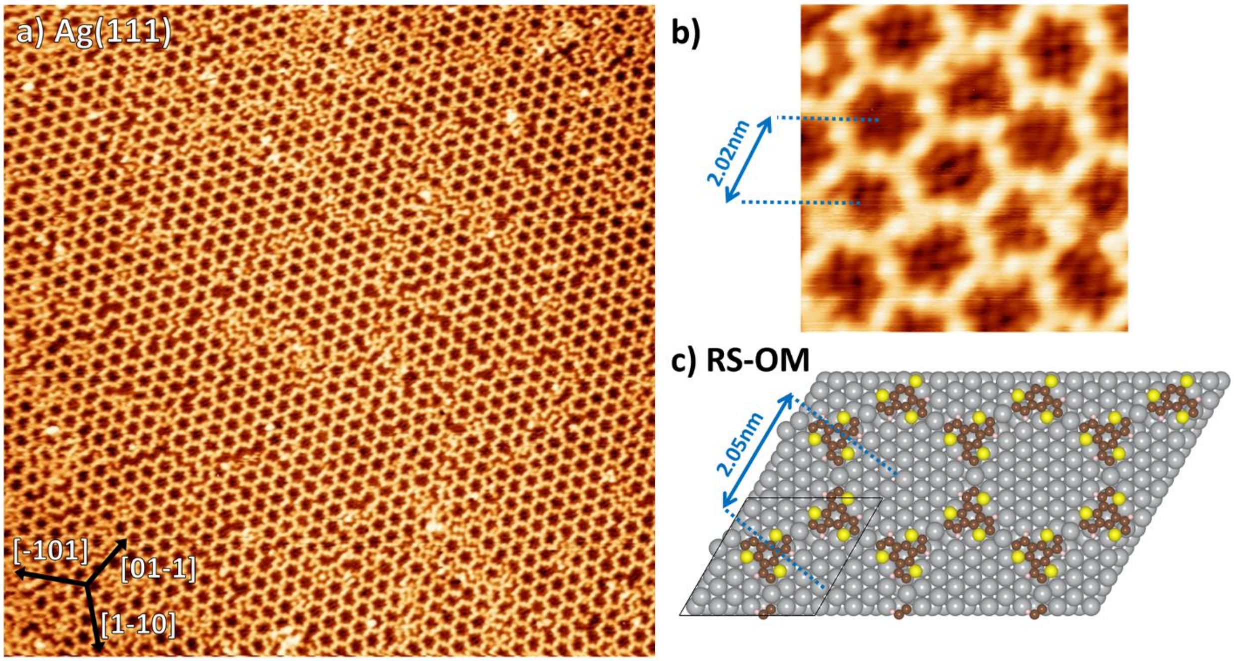

Figure 5-6 **a) 75×75 nm^2 STM images of TBTTB deposited on a heated Ag(111) surface kept at 200 °C (I_t = -0.27 nA ; V_t = -0.51 V). b) a 7×7 nm^2 zoom-in of (a), which exhibits the Br atoms decorating the molecular network (bright spots inside the hexagons) and the Ag adatoms between two molecules (bright spots between every connected molecules), therefore identifying the network as OM (I_t = -0.27 nA; V_t = -0.51 V). c) DFT optimized molecular structures for OM phase of TBTTB consisting of S and R enantiomer. Silver atoms are in grey, carbon in brown, sulphur in yellow and hydrogen in light pink.**

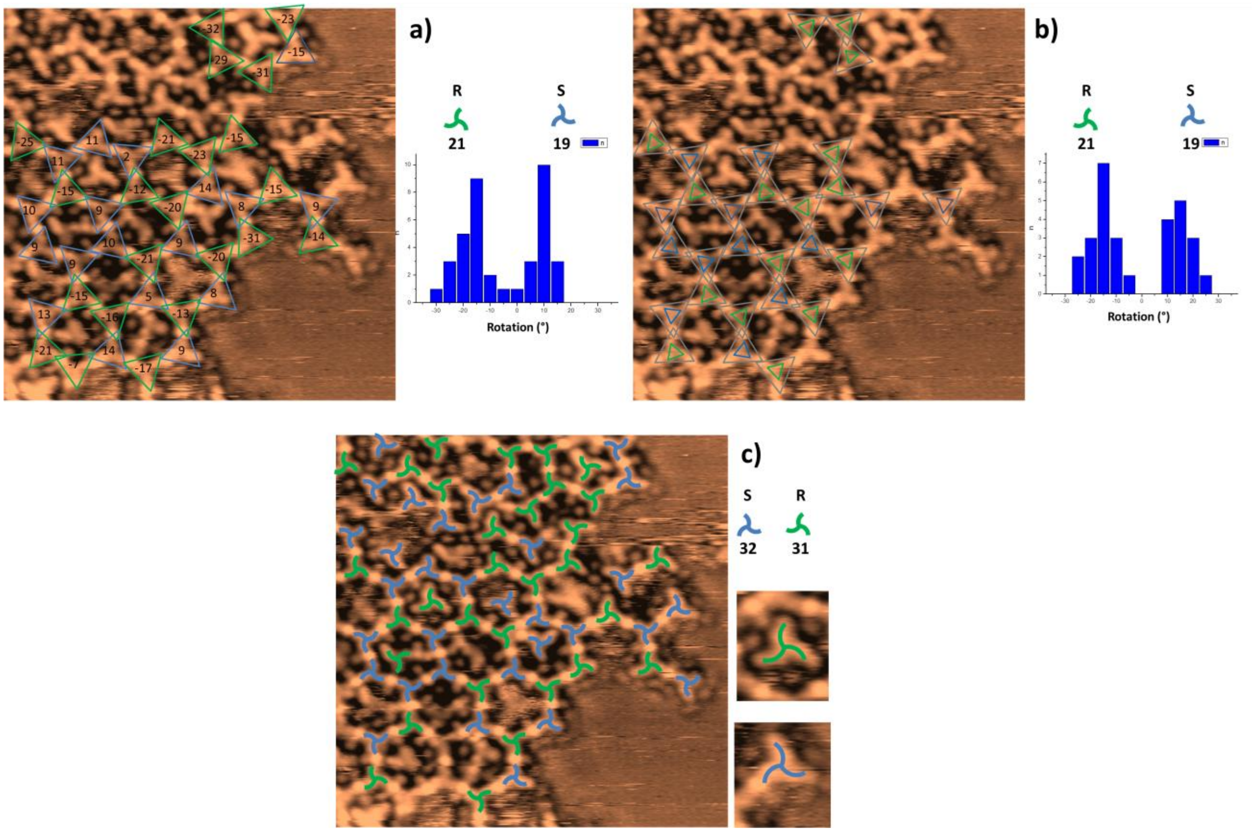

Figure 5-7 15×15 nm^2 STM image of TBTTB on Ag(111); in all the three cases, we attempted to identify the chirality of the molecules, using different approaches; the graphs in a, b report the angular differences evaluated in the relative figures, and in both cases we have a mixture of both the enantiomers; in the last case (c) two zoom-in of the image (1.5×1.5 nm^2) are reported.

In the case of self-assembly of intact molecules on Au, we assigned the chiral character to every molecule on the basis of its appearance in STM images. For the OM network, the molecules are dehalogenated and interact more strongly with the surface. Hence, the overall appearance in STM images can be related to the lattice site where the molecules are located; therefore, we used different procedures to identify the enantiomers, showed in Figure 5-7. In the first two we concentrated on the rotation between triangles overlapped on the STM observed moieties and the position of ordered hexagons or the Ag adatoms. Those two methods are coherent with a direct identification of the enantiomers (Figure 5-7c), as done in the Au case, which is therefore to be preferred. Annealing above 300 °C destroys the hexagonal structure, yielding a disordered network of distorted polygons (Figure 5-5, STM red inset) similar to the phase observed on gold. The 1.20±0.10 nm vertex-to-vertex distance of the OM phase is reduced to 0.90±0.10 nm after annealing to 400 °C (Figure 5-8a-d), consistent with the transformation of the C-Ag to C-C bonds.

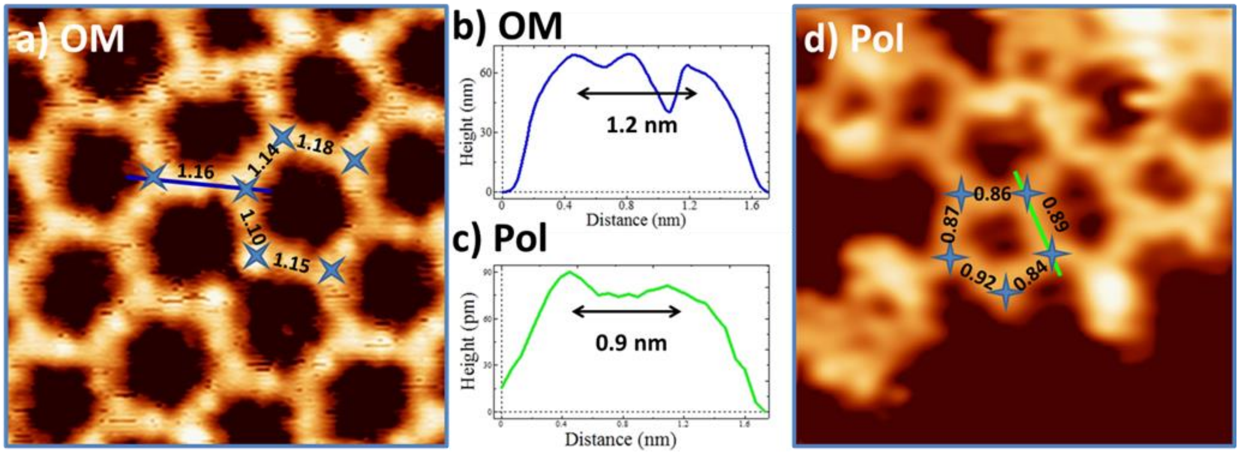

Figure 5-8. a) STM image of TBTTB dosed on Ag(111) at 200 °C, with various distances reported; b) line profile of the blue line in (a); c) line profile of the green line in (d); d) STM image of TBTTB dosed on Ag(111) at 300 °C with various distances reported.

XPS shows that the C1s peak shifts towards higher BE, as expected for the conversion from OM to polymer. The appearance of a second S 2p doublet at lower BE is attributed to the thiophene ring opening,[89] *via* breaking a C-S-C bond and formation of C-S-Ag bonds. This suggests that the polymerization reaction competes with desulphurization, which accounts for the lack of order in the polymer phase. Once again, we observe a decrease in the C 1s and S 2p peak intensities during annealing (between 200 °C and 400 °C), confirming that in addition to desulphurization, the molecular fragments desorb from the surface. To improve the domain size of the OM phase for such applications, we deposited TBTTB on a Ag(111) surface kept at 200 °C, which resulted in larger (>30 nm) hexagonally packed domains (Figure 5-6a). XPS shows no difference between depositions at 200 °C and RT depositions with post-annealing to the same temperature. These hexagonal domains obtained *via* hot-surface deposition still contain multiple line defects but exhibit much higher degree of order compared to the OM networks obtained at RT. The OM grown on Ag is more extended than the OM obtained on Au(111), similar to the observations by Bieri et al.,[108] who reported that high diffusivity of molecules and a low coupling probability are essential for achieving long-range ordered structures.

5.2.3 TBTTB on Cu(111)

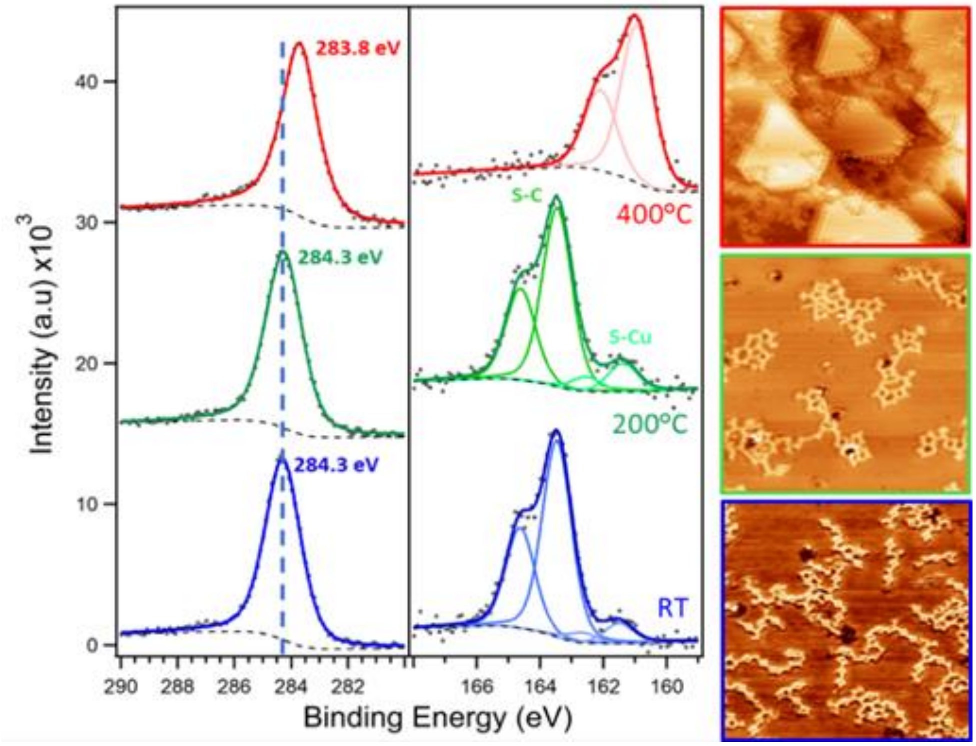

Figure 5-9 **STM images and XPS C 1s and S 2p spectra (left and middle panels) of TBTTB deposited on Cu(111) at RT (blue, I_t = -1.02 nA ; V_t = -1.50 V), and sequentially annealed to 200 °C (green, I_t = -0.53 nA ; V_t = -0.97 V) and 400 °C (red, I_t = -1.45 nA ; V_t = -0.98 V).**

Deposition of TBTTB on copper at RT results in branched OM chains on the surface (Figure 5-8). XPS analysis shows that the molecules are fully dehalogenated, and the C 1s peak position at 284.3 eV suggests the formation of the C-Cu bonds.[30] The observed chains are similar to those reported by Bieri *et al*.[108] for cyclohexa-*m*-phenylene on Cu(111). 2D networks were observed on gold and silver instead of the copper chain structure, presumably due to the faster diffusion of the molecules on the former substrates.[29] Annealing up to 200 °C increases the size of the molecular domains and the number of closed structures, but no long-range order is achieved (Figure 5-8). Further annealing above 200 °C does not improve the order. Instead, the STM contrast suggests fragmentation of the molecules (Figure 5-8, STM red inset). This is confirmed by the shift of S $2p_{3/2}$ peaks from 163.34 to 161.08 eV, characteristic of the copper-bonded sulphur. The sulphur atoms appear to be completely removed from the molecule, both decorating the step edges and forming a distinct 2×2 overlayer (Figure 5-8, STM red inset).[206] No long-range ordered structure was observed upon dosing TBTTB on a hot Cu(111) surface.

5.2.4 Surface comparison

The choice between the three coinage metals strongly affects the obtained result of TBTTB deposition. At RT we observe intact molecules on Au, partially dehalogenated on Ag and fully dehalogenated on Cu. This trend fits with the halogen affinity of the three surfaces: bond dissociation energies (BDEs) for Cu-Br, Ag-Br and Au-Br bonds are 331, 280 and 213 kJ/mol respectively.[204] The reported BDE values for Cu-S, Ag-S and Au-S bonds are 275, 217 and 254 kJ/mol respectively.[204] While the largest BDE of Cu-S bond is in line with the fastest thiophene ring opening on this surface, the second highest BDE belongs to Au-S bond, which does not explain the lowest reactivity observed on this surface. However, the BDE of a metal-sulfur bond relates to the reaction enthalpy, not the activation barrier. In practice, for a series of closely related reactions these two energies often correlate, under the Bell-Evans-Polanyi principle. This implies similar structure of the transition states, which is not always the case when the latter are formed by different types of atoms. The difference between Ag(111) and Au(111) - the two apparently similar surfaces (with almost the same nearest-neighbor distance, 2.88 and 2.89 A respectively), is well known and has been reported for the chemically related self-assembled monolayers of alkanethiols.[207] The high chemical ‘nobility’ of Au(111) comparing to all other metals is almost universally accepted, and is generally attributed to the high cohesive energy of the Au 5*d* states.[208] Although thermal annealing of the as-deposited layer permits to obtain an organometallic or polymeric domains regardless of the starting substrate, the nature of the surface is still decisive in determining the overall phase composition, as well as the molecular structure’s qualities. This is evident from the comparison in Figure 5-10, which shows the fraction of monomer in each state: intact, OM, polymer, broken. While for Ag it is possible to obtain a full OM layer stable in a wide temperature range (RT-200 °C), for Au these structures coexist with both intact and polymeric moieties. This is further reflected by the lack of long-range ordering in the TBTTB/Au annealed phase. For the polymeric phase, instead, the Au substrate is far more ideal, as it reaches a top efficiency of 90% at 400 °C, compared to 87% obtained on Ag at 350 °C and 64% on Cu at 300 °C. While these numbers seem to be in disagreement with the lack of hexagonal structures and the highly disordered polymeric overlayer obtained, it has to be taken in account that a 10% of broken thiophene rings corresponds to almost one defective TBTTB molecule over three.

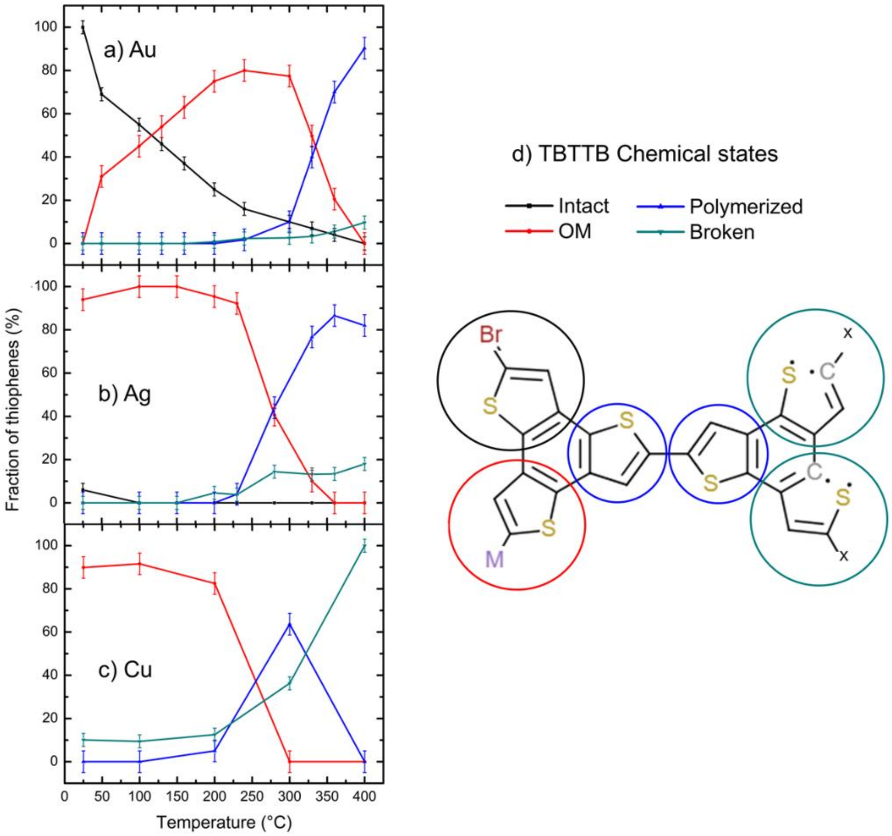

Figure 5-10 **Fraction of thiophenes in each observed chemical state for the three studied surfaces at each temperature. The values are extracted from the spectral decomposition of the C 1s, S 2p and Br 3p peaks, and do not consider molecular desorption.**

5.3 Conclusions and perspectives

The interactions between molecules and surfaces play a key role in steering many chemical phenomena. Our investigation of TBTTB deciphers the role of these interactions in four interweaved processes: (i) molecular self-assembly, (ii) carbon-halogen bond cleavage forming OM structures, (iii) carbon-carbon bond formation producing covalent polymers and (iv) carbon-sulfur bond cleavage which open the thiophene rings in the polymer. Deposition of the TBTTB monomer at RT resulted in non-covalent molecular networks on Au(111), OM structures on Ag(111) and partially broken molecules on Cu(111). We demonstrate that varying the substrate temperature *during the deposition* drives the growth process toward different final products. By depositing TBTTB on a hot surface, we formed an ordered 2D OM network on Au and a highly extended version of the same network on Ag. Further heating of the OM phase (>200 °C on Cu, >

250 °C on Ag, >300 °C on Au) triggers C-C coupling of the TTB core, but the polymerization cannot be completed because of concomitant C-S bond cleavage. The maximum efficiency of the C-C coupling peaks at ca. 90% for Au at 400 °C (Figure 5-10). Comparison with other thiophene-containing monomers suggests that the probability of side-reactions correlates with the S/C ratio, as expected from the statistical probability of desulphurization. Thus, in the case of tetrathienoanthracene (S/C = 0.182) small polymer domains could be prepared on Ag,[197] while for TTB (S/C = 0.25), even on the least reactive Au(111) surface, desulfurization is observed simultaneously with the polymerization. In addition, the non-fused thiophene rings might be more resistant to C-S scission due to a more significant aromatic stabilization, as observed for 3,4-(ethylenedioxy)thiophene on Ag.[209] Despite their lower prominence in the field of soluble (1D) conjugated polymers, O– and N– containing building blocks (furan, pyrrole, pyridine, *etc*) appear to present better alternatives for the design of surface-templated semiconducting materials, although ring opening reactions are still a problem when using highly reactive surfaces such as Cu.[210] On the other hand, this study marks the formation of long-range order OM phases, covering the whole surface. Such networks can be prepared at lower annealing temperature, where no desorption and ring-opening take place. The reaction efficiency on Ag is close to 100%, allowing to obtain extended domains larger than 20×20 nm^2 – a size comparable with the typical feature sizes of state-of-the-art silicon technology. Due to their high degree of order and promising electronic properties, such OM structures may find different applications in molecular recognition, 2D nanopatterning and non-linear optics.[211-212] The realization of these networks on the air-stable Au surface is a promising result, which opens new possibilities for their characterization outside the UHV, as well as a starting point for the development of OM-based devices.

6 DIFFERENT ROUTES FOR ON-SURFACE POLYMERIZATION: ACETYLENE-ACETYLENE COUPLING

Based on the work "*2D supramolecular network of dibenzonitrilediacetylene on Ag(111) designed by intermolecular hydrogen bonding*" published in Phys Chem Chem Phys, **2017**, *19*, 10602-10610. Contribution from: G. Galeotti, M. Ebrahimi, J. Lipton-Duffin,J. M. MacLeod, S. Rondeau-Gagné, J. -F. Morin and F. Rosei.[170] - where the author participated in all the experiments and data analysis, and wrote the manuscript.

6.1 Introduction

The balance between molecule-molecule and molecule-substrate interactions, which is strongly dependent on the molecules' functional groups, governs the physisorption and self-assembly of organic molecules at surfaces.[213] Intermolecular forces such as hydrogen bonding,[214-216] halogen bonding,[217-218] van der Waals (vdW) interactions,[219-221] and π-π stacking[222-223] can steer pattern formation in self-assembled molecular networks (SAMNs),[224] while dynamic self-healing (self-correction) mechanism which arises from the reversible nature of these non-covalent intermolecular forces allows for the formation of long-range ordered 2D structures.[225] These ordered SAMNs can be further transformed into polymers through diffusive processes, as explained in the previous chapter (3 to 5), but can also be used as templates to fabricate more robust structures held together by covalent bonds through topochemical polymerization which does not involves diffusion.[226-227] In such cases, the proximity and orientation required between the reactive centers of neighboring molecules may lead to 1D[17] and 2D[228-229] conjugated polymers on the surface. Various diacetylene derivatives containing long chains have been reported to form SAMNs with flat-lying and closely-packed lamella structures on different substrates such as MoS_2,[5, 230-231] highly oriented pyrolytic graphite (HOPG),[14, 232] and Au(111).[13] Subject to their arrangement, these molecules can undergo on-surface polymerization reactions induced by heat, UV light[14, 17, 228-229, 233-235] or by pulsing from an STM tip.[230-231, 236]

In this chapter we report the 2D self-assembly of 1,4-di(3-cyanophenyl)-1,3-butadiyne, here referred to as dibenzonitrile diacetylene (DBDA, Figure 6-1), on Ag(111). This molecule consists of two benzonitrile groups ($–C_6H_4–C≡N$) on each side of a diacetylene (–C≡C–C≡C–)

backbone. Diacetylene based materials have been widely studied for their chemical and astrochemical properties,[237-239] with potential applications varying from biomimetic membranes[240] to patterning of luminescent films,[241] while asymmetrical diphenyldiacetylene liquid crystals with non-polar end groups are a useful electro-optic medium to modulate infrared radiation and high-speed light shutters.[242-244] The free rotation of the benzonitrile group around the C–C *sigma* bond (attaching benzonitrile to diacetylene) in DBDA allows the molecule to exist as *cis* and *trans* stereoisomers at room temperature. The *trans* isomer is prochiral, leading to adsorption as two mirror-symmetric *R* and *S* forms, in addition to the *cis* structure (Figure 6-1). Transferring chirality from chiral or prochiral molecules to non-chiral surfaces has been widely studied as a means to impart selective characteristics to materials,[245-247] for various applications such as enantioselective catalysis, chiral separations, the pharmaceutical industry and non-linear optics.[247-248]

Diacetylene derivatives have been reported to form SAMNs on metallic surfaces.[17, 249] Oligophenyl (phenyl groups joined linearly by single covalent bonds) molecules with two terminal benzonitrile groups in the *para*[250-253] or *meta*[254-255] position form supramolecular structures. Particularly interesting is the study of *p*-terphenyl-*m*-dicarbonitrile[254] on Cu(111) and Ag(111), where the intermolecular interaction involving the terminal carbonitrile groups drives supramolecular ordering. Depending on molecular coverage, different phases – both planar and non-planar – are made by the molecule's three stereoisomers. The non-planar structure is driven by metal-organic coordination of the carbonitrile group with the surface, combined with π-π interactions between the phenyl groups of the adjacent standing-up molecules, with an average carbon-carbon distance of 3.92 Å between the interacting phenyls.[254] In our study, we substituted the terphenyl backbone with diphenyldiacetylene one, to study the difference in the self-assembly of the planar phase and to try to take advantage of the non-planar phase, were the acetylene groups would have been sufficiently close to undergo polymerization. Unfortunately, we were not able to obtain the non-planar assembly, but only planar self-assemblies driven by the terminal carbonitrile groups at the *meta* position of DBDA. STM images show that two polymorphs, assigned as *chevron* and *parallel* phase, are present simultaneously on the surface, in addition to a less often observed *butterfly* phase. Density functional theory (DFT) calculations illustrates that intermolecular interactions between the nitrile group and the phenyl ring of the neighboring molecule, control the formation of 2D SAMNs.

6.2 Results and discussion

6.2.1 STM data & DFT calculations

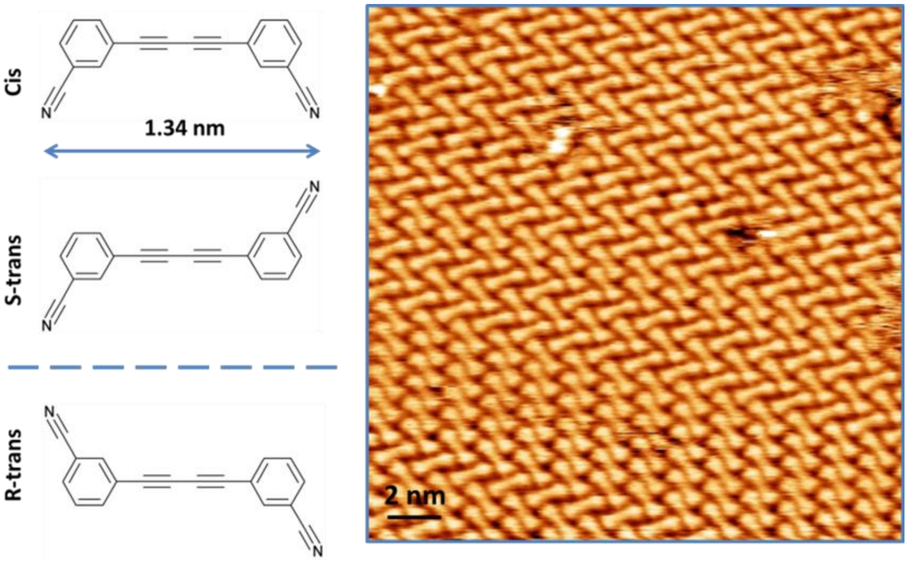

Figure 6-1. **(left) DBDA stereoisomers: cis, R-trans and S-trans. The reported N-to-N distance is retrieved from DFT calculation; (right) 20×20 nm^2 STM image of DBDA deposited on Ag(111) at RT.**

The three isomers of DBDA (*cis*, *R-trans*, and *S-trans*) are shown in Figure 6-1. The DFT calculated energy difference between *cis* and *trans* isomers was found to be < 0.2 meV (E_{trans} = -203.0030 eV and E_{cis} = -203.0032 eV), which is lower than the energy available to the molecules at RT. The natural composition of the dosed molecules is therefore expected to be 50% *cis* and 25% for each *trans* enantiomer. Nevertheless, the composition on the surface could be different depending on the interaction of different isomers with the substrate. At low coverage (< 0.5 ML), no molecule was identified by STM at RT, even if their presence was clearly confirmed by XPS (see Section 6.2.2), suggesting that the molecules diffuse rapidly on the surface. At sub-monolayer coverages (≥ 0.5 ML to < 1 ML), molecular islands are observed on small terraces, and at saturated coverage (1 ML), a complete monolayer of SAMNs is observed (Figure 6-1). The features contain two bright lobes, which we assign as a *bone* shape, with an end-to-end length of ~1.4 nm. The molecules self-assemble to form up to three distinct phases, identified as chevron, parallel and butterfly, which coexist on the surface (Figure 6-1 and Figure 6-2). These phases intermix seamlessly with each other, with no apparent deformation of the adjacent phase (Figure 6-1).

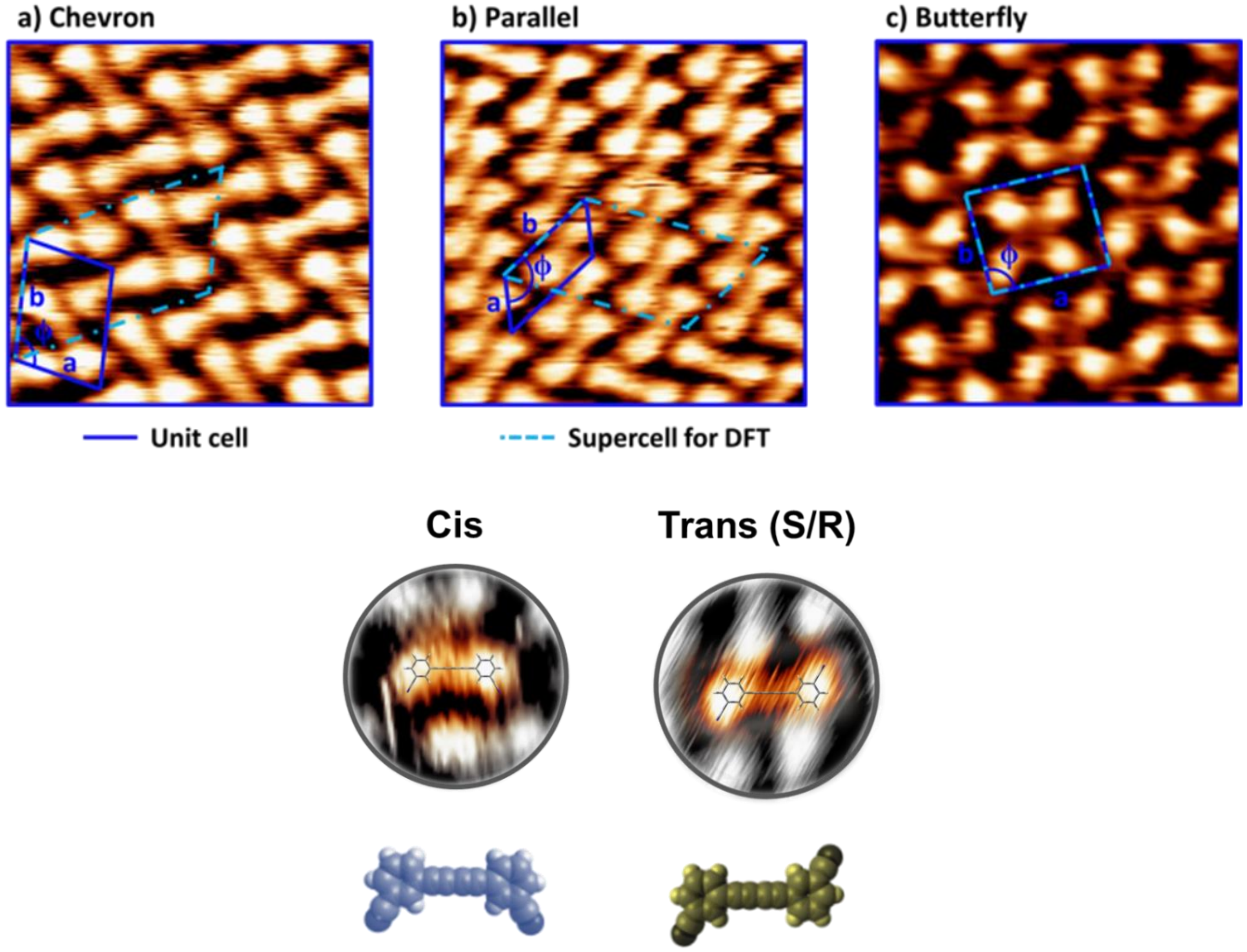

Figure 6-2. **a-c) 7×7 nm^2 STM images of DBDA on Ag(111) at RT, showing different self-assembled structures; the experimental unit cell (blue-continuous) and the supercell (light blue-dashed) for DFT calculations are shown, and the dimensions of the experimental unit cells are: a) Chevron phase: a = 2.0 nm, b = 2.3 nm, ϕ = 85°; b) Parallel phase: a = 1.0 nm, b = 2.1 nm, ϕ = 125°; c) Butterfly phase: 2.0 nm, b = 2.1 nm, ϕ = 90°; bottom: while *cis* and *trans* isomers appear differently in the STM images, the resolution was not sufficient to distinguish between the *R* and *S* enantiomers.**

The chevron and parallel phase coexisted on the surface in every STM measurement for each experiment. The butterfly phase was observed only occasionally (10-15% of the performed experiments). Although some insight into the isomeric identity (*cis* or *trans*) was obtained from the imaged features (Figure 6-2) the resolution offered by STM was not sufficient to discern the *R* and *S* enantiomers which constitute the phases. The analysis of the unit cell for each phase shows that while the parallel phase has a surface density of 0.58 molecules/nm^2, both the butterfly and the chevron phases have a slightly lower surface density of 0.48 molecules/nm^2. The angles and the dimensions of the unit cells for all the phases are reported in Figure 6-2. For the chevron and parallel phases shown in Figure 6-2, two-unit cells, a smaller (blue-continuous) and a bigger one (light blue-dashed), are displayed. For the butterfly phase, both cells are overlapped with the same dimensions. The dashed-line cells are the supercells used for DFT calculations. These large supercells, accommodating four molecules for chevron and parallel, and two molecules for butterfly, are used to account for every possible isomeric combination within the cell. Since the type of the isomers in the STM images could not be discerned, our calculations allow for more complex permutations of the three isomers that might initially be discerned by the STM data alone. The summary of the proposed structures for chevron, parallel, and butterfly motifs is presented in Figure 6-3.

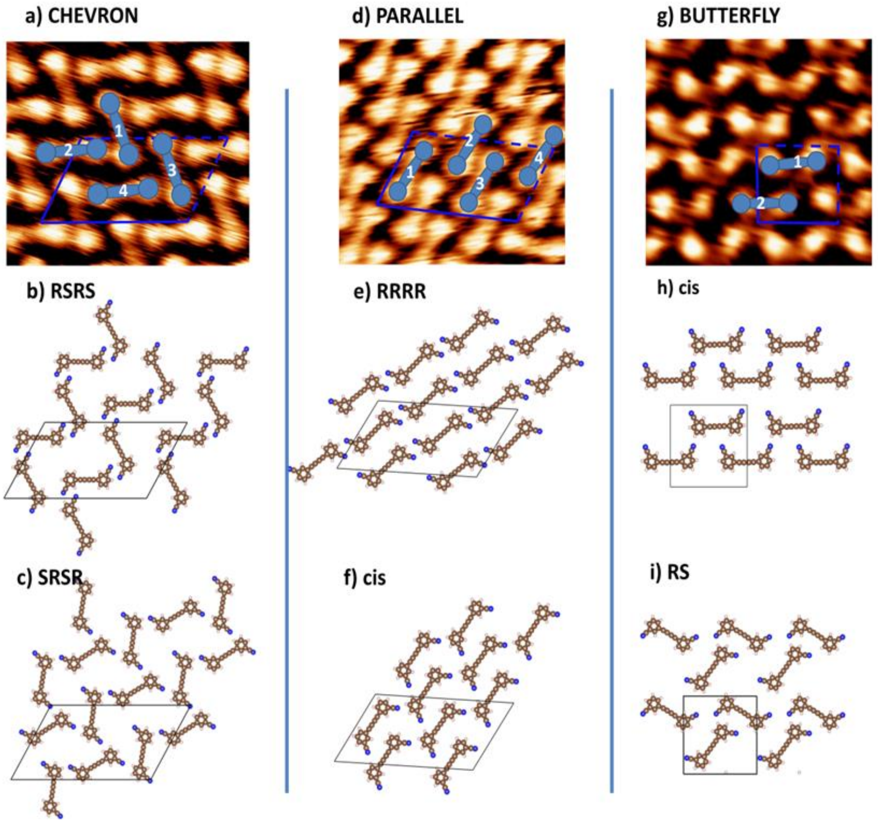

Figure 6-3. **First row- STM images of the chevron (a), parallel (d) and butterfly (g) phases, with the supercells used for the DFT calculation, and superimposed with the stylized (ball-and-stick) molecules corresponding to the molecular positions; Second row- the most energetically stable structures (b, e, h) obtained by DFT calculations for each phase. Third row- the second most energetically stable structures (f) and (i) for parallel and butterfly phases, respectively.**

The DBDA molecules were positioned in the locations (No. 1, 2, 3, 4) corresponding to the features imaged in STM. The structures that were too different from the experimentally observed STM images in terms of relative angle and location were not considered further, but the energies are still reported in Table 6-1. The self-assembled structures for the chevron phase reported in Figure 6-3b,c are *RSRS* and *SRSR.* As evidenced by their symmetry and shape (Figure 6-4), these structures resemble the observed SAMNs in the STM images. The cohesive energies reported in Table 6-1 for these chevron structures, composed of alternating *R* and *S* enantiomers, are -289.3 meV for *RSRS* and 230.2 meV for *SRSR*. Despite being among the second most energetically stable structures, the structures combined of *cis* and *trans* isomers do not fit the STM features (-256.5 meV and 232.0 meV, Figure 6-4c,d). In addition, in the STM images, the *bone*'s two bright lobes do not appear to be on the same side of the molecule, which is distinct from the butterfly phase appearance, interpreted as being composed of *cis* isomers only.

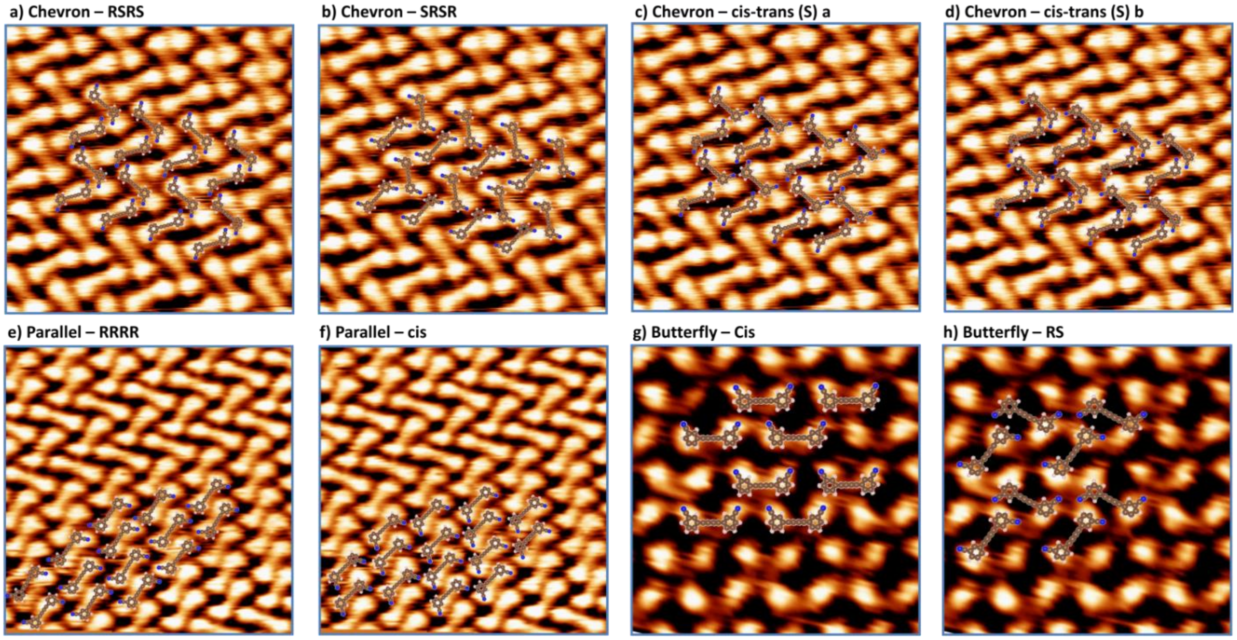

Figure 6-4. **The most energetically stable structures and/or the structures which fit the STM images, overlaid on their respective STM image for each phase. For the chevron phase, the four most energetically stable structures are shown (a-d), while two structures are displayed for parallel (e, f) and butterfly (g, h) phases.**

Table 6-1. Comparison between DFT calculated energy for the simulated chevron, parallel and butterfly phases - combinational conformations consisting of cis, R-trans, and S-trans DBDA. The most stable configuration for each structure is reported in bold. Results from three different DFT methods are reported here.

Simulated Phases	Structure	dE_{total} (eV) DFT-D3 [per molecule]
Chevron phase	***trans-RSRS***	**-1.1572[-0.2893]**
	trans-SRSR	-0.9208[-0.2302]
	trans-SSRR	-0.8745[-0.2186]
	trans-RRRR	-0.2597[-0.0649]
	trans-SRRS	-0.5068[-0.1267]
	cis	-0.8718[-0.2180]
	cis-trans(S) a	-0.9281[-0.2320]
	cis-trans(S) b	-1.0259[-0.2565]
Parallel phase	***trans-RRRR***	**-1.0880[-0.2720]**
	cis	-0.7924[-0.1981]
Butterfly phase	***cis***	**-0.2150[-0.1075]**
	trans	-0.1757[-0.0879]

A similar procedure was followed to identify the most stable arrangement of isomers in the parallel phase. The most energetically stable simulated self-assembled structures for this phase are reported in Figure 6-3e,f, and the relative energies are reported in Table 6-1. The STM images superimposed with the SAMNs calculated by DFT for all the phases are reported in Figure 6-4. The all-*trans* (*R*) parallel structure has a cohesive energy of -272.0 meV, while all-*cis* is 73.9 meV less stable (-198.1 meV). Similar to the chevron phase, the motif consisting of only-*trans* isomers produces the most stable configuration for the parallel phase. A complete enantiomeric separation is predicted for the parallel phase, with domains comprising *R*-only or *S*-only isomers. Both domains were simultaneously observed on the surface, sometimes forming alternating *R* and *S* stripes (Figure 6-5). Based on these energetic considerations, we propose that the chevron and parallel phases are exclusively composed of *trans* isomers, but the butterfly phase comprises *cis* isomers only.

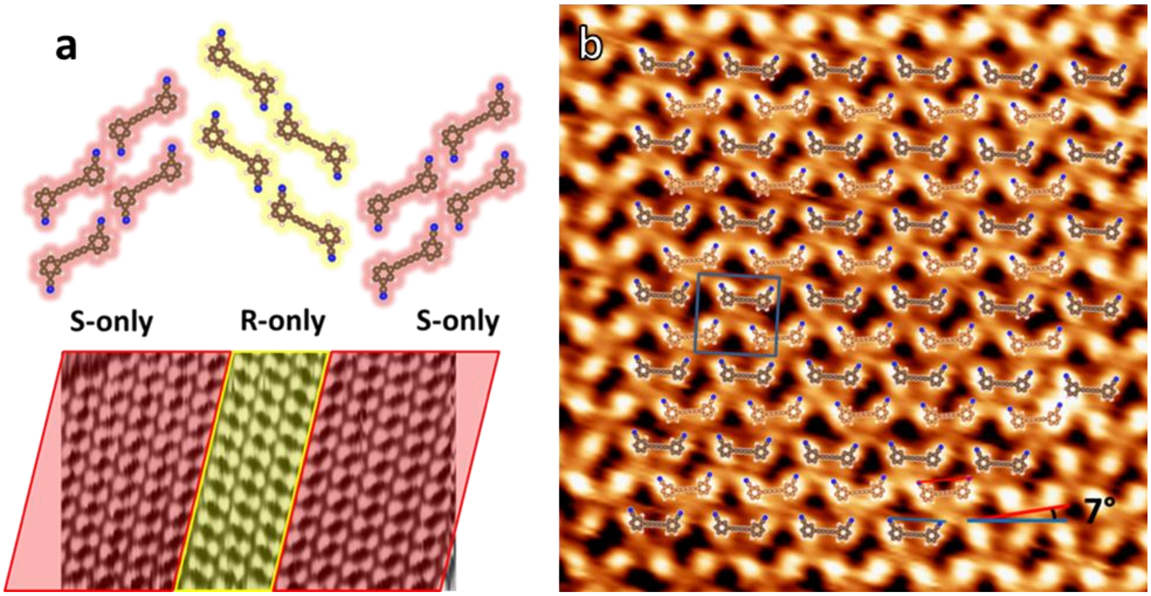

Figure 6-5. **a) 15×8 nm^2 STM image of DBDA on Ag(111) at RT; superimposed rhomboids shapes indicate the enantiomeric domains, red for S-only and yellow for R-only; b) 12×12 nm^2 STM image of DBDA on Ag(111) at RT; the angle between two adjacent molecular lines is 7°.**

This interpretation is supported by the appearance of the moieties in STM images, which show a *cis* molecular structure shape in the butterfly case (Figure 6-5). As shown in Figure 6-6, in all of the studied configurations (chevron, butterfly and parallel), two sets of intermolecular interactions between benzonitrile groups are predominant. In chevron and parallel phases, hydrogen bonding ($-CN\cdots H\text{-}C_6H_3$) stabilizes the SAMNs by having the $CN\cdots H$ distances of 2.37 Å and 2.63 Å, respectively (Figure 6-6). However, the $CN\cdots H$ bond lengths are different in the butterfly conformation, varying from 2.57 Å to 6.08 Å (Figure 6-6), which reduces the stability of the self-assembled network, as the equilibrium bond length for the $CN\cdots H$ distance lies within 2.29-2.35 Å for *trans* and 2.35-2.62 Å for *cis* isomers. This is consistent with previous studies reporting 2.3 Å[255] and 2.7 Å[256] for the $CN\cdots H$ distance. The variation in the $CN\cdots H$ distances of the butterfly unit cell is displayed as an asymmetry in the imaged features through the small 7° rotation (Figure 6-5) between the diacetylene backbones of the two molecules. This is shown in the DFT calculation by giving a less stable (-107.5 meV, Table 6-1) structure than either the chevron or parallel phase.

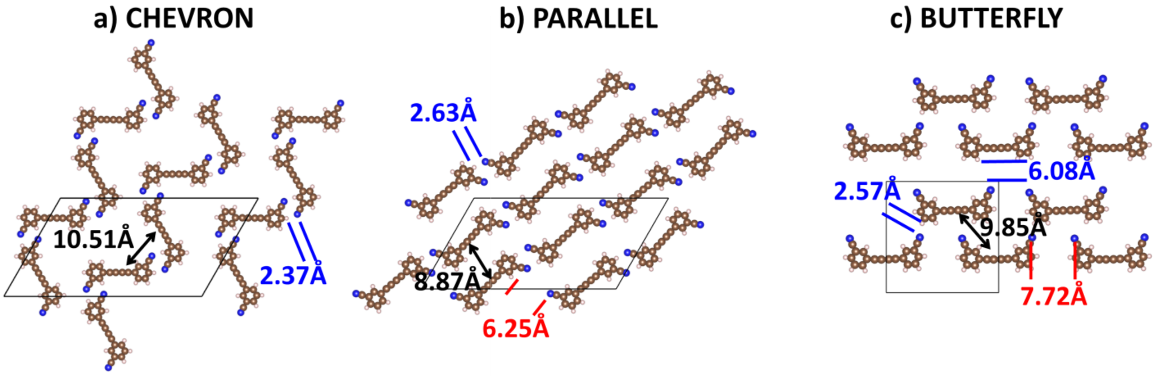

Figure 6-6. **The most energetically stable DFT-calculated structures for each phase; some distances are displayed for attractive hydrogen bonding (in blue), repulsive N···N (in red) and for acetylene-acetylene (in black) interaction; the acetylene groups are far apart in all the structures, hindering the possibility of topochemical polymerization.**

Although STM images show that the butterfly unit cell comprises two molecules with a 7°±2° rotation angle in between (Figure 6-5), the DFT calculation gives a more symmetrical structure, with only a small rotation angle of 2° between the molecules. Since the underlying Ag surface was not included in the DFT calculation, this difference likely results from a balance of molecule-substrate interactions.

6.2.2 XPS and Temperature-dependent multilayer stability

XPS measurements were performed to analyse the chemical state of the molecule upon adsorption. Experimental data, together with a spectral analysis of the C 1s region, are reported in Figure 6-7a. Four different C 1s components are identified, assigned to carbon in different chemical states. These peaks are attributed to the acetylene backbone, five carbons of the phenyl ring, the –CN group and the one carbon from the phenyl ring bound to nitrile, with a normalized area of 21%, 56%, 12% and 11% ± 2% respectively. The ratio between these components' normalized area is consistent with what is expected for intact molecules. The peak positions are assigned at 286.9 eV (–**C**N), 286.2 eV (**C**-CN), 285.3 eV (phenyl group), and 284.6 eV (diacetylene –**C**≡**C**–**C**≡**C**– backbone).[257] Adsorbing more than 1 ML results in a more intense peak showing a shift of the C 1s peak toward higher BE (from 285.2 to 285.6 eV) which is known as electrostatic effect observed in adsorbed multilayers.[30-31, 258] A similar shift toward higher BE was also observed for the N 1s peak, as shown in Figure 6-7b, which reports the N 1s spectra with increasing coverage of DBDA.

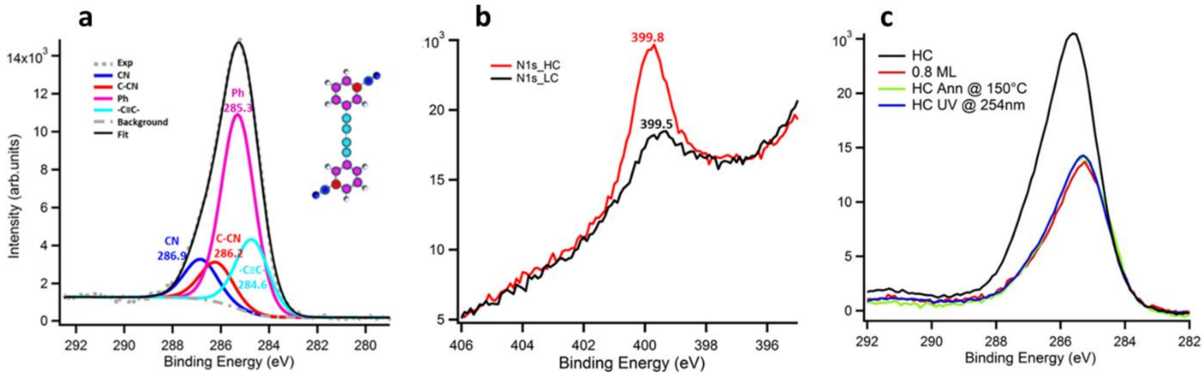

Figure 6-7. **a) XPS C 1s spectra of DBDA on Ag(111); the C 1s spectrum was fitted with four components, presented in the same color as their respective carbon atoms in the molecular scheme; both peak positions and relative percentage are consistent with intact molecules; b) N 1s spectra of sequential dosing of DBDA on Ag(111), black curve is relative to a low coverage, red curve to a multilayer; c) XPS C 1s spectra of DBDA on Ag(111); black and red spectra are for the high (HC, multilayer) and sub-monolayer (0.8 ML) coverages, respectively; green correspond to HC coverage annealed to 150 °C for 15 min, blue to HC exposed to UV light @ 254 nm for 180 min; their similarity to the 0.8 ML coverage, suggests that desorption has taken place.**

At low coverage, the main peak is located at 399.5 eV, which shifts toward a higher BE at 399.8 eV at high coverage. XPS measurements of a molecule with the same terminal *m*-cyanophenyls group[254] showed the peak at 399.5 eV for the sub-monolayer coverages (up to 0.7 ML). In their work, Marschall *et al.*[254] assigned this peak to a physisorbed state, with N atoms interacting with neighboring molecules only. Increasing the molecular coverage resulted in the growth of two additional peaks: one at 398.4 eV, whose intensity increased by increasing the coverage up to 1.5 ML, and one at 400.2 eV, which appeared only at the coverage above 2 ML. They assigned the 398.4 eV peak to N atoms interacting with the surface, and the 400.2 eV peak to the molecules not in contact with the surface. In our study, no peak is observed around 398.4 eV, suggesting that dosing more molecules does not result in a different geometry in which the molecules stand-up on the surface with their N atoms interacting directly with surface atoms. The multilayer structure is highly unstable, and annealing at 150 °C or UV irradiation led to desorption (the case for a starting coverage of ∼2 ML is reported in Figure 6-7c). This instability is further confirmed by an experiment in which a sample with a 2 ML coverage was kept for 24 hours at RT under UHV conditions, resulting in ∼50% molecular desorption. Under the same condition, a less drastic yet similar desorption of ∼10-15% was observed for a lower coverage of ≤ 1 ML. DFT calculations were used to optimize the adsorption of a single molecule on Ag(111), yielding an adsorption energy of -1.86 eV, which is in line with the values reported for the molecules with similar functional groups, such as phenylacetylene on Au(100)[259] and Si(100)[260] (-1.58 eV and -1.57 eV respectively), and scalable with the -0.72 eV obtained for benzene on Ag(111).[261] The adsorption energy of a molecule consisting of one central phenyl ring derived with three acetyl groups was calculated to vary from -1.19 eV to -1.40 for different configurations.[262] Therefore, together with our observation during STM measurements at low coverage which suggests that the molecules are highly diffusive on the surface, we believe that the described desorption is a kinetically controlled phenomenon.

6.2.3 Hydrogen bonding hinders topochemical polymerization on the surface

Molecules with conjugated triple bonds such as diacetylene derivatives are known to undergo solid-state topochemical polymerization upon UV or X-ray irradiation or annealing, to form conjugated polymers.[263-265] The correct alignment of the conjugated triple bonds is a prerequisite for polymerization, and is controlled through the intermolecular forces which stabilize the assembly of the diacetylene molecules. In depth studies of a series of diphenyldiacetylene derivatives[263] showed that the nature and relative position of the substituents is essential in this context. As such, being positioned at *meta* gave higher reaction yield than *ortho,* while *para* showed no reactivity. The free rotation of the single bond which connects the substituents to the phenyl ring offers the essential tilting which is required to bring the adjacent diacetylene close to each other to undergo a successive 1,4-addition polymerization reaction. If the molecular assemblies do not meet these requirements, the topochemical polymerization would not occur except under extreme conditions, for example diphenyldiacetylene polymerizes only at elevated pressure (0.86 GPa) and temperature (>230 °C) under solid-state conditions.[266-267] The solid-state topochemical polymerization of diacetylene derivatives can occur at temperatures as low as 50-80 °C[268] without any catalyst, with a yield up to nearly 100%. This is the original motivation to translate this classic reaction towards surface-confined polymerization, with the goal to make extended 2D conjugated polymers on surfaces[15, 228-229, 269-270]

The packaging criteria for obtaining large polymeric crystals of diacetylene monomers are quite stringent.[271] The best molecular stacking for the polymerization of diacetylene is d = 3.8-6.8

Å with an angle of γ = 30-65° (with d the distance between the centers of the diacetylene chains and γ the angle between this d vector and the diacetylene rod). Another relevant example pertains to diacetylene backbones containing alkanol (-R-OH) groups which form two polymorphs, parallel and herringbone phases, on HOPG at the solid-liquid interface.[272] The parallel arrangement showed a higher efficiency for the photo-induced polymerization reaction than the herringbone structure due to a shorter distance between the neighboring diacetylene groups (~3.9 Å *vs* 5.8 Å).[273] Our XPS data suggests that no diacetylene polymerization occurs for DBDA on Ag(111), because the line-shape and position of the C 1s peak, after UV irradiation or annealing, matches with that of as dosed DBDA, while a polymerization would have shifted the whole peak toward higher BE and reduced its width, due to a reduction of *sp* C≡C bonds in favor of sp^2 C=C bonds, located at higher BE[274] (285.0 eV for polyacetylene and polyphenylacetylene).[275,276] Our fitted C 1s component assigned to *sp* acetyl carbons (284.6 eV, Figure 6-7a) is close to the unreacted acetyl group of phenylacetylene, mostly reported at 284.7-285.0 eV on different substrates.[274, 277-279] The sp^2 C=C carbon, if formed, would be close to the component assigned to the phenyl whose two derived carbonitrile groups have also made it move towards a slightly higher BE (at 285.3 eV, Figure 6-7) than previously reported for PA[274] and benzene.[280]

We conclude that polymerization does not occur because the molecular packing on the surface does not fulfil the requirements of the topochemical reaction. Our STM images and DFT simulations illustrate that the diacetylene-diacetylene distance in the three observed supramolecular networks, 10.51 Å for the chevron, 8.87 Å for the parallel and 9.85 Å for the butterfly, was much higher than the proximity requirement for topochemical polymerization[271] (Figure 6-6). This is caused by the stiff bonds (due to a series of *sp* and sp^2 orbitals involved) which attach the nitrile, phenyl, and diacetylene to each other, which enforces a planar structure. The three isomers of DBDA are constrained to only rotate in plane rather than being out-of-plane or tilting the nitrile groups. Our observation, therefore, suggests that being locked in a hydrogen bonded assembly prevents the neighboring diacetylene groups of the obtained SAMNs from being sufficiently close to interact and form a polymer – a common reaction that has been widely studied by topochemical solid-state and surface-mediated polymerization.[17, 226, 229]

6.3 Conclusions and Perspectives

We reported the self-assembly of DBDA molecules on Ag(111), forming long range ordered patterns at RT. The results show the coexistence of all the possible molecular isomers: *cis*, *R-trans* and *S-trans*, assembled in distinctive networks, chevron, parallel and butterfly. While the chevron is formed by an ordered alternation of *R* and *S* isomers (racemic mixture), the other two phases incorporate isomerically pure constituents. The parallel phase consists of an enantiomeric *R* or *S* domain, while the butterfly is formed by the *cis* isomers only. The butterfly phase was less frequently observed compared to the others, and this is attributed to a lower stability of the network. Experimental observations are consistent with DFT calculations, which suggest a more energetically stable supramolecular network for the chevron and parallel phases. The relative position of the two nitrile groups, which determines the *cis* or *trans* geometry, steers the observed SAMN polymorphs *via* hydrogen bonding. The reduction in intensity of the C 1s peak after annealing (or exposing to UV) the adsorbed molecules without any further change in their chemical states, indicates that the molecules are more prone to desorption than reaction with the surface or with each other. This is due to the fact that the molecular arrangement of DBDA does not fulfil the requirements for topochemical polymerization, as is observed for diacetylene-derivatives under solid-state or surface-confined polymerization. A careful design of the supramolecular networks driven by intermolecular hydrogen bonding which can offer the proper orientation and distance between the diacetylene groups could potentially be used to make 2D conjugated surface-confined polymers.

7 CONCLUSIONS AND PERSPECTIVES

The study of the on-surface realization of organic nanostructures on metallic substrates has been performed using a combination of STM and various photoemission spectroscopy techniques, such as XPS, fast-XPS, ARPES and NEXAFS. The acquired experimental data have often been supported by modeling with DFT. All studies have been performed in UHV conditions, by dosing the precursors on metallic surfaces using Knudsen cell evaporators or through leak valves. The formation of nanostructures, from molecular self-assembly to organometallic intermediates and conjugated polymers, has been followed and analysed. Two different routes have been exploited to realize such covalent nanostructures: Ullmann coupling and diacetylene polymerization. In both cases the necessary conditions and parameters to achieve a succesful polymerization have been thoroughly studied, with the main focus have been to understand the chemical and physical principles that control the reaction, rather than focusing on the final structure.

1,4-dihalobenzenes: Depending on the specific physical and chemical properties under analysis, different molecules have been studied. Most of the thesis (Chapters 3-4) relates to the study of the Ullmann coupling of simple 1,4-dihalobenzenes (Figure 2-12), which have been used to identify and clarify the effect of coverage and the halogen, while at the same time improving our understanding of the reaction mechanism and modeling the polymerization reaction.

Effect of the coverage: dBB was used to explore the effect of molecular coverage and showed that it plays a pivotal role, leading to the formation of different self-assembled nanostructures (Figure 3-6 and Figure 3-9) that could follow different reaction pathways (Figure 3-7). Dosing 1 ML of dBB on Cu(110) at RT yields a so-called chevron phase made up of short OM chains, which react after annealing to form long-range ordered polymers along the [1-1±2] directions. Lower coverage yields longer linear OM chains, which counterintuitively form on-average shorter polymers along the [1-1 0] direction (Figure 3-6). By carefully studying this reaction process, two structurally distinct intermediate phases are observed. Prior to the polymerization, we observed that the linear OM chains phase converts into a 2D OM chessboard-like structure (Figure 3-9). This phase is observed during annealing of the surface at temperatures between 145 °C and 200 °C at sub-monolayer surface coverage (≤ 0.6 ML, Figure 3-8). By combining STM observations with DFT calculations, it was possible to describe the structural details of the phase, showing that it consists of phenyls bridging four-atom clusters of Cu adatoms (Figure 3-11). Annealing this phase yields polymers along the [1-1 0] direction. These results demonstrate that even for simple molecules – such as our dBB – on-surface Ullmann coupling can follow multiple pathways.

Reaction mechanism: For both cases – *i.e.* chevron to polymer or 2D OM to polymers – we provided a mechanistic picture of the surface-confined dehalogenative polymerization (Figure 3-4). We discovered that the fast-XPS data were accurately described by a kinetic model where the coupling probability between the monomers was low (Figure 3-4b, equations 3-2 to 3-4). We found that the reaction follows a nucleation-and-growth behavior preceded by the formation of a transient state (Figure 3-4a). The activation barriers for these processes were found to be 1.310±0.005 eV and 1.090±0.005 eV for the nucleation (dimerization) and growth respectively. The activation energies show that the growth of a polymer from an existing nucleus (*i.e.* a dimer) requires substantially less energy than creating the nucleus. These results suggest that the polymerization reaction is not *topotactic*, but instead is a diffusion-controlled process.

Effect of the halogen: Surprisingly, despite the large number of studies of Ullmann coupling, the effects of the halogen by-products had not been explored in detail at the beginning of my thesis. Therefore, we decided to study the role of the halogen in the Ullmann polymerization of five 1,4-dihalobenzene precursors containing Cl, Br, and I on Cu(110) using combined fast-XPS, NEXAFS and STM analysis (Chapter 4). We found that the nature of the halogen atom affects the temperature of the dehalogenation step (Figure 4-4). The halogen was also found to drive the geometry of the subsequent OM structures obtained at RT as well as the orientation of the polymers (Figure 4-6). We observed that *i.* the length of the OM chains depends on the carbon–halogen bond dissociation energy, and *ii.* the resultant OM structures for precursors containing Br and Cl (dBB, dCB, BCB, BIB) are aligned along the [1-1±1] directions, as opposed to an alignment along the [1-1±2] directions for precursors containing only iodine (dIB) (Figure 4-6 and Figure 4-7). By recording fast-XPS maps we showed that the OM structures followed different reaction kinetics, with dIB exhibiting a gradual transition, while the other precursors underwent a sudden transition into PPP polymers (Figure 4-5). The temperature range of the polymerization was also found to be affected by the type of halogen (Table 4-1), and to be qualitatively correlated to the halogen's diffusion energy (Figure 4-11). Our systematic study showed that the halogen is not merely a reaction by-product, but rather an important parameter governing the on-surface Ullmann polymerization reaction, that needs to be considered in the *a priori* design of precursors.

Long-range ordered 2D networks: This study of the basic reaction parameters and the effort to unveil the funadamental chemical-physical principles that underlie the Ullmann reaction was seminal to the quest of realizing long-range ordered 2D nanostructures, the goal of this thesis. We therefore undertook the study of molecules containing more than two halogens, which are able to form two-dimensional networks. Specifically, by investigating the reaction of the tridentate tribromoterthienobenzene (TBTTB, Figure 2-13 and Chapter 5) we achieved the realization of ordered covalent 2D OM polymers on a gold surface (Figure 5-4). 2D OM polymers on a gold have rarely been observed, only short linear OM chains. Furthermore, by dosing TBTTB onto an hot Ag(111) surface kept at 200 °C (Figure 5-6), we obtained long-range ordered 2D networks with domains greater than 30×30 nm^2, compatible with the current technology size for a FET. This hot dosing approach could be further exploited to finally achieve the systematic production of extended graphene-like materials.

Effect of the substrate & introduction of heteroatoms: The study of TBTTB also provided additional information on the importance of the composition of the building block and its interaction with the underlying substrate (Figure 5-2, Figure 5-5 and Figure 5-9), and therefore on the importance of the choice of the “molecule + substrate” system when embarking on this kind of research. It also remarked that, while heteroatoms are indeed key elements to modify the properties of the final product, they also add additional side effects that can be difficult to *a priori* identify and control. In this case, thiophene can undergo ring-opening to form S-M bonds rather than the desired C-C bonds, reducing the overall order and quality of the obtained polymeric networks (Figure 5-10).

Self-assembly vs polymerization: while being the most common – and successful – on-surface reaction to obtain a conjugated polymer, Ullmann coupling is not the only feasible route. In particular, we were interested in exploring reactions with a different mechanism and initiation method. We chose to explore diacetylene polymerization, a reaction that can easily be initiated by UV exposure. It is a non-diffusive reaction, *i.e.* the molecules self-assemble and react without further diffusion, and can be triggered only if certain conditions are fulfilled. With these things in mind, we studied DBDA, which is a prochiral precursor (Figure 2-14), on Ag(111). After dosing at RT, long range ordered self-assembled patterns are observed on the Ag(111) surface (Figure 6-1). Our results show the coexistence of all the possible molecular isomers: *cis*, *R-trans* and *S-trans*, assembled in distinctive networks, labelled as chevron, parallel and butterfly, respectively

(Figure 6-2). One of these, the chevron, was a racemic mixture of *R* and *S* isomers, while the others were isomerically pure, containing either *R* or *S* (parallel) or *cis* isomers only (butterfly). The self-assembly was also studied using DFT simulations, which reproduced the observed phases, with the chevron and parallel phases determined to be the energetically more stable supramolecular networks, consistent with our STM observations, and the butterfly network indicated as a minority phase (Figure 6-3, Table 6-1). The observed SAMN polymorphs are due to multiple isoenergetic assemblies, all steered *via* hydrogen bonding (Figure 6-6). Unfortunately, UV irradiation or annealing did not produce intramolecular C-C coupling, but instead the molecules were more prone to desorb than react, as indicated by a reduction in intensity of the C 1s peak (Figure 6-7). This study showed that careful design of the supramolecular networks – driven by intermolecular hydrogen bonding – is necessary to obtain the proper orientation and distance between the diacetylene group to trigger polymerization and the formation of 2D conjugated surface-confined polymers.

7.1 Future studies

While this thesis' work has provided insight into some chemical and physical properties of the on-surface Ullmann reaction, the main goal of the project, presented in Figure 1-1 of this thesis, has not yet been achieved. As a reminder, the key steps are to: *i.* understand the on-surface Ullmann reaction, in particular the role of the reaction parameters, *ii.* grow long-range ordered polymeric structures and *iii.* to detach the 2D polymer from the surface and realize this material in a device.

The first step proved to be more complex than expected, however it resulted in interesting discoveries, various publications and an advancement in our understanding of the behavior of small molecules on a surface. The second step was only partially fulfilled, and while long-range ordered structures were realized, they were OM polymers instead of having pure C-C bonds along the backbone. Nevertheless, while conducting our research we improved our understanding and control over the production of large 2D networks, in particular by developing the approach of molecular deposition on an hot surface, as demonstrated by the results with the molecule presented in Figure 2-13a. The OM structures show long-range order, covering the whole surface, with extended domains larger than 30×30 nm^2 on average (Figure 5-6). This domain size is greater than current transistor dimensions.

The inclusion of the metal atoms into the covalent network can lower the material bandgap, as confirmed by preliminary DFT calculations, which yield a HOMO-LUMO energy gap of ≈ 0.2 eV for the TBTTB-OM network (Figure 7-1), in agreement with similar OM systems.[281] This means that such OM structures could be exploited for technological applications, due to their high degree of order and electronic properties. Furthermore, the 2D OM structure is a metal-organic framework (MOF) which could be exploited as a robust porous hexagonal structure for applications in molecular recognition, 2D nanopatterning and non-linear optics.[211-212]

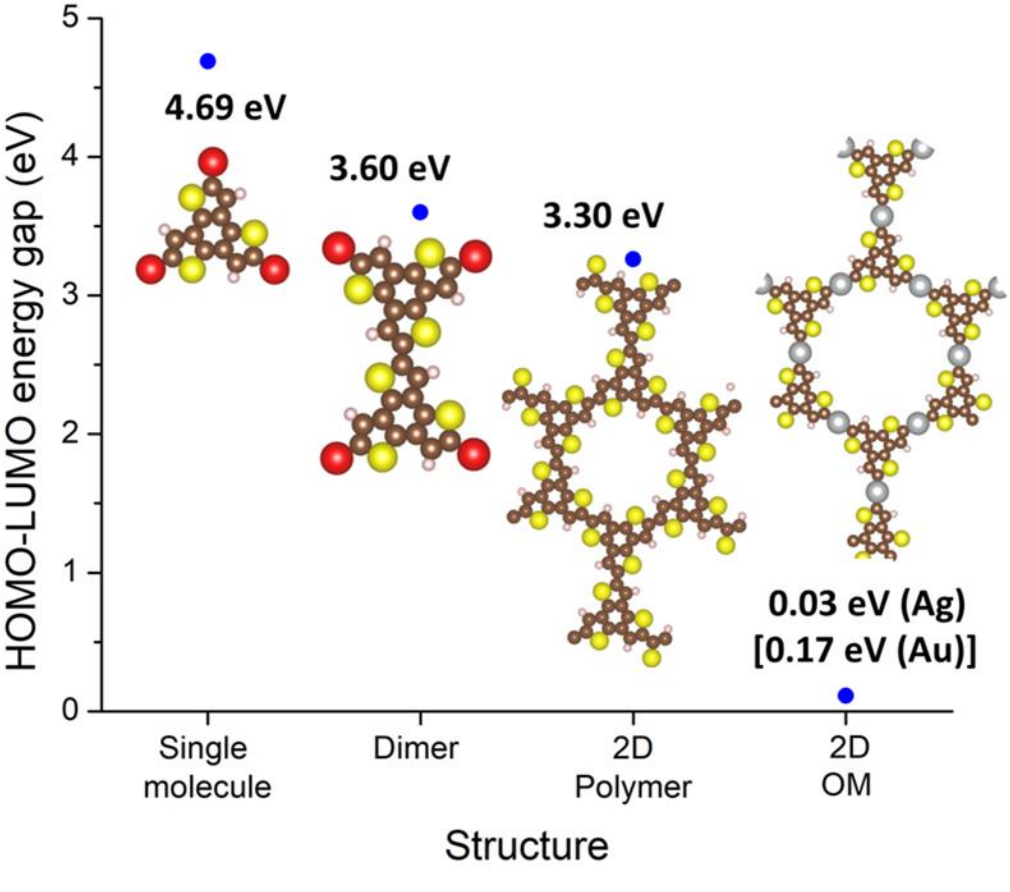

Figure 7-1 **Calculated HOMO-LUMO energy gaps of various structures of TBTTB: for the 2D structures (polymer and OM); the energy gap is the difference between their HOCO (highest occupied crystal orbital) and LUCO (lowest unoccupied crystal orbital) energy level.**

Finally, the last step, *i.e.* device fabrication (Figure 1-1d), was not addressed, and the first experiments are being done at the time of writing of this thesis. Future steps that need to be fulfilled to push the project forward are the following:

- The study of other tridentate molecules containing heteroatoms, with N and O preferred to S to avoid thiophene-ring opening.
- Studying the order of the obtained structures, to optimize the growth conditions.
- Decoupling of the resultant molecular layer.
- Device realization.

Some of these points are already in progress, though not reported in the body of this thesis. A glimpse into the ongoing work as well as a discussion on how to approach each point will be given in the following sub-sections.

7.2 Order of the structures

The obtained polymeric structures, regardless of their symmetry, are bound to contain defects, either point (a missing molecule), line (the borders between two domains) or spatial (a pentagon or heptagon is formed instead of a hexagon for example, or a void). In the study reported in Chapter 5, our molecules had three-fold symmetry and were chosen with the objective of an ideal honeycomb structure. The obtained structures are instead defective hexagonal patterns, as can be inferred from the images. A common procedure to try and reduce defects is to vary one parameter at a time and subsequently compare the result, improving them until a satisfactory structure is obtained. One issue is to find a suitable method to analyze such complex systems and assign a number to the defect density, which can be used to compare different structures and allow different recipes to be assessed from a statistical point of view.

There are several possible ways to quantify the disorder in molecular networks, with the easiest (and most obvious) being to simply count defects. This can be done by counting the fraction of molecules which react with each other (*i.e.* C-Br bonds which become C-M-C or C-C bonds). Such a method would fail to take into account other defects, such as stress-induced pattern distortions, or the presence of non-hexagonal networks, as observed in Figure 5-10, where the high C-C coupling efficiency does not have a counterpart in the order of the polymer network.

This is a problem common to multiple branches of research which has been tackled by various scientists. A good comparison of the most common methods used to perform the topographical analysis of spatial point patterns is presented by Wallet and Dussert in 1998.[282] In this work they used five different methods (nearest-neighbor distribution, radial distribution, Voronoi patterning, quadrat count, minimal spanning tree graph) to characterize specific patterns, and showed that multiparameter methods are better than single parameter ones, and that the minimal spanning tree (MST) edge length distribution graph yields the smallest standard error.

The MST method was developed by Dussert et al.[283] in 1986 and has subsequently been used as a common approach to quantify the order-disorder level of 2D patterns and networks, such as polymeric honeycomb structures.[284] The MST is defined as a graph that connects all the distribution points, and in which the sum of the edge lengths is a minimum. For a specific pattern there are multiple possible MSTs, but all of them are equivalent. The MST is built by first identifying the closed pores of the molecular network, and then by calculating their center-of-mass. All the centers are then connected to build the MST. The necessary steps to build the MST starting from an STM image of a molecular network are reported in Figure 7-2, by Ourdjini et al.[284]

The average (*m*) and standard deviation (σ) of the edge length extracted from the MST can subsequently be normalized, in order to plot the distribution in a (m, σ) diagram and compare it to other 2D arrangements.

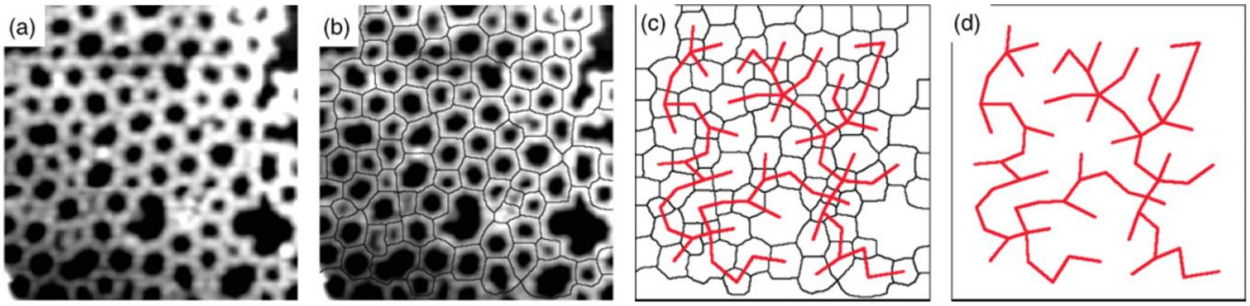

Figure 7-2. **Minimal spanning tree (MST) construction for an STM image of a polymer synthesized by Ourdjini et al., a) raw STM image; b) skeletonized STM image; c) skeleton superimposed with the minimal spanning tree; d) minimal spanning tree. Adapted from Ref.[284] with permission from American Physical Society**

The normalization equations are the following:

$$m = \frac{\pi m^*}{\sqrt{\langle S \rangle}} \frac{(N-1)}{N} \qquad and \qquad \sigma = \frac{\sigma^*}{\sqrt{\langle S \rangle}} \frac{(N-1)}{N} \tag{7-1}$$

Where $\langle S \rangle$ is the average cell area, and N is the number of cells used in the MST graph. N needs to be above 200 cells to obtain a good set of values, as demonstrated by Billia et al.[285] Points on the *x-axis* ($\sigma = 0$ values) are particular, and are defined as "mosaics". They are made by a regular set of periodic polygons, with no defects. The edge length of this mosaic (the m value) is defined by the mosaic symmetry. As an example, perfect hexagonal and square mosaics will have m values of 1.075 and 1 respectively. Inserting a defect into this perfect mosaic will change both σ and m values. Dussert et al. calculated all points from a perfect mosaic to a random arrangement of points, by progressively randomizing them.[283] Their results are represented as black lines in Figure 7-3 and Figure 7-4. The method here described was successfully used by Ourdjini et al.[284] to study the polymerization of 1,4-benzenediboronic acid on various metallic surfaces to analyze the resultant networks and assess the role of the substrate on the final network order.

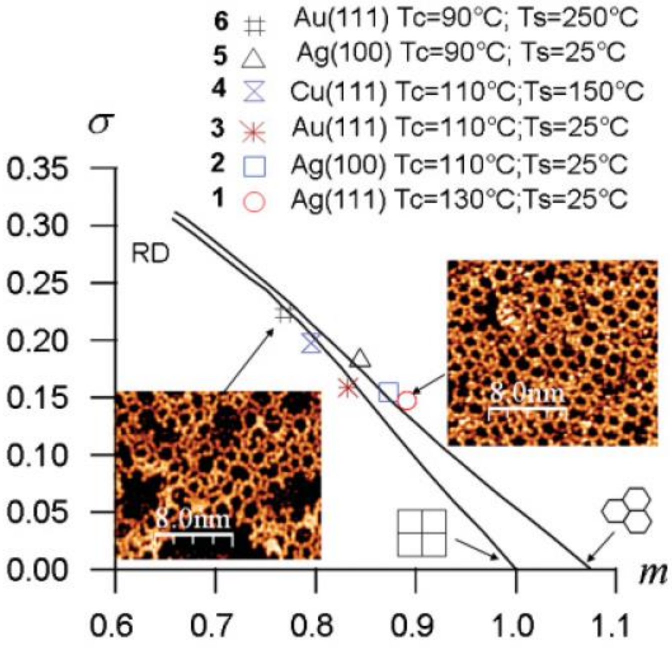

Figure 7-3. **(m, σ) diagram obtained using m and σ values derived using the MST method for BDBA networks grown on Ag, Au, and Cu surfaces. STM images show the overall appearance of the extreme points of the graph. Adapted from Ref.[284] with permission from American Physical Society**

We used the same procedure to analyze our data, in particular the long-range 2D OM networks discussed in Chapter 5. The preliminary results presented in Figure 7-4 indicate the high quality of our structures and the feasibility of this technique to analyze and compare molecular networks.

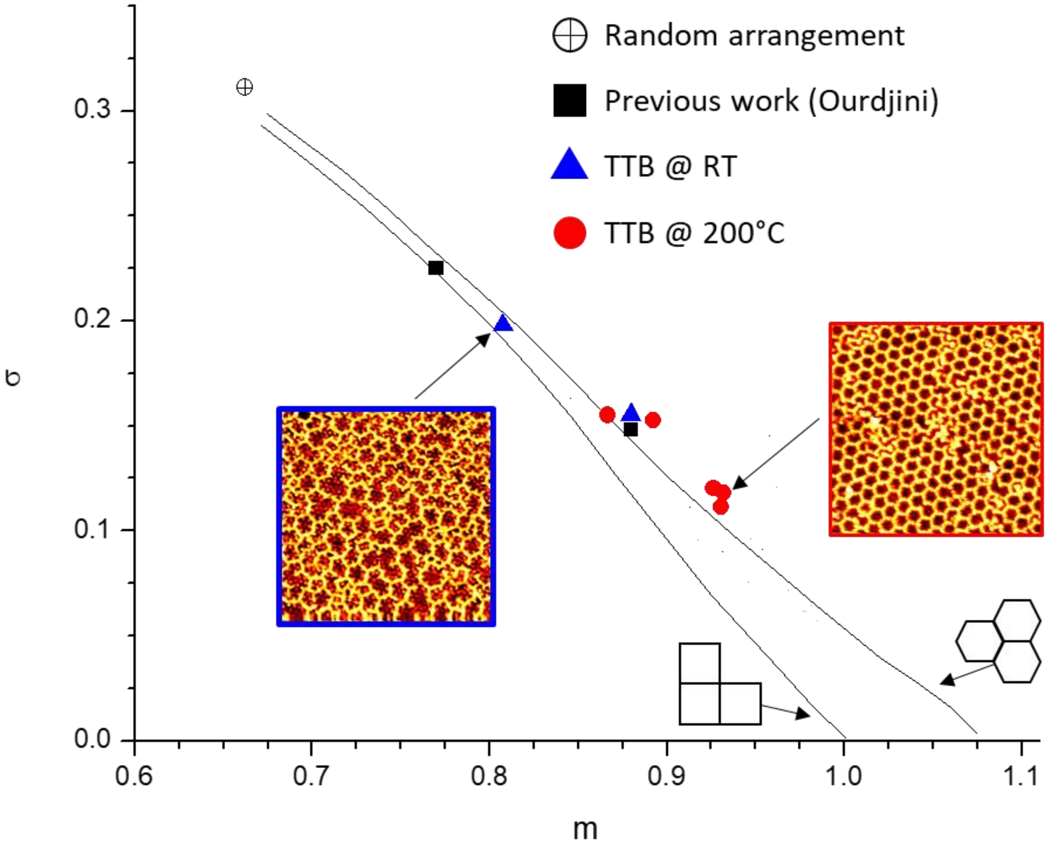

Figure 7-4. **(m, σ) diagram obtained using m and σ values derived using the MST method for TBTTB networks grown on Ag by dosing at RT or on a heated surface at 200 °C. STM images shows the overall appearance of the extreme points of the graph. The worst and best points shown in Figure 7.3 have also been reported to compare our results with the existing literature.**

7.3 Going real: how to incorporate graphene-like materials into a device

Once the 2D network growth is optimized, the focus will be shifted from making 2D networks to making devices. To do so, it will be necessary to decouple the polymer from the underlying metal. Such a process can be done in various ways, and I will present some of them below.

7.3.1 A graphene nanoribbons transistor

In 2017 Llinas et al.[286] demonstrated the feasibility of the fabrication of field-effect transistors (FET) using GNRs obtained from a bottom-up synthesis using Ullmann coupling and a subsequent dehydrogenation step. First they grew 9- and 13-armchair GNR structures on Au/mica samples with a 200nm thick gold layer (Figure 7-5a,b), by dosing either 3′,6′-dibromo-1,1′:2′,1″-terphenyl or 2,2′-di((1,1′-biphenyls)-2-yl)-10,10′-dibromo-9,9′-bianthracene precursors and then annealing them at 410 °C and 380 °C, respectively.

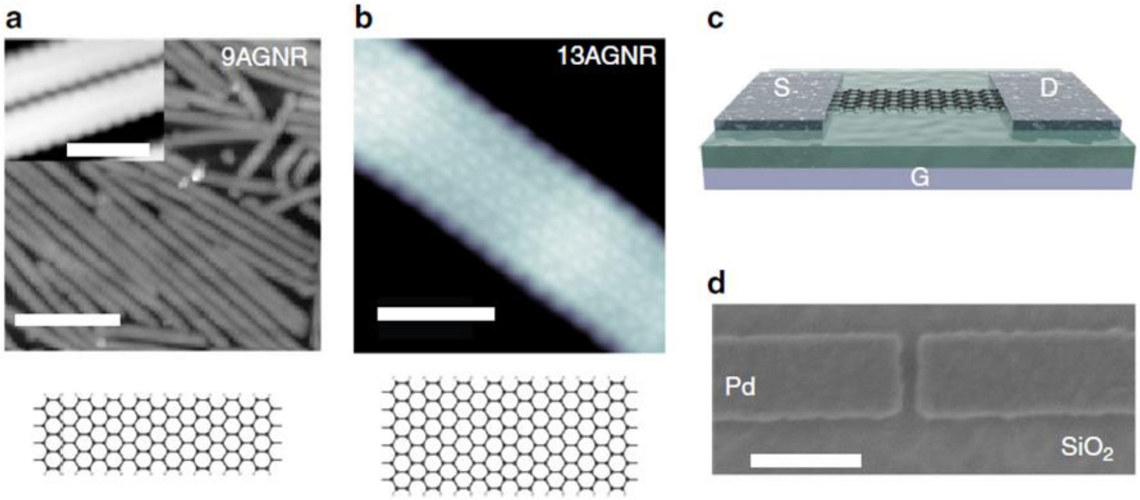

Figure 7-5. **a) STM image of as-synthesized 9-AGNR on Au/Mica, scale bar 10nm, inset scale bar 1 nm; b) STM image of as-synthesized 13-AGNR on Au/Mica, scale bar 2nm; c) Schematic of the FET with a 9-AGNR channel and Pd source-drain electrodes; d) Scanning electron microscope image of the fabricated Pd source-drain electrodes with a scale bar of 100 nm. Reproduced from Ref.[286]**

Once they demonstrated the quality of the GNR structures, they transferred the GNRs to the target substrates. The substrates were heavily-doped 150 mm Si wafers which were patterned into single units with a back gate, using standard photolithography and lift-off techniques. The transfer was done by first delaminating the mica layer from the Au film, using a 38% HCl solution, and then picking up the floating GNR/Au layer with the Si target substrate. The Au layer was removed by etching in a KI/I_2 solution. At this point, source and drain Pd electrodes (100 nm wide, 20 nm gaps) were patterned to obtain the final device (Figure 7-5d). The properties of the devices were then analyzed. This approach could be expanded to be used with different nanostructures and modified to obtain not only FETs but various electronic devices. A similar procedure was also successfully demonstrated by Moreno et al. in 2018.[134]

7.3.2 Going big: ways to scale-up the process

While the feasibility of device fabrication was demonstrated in the previous section, the complexity of the process, and the inherently low statistics of success (only 57 out of 300 devices realized were working FETs), means it is unlikely to be used in real-life applications and is unsuitable for industrial scale-up. Different and more appropriate ways to separate graphene or graphene-like materials from the growth substrate are therefore necessary, and have been the subject of extensive studies.[287] A promising approach to decoupling has been reported by Jung et al.[288] in 2014, in which they demonstrate a clean and dry method to transfer monolayers of graphene (up to 7×7 cm^2 sheets) using a mechano-electro-thermal process, to obtain a direct detachment of graphene from the Cu substrate onto glass, polydimethylsiloxane, or polyethylene terephthalate target substrates, as shown in Figure 7-6. The delamination is obtained by simultaneously applying mechanical pressure and a high voltage bias (200 to 900 V depending on the substrate) across the substrate, while at the same time heating (100 to 300 °C) the whole system in a low vacuum environment. Remarkably, this process also preserves the Cu substrate, which can therefore be used to grow additional graphitic layers. Another interesting transfer method was developed by Bae et al.[289] in 2010 who demonstrated the roll-to-roll production of graphene on large copper substrates with a 75 cm width. In this case a wet two-step method was employed. First, a polymeric support, specifically thermal release tape, is placed in contact with the graphene on the Cu foil. The copper layer is then etched away and the resultant graphene on the polymer support is placed in contact with the target substrate.

The whole stack is passed between two rollers and exposed to mild heat (90–120 °C), which results in the transfer of the graphene films from the polymer support to the target substrate. A transfer rate of 150–200 mm/minute was obtained.

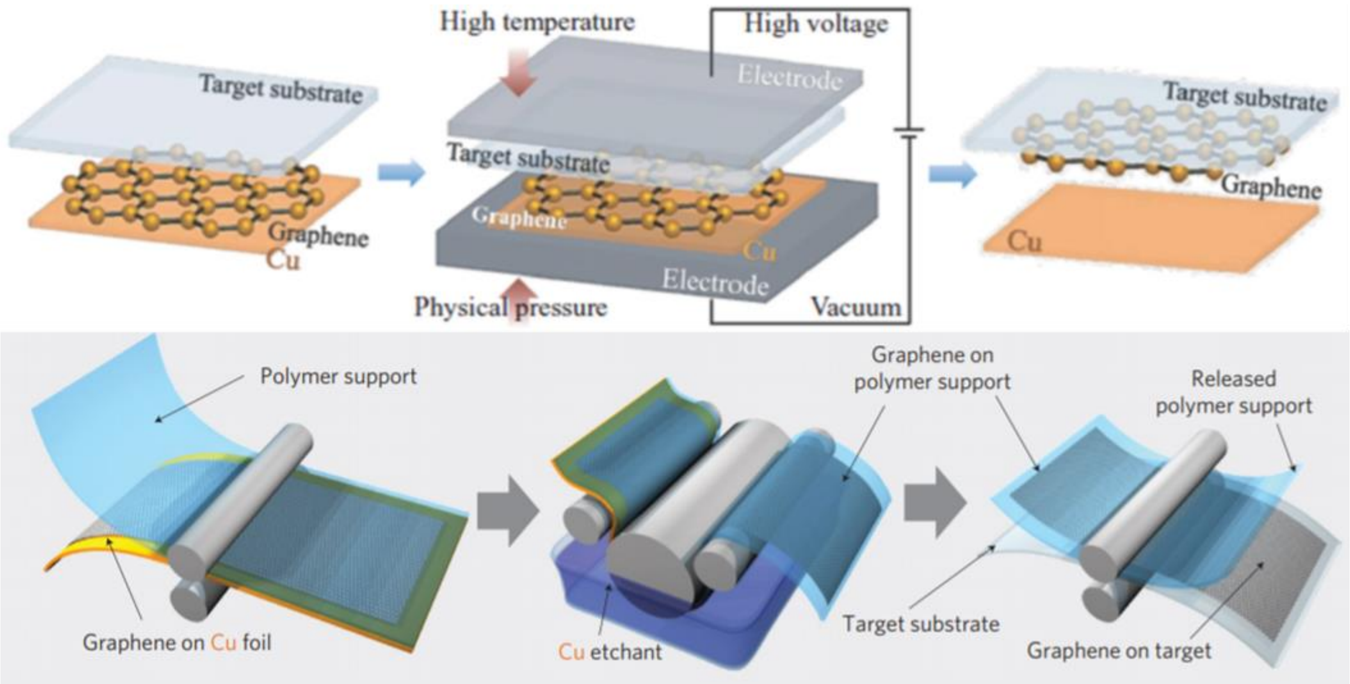

Figure 7-6. (Top panel) Schematic of the transfer method used by Jung et al.;[288] the target substrate is aligned with the Graphene on Cu foil; physical pressure, high temperature, and high voltage are applied in a low-vacuum ambient (10 mTorr): the graphene on the target substrate is thereby physically exfoliated from the Cu foil; Reproduced from Ref.[288] with permission from John Wiley and Sons.

(bottom panel) schematic of the roll-to-roll production of graphene films used by Bae et al.;[289] the process starts with the adhesion of the polymer support, and is then followed by copper etching, rinsing and dry transfer-printing on the target substrate. Reproduced from Ref.[289] with permission from Springer Nature.

8 RÉSUMÉ

8.1 Introduction

Au cours des dernières années, un effort considérable a été consenti pour développer des solutions nouvelles et innovantes susceptibles de révolutionner la conception et la fabrication de dispositifs électroniques.[1] La raison en est que la technologie à base de silicium, malgré le dynamisme de l'industrie des semi-conducteurs jusqu'à présent, pourrait bientôt devenir désuette face au besoin toujours croissant de constante miniaturisation, et d'amélioration des performances.[2-4] Une solution naturelle pourrait donc consister à procéder à un changement fondamental, en passant de la technologie du silicium, vraisembablement condamnée, à une technologie différente, mais la question a laissé de nombreux défis. Par ailleurs, la découverte du graphène[5] en 2004 a suscité un regain d'intérêt pour l'électronique à base de carbone. Cet intérêt s'explique aisément par les propriétés remarquables de ce matériau[6-7] qui démontre une étonnante conductivité thermique et électrique, propriétés qui peuvent être exploitées dans diverses applications, des transistors[8] à la séparation du gaz[9] (ou même de l'isotope[10]) aux nanodispositifs.[11] Malgré ses propriétés uniques, l'absence de bande interdite du graphène limite ses applications en électronique. Des études récentes ont abordé ce problème et tenté de proposer des solutions,[14] mais un processus facile et reproductible n'a pas encore été identifié. La flexibilité de la synthèse organique offre un vaste terrain de jeu pour créer des analogues organiques du graphène possédant une mobilité de charge élevée et une bande interdite ajustable. Parmi les matériaux organiques, les polymères peuvent être généralement obtenus avec des approches ascendantes qui permettent de construire de petites structures à l'échelle atomique ou moléculaire. Par conséquent, au lieu de fabriquer du graphène et d'essayer de le modifier, une approche différente et potentiellement plus prometteuse consisterait en la réalisation ascendante de différents polymères 2D analogues au graphène, mais avec une géométrie différente, dans laquelle des hétéroatomes pourraient être incorporés. L'idée est d'identifier les processus capables de polymériser de petites molécules organiques en polymères 2D dont les blocs de construction peuvent être choisis en fonction des propriétés souhaitées. Cette étape a priori pourrait être réalisée à l'aide de calculs *ab initio*.[15] Il est à noter qu'en solution, les polymères ont tendance à se plier et à s'enrouler, mais il est facile d'éliminer cette constrainteen limitant la croissance sur une surface pour obtenir des polymères 1D ou 2D. Le substrat peut également être utilisé comme catalyseur pour abaisser les barrières énergétiques et guider davantage la réaction.[16] Les résultats seront des polymères conjugués, avec des propriétés similaires à celles du graphène, mais avec des propriétés de transport différentes et une bande interdite ajustable.

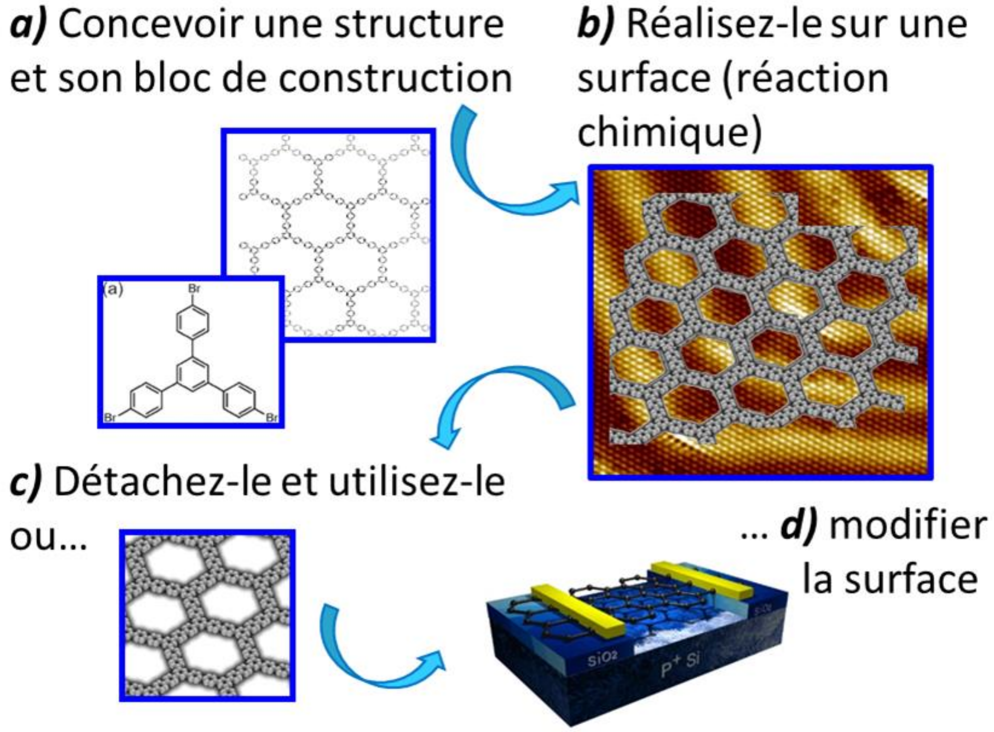

Figure 8-1 **Schéma simplifié des étapes nécessaires à la réalisation de dispositifs utilisant la polymérisation en surface; a) le bloc de construction sélectionné est choisi; b) il est dosé sur une surface où il réagit pour former des polymères 2D; à ce stade, il peut soit en être détaché (c), ou la surface sous-jacente peut être modifiée pour obtenir un dispositif fonctionnel (d).**

L'ensemble du processus nécessaire à la réalisation de dispositifs réels à partir de molécules simples est expliqué à la Figure 8-1, que l'on peut décrire comme le message à retenir de cette thèse. Parmi les travaux pionniers d'Okawa et d'Aono,[17] la plupart des efforts ont été consacrés à la recherche des bons monomères et à contrôler la réaction de polymérisation,[18] ce qui peut aboutir à la formation de polymères 1D[19] et 2D.[20] De nombreuses réactions différentes ont été étudiées en conséquence, telles que la polycondensation, le couplage de Glaser Hay et Sonogashira.[21-23] Une fois réalisées, les propriétés de ces matériaux dépendent de la densité de leurs défauts.[24] Il est également possible de comprendre comment la pureté chimique et l'ordre structurel est un paramètre essentiel à prendre en compte pour ces systèmes. Bien qu'il soit relativement facile d'obtenir des couches monomoléculaires auto-assemblées (SAM en anglais pour Self-Assembled Monolayer) ordonnées à grande étendue sur une surface, une telle étendue d'ordre est en grande partie supprimée pour les structures liées de manière covalente. La nature réversible des forces intermoléculaires des SAM donne aux molécules une mobilité de surface suffisante pour atteindre une géométrie d'énergie minimale, ce qui donne des domaines ordonnés de grande taille. Une approche possible pour former des structures covalentes ordonnées à longue portée consiste à utiliser une réaction en plusieurs étapes, dans laquelle les molécules se localiseraient et se disposeraient de manière que les groupes fonctionnels des molécules voisines puissent interagir facilement et efficacement. Cette étape peut conduire à la formation de liaisons covalentes irréversibles de la structure/du réseau ordonné final.[15, 25]

L'une des réactions les plus courantes qui expriment ces caractéristiques est le couplage Ullmann, une réaction en deux étapes qui exploite l'activité catalytique des substrat métallique,[26] pour déshalogéner des précurseurs d'halogénures d'aryle et ensuite coupler les radicaux en polymères.[27] Cependant, les deux étapes dépendent de la température,[16] et leur énergie d'activation dépendant de la molécule[28] et de la surface.[29] Dans la plupart des cas, la structure obtenue après dépôt sur les surfaces de métaux nobles est un composé organométallique (OM), intermédiaire de la réaction qui est stable jusqu'à la température de polymérisation.[30-31] Depuis le premier rapport d'une réaction d'Ullmann de surface,[32] différents groupes de recherche ont tenté de mieux comprendre le mécanisme de la réaction et la cinétique,[26-27, 33] mais nous pouvons affirmer en toute sécurité que même après une décennie d'études, des questions demeurent sur ces systèmes, en ce qui concerne à la fois la compréhension fondamentale et la réalisation pratique.[34]

Le travail présenté dans cette thèse vise à répondre à ces questions, à la fois d'un point de vue fondamental, en étudiant le rôle de l'halogène et du mécanisme de réaction de molécules simples (*Chapitres 3-4*), ainsi qu'en une perspective de réalisation pratique, guidant le lecteur à-travers les difficultés de formation de structures organiques bidimensionnelles (*Chapitre 5*). Le *Chapitre 6* explorera une autre façon de réaliser des structures polymères sur une surface, à savoir la polymérisation du diacétylène. Outre les résultats expérimentaux, les deux premiers chapitres porteront sur les connaissances nécessaires pour les comprendre, le *Chapitre 1* expliquant au lecteur le « pourquoi » de la recherche et le *Chapitre 2* mettant l'accent sur le « comment ». Le *Chapitre 7* concluant donnera un aperçu des résultats obtenus, de leur adaptation à la littérature existante et de la manière dont ils pourraient être développés et améliorés. Enfin, les *Chapitres 8* et *9* incluront une liste de publications et de travaux réalisés au cours des années de mon programme de doctorat, ainsi qu'une liste de références utilisées dans le texte. Ici, au lieu de cela, nous présenterons une courte synthèse de l'ensemble du travail pour le lecteur francophone.

8.1.1 Polymérisation en surface

La formation de nanostructures 2D par auto-assemblage sur des surfaces consiste en une approche ascendante, dans laquelle les molécules se réarrangent par elles-mêmes après le dépôt. L'auto-assemblage moléculaire permet la réalisation d'une structure moléculaire complexe, maintenue par des forces faibles et réversibles, telles que les interactions de Van der Waals ou par composés de coordination. Une autre caractéristique de ces structures est leur ordre élevé, ce qui permet de former des monocouches ordonnées. Cependant, les retombées sont identiques: les structures résultantes sont intrinsèquement fragiles, retenues par des forces faibles, prévenant la stabilité mécanique et limitant le transport de charges. Pour surmonter ces limitations, une liaison covalente robuste entre les molécules est nécessaire, ce qui nécessite que les précurseurs subissent des réactions chimiques en surface. Afin de contrôler et de réduire les possibilités de réactions secondaires indésirables, des conditions de vide très poussées (UHV en anglais pour Ultra-High Vacuum) sont souvent impliquées. Le principal avantage de l'UHV est la possibilité de travailler avec des surfaces hautement réactives, qui autrement réagiraient immédiatement avec l'oxygène de l'atmosphère. L'UHV permet d'éviter l'oxydation et ouvre la possibilité d'utiliser des techniques de caractérisation particulières pour suivre la réaction, telles que la diffraction d'électrons lents (LEED en anglais pour Low Energy Electron Diffraction), la microscopie à effet tunnel (STM en anglais pour Scanning Tunneling Micropscopy) et la spectroscopie photoélectronique à rayons X (XPS en anglais pour X-ray Photoemission Spectroscopy). Différentes voies ont été suivies pour synthétiser des polymères 2D : via des réactions réversibles et irréversibles. Bien que les réactions réversibles soient plus appropriées pour former un réseau régulier de molécules (en raison de propriétés d'auto-guérison intrinsèques), les polymères désirés devraient inclure des liaisons covalentes stables afin de pouvoir résister aux processus mécaniques et thermiques nécessaires pour l'incorporer en pratique.[15] Par ailleurs, les réactions irréversibles forment un lien plus stable, mais présentent l'inconvénient de ne pas pouvoir s'ajuster après la formation des liens. Il a été suggéré qu'une solution appropriée pourrait consister à utiliser une réaction en deux étapes, dans laquelle seule la deuxième étape est irréversible et conduit à une liaison covalente.[15, 25] De cette manière, il sera possible de déposer une molécule et de la disposer pour former la structure d'ordre désirée, et, dans un second temps, procéder à la réaction de polymérisation, obtenant ainsi des polymères stables liés par covalence.

8.1.1.1 Réaction d'Ullman

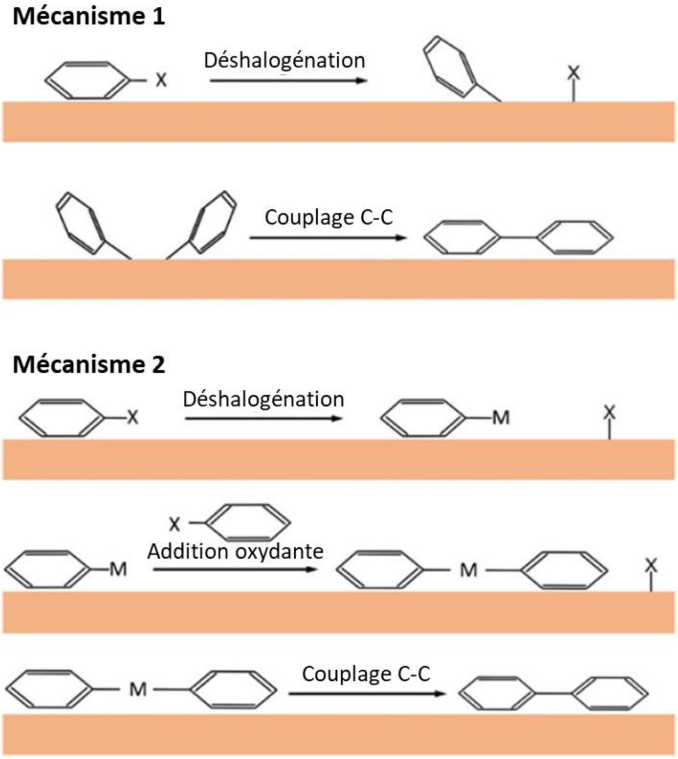

Figure 8-2 **Schéma du couplage Ullmann en surface; On peut observer deux mécanismes, selon que les atomes métalliques impliqués proviennent du réseau de surface (Mécanisme 1) ou soient des adatomes (Mécanisme 2).**

Découvert pour la première fois en 1901 par le scientifique allemand Fritz Ullmann,[96-97] la réaction d'Ullmann a depuis été utilisée comme moyen le plus courant de produire des biphényles à partir d'halogénures d'aryle en solution. La réaction est assistée par le cuivre, qui doit être présent dans la solution sous forme de poudre de cuivre. Le couplage d'Ullmann est une réaction complexe, où différents mécanismes réactionnels peuvent être suivis, en fonction des précurseurs de départ, comme décrit par Sambiagio et al.[98] En première approximation, il est possible de décrire deux mécanismes principaux, l'un dans lequel un radical d'aryle est produit comme intermédiaire, et un autre où l'intermédiaire est une espèce d'aryl-cuivre. Dans les deux cas, des dimères des mêmes précurseurs d'halogénure d'aryle (homocouplage) ou de ceux différents (couplage croisé) peuvent être produits. La première réaction d'Ullmann sur une surface a été observée par Xi et Bent en 1992. Dans une série d'études, ils ont décrit la réaction de précurseurs d'iodobenzène sur une surface de Cu (111).[26, 32, 99] Le mécanisme réactionnel a également été décrit, dans lequel un atome de cuivre est inséré dans la liaison Cu-I, pour former un intermédiaire OM. Les intermédiaires réagissent alors pour produire le biphényle final. Comme dans le cas de la chimie en solution, le chemin réactionnel à la surface dépend de l'état de l'atome de cuivre, qui peut être un atome de cuivre en réseau ou un adatome de cuivre en surface (Figure 8-2).

8.1.1.2 Réaction Ullmann en surface: propriétés et produits

Depuis 2010, le couplage Ullmann est devenu le moyen le plus courant de produire des polymères conjugués sur des surfaces métalliques. Les raisons de son succès sont multiples, mais les principales sont le contrôle précis des sites radicaux et la possibilité de réaliser une croissance hiérarchique (Figure 8-3).[18, 20] Combinés, ces deux facteurs permettent un contrôle précis des nanostructures cultivées, tel que confirmé par la diversité des structures réalisées, des polymères linéaires aux polymères bidimensionnels, en plus des macrocycles et même des nanorubans de graphène, terminés en « zig-zag » (Figure 8-4).

- **Contrôle précis des sites radicaux**

Tel qu'indiqué précédemment, le couplage d'Ullmann est une réaction en deux étapes, dans laquelle le premier produit des radicaux d'aryles réagit encore le couplage en un polymère. Les espèces radicalaires sont formées par la rupture des liaisons C-X. En sélectionnant le bloc de construction, il est facile de sélectionner la position de couplage et donc de décider a priori de la structure finale obtenue. Le nombre de sites de réaction (*c.-à-d.* les liaisons CX) contrôlera la dimensionnalité des nanostructures (Figure 8-3a-c).[18, 20] En utilisant différents précurseurs, avec un nombre croissant d'halogènes, de 1 à 4, des dimères, des chaînes linéaires et des polymères 2D peuvent être obtenus.

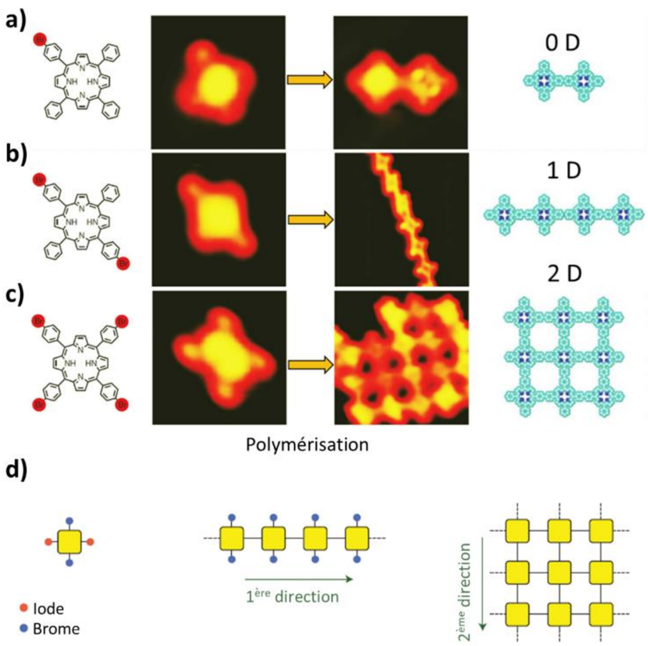

Figure 8-3 **Différents précurseurs de porphyrines avec des halogènes 1 (a), 2 (b) ou 4 (c), ainsi que leurs images STM d'une seule molécule et de la structure polymérique relative (schématisées dans la colonne de droite); les dimères sont formés avec le précurseur a, les chaînes linéaires avec b et les réseaux 2D avec c.**

- **Croissance hiérarchique**

Les deux étapes de la réaction de Ullmann peuvent être activées thermiquement, mais l'énergie d'activation requise pour chacune d'entre elles est différente et varie en fonction de la molécule et de la surface utilisée. De plus, la liaison C-X se rompra à une température différente en fonction de l’halogène impliqué. Ceci peut être exploité pour connaître une croissance hiérarchique, comme démontré par Lafferentz et al.[18] en 2012 (Figure 8-3d), puis utilisé avec succès par plusieurs chercheurs.[101-102] Cette approche intéressante augmente le contrôle global de la réaction, permettant produire des chaînes linéaires d’abord et seulement après cela, de les convertir en une structure conjuguée en 2D, ce qui permet également d’étudier comment les propriétés changent avec la dimension de la structure.[101]

- **Différentes nanostructures possibles**

Ces propriétés peuvent être exploitées pour réaliser les nanostructures souhaitées, allant du polymère linéaire simple aux macrocycles complexes ou réseau 2D, comme l'illustre la Figure 8-4.[100-101] Dans certains cas, la réaction d'Ullmann peut être couplée à des réactions de déshydrogénation pour produire différentes variétés de nanoparticules de graphène. [103-104]

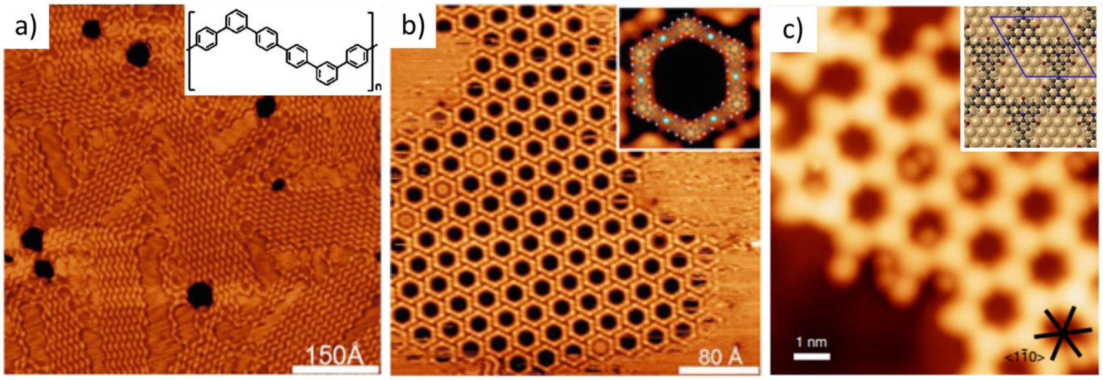

Figure 8-4 **Images STM de diverses structures 1D et 2D pouvant être obtenues avec un couplage d'Ullmann. Les unités précurseurs et répétitives utilisées sont rapportées pour chacune d'elles sous forme d'encart; a) des chaînes linéaires empilées pour former des domaines 2D; b) des macrocycles, à nouveau empilés pour obtenir un assemblage 2D; c) une structure conjuguée en 2D avec une symétrie en nid d'abeille.**

8.1.2 Microscope à effet tunnel

La technique principale utilisée pour réaliser ce travail de thèse est le microscope à effet tunnel. Cette dernière est une technique d'analyse de surface, qui permet de sonder la topographie d'une surface métallique ou semi-conductrice dans l'espace réelle, avec une résolution à l'échelle de l'atome. La résolution latérale peut atteindre jusqu'à 1 Å tandis que celle en profondeur 0.1 Å.[290] Le STM a été inventé par Binning et Rohrer en 1981 dans les laboratoires d'IBM et est composé d'une pointe conductrice fine et acérée montée sur un transducteur piézoélectrique qui assure un mouvement xyz à la pointe et contrôle son positionnement par rapport à la surface étudiée. Lorsque la pointe est relativement proche d'une surface conductrice, mais sans être en contact (1-10 Å), nous pouvons appliquer alors une tension entre la pointe et la surface. Cette tension permet aux électrons de passer de la pointe à l'échantillon (ou vice-versa) grâce à l'effet tunnel quantique. Ainsi, le courant tunnel collecté est proportionnel à la densité d'états locale de la surface, au voisinage de la pointe. Une description schématique du principe de fonctionnement du STM est montrée sur la Figure 8-5. Pour cette découverte, Binning et Rohrer ont été récompensés par le prix Nobel de la physique en 1986. Depuis sa découverte, de nombreux modèles de STM ont été construits, dans le but d'apporter de nouvelles fonctionnalités à la technique. Désormais, nous pouvons non seulement imager la tomographie de la surface à l'échelle atomique, mais pouvons également manipuler les atomes à la surface, et ce dans divers environnements (UHV, air, liquide), sur une plage en température large (de proche de 0 degré absolu jusqu'à plus de 1000K).

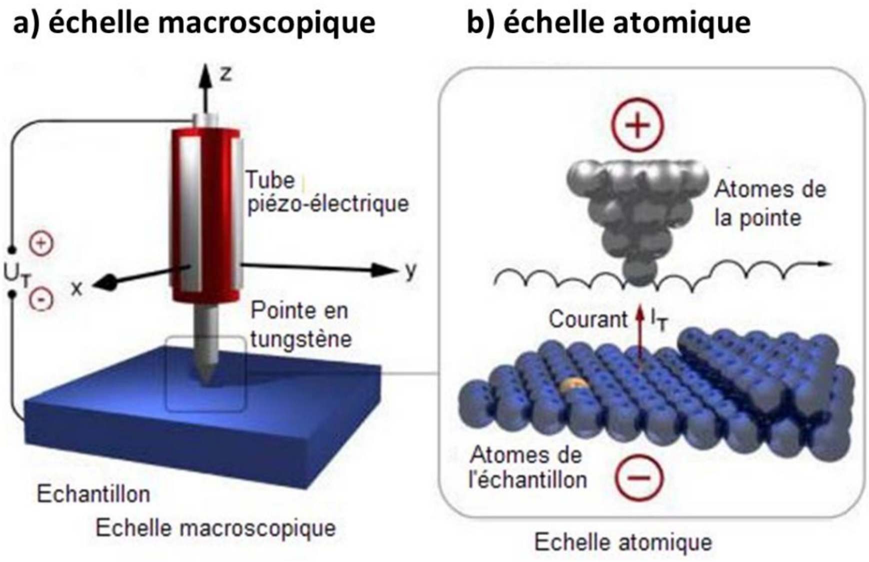

Figure 8-5 **a) Schéma d'un STM à l'échelle macroscopique. La pointe est montée sur un moteur piézoélectrique qui contrôle sa position, et mise à l'approche de la surface de l'échantillon. Une tension de consigne (U_T) est alors appliquée entre la pointe et la surface. b) Vue zoomée de la région pointe-échantillon. Le courant tunnel (IT) est représenté par une flèche rouche et le tracé noir représente le mouvement de la pointe lorsque l'on garde un courant I_T constant pendant le balayage de la surface.**

8.1.3 Spectrométrie de photoémission induits par rayons X

Les études STM sont souvent couplées avec une technique complémentaire qu'est la spectrométrie de photoélectrons induits par rayons X (X-ray Photoemission Spectroscopy XPS en anglais). La technique XPS est une technique nondestructive qui permet d'identifier les éléments chimiques constituants une surface et de définir leur état chimique. Un spectre XPS est obtenu en irradiant un matériau avec des rayons X avec des photons incidents de quelques keV généralement. On mesure l'énergie cinétique des électrons sortis des dernières couches atomiques (le libre parcours moyen des électrons dans le solide est de l’ordre de 1-10nm).[145] L’émission des électrons est due à l’effet photoélectrique décrite par l’équation suivante :[145]

$$E_k = h\upsilon - E_{BE} - \phi \tag{8-1}$$

Où E_K est l’énergie cinétique de l’électron détecté, E_{BE} l’énergie de liaison de l’électron dans le matériau, $h\upsilon$ l’énergie du photon incident et $\boldsymbol{\Phi}$ la fonction de travaille de l’échantillon donnée par la différence en énergie entre le niveau de Fermi du matériau et le niveau de vide de l’analyseur, et dépend donc de l’instrument de mesure utilisé. Il est alors possible d’obtenir des informations de manière qualitative en connaissant l’énergie de liaison E_{BE} de l’atome, mais aussi des informations quantitatives puisque les intensités des électrons détecté pour un élément en particulier est proportionnel à sa concentration.[145]

L’énergie de liaison peut également apporter des renseignements concernant l’état chimique de l’atome en question, et donc ses liaisons chimiques avec la molécule (ou atomes avoisinants). En effet, l’énergie du pic de photoémission mesurée dépend de l’état chimique de l’élément et certains décalages en énergie peuvent être observes. Les instruments nécessaires pour faire de telle mesure sont une source de rayons X et un analyseur d’électrons émis. La source de rayons X est généralement une « lampe » dans laquelle des rayons X sont obtenus par bombardement électronique de certains métaux spécifiques par l’effet Breemsstrahlung (voir Figure 8-6).

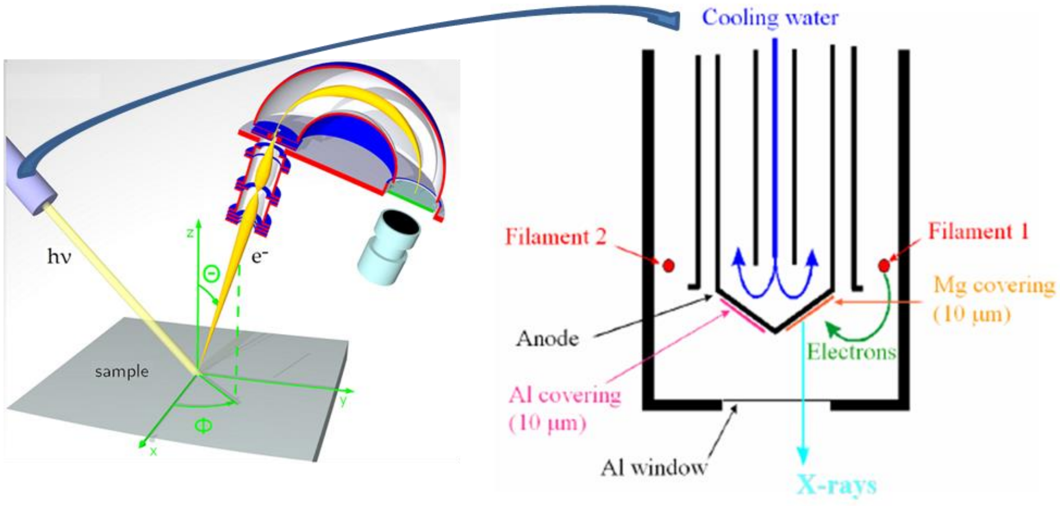

Figure 8-6 **Schéma de l'appareil XPS (à gauche) avec les détails d'une source de rayons X à double filament (à droite).**

8.1.4 Précurseurs utilisés

Les réactions sur surface dépendent de plusieurs paramètres, et l'un des plus importants est l'interaction entre la molécule déposée et la surface. Toutefois, en fonction de la réaction, différents paramètres sont à prendre en compte. Le but de cette thèse est d'étudier et de comprendre l'influence de ces paramètres, puis d'exploiter ces résultats afin d'élaborer la nanostructure polymérique désirée. En vue de cet objectif, nous avons étudié différentes molécules et l'influence des paramètres de croissance sur la polymérisation. Changer de précurseurs pourrait jouer sur la réaction chimique impliquée dans la formation du polymère conjugué. Une grande partie de cette thèse (chapitres 3 à 5) met en jeu la réaction d'Ullmann sur surface, tandis que dans le chapitre 6, nous allons nous concentrer sur polymérisation de diacétylène.

Comme présenté précédemment, la réaction d'Ullmann est une réaction en deux étapes. La première consiste à la déshalogénation de la molécule précurseur tandis que la seconde est une étape de polymérisation. Il est alors nécessaire d'étudier des molécules comprenant différents halogènes afin d'investiguer son rôle sur le processus de polymérisation ainsi que son influence sur le produit final. Pour ce faire, nous avons étudié cinq molécules benzéniques avec deux halogènes en position 1 et 4 : la 1,4-diiodobenzène (dIB), la 1,4-iodobromobenzène (IBB), la 1,4-dibromobenzène (dBB), la 1,4-bromoclorobenzène (BCB) et la 1,4-diclorobenzène (dCB), présentées dans la Figure 8-7a. Chaque molécule est composée d'un cycle phényle centrale et deux halogènes en position *para* (1 et 4), de telle sorte que le résultat de la polymérisation serait linéaire et identique, à savoir le poly-para-phényle (PPP). Les résultats obtenus à partir de ces molécules sont discutés dans les chapitres 3 et 4.

En vue d'applications futures, l'étude de la réaction d'Ullmann sur surface est motivée par la réalisation de polymères 2D, similaires au graphène. Ainsi nous avons étudié une molécule précurseur de symétrie d'ordre 3, qui conduit à la formation de polymères conjugués sous un motif bidimensionnel hexagonal. Cette molécule, la tribromoterthienobenzène (TBTTB), contient des hétéroatomes de soufre (Figure 8-7, et Chapter 5).

Outre les molécules contenant des halogènes pour l'étude du couplage d'Ullmann, nous avons également explorée d'autres réactions de polymérisation. Le couplage acétylénique est également intéressant car il est facilement induit par une exposition aux rayons UV ou encore à un recuit. Dans ce contexte, nous avons étudié l'auto assemblage et la polymérisation de la di-benzonitrildiacétylène (DBDA, Figure 8-7) sur l'Ag(111). L'étude de cette molécule est présentée dans le Chapitre 6. La TBTT et la DBDA sont toutes deux des molécules pro-chirales, ainsi après leur dépôt à la surface, plusieurs isomères peuvent se former.

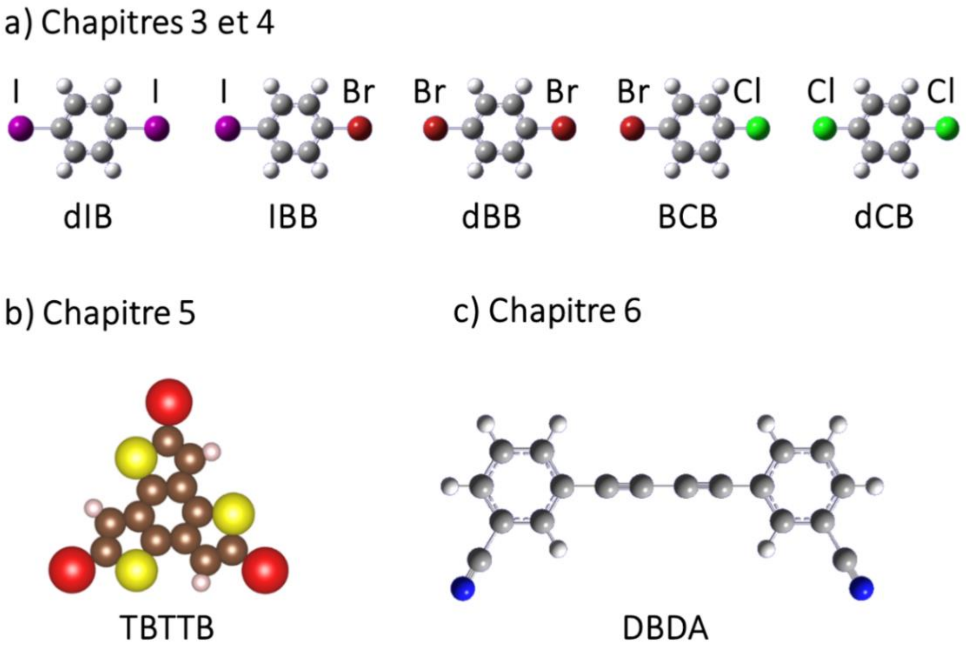

Figure 8-7 : **Schémas des molécules : a) Molécules benzéniques contenant différents halogènes; b) tribromoterthienobenzène; c) di-benzonitril-diacetylène**

8.2 Résultats et discussions

La réalisation d'un matériel de basse dimension « graphène like » avec des propriétés optoélectroniques explicitement choisies implique dans un premier temps la compréhension de l'influence des paramètres de croissances physiques et chimiques. Pour ce faire, il est nécessaire de choisir un système « modèle », se positionnant comme étant un cas d'école, pour lequel il est possible de Controller indépendamment chaque paramètre de contrôle, et d'en comprendre les effets. Nous démontrerons alors, grâce à ce système « modèle », la viabilité du processus d'élaboration avant de travailler avec des systèmes plus complexes. C'est ainsi que nous avons commencé par l'étude de l'adsorption de dBB sur Cu(110). Une telle molécule est choisie pour deux raisons principales :la première est la simplicité de sa géométrie, elle est composée d'un cycle phényle et deux atomes d’halogène identiques en position para); la seconde est le fait qu’elle permet d’obtenir à la fois une structure organométallique et polymérique après dépôt sur Cu(110).[30] Ce système s’est finalement avéré plus complexe, reflétant la versatilité de la réaction d’Ullmann et comment chaque paramètre conditionne de manière significative l’ensemble de la réaction.

8.2.1 dBB/Cu(110) – Effet du taux de recouvrement

Avec un taux de recouvrement à une monocouche de dBB sur la surface de Cu(110), on obtient une phase organométallique de type Chevron, dont la relation épitaxiale peut s’écrire comme (1, -4 | 6, 0) et (1, -1 | 4, 1). Cette phase organométallique est transformée en polymère après recuit, et les polymères sont alignés dans les directions [1-1±2]. Cependant on note que le même système, à un taux de recouvrement moindre, peut former des chaînes OM selon les directions [1-1±1], avec des relations épitaxiales de type (2, -2 | 4, 9) et (2, 2 | -4, 9). Des chaînes OM sont à l’origine des polymères dans la direction [1-1 0] comme le montre la Figure 8-8. Une telle différence remarquable démontre l’importance du taux de recouvrement dans la réaction d’Ullmann. Les différentes directions de croissance du polymère suggèrent des variations de propriétés de ce dernier. En effet, en fonction de sa commensurabilité avec le substrat, la distance polymère/surface peut varier ainsi que l’interaction molécule/substrat. Le polymère croissant selon la direction [1-1±2] est commensurable avec la surface de Cu(110), et peut alors atteindre des longueurs plus importantes que la moyenne comme nous pouvons le constater sur la Figure 8-8. Une telle croissance facilitée par la commensurabilité avec le substrat, permet également d’obtenir des domaines de polymère plus large, rendant ainsi possible leur caractérisation par des techniques de mesure non locales, telles que l’ARPES.

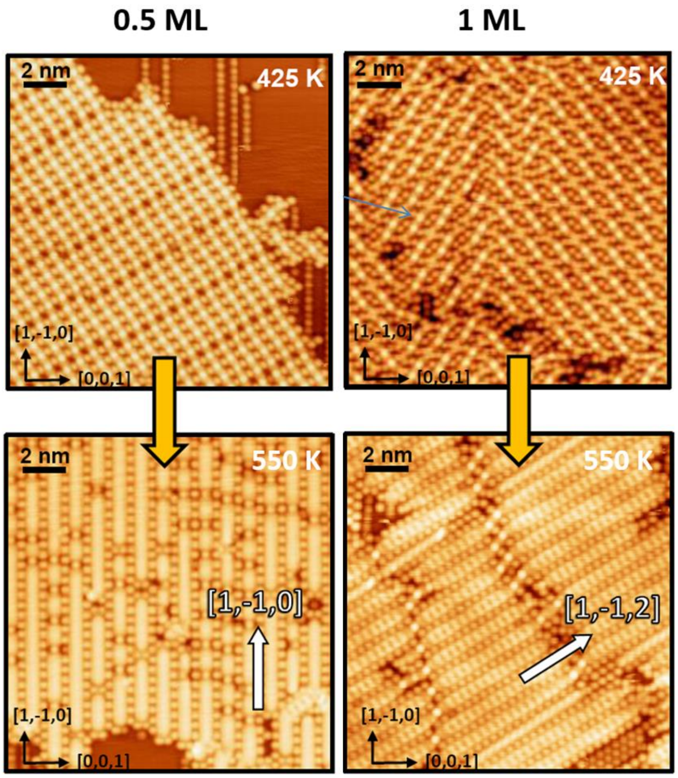

Figure 8-8. **Images STM de dBB/Cu(110) à un taux de 0.5 monocouche (gauche) et 1 monocouche (droite) avant et après polymérisation. Le taux de recouvrement a un impact à la fois sur la structure organométallique et polymérique, influençant leur longueur et orientation sur la surface.**

8.2.2 dBB/Cu(110) haut taux de recouvrement : cinétique de la réaction

Si le couplage d’Ullmann est l’une des réactions les plus connues pour élaborer des polymères sur surface, le mécanisme de couplage n’est pas encore complètement compris. Nous avons alors étudié la cinétique de la réaction de dBB/Cu(110) avec un taux de recouvrement d’une monocouche pour la formation de chaînes polymériques π-conjuguées, ordonnées et épitaxiées. Nous avons pu dresser une image complète du mécanisme de la polymérisation par déhalogétation de la molécule, assistée par le confinement de la surface, en combinant des mesures STM et un modèle cinétique extrait des mesures fast-XPS (Figure 8-9).

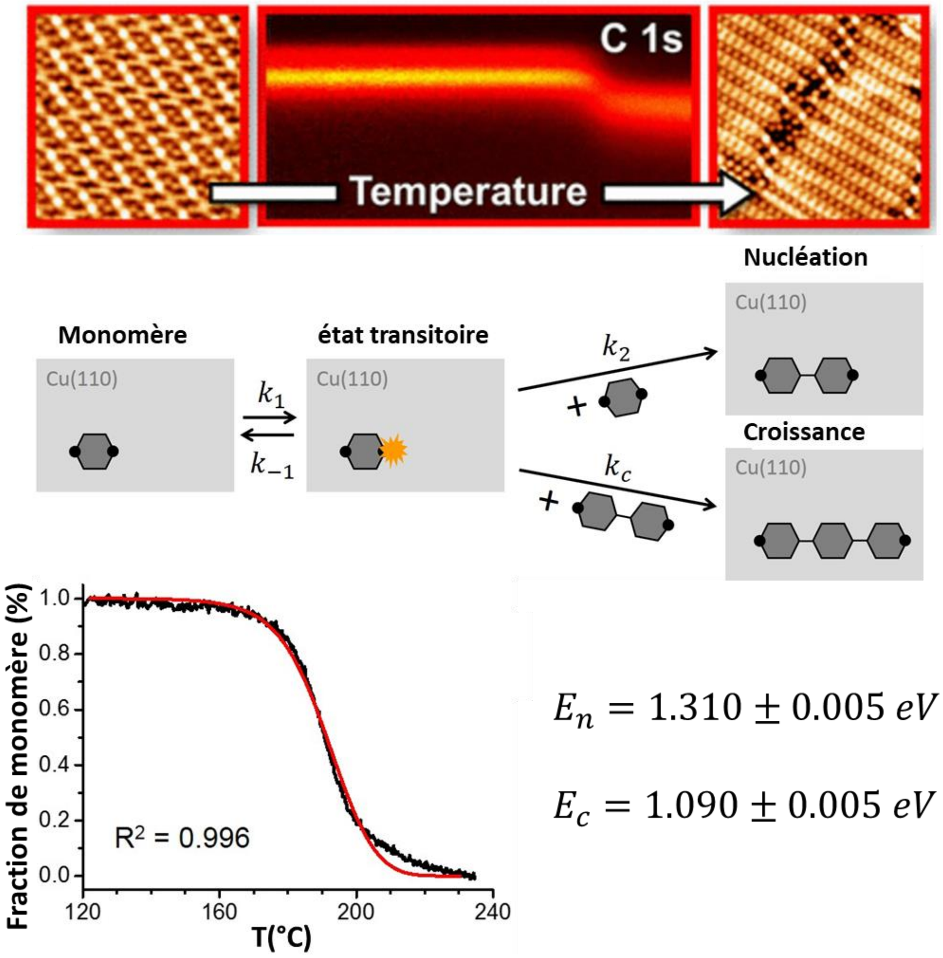

Figure 8-9. **(Haut) Image STM de dBB/Cu(110) avant et après la réaction de polymérisation, cette réaction étant mesurée par du fast-XPS. (Centre) Modèle cinétique proposé prenant en compte l'existence d'un état transitoire. (Bas) Ajustement des données expérimentales pour le cas où la probabilité de couplage est faible. Les énergies d'activation résultante pour la nucléation et la croissance sont également données.**

Nous avons démontré que les données expérimentales de fast-XPS peuvent être précisément décrites par un scénario où le couplage entre monomères est faible (Figure 8-9, partie basse), en accord avec les observations de domaines composés de longs polymères par STM. Nous prouvons alors que la réaction suit un comportement de nucléation-croissance, qui est précédé de la formation d'un état transitoire, et nous déterminons alors les différentes barrières d'activation pour ce processus (Figure 8-9, partie basse). Les énergies d'activations résultantes montrent que la formation d'un polymère partant d'un nucléus (dimère) demande considérablement moins d'énergie que la création directe d'un nucléus à partir de la phase stable à température ambiante. Ces résultats suggèrent que la réaction de polymérisation n'est pas topotactique, mais relève plutôt d'un processus où la diffusion prédomine.

8.2.3 dBB/Cu(110) faible couverture : état intermédiaire transitoire

Lors de l'étude du système dBB/Cu(110) à faible couverture, nous avons observé la présence de deux structures intermédiaires distinctes pendant le processus de polymérisation (Figure 8-10). Ces deux phases se trouvent à des plages de températures bien définies. La phase organométallique bien connue jusqu'alors (celle montrée sur la Figure 8-8) se transforme en une formation 2D de type « échiquier ». Cette dernière phase est observée pendant le recuit de la surface à une température comprise entre 145 °C et 200 °C pour un taux de couverture en dessous de la monocouche (≤ 0.6 monocouche) et reste stable durant le refroidissement de l'échantillon à la température ambiante voire plus bas. Nous avons alors combiné une étude STM avec des calculs DFT, et avons pu décrire les détails structuraux de la phase, mettant à jour la formation de cet « échiquier » par des cycles phényles pontés de 4 groupements d'adatomes de Cu (Figure 8-10). Ces résultats démontrent que même avec de simples molécules, telle que la dBB dans notre cas d'étude, la réaction d'Ullmann sur surface peut être menée de différentes façons. L'observation de deux phases organométalliques stables, avec des morphologies distinctes et des signatures spectroscopiques différentes, nous mène à penser à la complexité des mécanismes sur surface, offrant également l'opportunité d'un réglage fin pour la croissance des structures spécifiques.

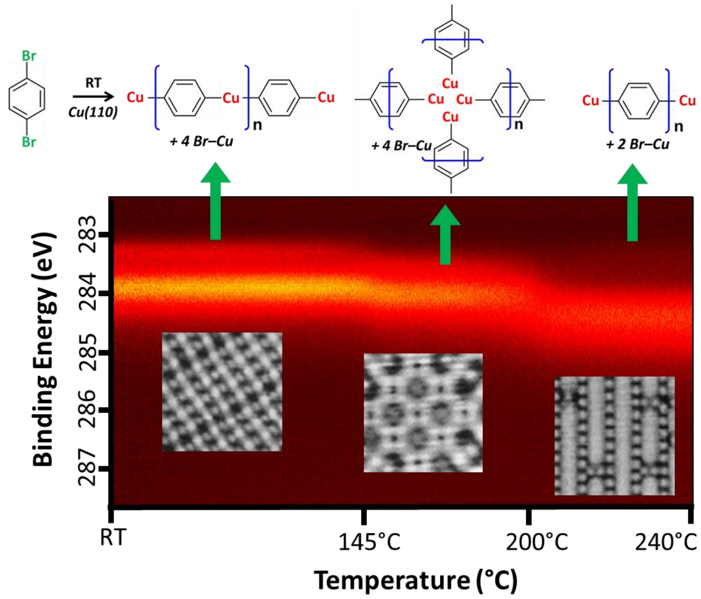

Figure 8-10 **(Haut) Schéma de la réaction d'Ullmann sur surface pour dBB/Cu(110) à faible taux de couverture (<0.6 monocouche) ; (Bas) Map extrait de mesures fast-XPS de la réaction de polymérisation, montrant distinctement deux décalage en énergie dans le spectre du C 1s, et correspondent respectivement à la formation de l'organométallique 2D, et de la phase polymérique. Les images STM correspondantes sont également montrées.**

8.2.4 Di-halobenzenes on Cu(110) – Effet de l'halogène

Si de nombreux études ont été publiées ce dernier décade sur le couplage d'Ullmann sur surface[25, 34, 178-179] , la majorité d'entre elles se concentre sur la compréhension de la structure et l'ordre des polymères sur différents substrats,[108] ou encore la densité des défauts de telle structure,[24] l'influence des dérivés halogénés, n'ont pas été explorée en détail. Quelques études théoriques[16] et expérimentales[180-181] ont mentionné la dissociation des halobenzènes à la surface d'un métal sans donner de détail sur leur effet. Au début de mon projet de doctorat, ce point restait une question ouverte, et l'état de l'art sur la question était peu avancé. L'un des seuls travaux concernant ce point est réalisé par Di Giovannantonio et al. ACS nano 2013, où il décrit la contribution de l'halogène dans la formation du polymère 1D *via* le couplage d'Ullmann sur surface,[30-31] et met en évidence leur présence dans la maille élémentaire de l'ogranométallique après le dépôt de la dBB sur Cu(110). Cette étude présente également la différence structurales des réseaux obtenus avec la dBB[30] ou la dIB[19] sur Cu(110) structures obtenues. Cette différence remarquable conforte la nécessité d'étudier l'influence des halogènes dans le processus de polymérisation, amenant la phase organométallique dans sa structure polymérique.

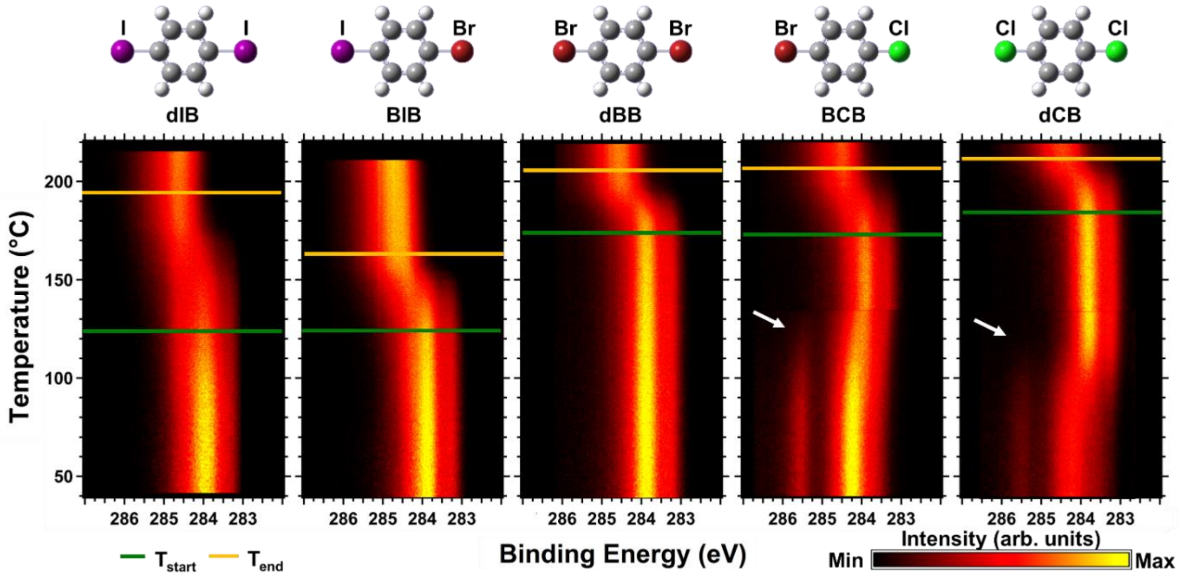

Figure 8-11. **Mesures Fast-XPS de la raie C 1S pendant le recuit (0.2 °C/s) d'une monocouche saturée en prenant chaque espèce de précurseur sur Cu(110) , le dépôt étant fait à température ambiante. Les températures pour lesquelles 10% et 90% de la réaction de polymérisation sont accomplies, sont marquées par T_{start} (vert) et T_{end} (orange) respectivement. Les flèches blanches indiquent le changement de la raie C1s due à la dissociation C-Cl.**

En accord avec les résultats précédents, il est intéressant de dresser quel type d'halogène peut influencer la croissance de l'organométallique et les structures polymériques. C'est ainsi que nous avons étudié le rôle de l'halogène dans la réaction d'Ullmann avec cinq précurseurs 1,4-dihalobenzènes contenant du chlore, du brome, et de l'iode sur Cu(110) en combinant des mesures fast-XPS, NEXAFS et STM. Nous déterminons alors que la nature de l'halogène contenu dans le précurseur affecte la température de deshalogénation (Figure 8-11). L'halogène influence aussi bien la structure de l'OM obtenue à température ambiante que l'orientation du polymère final (Figure 4-6). Nous démontrons alors que (i) la longueur des chaînes organométalliques dépend de l'énergie de dissociation de la liaison carbone-halogène, et (ii) les structures OM obtenues avec les précurseurs contenant du Br et du Cl (dBB, dCB, BCB, BIB) s'orientent selon les directions [1-1±1], tandis que pour les précurseurs contenant de l'iode (dIB) les directions [1-1±2] sont privilégiées. Les maps fast –XPS montrent également que les structures OM suivent différentes cinétiques de réactions, avec une transition graduelle pour le cas de la dIB tandis que pour les autres précurseurs la transition vers l'état polymérique est abrupte. La fenêtre en température de la polymérisation peut également varier en fonction du type d'halogène (Figure 8-11), et peut être corrélée de manière qualitative à l'énergie de diffusion de l'halogène (Figure 4-11).

Notre étude systématique montre que l'halogène n'est pas seulement un sous-produit de la réaction, mais plutôt un paramètre important qui gouverne la polymérisation sur surface par le couplage d'Ullmann, qui a besoin d'être pris en compte lors de la conception et le choix du précurseur.

8.2.5 Effet de la surface

Les molécules de thiophènes sont souvent présentées comme un précurseur prometteur pour la réalisation de systèmes conjugués,[125, 291] et les travaux précédents ont démontré avec succès l'utilisation de la réaction d'Ullmann sur surface pour la préparation des polymères 1D/2D ainsi que des nano rubans de graphène avec des précurseurs contenant du thiophène. Toutefois, il a été prouvé que la polymérisation peut être interrompue par l'ouverture des cycles thiophène,[197, 209] mais une analyse profonde du phénomène en particulier sur quel type de surface, et comment la température de dépôt peut influencer l'ouverture de ces cycles reste manquante.

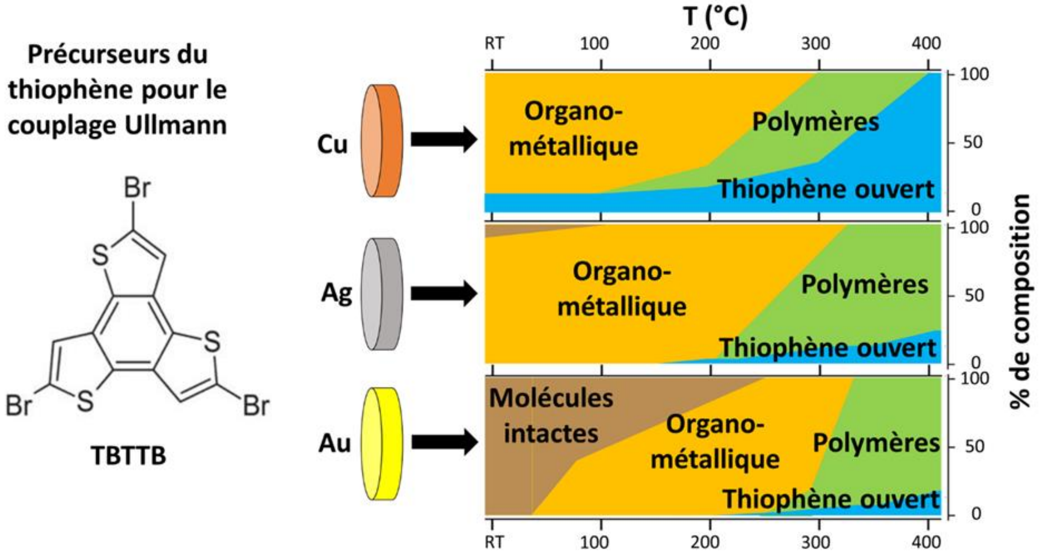

Figure 8-12. **Diagramme de phase de la tribromoterthienobenzène sur les surfaces (111) des métaux nobles en fonction de la température.**

Ainsi, nous investiguons cet aspect, mettant en évidence l'effet de la surface sur la réactivité moléculaire, et la compétition entre la liaison C-C et l'ouverture du cycle thiophène sur trois surfaces de métaux nobles (Cu, Ag, Au). En utilisant des mesures STM et XPS, et en comparant les résultats aux calculs DFT, nous avons suivi la réaction des molécules de tribromoterthienobenzène (TBTTB) à différentes températures et avons déterminé la formation de réseaux organométalliques différents, en particulier sur le substrat d'Au qui a été très peu reporté dans la littérature. Nous démontrons également que la polymérisation et la désulfurisation de la TBTTB se comportent comme deux précessus antagonistes. La désulfurisation se produit à température ambiante sur Cu(111), au-delà de 250 °C sur Ag(111) et uniquement à 300 °C sur Au(111) (Figure 8-12).

8.2.6 Dépôt à chaud – Réseaux organométalliques ordonnés de TBTTB

En accord avec le diagramme de phase présenté dans la Figure 8-12, nous avons optimisé la condition de préaparation et avons pu obtenir de réseaux organométalliques hautement ordonnés sur Ag(111) en déposant la TBTTB directement sur une surface à 200 °C (Figure 8-13). Les domaines ainsi obtenus recouvrent toute la surface du subtrat, et ont en moyenne, une taille de 30x30nm^2, plus grande que l'actuel nœud technologique pour les transistors.

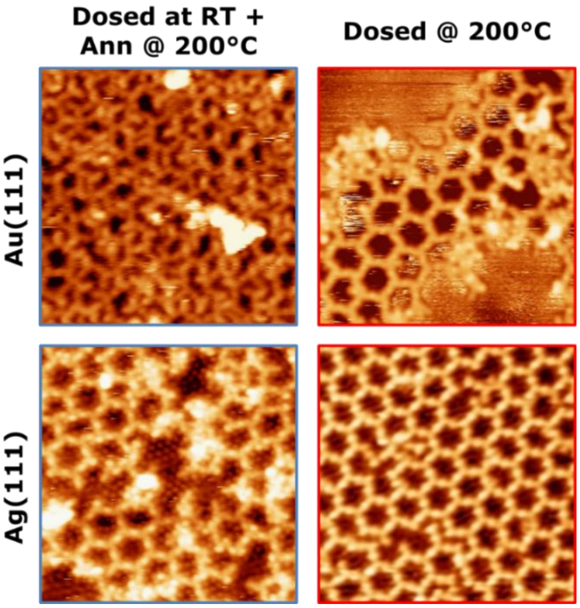

Figure 8-13. **Images STM de TBTTB sur Au(111) et Ag(111), déposé à température ambiante puis recuit à 200 °C (gauche), et déposé sur une surface chaude maintenue à 200 °C (droite).**

La même approche sur une surface d’Au stable à l’air libre mène à la formation de domaines faiblement ordonnés de type hexagonal (Figure 8-13), Ce résultat est alors une première étape importante dans la poursuite de l’élaboration des matériaux organométalliques 2D dans un environnement adapté aux applications.

8.3 Conclusions et perspectives

Dans ce travail de thèse, la réalisation sur substrats métalliques des nanostructures organiques a été étudiée par des mesures de microscopie par effet tunnel et différentes spectroscopies par photoémission et les résultats sont souvent comparés avec des calculs par la théorie de la fonctionnelle de la densité. Toutes les mesures ont été réalisées dans des conditions ultra-vide, en utilisant des évaporateurs de type Knudsen, et des vannes de fuite pour doser les précurseurs sur des surfaces métalliques. La formation des nanostructures – de l’auto-assemblage moléculaire aux polymères conjugués en passant par les intermédiaires organométalliques – a été observée et analysée. Deux différentes voies ont été exploitées pour réaliser de telles structures covalentes : le couplage d’Ullmann (Chapitre 3-5) et la polymérisation diacétylène (Chapitre 6). Dans les deux cas, les conditions nécessaires et les paramètres optimisés pour la croissance polymérique ont été largement étudiés, et nous avons mis l’accent plus sur les principes chimiques et physiques qui contrôlent la réaction plutôt que sur la structure finale obtenue. Ce travail débute avec l'étude du taux de recouvrement des molécules sur surface, montrant ainsi que ce taux joue un rôle prédominant, pouvant impliquer la formation de différentes structures auto-assemblées (Figure 3-6), qui suivent différents chemins de réaction (Figure 3-7 et Figure 3-8).

Dans un deuxième temps, nous avons investigué l'importance de l'halogène dans le couplage d'Ullmann. Nous avons montré que les halogènes ne sont pas à considérer comme des sous-produits uniquement, mais sont également impliqué dans formation de la structure finale et au processus de la réaction. Nous avons démontré, en utilisant des précurseurs 1,4 dihalobenzène, la présence de brome ou de chlore peut amener les nanostructures organométalliques à s'aligner sur la surface de Cu(110) dans des directions différentes que si le précurseur contenait de l'iode (Figure 4-6 et Figure 4-7). Les interactions entre le squelette carboné, l'halogène utilisé et la surface peuvent modifier la cinétique de la réaction et la thermodynamique du processus de polymérisation, entraînant parfois à la création de réactions intermédiaires supplémentaires (Figure 4-1), en changeant les énergies d'activation pour la polymérisation (Figure 4-4 et Figure 4-12), ainsi que le mécanisme de réaction (Figure 4-5).

Le projet de thèse s'appuie sur la tâche fondamentale dans la quête de la réalisation des nanostructures bi-dimensionnelles hautement ordonnées qu'est l'étude des paramètres de la réaction et l'effort que l'on apporte à dévoiler les principes chimico-physiques déterminants de la réaction d'Ullmann sur surface (Figure 8-1). L'étude des molécules contenant plus de deux halogènes, et capables de former des réseaux 2D était alors réalisée, en investiguant la réaction d'un précurseur tridenté de terthienobenzène. Cette dernière a révélé la possibilité de construction d'un réseau de polymères organométalliques covalents même sur une surface d'or considérée comme peu propice à la réaction (Figure 5-4). Une telle étude nous a également permis d'acquérir des informations supplémentaires sur l'importance de la composition de la molécule précurseur ainsi que son interaction avec le substrat sous-jacent (Figure 5-2, Figure 5-5 et Figure 5-9), montrant ainsi la nécessité de réfléchir à l'ensemble « molécule + substrat » avant toute étude de polymérisation sur surface. Cette même étude a démontré que si les hétéro atomes sont en effet des éléments clés dans la modification du produit final, ils apportent également des effets secondaires qui peuvent être difficiles d'identifier et contrôler à priori. Nous avons ainsi mis en lumière la possibilité d'un chemin de réaction supplémentaire où les molécules forment soit des liaisons C-C, soit subissent une ouverture du cycle thiophène avec la formation des liaisons S-Me réduisant alors l’ordre à grande échelle et la qualité du réseau de polymères (Figure 5-2, Figure 5-5 et Figure 5-9). Finallement, il est judicieux de noter que l’ordre à grande distance de réseaux organométallique a été obtenue grâce à un dépôt sur une surface chaude maintenue à 200 °C (Figure 5-6), Ce résultat nous donne l’espoir d’un processus exploitable pour la fabrication à grande échelle des matériaux de type graphène.

8.3.1 Etudes futures

Si ce travail de thèse a pu contribuer grandement à l’analyse et la compréhension profonde de certaines propriétés chimique et physique de la réaction d’Ullmann sur surface, l’objectif final du projet reste néanmoins infécond (Figure 8-1). Les buts principaux identifiés étaient alors : *i.* comprendre la réaction d’Ullmann sur surface, en particulier le rôle des paramètres de croissance, *ii.* Croître des structures polymériques hautement ordonnées à grande distance et *iii.* Isoler le polymère 2D ainsi formé de la surface et l’intégrer dans un dispositif.

La première étape s’est avérée plus compliquée qu’attendue, et a mené à des découvertes intéressantes donnant lieu à un nombre conséquent de publications ainsi qu’un progrès sans précédent dans la compréhension du comportement des petites molécules sur surface. Le deuxième objectif a été partiellement rempli : nous avons pu créer de structures hautement ordonnées, mais ces structures sont en fait formées de polymères organométalliques au lieu de liaisons C-C. Toutefois, cette etude nous a permis d’améliorer le contrôle de la croissance 2D des réseaux polymériques, en mettant en place ce procédé de dépôt à chaud sur la surface. Finallement, la dernière étape, *i.e*, la production de dispositif (Figure 8-1). N’a pas été abordée, et les premiers essais sont réalisés à l’heure de la réaction de cette thèse. Les futures tâches à réaliser dans la maturation du projet sont les suivantes :

- L’étude des autres molécules tridentées comportant des hétéro atomes, tels que N ou O à la place de S, afin d’éviter l’ouverture du cycle thiophène pendant la réaction.
- L’étude de l’ordre des structures obtenues et optimisation des conditions de croissance.
- Isolation de la couche moléculaire et son intégration dans un dispositif.

9 REFERENCES, FIGURES AND TABLES

1. Cavin, R. K.; Lugli, P.; Zhirnov, V. V., Science and Engineering Beyond Moore's Law. *Proc. IEEE* **2012,** *100* (Special Centennial Issue), 1720-1749.
2. Schulz, M., The end of the road for silicon? *Nature* **1999,** *399* (6738), 729-730.
3. Meindl, J. D.; Chen, Q.; Davis, J. A., Limits on silicon nanoelectronics for terascale integration. *Science* **2001,** *293* (5537), 2044-9.
4. Thompson, S. E.; Parthasarathy, S., Moore's law: the future of Si microelectronics. *Materials today* **2006,** *9* (6).
5. Giridharagopal, R.; Kelly, K. F., Substrate-Dependent Properties of Polydiacetylene Nanowires on Graphite and MoS2. *ACS Nano* **2008,** *2* (8), 1571-1580.
6. Castro Neto, A. H.; Guinea, F.; Peres, N. M. R.; Novoselov, K. S.; Geim, A. K., The electronic properties of graphene. *Rev. Mod. Phys.* **2009,** *81* (1), 109-162.
7. Lee, C.; Wei, X.; Kysar, J. W.; Hone, J., Measurement of the elastic properties and intrinsic strength of monolayer graphene. *Science* **2008,** *321* (5887), 385-388.
8. Andryushechkin, B. V., Halogen Adsorption on Metals. In *Surf. Interface Sci.*, Wandelt, K., Ed. Wiley-VCH Verlag GmbH & Co. KGaA: Weinheim, Germany, 2016; Vol. 5, pp 207-254.
9. Jiang, D.-e.; Cooper, V. R.; Dai, S., Porous graphene as the ultimate membrane for gas separation. *Nano Lett.* **2009,** *9* (12), 4019-4024.
10. Hankel, M.; Jiao, Y.; Du, A.; Gray, S. K.; Smith, S. C., Asymmetrically decorated, doped porous graphene as an effective membrane for hydrogen isotope separation. *J. Phys. Chem. C* **2012,** *116* (11), 6672-6676.
11. Min, S. K.; Kim, W. Y.; Cho, Y.; Kim, K. S., Fast DNA sequencing with a graphene-based nanochannel device. *Nat. Nanotechnol.* **2011,** *6* (3), 162-165.
12. De Feyter, S.; De Schryver, F. C., Self-Assembly at the Liquid/Solid Interface: STM Reveals. *J. Phys. Chem. B* **2005,** *109* (10), 4290-4302.
13. Endo, O.; Furuta, T.; Ozaki, H.; Sonoyama, M.; Mazaki, Y., Structures of 17,19-Hexatriacontadiyne Monolayers on Au(111) Studied by Infrared Reflection Absorption Spectroscopy and Scanning Tunneling Microscopy. *J. Phys. Chem. B* **2006,** *110* (26), 13100-13106.
14. Zhang, X.-m.; Xu, S.-d.; Li, M.; Shen, Y.-t.; Wei, Z.-q.; Wang, S.; Zeng, Q.-d.; Wang, C., Photo-Induced Polymerization and Isomerization on the Surface Observed by Scanning Tunneling Microscopy. *J. Phys. Chem. C* **2012,** *116* (16), 8950-8955.
15. Perepichka, D. F.; Rosei, F., Chemistry. Extending polymer conjugation into the second dimension. *Science* **2009,** *323* (5911), 216-217.
16. Björk, J.; Hanke, F.; Stafström, S., Mechanisms of halogen-based covalent self-assembly on metal surfaces. *J. Am. Chem. Soc.* **2013,** *135* (15), 5768-5775.

17. Okawa, Y.; Aono, M., Materials science: Nanoscale control of chain polymerization. *Nature* **2001,** *409* (6821), 683-684.

18. Lafferentz, L.; Eberhardt, V.; Dri, C.; Africh, C.; Comelli, G.; Esch, F.; Hecht, S.; Grill, L., Controlling on-surface polymerization by hierarchical and substrate-directed growth. *Nat. Chem.* **2012,** *4* (3), 215-220.

19. Lipton-Duffin, J.; Ivasenko, O.; Perepichka, D.; Rosei, F., Synthesis of Polyphenylene Molecular Wires by Surface-Confined Polymerization. *Small* **2009,** *5* (5), 592-597.

20. Grill, L.; Dyer, M.; Lafferentz, L.; Persson, M.; Peters, M. V.; Hecht, S., Nano-architectures by covalent assembly of molecular building blocks. *Nat. Nanotechnol.* **2007,** *2* (11), 687-691.

21. Matena, M.; Stöhr, M.; Riehm, T.; Björk, J.; Martens, S.; Dyer, M. S.; Persson, M.; Lobo-Checa, J.; Müller, K.; Enache, M., Aggregation and Contingent Metal/Surface Reactivity of 1, 3, 8, 10-Tetraazaperopyrene (TAPP) on Cu (111). *Chem. - Eur. J.* **2010,** *16* (7), 2079-2091.

22. Zhang, Y. Q.; Kepcija, N.; Kleinschrodt, M.; Diller, K.; Fischer, S.; Papageorgiou, A. C.; Allegretti, F.; Bjork, J.; Klyatskaya, S.; Klappenberger, F.; Ruben, M.; Barth, J. V., Homo-coupling of terminal alkynes on a noble metal surface. *Nat Commun* **2012,** *3*, 1286.

23. Kanuru, V. K.; Kyriakou, G.; Beaumont, S. K.; Papageorgiou, A. C.; Watson, D. J.; Lambert, R. M., Sonogashira coupling on an extended gold surface in vacuo: reaction of phenylacetylene with iodobenzene on Au(111). *J Am Chem Soc* **2010,** *132* (23), 8081-6.

24. Cardenas, L.; Gutzler, R.; Lipton-Duffin, J.; Fu, C.; Brusso, J. L.; Dinca, L. E.; Vondráček, M.; Fagot-Revurat, Y.; Malterre, D.; Rosei, F., Synthesis and electronic structure of a two dimensional π-conjugated polythiophene. *Chem. Sci.* **2013,** *4*, 3263-3268.

25. Di Giovannantonio, M.; Contini, G., Reversibility and intermediate steps as key tools for the growth of extended ordered polymers via on-surface synthesis. *J. Phys. Condens. Matter* **2018,** *30* (9), 093001.

26. Xi, M.; Bent, B. E., Mechanisms of the Ullmann coupling reaction in adsorbed monolayers. *J. Am. Chem. Soc.* **1993,** *115* (16), 7426-7433.

27. Hla, S.-W.; Bartels, L.; Meyer, G.; Rieder, K.-H., Inducing All Steps of a Chemical Reaction with the Scanning Tunneling Microscope Tip: Towards Single Molecule Engineering. *Phys. Rev. Lett.* **2000,** *85* (13), 2777-2780.

28. Schlögl, S.; Heckl, W. M.; Lackinger, M., On-surface radical addition of triply iodinated monomers on Au (111)—the influence of monomer size and thermal post-processing. *Surf. Sci.* **2012,** *606* (13), 999-1004.

29. Gutzler, R.; Walch, H.; Eder, G.; Kloft, S.; Heckl, W. M.; Lackinger, M., Surface mediated synthesis of 2D covalent organic frameworks: 1, 3, 5-tris (4-bromophenyl) benzene on graphite (001), Cu (111), and Ag (110). *Chem. Commun.* **2009,** (29), 4456-4458.

30. Di Giovannantonio, M.; El Garah, M.; Lipton-Duffin, J.; Meunier, V.; Cardenas, L.; Fagot Revurat, Y.; Cossaro, A.; Verdini, A.; Perepichka, D. F.; Rosei, F.; Contini, G., Insight into Organometallic Intermediate and Its Evolution to Covalent Bonding in Surface-Confined Ullmann Polymerization. *ACS Nano* **2013,** *7* (9), 8190-8198.

31. Di Giovannantonio, M.; El Garah, M.; Lipton-Duffin, J.; Meunier, V.; Cardenas, L.; Fagot-Revurat, Y.; Cossaro, A.; Verdini, A.; Perepichka, D. F.; Rosei, F.; Contini, G., Reply to "Comment on 'Insight into Organometallic Intermediate and Its Evolution to Covalent Bonding in Surface-Confined Ullmann Polymerization'". *ACS Nano* **2014,** *8* (3), 1969-1971.

32. Xi, M.; Bent, B. E., Iodobenzene on Cu(111): formation and coupling of adsorbed phenyl groups. *Surf. Sci.* **1992,** *278* (1), 19-32.

33. Meyers, J. M.; Gellman, A. J., Effect of substituents on the phenyl coupling reaction on Cu(111). *Surf. Sci.* **1995,** *337* (1), 40-50.

34. Lackinger, M., Surface-assisted Ullmann coupling. *Chem. Commun.* **2017,** *53* (56), 7872-7885.

35. Moore, G. E., Cramming more components onto integrated circuits. *Electronics* **1965,** *38*.

36. Loughran, J., Moore's Law 2017: an uphill battle. *Engineering and Technology* 2017.

37. Meindl, J. D.; Chen, Q.; Davis, J. A., Limits on Silicon Nanoelectronics for Terascale Integration. *Science* **2001,** *293* (5537), 2044-2049.

38. Davis, J. A.; Venkatesan, R.; Kaloyeros, A.; Beylansky, M.; Souri, S. J.; Banerjee, K.; Saraswat, K. C.; Rahman, A.; Reif, R.; Meindl, J. D., Interconnect limits on gigascale integration (GSI) in the 21st century. *Proceedings of the IEEE* **2001,** *89* (3), 305-324.

39. Markov, I. L., Limits on fundamental limits to computation. *Nature* **2014,** *512*, 147.

40. Nohira, H.; Omura, A.; Katayama, M.; Hattori, T., Valence band edge of ultra-thin silicon oxide near the interface. *Appl. Surf. Sci.* **1998,** *123-124*, 546-549.

41. Mueller, H. H.; Schulz, M., Random telegraph signal: An atomic probe of the local current in field-effect transistors. *Journal of Applied Physics* **1998,** *83* (3), 1734-1741.

42. Thompson, S. E.; Parthasarathy, S., Moore's law: the future of Si microelectronics. *Mater. Today* **2006,** *9* (6), 20-25.

43. Franklin, A. D., Nanomaterials in transistors: From high-performance to thin-film applications. *Science* **2015,** *349* (6249), aab2750.

44. Mishra, P.; Muttreja, A.; Jha, N. K., FinFET circuit design. In *Nanoelectronic Circuit Design*, Springer: 2011; pp 23-54.

45. Nowak, E. J.; Aller, I.; Ludwig, T.; Kim, K.; Joshi, R. V.; Ching-Te, C.; Bernstein, K.; Puri, R., Turning silicon on its edge [double gate CMOS/FinFET technology]. *IEEE Circuits Devices Mag.* **2004,** *20* (1), 20-31.

46. So, F., *Organic electronics: materials, processing, devices and applications*. CRC press: 2009.

47. Burroughes, J. H.; Bradley, D. D. C.; Brown, A. R.; Marks, R. N.; Mackay, K.; Friend, R. H.; Burns, P. L.; Holmes, A. B., Light-emitting diodes based on conjugated polymers. *Nature* **1990,** *347* (6293), 539-541.

48. Gustafsson, G.; Cao, Y.; Treacy, G. M.; Klavetter, F.; Colaneri, N.; Heeger, A. J., Flexible light-emitting diodes made from soluble conducting polymers. *Nature* **1992,** *357*, 477.

49. Shirakawa, H.; Louis, E. J.; MacDiarmid, A. G.; Chiang, C. K.; Heeger, A. J., Synthesis of electrically conducting organic polymers: halogen derivatives of polyacetylene,(CH) x. *Journal of the Chemical Society, Chemical Communications* **1977,** (16), 578-580.

50. Chiang, C. K.; Fincher, C. R.; Park, Y. W.; Heeger, A. J.; Shirakawa, H.; Louis, E. J.; Gau, S. C.; MacDiarmid, A. G., Electrical Conductivity in Doped Polyacetylene. *Phys. Rev. Lett.* **1977,** *39* (17), 1098-1101.

51. Tsumura, A.; Koezuka, H.; Ando, T., Macromolecular electronic device: Field-effect transistor with a polythiophene thin film. *Appl. Phys. Lett.* **1986,** *49* (18), 1210-1212.

52. Skotheim, T. A., *Handbook of conducting polymers*. CRC press: 1997.

53. Facchetti, A., π-Conjugated Polymers for Organic Electronics and Photovoltaic Cell Applications. *Chem. Mater.* **2011,** *23* (3), 733-758.

54. McGehee, M. D.; Heeger, A. J., Semiconducting (Conjugated) Polymers as Materials for Solid-State Lasers. *Advanced Materials* **2000,** *12* (22), 1655-1668.

55. Heeger, A. J.; Moses, D.; Sinclair, M., Semiconducting polymers: Fast response non-linear optical materials. *Synthetic Metals* **1986,** *15* (2), 95-104.

56. Vladsinger Orbital hybridization in benzene rings. https://en.wikipedia.org/wiki/Conjugated_system (accessed 15 April 2019).

57. Novoselov, K. S.; Geim, A. K.; Morozov, S. V.; Jiang, D.; Zhang, Y.; Dubonos, S. V.; Grigorieva, I. V.; Firsov, A. A., Electric Field Effect in Atomically Thin Carbon Films. *Science* **2004,** *306* (5696), 666-669.

58. Geim, A. K.; Novoselov, K. S., The rise of graphene. *Nat. Mater.* **2007,** *6* (3), 183-191.

59. AlexanderAlUS The ideal crystalline structure of graphene is a hexagonal grid. https://en.wikipedia.org/wiki/Graphene (accessed 30 March 2019).

60. Novoselov, K. S.; Geim, A. K.; Morozov, S. V.; Jiang, D.; Katsnelson, M. I.; Grigorieva, I. V.; Dubonos, S. V.; Firsov, A. A., Two-dimensional gas of massless Dirac fermions in graphene. *Nature* **2005,** *438* (7065), 197-200.

61. Lang, B., A LEED study of the deposition of carbon on platinum crystal surfaces. *Surf. Sci.* **1975,** *53* (1), 317-329.

62. Eizenberg, M.; Blakely, J. M., Carbon monolayer phase condensation on Ni(111). *Surface Science* **1979,** *82* (1), 228-236.

63. Lu, X.; Yu, M.; Huang, H.; Ruoff, R. S., Tailoring graphite with the goal of achieving single sheets. *Nanotechnology* **1999,** *10* (3), 269-272.

64. Viculis, L. M.; Mack, J. J.; Kaner, R. B., A Chemical Route to Carbon Nanoscrolls. *Science* **2003,** *299* (5611), 1361-1361.

65. Park, S.; Ruoff, R. S., Chemical methods for the production of graphenes. *Nat. Nanotechnol.* **2009,** *4*, 217.

66. Reina, A.; Jia, X.; Ho, J.; Nezich, D.; Son, H.; Bulovic, V.; Dresselhaus, M. S.; Kong, J., Large Area, Few-Layer Graphene Films on Arbitrary Substrates by Chemical Vapor Deposition. *Nano Lett.* **2009,** *9* (1), 30-35.

67. Jiao, L.; Wang, X.; Diankov, G.; Wang, H.; Dai, H., Facile synthesis of high-quality graphene nanoribbons. *Nat. Nanotechnol.* **2010,** *5*, 321.

68. Xin, G.; Hwang, W.; Kim, N.; Cho, S. M.; Chae, H., A graphene sheet exfoliated with microwave irradiation and interlinked by carbon nanotubes for high-performance transparent flexible electrodes. *Nanotechnology* **2010,** *21* (40), 405201.

69. Jariwala, D.; Srivastava, A.; Ajayan, P. M., Graphene Synthesis and Band Gap Opening. *J. Nanosci. Nanotechnol.* **2011,** *11* (8), 6621-6641.

70. Bhuyan, M. S. A.; Uddin, M. N.; Islam, M. M.; Bipasha, F. A.; Hossain, S. S., Synthesis of graphene. *Int. Nano Lett.* **2016,** *6* (2), 65-83.

71. Schwierz, F., Graphene transistors. *Nat. Nanotechnol.* **2010,** *5* (7), 487-496.

72. Kawasaki, T.; Ichimura, T.; Kishimoto, H.; Asneil Akbar, A.; Ogawa, T.; Oshima, C., Double atomic layers of graphene/monolayer h-BN on Ni(111) studied by scanning tunneling microscopy and scanning tunneling spectroscopy. *Surf. Rev. Lett.* **2002,** *09* (03n04), 1459-1464.

73. Hildebrand, M.; Abualnaja, F.; Makwana, Z.; Harrison, N. M., Strain Engineering of Adsorbate Self-Assembly on Graphene for Band Gap Tuning. *J. Phys. Chem. C* **2019,** *123* (7), 4475-4482.

74. Balog, R.; Jørgensen, B.; Nilsson, L.; Andersen, M.; Rienks, E.; Bianchi, M.; Fanetti, M.; Lægsgaard, E.; Baraldi, A.; Lizzit, S., Bandgap opening in graphene induced by patterned hydrogen adsorption. *Nat. Mater.* **2010,** *9* (4), 315-319.

75. Li, X.; Wang, X.; Zhang, L.; Lee, S.; Dai, H., Chemically Derived, Ultrasmooth Graphene Nanoribbon Semiconductors. *Science* **2008,** *319* (5867), 1229-1232.

76. Zhou, S.; Gweon, G.-H.; Fedorov, A.; First, P.; De Heer, W.; Lee, D.-H.; Guinea, F.; Neto, A. C.; Lanzara, A., Substrate-induced bandgap opening in epitaxial graphene. *Nat. Mater.* **2007,** *6* (10), 770-775.

77. Ci, L.; Song, L.; Jin, C.; Jariwala, D.; Wu, D.; Li, Y.; Srivastava, A.; Wang, Z. F.; Storr, K.; Balicas, L.; Liu, F.; Ajayan, P. M., Atomic layers of hybridized boron nitride and graphene domains. *Nat. Mater.* **2010,** *9,* 430.

78. Chen, Y.-C.; de Oteyza, D. G.; Pedramrazi, Z.; Chen, C.; Fischer, F. R.; Crommie, M. F., Tuning the Band Gap of Graphene Nanoribbons Synthesized from Molecular Precursors. *ACS Nano* **2013,** *7* (7), 6123-6128.

79. Wei, D.; Liu, Y.; Wang, Y.; Zhang, H.; Huang, L.; Yu, G., Synthesis of N-Doped Graphene by Chemical Vapor Deposition and Its Electrical Properties. *Nano Lett.* **2009,** *9* (5), 1752-1758.

80. Schlüter, A. D. Structural difference between a linear and a two-dimensional (2D) polymer. https://en.wikipedia.org/wiki/Two-dimensional_polymer (accessed 15 December 2018).

81. Staudinger, H., Über Polymerisation. *Berichte der deutschen chemischen Gesellschaft (A and B Series)* **1920,** *53* (6), 1073-1085.

82. Sakamoto, J.; van Heijst, J.; Lukin, O.; Schlüter, A. D., Two-Dimensional Polymers: Just a Dream of Synthetic Chemists? *Angew. Chem., Int. Ed.* **2009,** *48* (6), 1030-1069.

83. Peierls, R. In *Quelques propriétés typiques des corps solides*, Annales de l'institut Henri Poincaré, 1935; pp 177-222.

84. Landau, L., Zur Theorie der phasenumwandlungen II. *Phys. Z. Sowjetunion* **1937,** *11* (545), 26-35.

85. Mermin, N. D., Crystalline Order in Two Dimensions. *Phys. Rev.* **1968,** *176* (1), 250-254.

86. Venables, J. A.; Spiller, G. D. T.; Hanbucken, M., Nucleation and growth of thin films. *Reports on Progress in Physics* **1984,** *47* (4), 399-459.

87. Evans, J. W.; Thiel, P. A.; Bartelt, M. C., Morphological evolution during epitaxial thin film growth: Formation of 2D islands and 3D mounds. *Surf. Sci. Rep.* **2006,** *61* (1), 1-128.

88. Nelson, D. P., T., Weinberg, S., *Statistical Mechanics of Membranes and Surfaces*. World Scientific, 2nd edition, 2004.

89. Meyer, J. C.; Geim, A. K.; Katsnelson, M. I.; Novoselov, K. S.; Booth, T. J.; Roth, S., The structure of suspended graphene sheets. *Nature* **2007,** *446*, 60.

90. Burwell, R., Manual of symbols and therminology for physicochemical quantities and units. In *Pure and Applied Chemistry*, International union of pure and applied chemistry: 1976; Vol. 46, pp 71-90.

91. Gutzler, R.; Cardenas, L.; Rosei, F., Kinetics and thermodynamics in surface-confined molecular self-assembly. *Chem. Sci.* **2011,** *2* (12), 2290-2300.

92. Whitesides, G. M.; Grzybowski, B., Self-Assembly at All Scales. *Science* **2002,** *295* (5564), 2418-2421.

93. Whitesides, G. M.; Mathias, J. P.; Seto, C. T., Molecular self-assembly and nanochemistry: a chemical strategy for the synthesis of nanostructures. *Science* **1991,** *254* (5036), 1312-1319.

94. Zhang, S., Fabrication of novel biomaterials through molecular self-assembly. *Nat. Biotechnol.* **2003,** *21*, 1171.

95. Name-Reaction.com https://www.name-reaction.com/ullmann-reaction (accessed 18 April 2019).

96. Ullmann, F.; Bielecki, J., Ueber Synthesen in der Biphenylreihe. *Ber. Dtsch. Chem. Ges.* **1901,** *34* (2), 2174-2185.

97. Ullmann, F.; Sponagel, P., Ueber Phenylirung von Phenolen. *Justus Liebigs Annalen der Chemie* **1906,** *350* (1-2), 83-107.

98. Sambiagio, C.; Marsden, S. P.; Blacker, A. J.; McGowan, P. C., Copper catalysed Ullmann type chemistry: from mechanistic aspects to modern development. *Chem. Soc. Rev.* **2014,** *43* (10), 3525-3550.

99. Lin, J. L.; Bent, B. E., Carbon-halogen bond dissociation on copper surfaces: effect of alkyl chain length. *J. Phys. Chem.* **1992,** *96* (21), 8529-8538.

100. Fan, Q.; Zhu, J.; Gottfried, J. M., On-Surface Ullmann Reaction for the Synthesis of Polymers and Macrocycles. In *On-Surface Synthesis II*, Springer: 2018; pp 83-112.

101. Steiner, C.; Gebhardt, J.; Ammon, M.; Yang, Z.; Heidenreich, A.; Hammer, N.; Görling, A.; Kivala, M.; Maier, S., Hierarchical on-surface synthesis and electronic structure of carbonyl-functionalized one- and two-dimensional covalent nanoarchitectures. *Nat. Commun.* **2017,** *8*, 14765.

102. Eichhorn, J.; Nieckarz, D.; Ochs, O.; Samanta, D.; Schmittel, M.; Szabelski, P. J.; Lackinger, M., On-Surface Ullmann Coupling: The Influence of Kinetic Reaction Parameters on the Morphology and Quality of Covalent Networks. *ACS Nano* **2014,** *8* (8), 7880-7889.

103. Cai, J.; Ruffieux, P.; Jaafar, R.; Bieri, M.; Braun, T.; Blankenburg, S.; Muoth, M.; Seitsonen, A. P.; Saleh, M.; Feng, X., Atomically precise bottom-up fabrication of graphene nanoribbons. *Nature* **2010,** *466* (7305), 470-473.

104. Talirz, L.; Ruffieux, P.; Fasel, R., On-Surface Synthesis of Atomically Precise Graphene Nanoribbons. *Adv. Mater*. **2016,** *28* (29), 6222-6231.

105. McCarty, G. S.; Weiss, P. S., Formation and Manipulation of Protopolymer Chains. *J. Am. Chem. Soc.* **2004,** *126* (51), 16772-16776.

106. Blake, M. M.; Nanayakkara, S. U.; Claridge, S. A.; Fernández-Torres, L. C.; Sykes, E. C. H.; Weiss, P. S., Identifying Reactive Intermediates in the Ullmann Coupling Reaction by Scanning Tunneling Microscopy and Spectroscopy. *J. Phys. Chem. A* **2009,** *113* (47), 13167-13172.

107. Wang, W.; Shi, X.; Wang, S.; Van Hove, M. A.; Lin, N., Single-Molecule Resolution of an Organometallic Intermediate in a Surface-Supported Ullmann Coupling Reaction. *J. Am. Chem. Soc.* **2011,** *133* (34), 13264-13267.

108. Bieri, M.; Nguyen, M. T.; Groning, O.; Cai, J. M.; Treier, M.; Ait-Mansour, K.; Ruffieux, P.; Pignedoli, C. A.; Passerone, D.; Kastler, M.; Mullen, K.; Fasel, R., Two-Dimensional Polymer Formation on Surfaces: Insight into the Roles of Precursor Mobility and Reactivity. *J. Am. Chem. Soc.* **2010,** *132* (46), 16669-16676.

109. Rastgoo Lahrood, A.; Bjork, J.; Heckl, W. M.; Lackinger, M., 1,3-Diiodobenzene on Cu(111) - an exceptional case of on-surface Ullmann coupling. *Chem. Commun.* **2015,** *51* (68), 13301-13304.

110. Björk, J., Reaction mechanisms for on-surface synthesis of covalent nanostructures. *J. Phys.: Condens. Matter* **2016,** *28* (8), 083002.

111. Balajka, J.; Pavelec, J.; Komora, M.; Schmid, M.; Diebold, U., Apparatus for dosing liquid water in ultrahigh vacuum. *Rev. Sci. Instrum.* **2018,** *89* (8), 083906.

112. Dai, J.; Fan, Q.; Wang, T.; Kuttner, J.; Hilt, G.; Gottfried, J. M.; Zhu, J., The role of the substrate structure in the on-surface synthesis of organometallic and covalent oligophenylene chains. *Phys. Chem. Chem. Phys.* **2016,** *18* (30), 20627-20634.

113. Fan, Q.; Wang, T.; Dai, J.; Kuttner, J.; Hilt, G.; Gottfried, J. M.; Zhu, J., On-Surface Pseudo-High-Dilution Synthesis of Macrocycles: Principle and Mechanism. *ACS Nano* **2017,** *11* (5), 5070-5079.

114. Perepichka, D. F.; Rosei, F., Extending Polymer Conjugation into the Second Dimension. *Science* **2009,** *323* (5911), 216-217.

115. Vasseur, G.; Fagot-Revurat, Y.; Sicot, M.; Kierren, B.; Moreau, L.; Malterre, D.; Cardenas, L.; Galeotti, G.; Lipton-Duffin, J.; Rosei, F.; Di Giovannantonio, M.; Contini, G.; Le Fèvre, P.; Bertran, F.; Liang, L.; Meunier, V.; Perepichka, D. F., Quasi one-dimensional band dispersion and surface metallization in long-range ordered polymeric wires. *Nat. Commun.* **2016,** *7*, 10235.

116. Carbonell-Sanromà, E.; Garcia-Lekue, A.; Corso, M.; Vasseur, G.; Brandimarte, P.; Lobo-Checa, J.; de Oteyza, D. G.; Li, J.; Kawai, S.; Saito, S.; Yamaguchi, S.; Ortega, J. E.; Sánchez-Portal, D.; Pascual, J. I., Electronic Properties of Substitutionally Boron-Doped Graphene Nanoribbons on a Au(111) Surface. *J. Phys. Chem. C* **2018,** *122* (28), 16092-16099.

117. Nguyen, G. D.; Toma, F. M.; Cao, T.; Pedramrazi, Z.; Chen, C.; Rizzo, D. J.; Joshi, T.; Bronner, C.; Chen, Y.-C.; Favaro, M.; Louie, S. G.; Fischer, F. R.; Crommie, M. F., Bottom-Up Synthesis of N = 13 Sulfur-Doped Graphene Nanoribbons. *J. Phys. Chem. C* **2016,** *120* (5), 2684-2687.

118. Ruffieux, P.; Wang, S.; Yang, B.; Sánchez-Sánchez, C.; Liu, J.; Dienel, T.; Talirz, L.; Shinde, P.; Pignedoli, C. A.; Passerone, D.; Dumslaff, T.; Feng, X.; Müllen, K.; Fasel, R., On-surface synthesis of graphene nanoribbons with zigzag edge topology. *Nature* **2016,** *531* (7595), 489-492.

119. Bronner, C.; Durr, R. A.; Rizzo, D. J.; Lee, Y.-L.; Marangoni, T.; Kalayjian, A. M.; Rodriguez, H.; Zhao, W.; Louie, S. G.; Fischer, F. R.; Crommie, M. F., Hierarchical On-Surface Synthesis of Graphene Nanoribbon Heterojunctions. *ACS Nano* **2018,** *12* (3), 2193-2200.

120. Zhang, W.; Chen, Z.; Yang, B.; Wang, X.-Y.; Berger, R.; Narita, A.; Barin, G. B.; Ruffieux, P.; Fasel, R.; Feng, X.; Räder, H. J.; Müllen, K., Monitoring the On-Surface Synthesis of Graphene Nanoribbons by Mass Spectrometry. *Analytical Chemistry* **2017,** *89* (14), 7485-7492.

121. Dong, L.; Wang, S.; Wang, W.; Chen, C.; Lin, T.; Adisoejoso, J.; Lin, N., Transition Metals Trigger On-Surface Ullmann Coupling Reaction: Intermediate, Catalyst and Template. In *On-Surface Synthesis*, Springer: 2016; pp 23-42.

122. Gutzler, R.; Walch, H.; Eder, G.; Kloft, S.; Heckl, W. M.; Lackinger, M., Surface mediated synthesis of 2D covalent organic frameworks: 1,3,5-tris(4-bromophenyl)benzene on graphite(001), Cu(111), and Ag(110). *Chem. Commun.* **2009,** (29), 4456-4458.

123. Bieri, M.; Treier, M.; Cai, J.; Aït-Mansour, K.; Ruffieux, P.; Gröning, O.; Gröning, P.; Kastler, M.; Rieger, R.; Feng, X., Porous graphenes: two-dimensional polymer synthesis with atomic precision. *Chem. Commun.* **2009,** (45), 6919-6921.

124. Bombis, C.; Ample, F.; Lafferentz, L.; Yu, H.; Hecht, S.; Joachim, C.; Grill, L., Single Molecular Wires Connecting Metallic and Insulating Surface Areas. *Angew. Chem. Int. Ed.* **2009,** *48* (52), 9966-9970.

125. Lipton-Duffin, J. A.; Miwa, J. A.; Kondratenko, M.; Cicoira, F.; Sumpter, B. G.; Meunier, V.; Perepichka, D. F.; Rosei, F., Step-by-step growth of epitaxially aligned polythiophene by surface-confined reaction. *Proc. Natl. Acad. Sci.* **2010,** *107* (25), 11200-11204.

126. Blunt, M. O.; Russell, J. C.; Champness, N. R.; Beton, P. H., Templating molecular adsorption using a covalent organic framework. *Chem. Commun.* **2010,** *46* (38), 7157-7159.

127. Lin, T.; Shang, X. S.; Adisoejoso, J.; Liu, P. N.; Lin, N., Steering On-Surface Polymerization with Metal-Directed Template. *J. Am. Chem. Soc.* **2013,** *135* (9), 3576-3582.

128. Adisoejoso, J.; Lin, T.; Shang, X. S.; Shi, K. J.; Gupta, A.; Liu, P. N.; Lin, N., A Single-Molecule-Level Mechanistic Study of Pd-Catalyzed and Cu-Catalyzed Homocoupling of Aryl Bromide on an Au(111) Surface. *Chemistry – A European Journal* **2014,** *20* (14), 4111-4116.

129. Basagni, A.; Ferrighi, L.; Cattelan, M.; Nicolas, L.; Handrup, K.; Vaghi, L.; Papagni, A.; Sedona, F.; Valentin, C. D.; Agnoli, S.; Sambi, M., On-surface photo-dissociation of C–Br bonds: towards room temperature Ullmann coupling. *Chemical Communications* **2015,** *51* (63), 12593-12596.

130. Zhao, W.; Dong, L.; Huang, C.; Win, Z. M.; Lin, N., Cu- and Pd-catalyzed Ullmann reaction on a hexagonal boron nitride layer. *Chemical Communications* **2016,** *52* (90), 13225-13228.

131. Blankenburg, S.; Cai, J.; Ruffieux, P.; Jaafar, R.; Passerone, D.; Feng, X.; Müllen, K.; Fasel, R.; Pignedoli, C. A., Intraribbon Heterojunction Formation in Ultranarrow Graphene Nanoribbons. *ACS Nano* **2012,** *6* (3), 2020-2025.

132. Han, P.; Akagi, K.; Federici Canova, F.; Mutoh, H.; Shiraki, S.; Iwaya, K.; Weiss, P. S.; Asao, N.; Hitosugi, T., Bottom-Up Graphene-Nanoribbon Fabrication Reveals Chiral Edges and Enantioselectivity. *ACS Nano* **2014,** *8* (9), 9181-9187.

133. Basagni, A.; Sedona, F.; Pignedoli, C. A.; Cattelan, M.; Nicolas, L.; Casarin, M.; Sambi, M., Molecules–Oligomers–Nanowires–Graphene Nanoribbons: A Bottom-Up Stepwise On-Surface Covalent Synthesis Preserving Long-Range Order. *J. Am. Chem. Soc.* **2015,** *137* (5), 1802-1808.

134. Moreno, C.; Vilas-Varela, M.; Kretz, B.; Garcia-Lekue, A.; Costache, M. V.; Paradinas, M.; Panighel, M.; Ceballos, G.; Valenzuela, S. O.; Peña, D.; Mugarza, A., Bottom-up synthesis of multifunctional nanoporous graphene. *Science* **2018,** *360* (6385), 199-203.

135. Beyer, D.; Wang, S.; Pignedoli, C. A.; Melidonie, J.; Yuan, B.; Li, C.; Wilhelm, J.; Ruffieux, P.; Berger, R.; Müllen, K.; Fasel, R.; Feng, X., Graphene Nanoribbons Derived from Zigzag Edge-Encased Poly(para-2,9-dibenzo[bc,kl]coronenylene) Polymer Chains. *J. Am. Chem. Soc.* **2019,** *141* (7), 2843-2846.

136. Faury, T.; Clair, S.; Abel, M.; Dumur, F.; Gigmes, D.; Porte, L., Sequential Linking to Control Growth of a Surface Covalent Organic Framework. *J. Phys. Chem. C* **2012,** *116*, 4819.

137. Gutzler, R.; Perepichka, D. F., π-Electron Conjugation in Two Dimensions. *J. Am. Chem. Soc.* **2013,** *135* (44), 16585-16594.

138. Gutzler, R., Band-structure engineering in conjugated 2D polymers. *Phys. Chem. Chem. Phys.* **2016,** *18* (42), 29092-29100.

139. Gutzler, R.; Perepichka, D. F., π-Electron conjugation in two dimensions. *J. Am. Chem. Soc.* **2013,** *135* (44), 16585-94.

140. Woedkte, S. PhD thesis, CAU Kiel, 2002.

141. Chen, C. J., Origin of atomic resolution on metal surfaces in scanning tunneling microscopy. *Physical Review Letters* **1990,** *65* (4), 448-451.

142. Advanced Photon Source, A. N. L. https://www.aps.anl.gov/SXSPM/Research/Physical-Concept (accessed 18 April 2019).

143. Blanco, J. M.; Flores, F.; Pérez, R., STM-theory: Image potential, chemistry and surface relaxation. *Prog. Surf. Sci.* **2006,** *81* (10), 403-443.

144. Murphy, B. E. The physico-chemical properties of fullerenes and porphyrin derivatives deposited on conducting surfaces. Trinity College Dublin, 2014.

145. Chastain, J., Handbook of X-ray photoelectron spectroscopy. *Perkin-Elmer Corporation* **1992,** *40*, 221.

146. Saiht Prinzipbild der winkelaufgelösten PhotoElektronSpektroskopie mit einem Scienta. https://en.wikipedia.org/wiki/Photoemission_spectroscopy (accessed 18 April 2019).

147. PhysicsOpenLab http://physicsopenlab.org/2017/08/02/bremsstrahlung-radiation/ (accessed 18 April 2019).

148. R. Bartolini, A. H. https://en.wikipedia.org/wiki/Synchrotron_radiation (accessed 18 April 2019).

149. Santarelli/EPSIM 3D, J. F. Synchrotron Soleil: schéma de principe. https://fr.wikipedia.org/wiki/Synchrotron (accessed 18 April 2019).

150. Baraldi, A.; Comelli, G.; Lizzit, S.; Cocco, D.; Paolucci, G.; Rosei, R., Temperature programmed X-ray photoelectron spectroscopy: a new technique for the study of surface kinetics. *Surf. Sci.* **1996,** *367* (3), L67-L72.

151. Ebashi, S.; Koch, M.; Rubenstein, E., *Handbook on synchrotron radiation*. Elsevier Science Pub Co, Inc: United States, 1991.

152. Mahan, G. D., Theory of Photoemission in Simple Metals. *Phys. Rev. B* **1970,** *2* (11), 4334-4350.

153. Mahan, G. D., Angular Dependence of Photoemission in Metals. *Phys. Rev. Lett.* **1970,** *24* (19), 1068-1070.

154. Berglund, C. N.; Spicer, W. E., Photoemission Studies of Copper and Silver: Theory. *Phys. Rev.* **1964,** *136* (4A), A1030-A1044.

155. Hüfner, S., *Photoelectron spectroscopy: principles and applications*. Springer Science & Business Media: 2013.

156. Damascelli, A., Probing the Electronic Structure of Complex Systems by ARPES. *Phys. Scr.* **2004,** *T109*, 61.

157. Hahner, G., Near edge X-ray absorption fine structure spectroscopy as a tool to probe electronic and structural properties of thin organic films and liquids. *Chem. Soc. Rev.* **2006,** *35* (12), 1244-1255.

158. Stöhr, J., *NEXAFS spectroscopy*. Springer-Verlag Berlin Heidelberg: 1992; Vol. 25.

159. Di Giovannantonio, M.; Tomellini, M.; Lipton-Duffin, J.; Galeotti, G.; Ebrahimi, M.; Cossaro, A.; Verdini, A.; Kharche, N.; Meunier, V.; Vasseur, G.; Fagot-Revurat, Y.; Perepichka, D. F.; Rosei, F.; Contini, G., Mechanistic Picture and Kinetic Analysis of Surface-Confined Ullmann Polymerization. *J. Am. Chem. Soc.* **2016,** *138* (51), 16696-16702.

160. Galeotti, G.; Di Giovannantonio, M.; Cupo, A.; Xing, S.; Lipton-Duffin, J.; Ebrahimi, M.; Vasseur, G.; Kierren, B.; Fagot-Revurat, Y.; Tristant, D.; Meunier, V.; Perepichka, D.; Rosei, F. C., Giorgio, Unexpected Organometallic Intermediate in Surface-confined Ullmann Coupling. *Nanoscale* **2019**, *11*, 7682-7689.

161. Bieri, M.; Nguyen, M.-T.; Groning, O.; Cai, J.; Treier, M.; Ait-Mansour, K.; Ruffieux, P.; Pignedoli, C. A.; Passerone, D.; Kastler, M.; Mullen, K.; Fasel, R., Two-Dimensional Polymer Formation on Surfaces: Insight into the Roles of Precursor Mobility and Reactivity. *J. Am. Chem. Soc.* **2010,** *132* (46), 16669-16676.

162. Kollmar, C.; Sixl, H., Reaction kinetics of the solid state polymerization in diacetylene crystals. *J. Chem. Phys.* **1987,** *87* (9), 5541-5553.

163. Vogg, G.; Brandt, M. S.; Stutzmann, M., Kinetics of the Topotactic Formation of Siloxene. *Chem. Mater.* **2003,** *15* (4), 910-915.

164. Brune, H., Microscopic view of epitaxial metal growth: nucleation and aggregation. *Surf. Sci. Rep.* **1998,** *31* (4), 125-229.

165. Tomellini, M.; Fanfoni, M., Kinetics of Clustering on Surfaces. In *Interfacial Science - A chemistry for the 21st Century' Monograph*, Roberts, M. W., Ed. 1997; pp 129-161.

166. Koller, G.; Berkebile, S.; Oehzelt, M.; Puschnig, P.; Ambrosch-Draxl, C.; Netzer, F. P.; Ramsey, M. G., Intra- and Intermolecular Band Dispersion in an Organic Crystal. *Science* **2007,** *317* (5836), 351-355.

167. Puschnig, P.; Berkebile, S.; Fleming, A. J.; Koller, G.; Emtsev, K.; Seyller, T.; Riley, J. D.; Ambrosch-Draxl, C.; Netzer, F. P.; Ramsey, M. G., Reconstruction of Molecular Orbital Densities from Photoemission Data. *Science* **2009,** *326* (5953), 702-706.

168. Wießner, M.; Hauschild, D.; Sauer, C.; Feyer, V.; Schöll, A.; Reinert, F., Complete determination of molecular orbitals by measurement of phase symmetry and electron density. *Nat. Commun.* **2014,** *5*, 4156.

169. Galeotti, G.; Di Giovannantonio, M.; Lipton-Duffin, J.; Ebrahimi, M.; Tebi, S.; Verdini, A.; Floreano, L.; Fagot-Revurat, Y.; Perepichka, D.; Rosei, F.; Contini, G., The role of halogens in on-surface Ullmann polymerization. *Farad. Discuss.* **2017**, *204*, 453-469.

170. Galeotti, G.; Di Giovannantonio, M.; Lipton-Duffin, J.; Ebrahimi, M.; Tebi, S.; Verdini, A.; Floreano, L.; Fagot-Revurat, Y.; Perepichka, D. F.; Rosei, F.; Contini, G., The role of halogens in on-surface Ullmann polymerization. *Faraday Discuss.* **2017,** *204* (0), 453-469.

171. Suss-Fink, G.; Meister, G., Transition Metal Clusters In Homogeneous Catalysis. In *Advances in Organometallic Chemistry*, Stone, F. G. A.; West, R., Eds. Academic Press: 1993; Vol. 35, pp 41-134.

172. Fan, Q.; Liu, L.; Dai, J.; Wang, T.; Ju, H.; Zhao, J.; Kuttner, J.; Hilt, G.; Gottfried, J. M.; Zhu, J., Surface Adatom Mediated Structural Transformation in Bromoarene Monolayers: Precursor Phases in Surface Ullmann Reaction. *ACS Nano* **2018,** *12* (3), 2267-2274.

173. Shu, C.-H.; Zhang, S.-Z.; Wang, C.-X.; Chen, J.-L.; He, Y.; Shi, K.-J.; Liu, P.-N., Diverse supramolecular structures self-assembled by a simple aryl chloride on Ag(111) and Cu(111). *Chem. Commun.* **2018,** *54* (97), 13670-13673.

174. Shchyrba, A.; Wäckerlin, C.; Nowakowski, J.; Nowakowska, S.; Björk, J.; Fatayer, S.; Girovsky, J.; Nijs, T.; Martens, S. C.; Kleibert, A.; Stöhr, M.; Ballav, N.; Jung, T. A.; Gade, L. H., Controlling the Dimensionality of On-Surface Coordination Polymers via Endo- or Exoligation. *J. Am. Chem. Soc.* **2014,** *136* (26), 9355-9363.

175. Urgel, J. I.; Écija, D.; Lyu, G.; Zhang, R.; Palma, C.-A.; Auwärter, W.; Lin, N.; Barth, J. V., Quasicrystallinity expressed in two-dimensional coordination networks. *Nat. Chem.* **2016,** *8*, 657.

176. Écija, D.; Urgel, J. I.; Seitsonen, A. P.; Auwärter, W.; Barth, J. V., Lanthanide-Directed Assembly of Interfacial Coordination Architectures–From Complex Networks to Functional Nanosystems. *Acc. Chem. Res.* **2018,** *51* (2), 365-375.

177. Dong, L.; Gao, Z. A.; Lin, N., Self-assembly of metal–organic coordination structures on surfaces. *Prog. Surf. Sci.* **2016,** *91* (3), 101-135.

178. De Oteyza, D. G.; Rogero, C., *On-Surface Synthesis II*. Springer International Publishing: 2018.

179. Gourdon, A., *On-Surface Synthesis*. Springer International Publishing: 2016.

180. Leung, L.; Lim, T.; Ning, Z.; Polanyi, J. C., Localized Reaction at a Smooth Metal Surface: p-Diiodobenzene at Cu(110). *J. Am. Chem. Soc.* **2012,** *134* (22), 9320-9326.

181. Eisenstein, A.; Leung, L.; Lim, T.; Ning, Z.; Polanyi, J. C., Reaction dynamics at a metal surface; halogenation of Cu(110). *Faraday Discuss.* **2012,** *157* (0), 337-353.

182. Chen, M.; Xiao, J.; Steinrück, H.-P.; Wang, S.; Wang, W.; Lin, N.; Hieringer, W.; Gottfried, J. M., Combined Photoemission and Scanning Tunneling Microscopy Study of the Surface-Assisted Ullmann Coupling Reaction. *J. Phys. Chem. C* **2014,** *118* (13), 6820-6830.

183. Eichhorn, J.; Strunskus, T.; Rastgoo-Lahrood, A.; Samanta, D.; Schmittel, M.; Lackinger, M., On-surface Ullmann polymerization via intermediate organometallic networks on Ag(111). *Chem. Commun.* **2014,** *50* (57), 7680-7682.

184. Shi, K. J.; Yuan, D. W.; Wang, C. X.; Shu, C. H.; Li, D. Y.; Shi, Z. L.; Wu, X. Y.; Liu, P. N., Ullmann Reaction of Aryl Chlorides on Various Surfaces and the Application in Stepwise Growth of 2D Covalent Organic Frameworks. *Organic Letters* **2016,** *18* (6), 1282-1285.

185. Sheppard, T. D., Metal-catalysed halogen exchange reactions of aryl halides. *Org. Biomol. Chem.* **2009,** *7* (6), 1043-1052.

186. Blanksby, S. J.; Ellison, G. B., Bond Dissociation Energies of Organic Molecules. *Acc. Chem. Res.* **2003,** *36* (4), 255-263.

187. Andryushechkin, B. V.; Eltsov, K. N.; Shevlyuga, V. M., Atomic structure of chemisorbed iodine layer on Cu(1 1 0). *Surf. Sci.* **2005,** *584* (2–3), 278-286.

188. Yang, M. X.; Xi, M.; Yuan, H.; Bent, B. E.; Stevens, P.; White, J. M., NEXAFS studies of halobenzenes and phenyl groups on Cu(111). *Surf. Sci.* **1995,** *341* (1), 9-18.

189. Novak, J.; Oehzelt, M.; Berkebile, S.; Koini, M.; Ules, T.; Koller, G.; Haber, T.; Resel, R.; Ramsey, M. G., Crystal growth of para-sexiphenyl on clean and oxygen reconstructed Cu(110) surfaces. *Phys. Chem. Chem. Phys.* **2011,** *13* (32), 14675-14684.

190. Stickney, J. L.; Ehlers, C. B.; Gregory, B. W., Adsorption of gaseous and aqueous hydrochloric acid on the low-index planes of copper. *Langmuir* **1988,** *4* (6), 1368-1373.

191. Wan, L.-J.; Itaya, K., In situ scanning tunneling microscopy of Cu(110): atomic structures of halide adlayers and anodic dissolution. *J. Electroanal. Chem.* **1999,** *473* (1–2), 10-18.

192. Rosei, F., Nanostructured surfaces: challenges and frontiers in nanotechnology. *J. Phys. Condens. Matter* **2004,** *16* (17), S1373.

193. Sakamoto, J.; van Heijst, J.; Lukin, O.; Schlüter, A. D., Two-Dimensional Polymers: Just a Dream of Synthetic Chemists? *Angew. Chem. Int. Ed.* **2009,** *48* (6), 1030-1069.

194. Franc, G.; Gourdon, A., Covalent networks through on-surface chemistry in ultra-high vacuum: state-of-the-art and recent developments. *Phys. Chem. Chem. Phys.* **2011,** *13* (32), 14283-14292.

195. Perepichka, I. F.; Perepichka, D. F.; Meng, H., Thiophene-Based Materials for Electroluminescent Applications. In *Handbook of Thiophene-Based Materials*, John Wiley & Sons, Ltd: 2009; pp 695-756.

196. Nacci, C.; Ample, F.; Bleger, D.; Hecht, S.; Joachim, C.; Grill, L., Conductance of a single flexible molecular wire composed of alternating donor and acceptor units. *Nat. Commun.* **2015,** *6*, 7397.

197. Gutzler, R.; Cardenas, L.; Lipton-Duffin, J.; El Garah, M.; Dinca, L. E.; Szakacs, C. E.; Fu, C.; Gallagher, M.; Vondracek, M.; Rybachuk, M.; Perepichka, D. F.; Rosei, F., Ullmann-type coupling of brominated tetrathienoanthracene on copper and silver. *Nanoscale* **2014,** *6* (5), 2660-2668.

198. Pham, T. A.; Song, F.; Nguyen, M.-T.; Li, Z.; Studener, F.; Stöhr, M., Comparing Ullmann Coupling on Noble Metal Surfaces: On-Surface Polymerization of 1,3,6,8-Tetrabromopyrene on Cu(111) and Au(111). *Chem. - Eur. J* **2016,** *22* (17), 5937-5944.

199. Sun, Q.; Cai, L.; Ma, H.; Yuan, C.; Xu, W., Dehalogenative Homocoupling of Terminal Alkynyl Bromides on Au(111): Incorporation of Acetylenic Scaffolding into Surface Nanostructures. *ACS Nano* **2016,** *10* (7), 7023-7030.

200. Saywell, A.; Greń, W.; Franc, G.; Gourdon, A.; Bouju, X.; Grill, L., Manipulating the Conformation of Single Organometallic Chains on Au(111). *J. Phys. Chem. C* **2014,** *118* (3), 1719-1728.

201. Liu, M.; Liu, M.; She, L.; Zha, Z.; Pan, J.; Li, S.; Li, T.; He, Y.; Cai, Z.; Wang, J.; Zheng, Y.; Qiu, X.; Zhong, D., Graphene-like nanoribbons periodically embedded with four- and eight-membered rings. *Nat. Commun.* **2017,** *8*, 14924.

202. Liu, J.; Ruffieux, P.; Feng, X.; Mullen, K.; Fasel, R., Cyclotrimerization of arylalkynes on Au(111). *Chem. Commun.* **2014,** *50* (76), 11200-11203.

203. Pham, T. A.; Song, F.; Stohr, M., Supramolecular self-assembly of metal-free naphthalocyanine on Au(111). *Phys. Chem. Chem. Phys.* **2014,** *16* (19), 8881-8885.

204. Luo, Y.-R., *Comprehensive handbook of chemical bond energies*. CRC press: 2007.

205. MacLeod, J. M.; Ivasenko, O.; Fu, C.; Taerum, T.; Rosei, F.; Perepichka, D. F., Supramolecular Ordering in Oligothiophene−Fullerene Monolayers. *J. Am. Chem. Soc.* **2009,** *131* (46), 16844-16850.

206. Walen, H.; Liu, D.-J.; Oh, J.; Lim, H.; Evans, J. W.; Kim, Y.; Thiel, P. A., Reconstruction of steps on the Cu(111) surface induced by sulfur. *J. Chem. Phys.* **2015,** *142* (19), 194711.

207. Ulman, A., Formation and Structure of Self-Assembled Monolayers. *Chem. Rev.* **1996,** *96* (4), 1533-1554.

208. Hammer, B.; Norskov, J. K., Why gold is the noblest of all the metals. *Nature* **1995,** *376* (6537), 238-240.

209. Di Bernardo, I.; Hines, P.; Abyazisani, M.; Motta, N.; MacLeod, J.; Lipton-Duffin, J., On-surface synthesis of polyethylenedioxythiophene. *Chem. Commun.* **2018,** *54* (30), 3723-3726.

210. Abyazisani, M.; Bradford, J.; Motta, N.; Lipton-Duffin, J.; MacLeod, J., Adsorption and Reactivity of Pyridine Dicarboxylic Acid on Cu(111). *J. Phys. Chem. C* **2018,** *122* (31), 17836-17845.

211. Furukawa, H.; Cordova, K. E.; O'Keeffe, M.; Yaghi, O. M., The Chemistry and Applications of Metal-Organic Frameworks. *Science* **2013,** *341* (6149).

212. Zhou, H.-C.; Long, J. R.; Yaghi, O. M., Introduction to Metal–Organic Frameworks. *Chemical Reviews* **2012,** *112* (2), 673-674.

213. Rosei, F.; Schunack, M.; Naitoh, Y.; Jiang, P.; Gourdon, A.; Laegsgaard, E.; Stensgaard, I.; Joachim, C.; Besenbacher, F., Properties of large organic molecules on metal surfaces. *Progr. Surf. Sci.* **2003,** *71* (5–8), 95-146.

214. Nath, K. G.; Ivasenko, O.; Miwa, J. A.; Dang, H.; Wuest, J. D.; Nanci, A.; Perepichka, D. F.; Rosei, F., Rational Modulation of the Periodicity in Linear Hydrogen-Bonded Assemblies of Trimesic Acid on Surfaces. *J. Am. Chem. Soc.* **2006,** *128* (13), 4212-4213.

215. MacLeod, J. M.; Ivasenko, O.; Perepichka, D. F.; Rosei, F., Stabilization of exotic minority phases in a multicomponent self-assembled molecular network. *Nanotechnology* **2007,** *18* (42), 424031.

216. Lackinger, M.; Griessl, S.; Heckl, W. M.; Hietschold, M.; Flynn, G. W., Self-Assembly of Trimesic Acid at the Liquid−Solid Interfacea Study of Solvent-Induced Polymorphism. *Langmuir* **2005,** *21* (11), 4984-4988.

217. Gutzler, R.; Fu, C.; Dadvand, A.; Hua, Y.; MacLeod, J. M.; Rosei, F.; Perepichka, D. F., Halogen bonds in 2D supramolecular self-assembly of organic semiconductors. *Nanoscale* **2012,** *4* (19), 5965-5971.

218. Gatti, R.; MacLeod, J. M.; Lipton-Duffin, J. A.; Moiseev, A. G.; Perepichka, D. F.; Rosei, F., Substrate, Molecular Structure, and Solvent Effects in 2D Self-Assembly via Hydrogen and Halogen Bonding. *J. Phys. Chem. C* **2014,** *118* (44), 25505-25516.

219. Nath, K. G.; Ivasenko, O.; MacLeod, J. M.; Miwa, J. A.; Wuest, J. D.; Nanci, A.; Perepichka, D. F.; Rosei, F., Crystal Engineering in Two Dimensions: An Approach to Molecular Nanopatterning. *J. Phys. Chem. C* **2007,** *111* (45), 16996-17007.

220. Mali, K. S.; Lava, K.; Binnemans, K.; De Feyter, S., Hydrogen Bonding Versus van der Waals Interactions: Competitive Influence of Noncovalent Interactions on 2D Self-Assembly at the Liquid–Solid Interface. *Chem. - Eur. J* **2010,** *16* (48), 14447-14458.

221. Liao, L.-y.; Li, Y.-b.; Xu, J.; Geng, Y.-f.; Zhang, J.-y.; Xie, J.-l.; Zeng, Q.-d.; Wang, C., Competitive Influence of Hydrogen Bonding and van der Waals Interactions on Self-Assembled Monolayers of Stilbene-Based Carboxylic Acid Derivatives. *J. Phys. Chem. C* **2014,** *118* (49), 28625-28630.

222. Grimme, S., Do Special Noncovalent π–π Stacking Interactions Really Exist? *Angew. Chem., Int. Ed.* **2008,** *47* (18), 3430-3434.

223. Baris, B.; Luzet, V.; Duverger, E.; Sonnet, P.; Palmino, F.; Cherioux, F., Robust and Open Tailored Supramolecular Networks Controlled by the Template Effect of a Silicon Surface. *Angew. Chem., Int. Ed.* **2011,** *50* (18), 4094-4098.

224. Cicoira, F.; Santato, C.; Rosei, F., Two-Dimensional Nanotemplates as Surface Cues for the Controlled Assembly of Organic Molecules. In *STM and AFM Studies on (Bio)molecular Systems: Unravelling the Nanoworld*, Samorì, P., Ed. Springer Berlin Heidelberg: Berlin, Heidelberg, 2008; pp 203-267.

225. Mali, K. S.; Adisoejoso, J.; Ghijsens, E.; De Cat, I.; De Feyter, S., Exploring the Complexity of Supramolecular Interactions for Patterning at the Liquid–Solid Interface. *Acc. Chem. Res.* **2012,** *45* (8), 1309-1320.

226. Hirshfeld, F. L.; Schmidt, G. M. J., Topochemical control of solid-state polymerization. *J. Polym. Sci., Part A: Gen. Pap.* **1964,** *2* (5), 2181-2190.

227. Colson, J. W.; Dichtel, W. R., Rationally synthesized two-dimensional polymers. *Nat. Chem.* **2013,** *5* (6), 453-465.

228. Ozaki, H.; Kasuga, M.; Tsuchiya, T.; Funaki, T.; Mazaki, Y.; Aoki, M.; Masuda, S.; Harada, Y., Formation of atomic cloth observed by Penning ionization electron spectroscopy. *J. Chem. Phys.* **1995,** *103* (3), 1226-1228.

229. Takami, T.; Ozaki, H.; Kasuga, M.; Tsuchiya, T.; Ogawa, A.; Mazaki, Y.; Fukushi, D.; Uda, M.; Aono, M., Periodic Structure of a Single Sheet of a Clothlike Macromolecule (Atomic Cloth) Studied by Scanning Tunneling Microscopy. *Angew. Chem. Int. Ed.* **1997,** *36* (24), 2755-2757.

230. Mandal, S. K.; Okawa, Y.; Hasegawa, T.; Aono, M., Rate-Determining Factors in the Chain Polymerization of Molecules Initiated by Local Single-Molecule Excitation. *ACS Nano* **2011,** *5* (4), 2779-2786.

231. Okawa, Y.; Akai-Kasaya, M.; Kuwahara, Y.; Mandal, S. K.; Aono, M., Controlled chain polymerisation and chemical soldering for single-molecule electronics. *Nanoscale* **2012,** *4* (10), 3013-3028.

232. Okawa, Y.; Aono, M., Linear chain polymerization initiated by a scanning tunneling microscope tip at designated positions. *J. Chem. Phys.* **2001,** *115* (5), 2317-2322.

233. Miura, A.; De Feyter, S.; Abdel-Mottaleb, M. M. S.; Gesquière, A.; Grim, P. C. M.; Moessner, G.; Sieffert, M.; Klapper, M.; Müllen, K.; De Schryver, F. C., Light- and STM-Tip-Induced Formation of One-Dimensional and Two-Dimensional Organic Nanostructures. *Langmuir* **2003,** *19* (16), 6474-6482.

234. Muraoka, T.; Kinbara, K.; Aida, T., Mechanical twisting of a guest by a photoresponsive host. *Nature* **2006,** *440* (7083), 512-515.

235. Grim, P. C. M.; De Feyter, S.; Gesquière, A.; Vanoppen, P.; Rüker, M.; Valiyaveettil, S.; Moessner, G.; Müllen, K.; De Schryver, F. C., Submolecularly Resolved Polymerization of Diacetylene Molecules on the Graphite Surface Observed with Scanning Tunneling Microscopy. *Angew. Chem., Int. Ed.* **1997,** *36* (23), 2601-2603.

236. MacLeod, J. M.; Lipton-Duffin, J.; Fu, C.; Rosei, F., Inducing Nonlocal Reactions with a Local Probe. *ACS Nano* **2009,** *3* (11), 3347-3351.

237. Bohme, D. K., PAH [polycyclic aromatic hydrocarbons] and fullerene ions and ion/molecule reactions in interstellar and circumstellar chemistry. *Chem. Rev.* **1992,** *92* (7), 1487-1508.

238. Baccarelli, I.; Sebastianelli, F.; Nestmann, B. M.; Gianturco, F. A., Forming metastable carbon-rich anions in planetary atmospheres: the case of diacetylene. *Eur. Phys. J. D* **2013,** *67* (5), 93.

239. Kołos, R.; Grabowski, Z. R., The chemistry and prospects for interstellar detection of somedicyanoacetylenes and other cyanoacetylene-related species. *Astrophys. Space Sci.* **2000,** *271* (1), 65-72.

240. Morigaki, K.; Baumgart, T.; Jonas, U.; Offenhäusser, A.; Knoll, W., Photopolymerization of Diacetylene Lipid Bilayers and Its Application to the Construction of Micropatterned Biomimetic Membranes. *Langmuir* **2002,** *18* (10), 4082-4089.

241. Kim, J.-H.; Lee, E.; Jeong, Y.-H.; Jang, W.-D., Unique Photoluminescence of Diacetylene Containing Dendrimer Self-Assemblies: Application in Positive and Negative Luminescence Patterning. *Chem. Mat.* **2012,** *24* (12), 2356-2363.

242. Wu, S. T.; Margerum, J. D.; Meng, H. B.; Dalton, L. R.; Hsu, C. S.; Lung, S. H., Room-temperature diphenyl-diacetylene liquid crystals. *Appl. Phys. Lett.* **1992,** *61* (6), 630-632.

243. Wu, S. T.; Hsu, C. S.; Chen, Y. N.; Wang, S. R., Fluorinated diphenyl-diacetylene and tolane liquid crystals with low threshold voltage. *Appl. Phys. Lett.* **1992,** *61* (19), 2275-2277.

244. Wu, S. T.; Margerum, J. D.; Meng, H. H. B.; Dalton, L. R., Asymmetrical nonpolar diphenyl-diacetylene liquid crystals eutectic mixtures. Google Patents: 1994.

245. Zaera, F., Chiral Modification of Solid Surfaces: A Molecular View. *J. Phys. Chem. C* **2008,** *112* (42), 16196-16203.

246. Gellman, A. J.; Tysoe, W. T.; Zaera, F., Surface Chemistry for Enantioselective Catalysis. *Catal. Lett.* **2015,** *145* (1), 220-232.

247. Gellman, A. J., Chiral Surfaces: Accomplishments and Challenges. *ACS Nano* **2010,** *4* (1), 5-10.

248. Hicks, J. M.; Petralli-Mallow, T., Nonlinear optics of chiral surface systems. *Appl. Phys. B* **1999,** *68* (3), 589-593.

249. Mena-Osteritz, E.; Bäuerle, P., Self-Assembled Hexagonal Nanoarrays of Novel Macrocyclic Oligothiophene-Diacetylenes. *Adv. Mater.* **2001,** *13* (4), 243-246.

250. Schlickum, U.; Decker, R.; Klappenberger, F.; Zoppellaro, G.; Klyatskaya, S.; Auwärter, W.; Neppl, S.; Kern, K.; Brune, H.; Ruben, M.; Barth, J. V., Chiral Kagomé Lattice from Simple Ditopic Molecular Bricks. *J. Am. Chem. Soc.* **2008,** *130* (35), 11778-11782.

251. Schlickum, U.; Klappenberger, F.; Decker, R.; Zoppellaro, G.; Klyatskaya, S.; Ruben, M.; Kern, K.; Brune, H.; Barth, J. V., Surface-Confined Metal−Organic Nanostructures from Co-Directed Assembly of Linear Terphenyl-dicarbonitrile Linkers on Ag(111). *J. Phys. Chem. C* **2010,** *114* (37), 15602-15606.

252. Klyatskaya, S.; Klappenberger, F.; Schlickum, U.; Kühne, D.; Marschall, M.; Reichert, J.; Decker, R.; Krenner, W.; Zoppellaro, G.; Brune, H.; Barth, J. V.; Ruben, M., Surface-Confined Self-Assembly of Di-carbonitrile Polyphenyls. *Adv. Funct. Mater.* **2011,** *21* (7), 1230-1240.

253. Kühne, D.; Klappenberger, F.; Decker, R.; Schlickum, U.; Brune, H.; Klyatskaya, S.; Ruben, M.; Barth, J. V., Self-Assembly of Nanoporous Chiral Networks with Varying Symmetry from Sexiphenyl-dicarbonitrile on Ag(111). *J. Phys. Chem. C* **2009,** *113* (41), 17851-17859.

254. Marschall, M.; Reichert, J.; Diller, K.; Klyatskaya, S.; Ruben, M.; Nefedov, A.; Wöll, C.; Kantorovich, L. N.; Klappenberger, F.; Barth, J. V., Meta-Positioning of Carbonitrile Functional Groups Induces Interfacial Edge-On Phase of Oligophenyl Derivatives. *J. Phys. Chem. C* **2014,** *118* (5), 2622-2633.

255. Marschall, M.; Reichert, J.; Seufert, K.; Auwärter, W.; Klappenberger, F.; Weber-Bargioni, A.; Klyatskaya, S.; Zoppellaro, G.; Nefedov, A.; Strunskus, T.; Wöll, C.; Ruben, M.; Barth, J. V., Supramolecular Organization and Chiral Resolution of p-Terphenyl-m-Dicarbonitrile on the Ag(111) Surface. *ChemPhysChem* **2010,** *11* (7), 1446-1451.

256. Arras, E.; Seitsonen, A. P.; Klappenberger, F.; Barth, J. V., Nature of the attractive interaction between proton acceptors and organic ring systems. *Phys. Chem. Chem. Phys.* **2012,** *14* (46), 15995-16001.

257. Nakayama, T.; Inamura, K.; Inoue, Y.; Ikeda, S.; Kishi, K., Adsorption of benzonitrile and alkyl cyanides on evaporated nickel and palladium films studied by XPS. *Surf. Sci.* **1987,** *179* (1), 47-58.

258. Smith, N. V.; Chen, C. T.; Weinert, M., Distance of the image plane from metal surfaces. *Phys. Rev. B* **1989,** *40* (11), 7565-7573.

259. Sánchez-Sánchez, C.; Yubero, F.; González-Elipe, A. R.; Feria, L.; Sanz, J. F.; Lambert, R. M., The Flexible Surface Revisited: Adsorbate-Induced Reconstruction, Homocoupling, and

Sonogashira Cross-Coupling on the Au(100) Surface. *J. Phys. Chem. C* **2014,** *118* (22), 11677-11684.

260. Carbone, M.; Caminiti, R., ADSORPTION STATES AND SITE CONVERSIONS OF PHENYLACETYLENE ON Si(100)2 × 1 CALCULATED BY DFT. *J. Theor. Comput. Chem.* **2012,** *11* (05), 1089-1099.
261. Liu, W.; Carrasco, J.; Santra, B.; Michaelides, A.; Scheffler, M.; Tkatchenko, A., Benzene adsorbed on metals: Concerted effect of covalency and van der Waals bonding. *Phys. Rev. B* **2012,** *86* (24), 245405.
262. Yan, J.; Fan, Z.; Sun, W.; Ning, G.; Wei, T.; Zhang, Q.; Zhang, R.; Zhi, L.; Wei, F., Advanced asymmetric supercapacitors based on Ni (OH) 2/graphene and porous graphene electrodes with high energy density. *Advanced Functional Materials* **2012,** *22* (12), 2632-2641.
263. Wegner, G., Topochemical reactions of monomers with conjugated triple bonds. III. Solid-state reactivity of derivatives of diphenyldiacetylene. *J. Polym. Sci., Part B: Polym. Lett.* **1971,** *9* (2), 133-144.
264. Kaiser, J.; Wegner, G.; Fischer, E. W., Topochemical Reactions of Monomers with Conjugated Triple-Bonds VII Mechanism of Transition from Monomer to Polymer Phase During Solid-State Polymerisation. *Isr. J. Chem.* **1972,** *10* (2), 157-171.
265. Kiji, J.; Kaiser, J.; Wegner, G.; Schulz, R. C., Solid-state polymerization of derivatives of 2,4,6-octatriyne: 9. Topochemical reactions of monomers with conjugated triple bonds. *Polymer* **1973,** *14* (9), 433-439.
266. Kojima, Y.; Matsuoka, T.; Takahashi, H., Electrorheological properties of suspension of diphenyldiacetylene annealed under elevated pressure. *J. Appl. Polym. Sci.* **1994,** *53* (10), 1393-1396.
267. Kojima, Y.; Matsuoka, T.; Takahashi, H., High-pressure solid-state polymerization of diphenyldiacetylene. *J. Mater. Sci. Lett.* **1996,** *15* (6), 539-541.
268. Wegner, G., Topochemical reactions of monomers with conjugated triple-bonds. IV. Polymerization of bis-(p-toluene sulfonate) of 2.4-hexadiin-1.6-diol. *Makromol. Chem.* **1971,** *145* (1), 85-94.
269. Liu, W.; Luo, X.; Bao, Y.; Liu, Y. P.; Ning, G.-H.; Abdelwahab, I.; Li, L.; Nai, C. T.; Hu, Z. G.; Zhao, D.; Liu, B.; Quek, S. Y.; Loh, K. P., A two-dimensional conjugated aromatic polymer via C–C coupling reaction. *Nat. Chem.* **2017**.
270. Ebrahimi, M.; Rosei, F., Materials science: Organic analogues of graphene. *Nature* **2017,** *542* (7642), 423-424.
271. Baughman, R. H., Solid-state synthesis of large polymer single crystals. *J. Polym. Sci. Polym. Phys. Ed.* **1974,** *12* (8), 1511-1535.
272. Takajo, D.; Inaba, A.; Sudoh, K., Two polymorphic forms of 10,12-pentacosadiyn-1-ol molecular layers on graphite transferred from an aqueous surface. *Surf. Sci.* **2014,** *620*, 38-44.

273. Takajo, D.; Inaba, A.; Sudoh, K., Two-Dimensional Solid-State Topochemical Reactions of 10,12-Pentacosadiyn-1-ol Adsorbed on Graphite. *Langmuir* **2014,** *30* (10), 2738-2744.

274. Iucci, G.; Carravetta, V.; Altamura, P.; Russo, M. V.; Paolucci, G.; Goldoni, A.; Polzonetti, G., XPS, NEXAFS and theoretical study of phenylacetylene adsorbed on Cu(1 0 0). *Chem. Phys.* **2004,** *302* (1–3), 43-52.

275. Retzko, I.; Friedrich, J. F.; Lippitz, A.; Unger, W. E. S., Chemical analysis of plasma-polymerized films: The application of X-ray photoelectron spectroscopy (XPS), X-ray absorption spectroscopy (NEXAFS) and fourier transform infrared spectroscopy (FTIR). *J. Electron. Spectrosc. Relat. Phenom.* **2001,** *121* (1–3), 111-129.

276. Polzonetti, G.; Russo, M. V., H2O surface interaction of oxygen-free polyphenylacetylene films investigated by XPS. *J. Electron. Spectrosc. Relat. Phenom.* **1992,** *60* (4), R7-R14.

277. Kanuru, V. K.; Kyriakou, G.; Beaumont, S. K.; Papageorgiou, A. C.; Watson, D. J.; Lambert, R. M., Sonogashira coupling on an extended gold surface in vacuo: reaction of phenylacetylene with iodobenzene on Au(111). *J. Am. Chem. Soc.* **2010,** *132* (23), 8081-6.

278. Sohn, Y.; Wei, W.; White, J. M., Phenylacetylene on Cu(111): Adsorption Geometry, Interfacial Electronic Structures and Thermal Chemistry. *J. Phys. Chem. C* **2007,** *111* (13), 5101-5110.

279. Iucci, G.; Carravetta, V.; Paolucci, G.; Goldoni, A.; Russo, M. V.; Polzonetti, G., Phenylacetylene adsorption on Rh(1 0 0): a photoemission and photoabsorption investigation. *Chem. Phys.* **2005,** *310* (1–3), 43-49.

280. Solomon, J. L.; Madix, R. J.; Stöhr, J., Orientation and absolute coverage of benzene, aniline, and phenol on Ag(110) determined by NEXAFS and XPS. *Surf. Sci.* **1991,** *255* (1), 12-30.

281. Wang, S.; Wang, W.; Tan, L. Z.; Li, X. G.; Shi, Z.; Kuang, G.; Liu, P. N.; Louie, S. G.; Lin, N., Tuning two-dimensional band structure of Cu(111) surface-state electrons that interplay with artificial supramolecular architectures. *Phys. Rev. B* **2013,** *88* (24), 245430.

282. Wallet, F.; Dussert, C., Comparison of spatial point patterns and processes characterization methods. *EPL* **1998,** *42* (5), 493.

283. Dussert, C.; Rasigni, G.; Rasigni, M.; Palmari, J.; Llebaria, A., Minimal spanning tree: A new approach for studying order and disorder. *Phys. Rev. B* **1986,** *34* (5), 3528-3531.

284. Ourdjini, O.; Pawlak, R.; Abel, M.; Clair, S.; Chen, L.; Bergeon, N.; Sassi, M.; Oison, V.; Debierre, J.-M.; Coratger, R.; Porte, L., Substrate-mediated ordering and defect analysis of a surface covalent organic framework. *Phys. Rev. B* **2011,** *84* (12), 125421.

285. Billia, B.; Jamgotchian, H.; Nguyen Thi, H., Statistical analysis of the disorder of two-dimensional cellular arrays in directional solidification. *Metall. Mater. Trans. A* **1991,** *22* (12), 3041-3050.

286. Llinas, J. P.; Fairbrother, A.; Borin Barin, G.; Shi, W.; Lee, K.; Wu, S.; Yong Choi, B.; Braganza, R.; Lear, J.; Kau, N.; Choi, W.; Chen, C.; Pedramrazi, Z.; Dumslaff, T.; Narita, A.; Feng, X.; Müllen, K.; Fischer, F.; Zettl, A.; Ruffieux, P.; Yablonovitch, E.; Crommie, M.; Fasel, R.; Bokor, J., Short-channel field-effect transistors with 9-atom and 13-atom wide graphene nanoribbons. *Nat. Commun.* **2017,** *8* (1), 633.

287. Choon-Ming, S.; Brigitte, V.; Siang-Piao, C.; Abdul Rahman, M., Transfer of wafer-scale graphene onto arbitrary substrates: steps towards the reuse and recycling of the catalyst. *2D Materials* **2018,** *5* (4), 042001.

288. Jung, W.; Kim, D.; Lee, M.; Kim, S.; Kim, J.-H.; Han, C.-S., Ultraconformal Contact Transfer of Monolayer Graphene on Metal to Various Substrates. *Advanced Materials* **2014,** *26* (37), 6394-6400.

289. Bae, S.; Kim, H.; Lee, Y.; Xu, X.; Park, J.-S.; Zheng, Y.; Balakrishnan, J.; Lei, T.; Ri Kim, H.; Song, Y. I.; Kim, Y.-J.; Kim, K. S.; Özyilmaz, B.; Ahn, J.-H.; Hong, B. H.; Iijima, S., Roll-to-roll production of 30-inch graphene films for transparent electrodes. *Nat. Nanotechnol.* **2010,** *5*, 574.

290. Binnig, G.; Rohrer, H., Scanning tunneling microscopy. *Surface Science* **1983,** *126* (1), 236-244.

291. Cardenas, L.; Gutzler, R.; Lipton-Duffin, J.; Fu, C.; Brusso, J. L.; Dinca, L. E.; Vondracek, M.; Fagot-Revurat, Y.; Malterre, D.; Rosei, F.; Perepichka, D. F., Synthesis and electronic structure of a two dimensional [small pi]-conjugated polythiophene. *Chem. Sci.* **2013,** *4* (8), 3263-3268.

LIST OF TABLES

LIST OF FIGURES